ELECTRICAL RESISTANCE AND X-RAY DIFFRACTION STUDIES OF FACTORS AFFECTING THE FORMATION AND STABILITY OF THE SIGMA PHASE IN IRON BASED ALLOYS

A thesis presented for the degree of

DOCTOR OF PHILOSOPHY

in the

VICTORIA UNIVERSITY OF MANCHESTER

by

Gerald Montgomery Bedford, B.Sc.(Manchester)

October 1967.

ProQuest LLC.
789 East Eisenhower Parkway
P.O. Box 1346
Ann Arbor, MI 48106 – 1346

Summary of the author's education and experience

The author graduated in June 1963, B.Sc. Honours in Metallurgy, in the Faculty of Science of the University of Manchester. After spending one year in industry he has pursued full time research in the Metallurgy Department, in the Faculty of Technology, since October 1964, with the support of a grant from the Ministry of Technology (Aviation Department). During this time he has also attended courses in Physical Metallurgy and Computer Programming, and has been a part-time demonstrator in the Metallurgy Department.

ACKNOWLEDGEMENTS

The author is indebted to his supervisor Dr. W. J. Kitchingman for the constant help and advice received throughout the work. He would like to thank Dr. W. D. Hoff for the many invaluable discussions on the computation procedures and also members of the staff of the Metallurgy Department for some helpful discussions.

The author is also grateful to Professor K. M. Entwistle, Head of the Department of Metallurgy for the facilities provided, and to the Ministry of Technology (Aviation Department) for financial support.

He acknowledges with thanks the cooperation and support of the laboratory staff.

ABSTRACT

The alpha to sigma transformation in an equiatomic iron-vanadium alloy and six ternary alloys based on iron-vanadium has been investigated by resistivity, X-ray diffraction and metallographic techniques. Variations of electrical resistivity with temperature suggest that ordering of the atoms plays an important part in the transformation. Isothermal transformation studies using electrical resistivity methods show that small percentages of ternary alloying elements only affect the TTT curves to a small degree. The curves suggest that more than one possible mechanism of the transformation occurs. Metallographic results indicate that there is no difference in the morphology of the product phase over the temperature range investigated. These results suggest that the transformation has some of the metallographic characteristics of a massive transformation. Accurate lattice parameters of both the body centred cubic and sigma structures have been determined for the binary and ternary alloys. They do not show any systematic changes with ternary alloying additions. Line broadening in the X-ray powder diffraction photographs of certain of the ternary alloys suggests that they may be capable of deformation.

CONTENTS

INTRODUCTION AND ORIGINS OF WORK

The sigma phase is hard and brittle, and non-magnetic at ordinary temperatures. Its structure is tetragonal with 30 atoms per unit cell.

Under certain conditions brought about by variations of composition and heat treatment the sigma phase may precipitate in heat resisting and complex steels of both the austenitic and the ferritic type. This can cause inferior mechanical properties leading to failure. Consequently the mechanism and conditions of its formation and the various aspects of the kinetics of its precipitation are of considerable interest. Furthermore alloy sigma phases are brittle whereas the structurally similar β-uranium and β-uranium with small alloying additions is relatively ductile and may be drawn into wire.

In theoretical metallurgy the fundamental reasons for the existence of a sigma phase in binary and ternary alloy systems constitute an important problem. The positions in the Periodic Table of the constituent atoms in alloy sigma phases governs the particular positions occupied in the structure. The relation between these facts, the brittleness of alloy sigma phases and the ductility of βU is not understood. The work in this thesis is an attempt to investigate these problems.

Previous investigators have studied the bcc → σ transformation in iron-chromium alloys and have found it to be very sluggish. The author has not been able to find any previous work on the kinetics of the transformation in the iron-vanadium system. Early experiments by the author in both these alloy systems showed that the transformation in the iron-vanadium alloys is more rapid, and hence is more suited to the available laboratory conditions.

In the present work the bcc → σ transformation in an equiatomic iron-vanadium alloy has been studied by means of electrical resistivity, X-ray diffraction and metallographic techniques. The effects of six separate additions on the formation and stability of the sigma phase in this alloy have also been investigated using the same techniques.

In the first three chapters the present knowledge of the sigma phase is reviewed followed by a detailed description of the past work on the bcc → σ transformation in iron-chromium alloys and a review of the theoretical considerations.

In succeeding chapters the development of apparatus has been traced along with specimen preparation and fabrication. This is followed by the results and a discussion of the results in terms of a possible model for the transformation. Some suggestions for future work have also been proposed.

CHAPTER 1

REVIEW OF PREVIOUS WORK

I THE SIGMA PHASE

Introduction

The hard, brittle and non-magnetic iron-chromium sigma phase was first reported by Bain in 1923 (1). Although, initially, the existence of this sigma phase was contradicted by other workers (3), probably because of the very sluggish nature of its formation, it was later adequately confirmed by several investigators (4,5,6). Since its discovery new sigma phases have been reported in many binary and ternary alloys of the transition elements (7,8,9).

Occurrence

All the currently known binary σ-phases are shown in Fig. (1). Each rectangle represents a binary system; the A components on the left belong to the V, Cr and Mn groups and are body-centred cubic; the B components on the right are either face-centred cubic or close-packed hexagonal and belong to the Mn, Fe, Co, Ni and Cu groups. The bar indicates the approximate composition ranges of the σ-phases. In some cases a dotted line is used to denote an unconfirmed report of a σ-phase. Technetium and rhenium are shown in ambivalent positions, acting as either A or B, for reasons to be discussed later. The currently known ternary σ-phases are listed in Fig. (2).

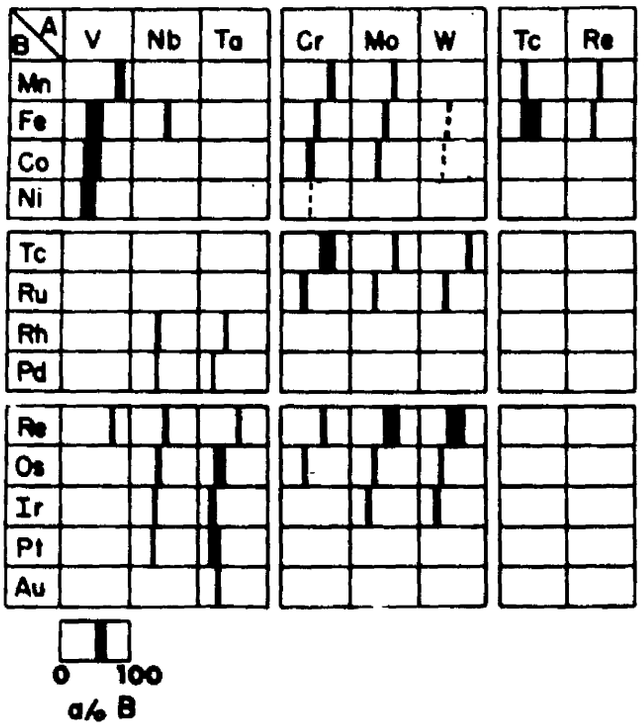

Occurrence of sigma phases in binary systems of transition metals.

Fig. 1

Ternary Sigma-Phase Studies

System	Ref.	Temp. of Section, °C
Two 1st Period + Group V:		
Mn–Fe + V	1	1000
Mn–Co + V	1	1000
Mn–Ni + V	1	1000
Fe–Co + V	1	1200
Fe–Ni + V	1	1200
Co–Ni + V	1	1200
Two 1st Period + Group VI		
Fe–Co + Cr	2	1200
Fe–Ni + Cr	3	650
Co–Ni + Cr	2	1200
Mn–Fe + Mo	4	1240
Mn–Co + Mo	4	1175
One 1st Period + Two Group VI:		
Fe + Cr–Mo	5	1300
	2	900
	6	600
Co + Cr–Mo	7	1300
	8	1200
	9	600
Ni + Cr–Mo	10	1250
	2	1200
	9	600
Fe + Cr–W	6	600
Ni + Cr–W	9	600
One 1st Period + Group V + Group VI		
Fe + V + Cr	11	700

System	Ref.	Temp. of Section, °C
C, N, and B Additions:		
Fe–Cr + C	12	
Fe–(Cr, Ni) + N	13	
Fe–(Cr, Ni) + B	14	
Al, Si, and P Additions		
Fe–V + Si	15	1175
Co–V + Si	15	1175
Ni–V + Si	15	1175
Mn–Cr + Si	15	1000
Co–Cr + Si	15	1175
Ni–Cr + Si	15	1175
Fe–Nb + Si	16	1000
Fe–V + Al	15	1175
Co–Cr + Al	15	1175
Fe–Cr + Al	17	
	18	
Ni–Cr + P	19	1050
2nd and 3rd Periods		
Re–Mo–Hf	20	2000
Re–Ta–W	21	2680
Re–Ta–Mo	22	1000 & 1500
Re–Mo–W	22	1000 & 1500
Re–Cr–W	22	1000
Os–Ta–W	22	1000 & 1500
Re–Os–W	22	1000 & 1500
Miscellaneous		
Nb–Al–Ti	23	1200
Ta–Al–Si	24	1400

Fig. 2

Crystallography

The crystal structure of the σ-phase has been carefully determined for several representative alloys (10,11,12). Its structure is tetragonal, belonging to the space group D_{4h}^{14} - $P4_2/mnm$ and containing 30 atoms per unit cell. The σ-phase has a characteristic powder diffraction pattern. It contains a group of about 8 strong lines with spacings close to 2Å, only a few very weak lines at larger spacings, and a few weak lines with spacings in the range 1.8 to 1.3Å. These general features are not unique to the σ-phase as similar powder diffraction patterns are given by other phases, such as the μ-phase (13,14,15) and the phases designated δ, P and R (16).

The structure of the σ-phase in projection on the (001) plane is shown as Fig. (7). It has been pointed out that the sigma structure is similar to that of β-uranium (17) and may be regarded as a simple layer structure Fig. (3). Two hexagonal nets at right angles form the main layers and in between these layers are the subsidiary, or diamond net layers. Atoms of successive diamond net layers are placed above and below the holes of the main layers. They have close contact with each other in the [001] direction forming straight rows perpendicular to the layers. The stacking sequence of the layers is ABACABAC, where A signifies a diamond net layer

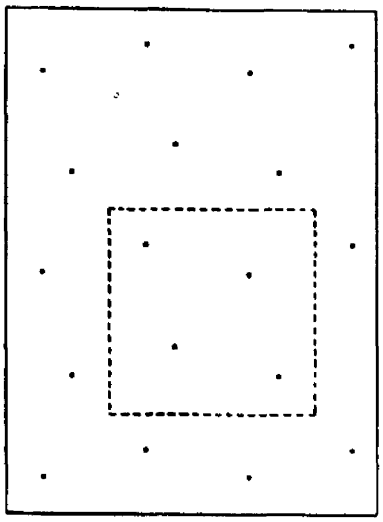

A-type layer (unit cell shown by broken lines).

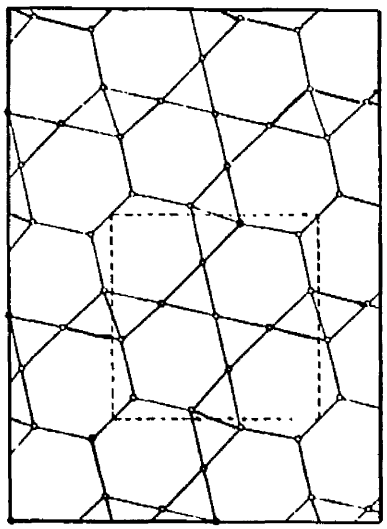

B-type layer (unit cell shown by broken lines).

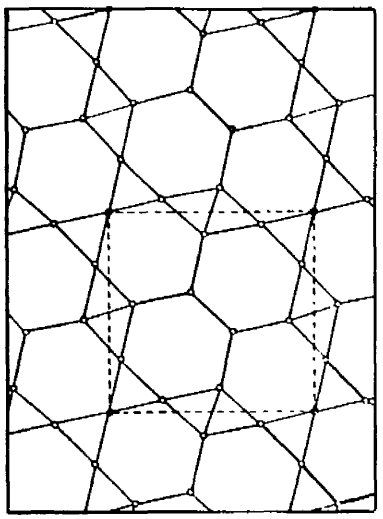

C-type layer (unit cell shown by broken lines).

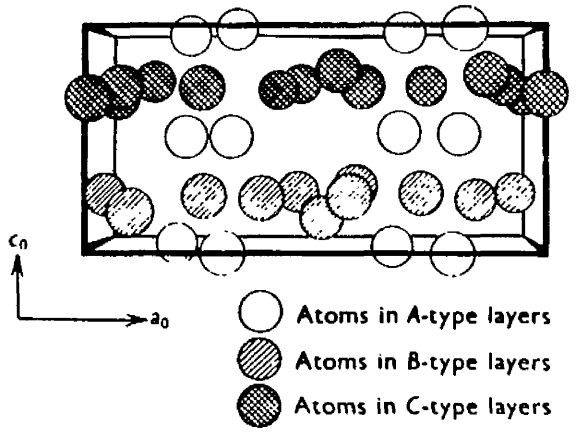

View of unit cell showing layer structure.

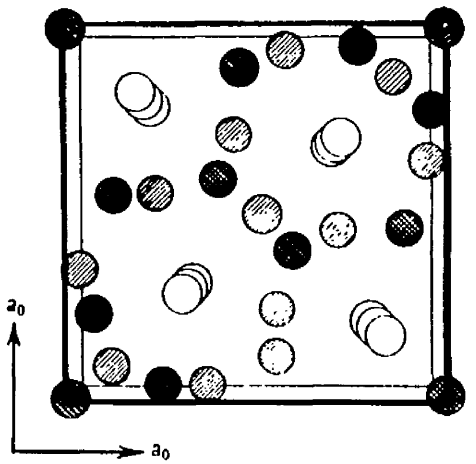

View of unit cell along fourfold axis.
Key as for Fig. 10.

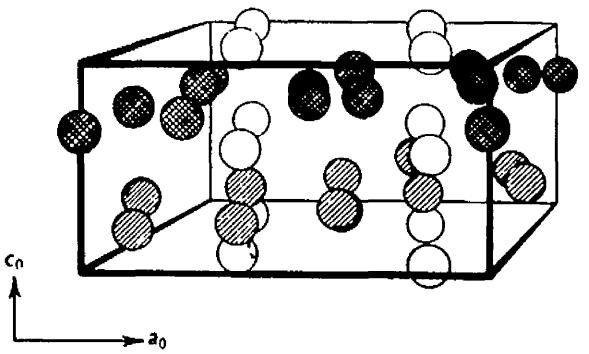

View of unit cell along (410) planes.

Fig. 3

and B and C hexagonal net layers, Fig. (3).

Recently Frank and Kasper (43) have shown that complex alloy structures, including the sigma and related phases, may be considered to be determined by the geometrical requirements for sphere packing. A characteristic of this class of structures is that tetrahedral groupings of atoms occur everywhere in the structure Fig. (4). Frank and Kasper (43) have discussed the general principles regarding the combination of these polyhedra into full structures as well as the nature and stacking of the layers termed "Kagomé-tiling" Fig. (5).

To facilitate the detailed discussion of the sigma structure, the model of its formation from the body-centred cubic structure and its brittleness, the general principles and definitions laid down by Frank and Kasper (43) have been outlined in the Appendix.

In accord with the notation of Frank and Kasper, the borders of the Kagome-tiling pattern of Fig. (5) together with the rows of atoms (4 per tile) normal to the plane represent the major skeleton of the σ-phase. Atoms at the tile corners are 15-coordinated and those in the tile edges and in the vertical rows are 14-coordinated. Alternate layers have the same Kagome-tiling but are rotated 90° relative to

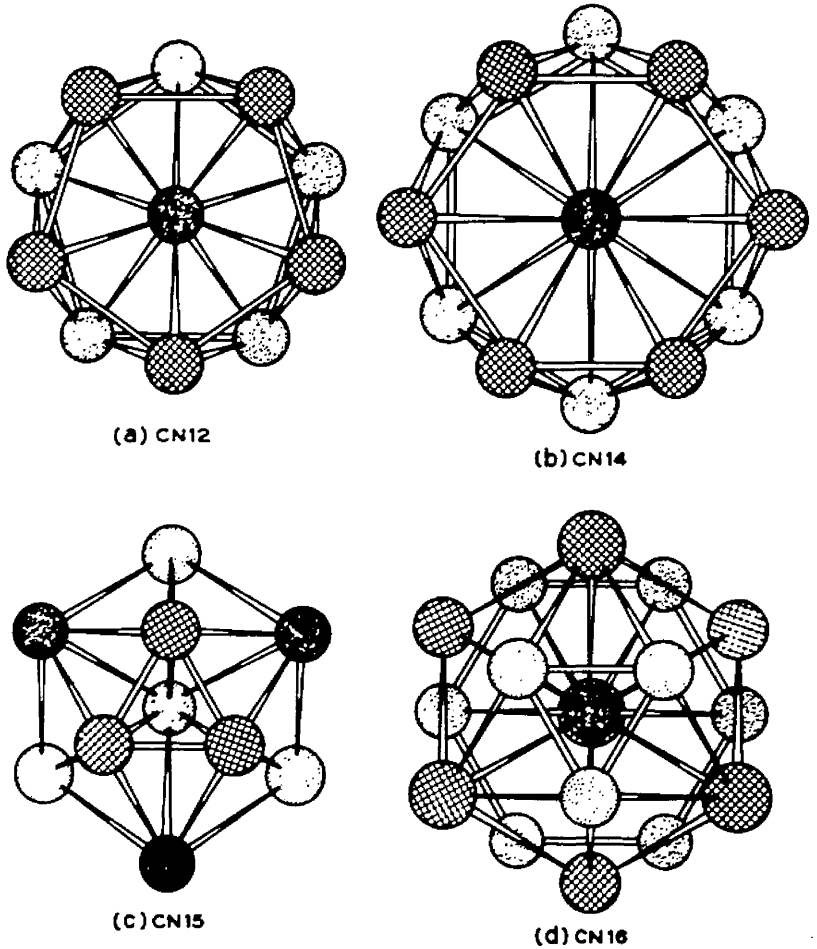

The four 'normal coordination polyhedra' of complex alloy structures. For C.N. 12, two spheres above and below the central sphere, along the fivefold axis, are not shown. Similarly, two spheres above and below the central one of C.N. 14, along the sixfold axis are not shown. For C.N. 16 one sphere below the central one is not shown.

(*a*) Icosahedron, C.N. 12. (*b*) C.N. 14. (*c*) C.N. 15. (*d*) C.N. 16.

Fig. 4

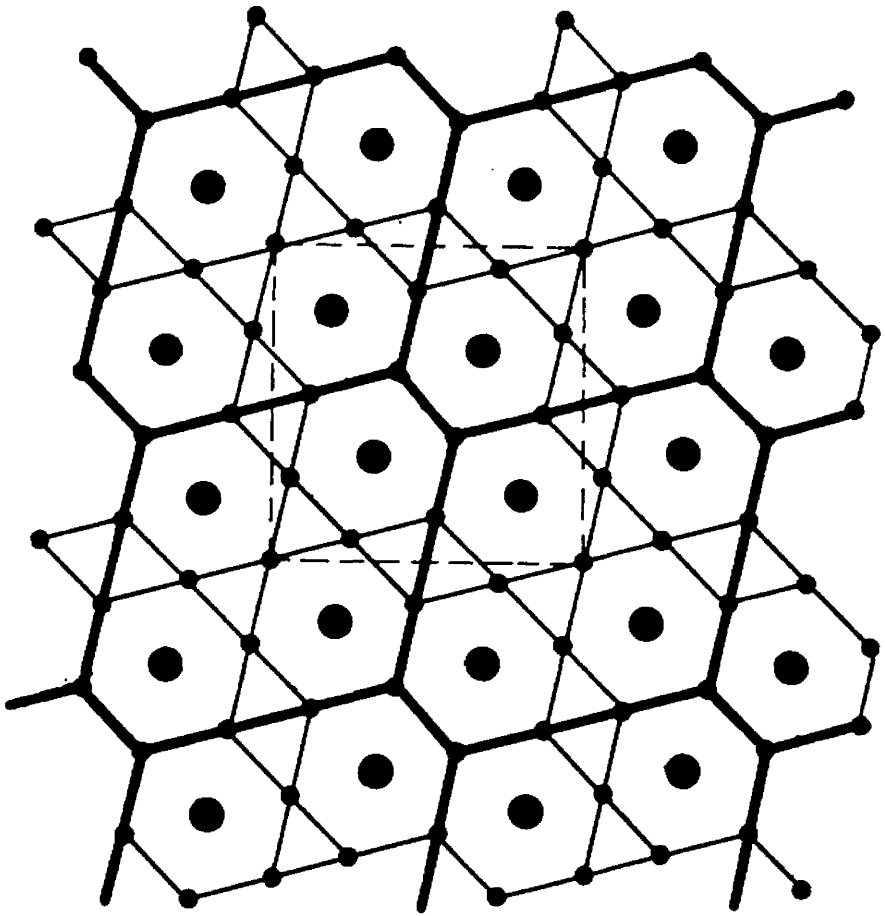

Kagomé tiling.

Fig. 5

one another. There is no connection between the layers in the structure of the skeleton.

Frank and Kasper also point out that the Kagomé-tiling may be dissected into hexagon strips termed right-handed R Fig. (6a) and left-handed L Fig. (6b). The vertical rows of triangle pairs are designated p. Two interesting features become apparent when the layers are analysed in this manner.

Firstly the sigma structure may be described in terms of R, L and p. It can be seen from Figs. (6ab) that the relationship between the two contiguous L's is plus while that between R's is minus, where + means a positive displacement between adjacent strips and - a negative displacement. If, on the other hand p is placed between either of these pairs the sign is reversed. It follows that p must never lie above p. These conditions must be fulfilled if the coordination relationships between atoms are to be satisfied. The sigma structure may thus be described

p	L.Lp	L.Lp
.	+ -	+ -
.	RpR.	RpR.

Secondly the Kagome-tiling pattern of the σ-phase allows certain types of mistakes in the sequence of vertical strips without changing either the number or distance

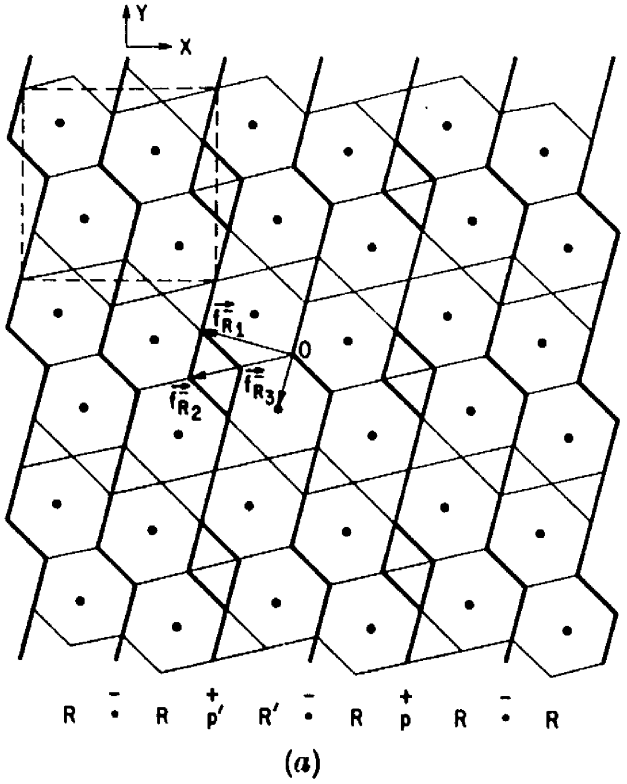

(*a*) Kagomé-tiling net derived from $Z = \pm \frac{1}{2}c_0$ layer of unit cell shown in fig. 1. Heavy lines represent division of net into right-handed hexagon strips; (*b*) kagomé-tiling net derived from $Z = 0$ layer of unit cell shown in fig. 1. Heavy lines represent division of net into left-handed hexagon strips.

Fig. 6

between the nearest neighbour atoms. These faults termed sequence faults are therefore expected to be of low energy and thus might occur frequently in σ-phase alloys. Recently Marcinkowski and Miller (33) have observed directly by means of transmission electron microscopy a number of these predicted sequence faults in (FeCr)σ lying on the (100) and (010) planes.

The three basic sequence faults which can be produced on the (100) plane, $R_1R_2R_3$ are shown in Fig. (6a). The letter O designates the origin of the displacement while the tip of the arrow denotes the terminal point of the displacement. In an analogous way the faults in Fig. (6b) may be described $L_1L_2L_3$. The schematic model of the manner in which an f_{R_1}-fault is formed, shown as Fig. (8), is due to Marcinkowski and Miller (33). They also show that in addition to the three basic sequence faults it is possible to combine several faults. This may lead to either an increase in the strain associated with faults and consequently multiple sequence faults would in general be unstable in the σ-phase, or the faults would annihilate one another.

Fig. (9) shows the sequence faults and Fig. (10) that the faults lie nearly at right-angles to the α (bcc) boundary. In many cases the faults terminate there thus growing with it; this can be seen just above the crack AB.

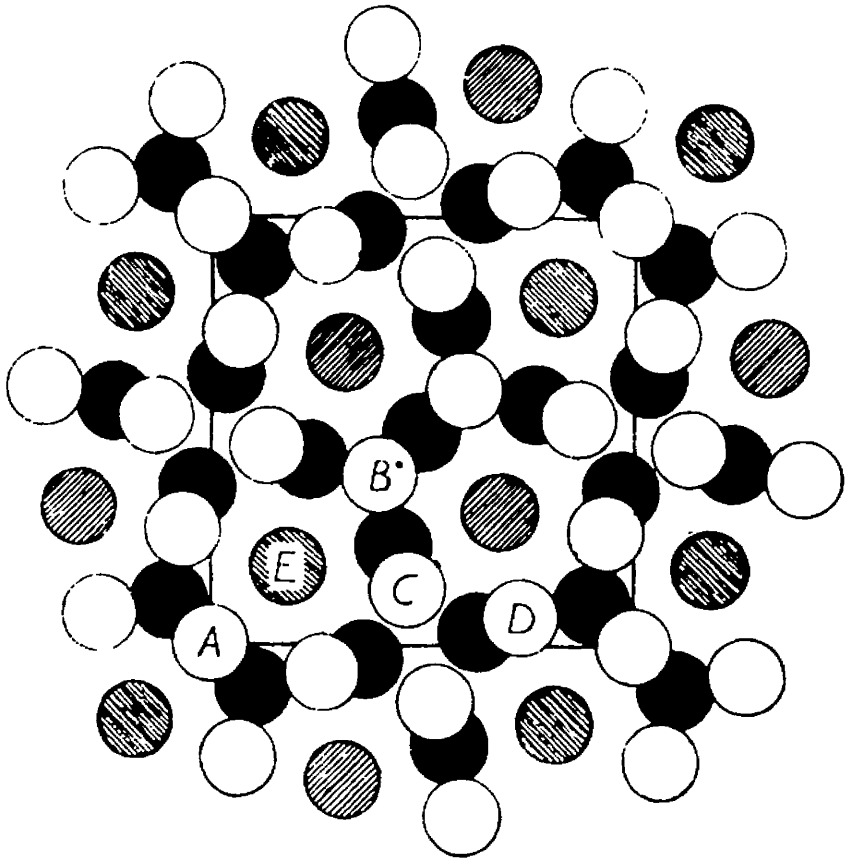

The structure of the σ phase, in projection on (001). Open circles: atoms in the planes $z = 0, 1, \ldots$; filled circles: atoms in the planes $z = \frac{1}{2}, \ldots$; shaded circles: each represents two atoms per unit cell with z coordinates equal to approximately $\frac{1}{4}$ and $\frac{3}{4}$, ...

Fig. 7

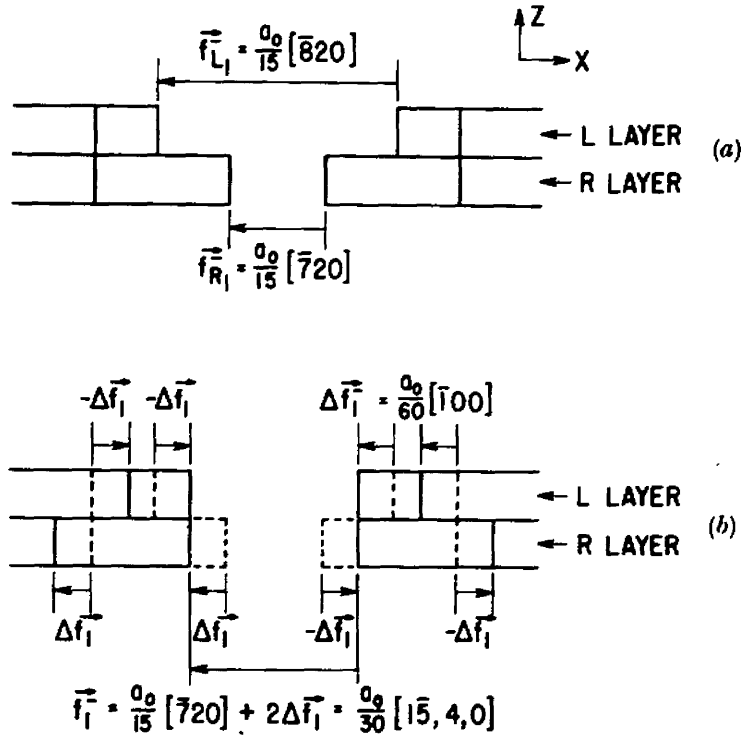

(*a*) Highly schematic illustration of the manner in which a $\mathbf{f}_1^-$ type fault is formed. Above figure illustrates situation immediately after L′, p′ and R′ rows are removed. Crystal viewed along Y axis; (*b*) above shows how material in vicinity of potential fault of fig. 5 (*a*) must be mutually constrained so that continuity of material can be preserved across the fault. Fault is produced simply by displacing material to the right of gap by $\mathbf{f}_1^- = (a_0/30)[15, 4, 0]$.

Fig. 8

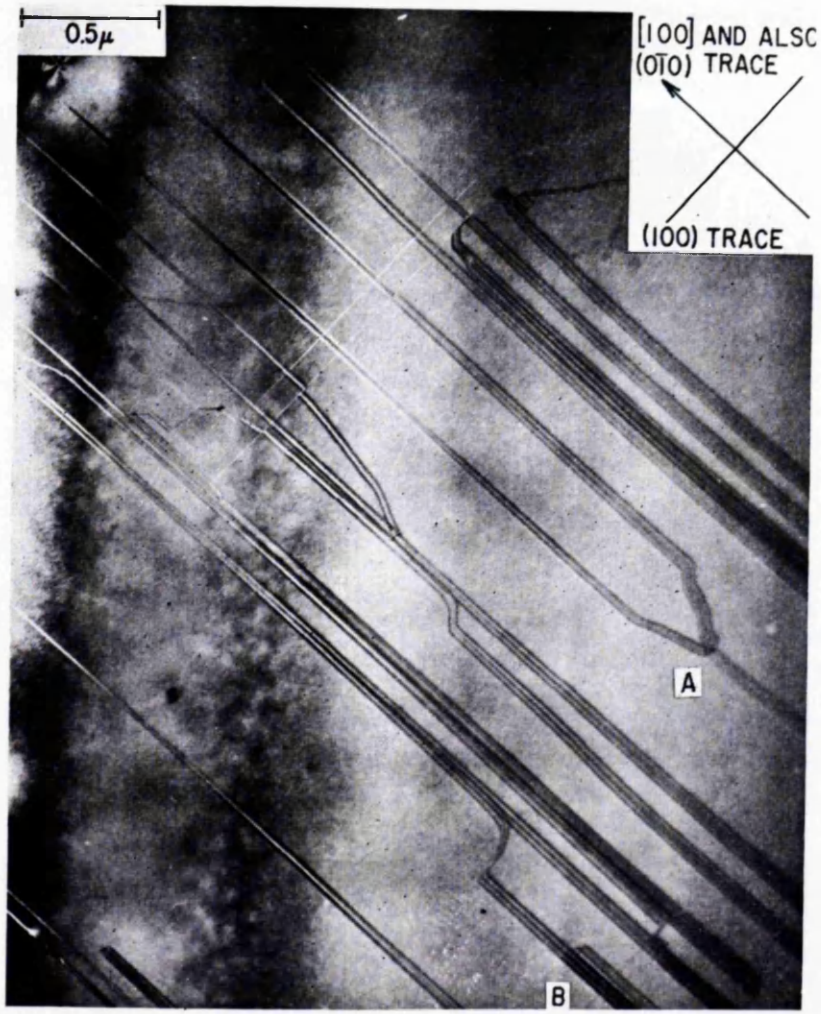

Sequence faults in the Fe–Cr σ phase, formed by cooling from 828°C to 500°C at a rate of 2·74°C/hr. Direction normal to foil is [0$\bar{1}$1].

Fig. 9

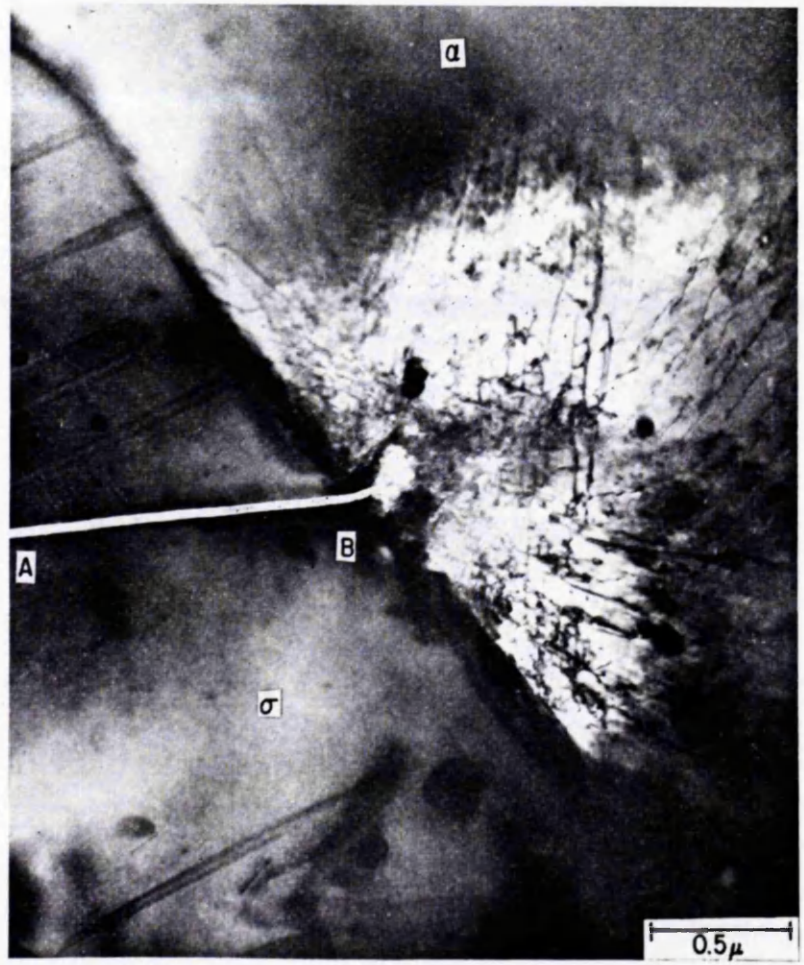

Generation of dislocations in ferrite (α) at the σ phase interface resulting from the propagation of a crack in the σ phase. σ phase formed from 70% cold-rolled ferrite by annealing for 2 hours at 725°C.

Fig. 10

Although extensive faulting was observed no instances of glissile dislocations were observed, only fixed dislocations. Consequently, Marcinkowski and Miller (33) propose that the faults formed do so thermally as a result of the transformation of $\alpha \rightarrow \sigma$ and not by the motion of glissile dislocations. However, very recently evidence has been put forward to suggest that conventional deformation modes can operate in the sigma structure under favourable conditions. The evidence for this viewpoint will be discussed later in the section dealing with the mechanical properties of the σ-phase.

Ordering in Sigma Phase Alloys

Since both binary and ternary σ-phases are stable over a very wide range of composition it is unlikely that there is complete ordering of the atoms into definite positions. It is also unlikely that there is equivalence of atomic sites as in a solid solution. It is probable however that there is an ordering of atoms in the sense that there are preferences for a given kind of atom for certain of the crystallographic sites in the unit cell. Considerable interest has developed as to the nature of this ordering since it helps to provide a clarification of the influences of atomic size and the electronic factors on site preference.

Bergman and Shoemaker (10) using powder and single

crystal X-ray diffraction methods were unable to reach any reliable conclusions regarding the distribution of atoms among the various positions in either (FeCr)σ or (FeMo)σ. However, the results did indicate that there was a strong tendency towards ordering, with iron atoms occupying exactly the same positions in the two alloys. A significant contribution to the problem was made by Kasper and Waterstrat(31) who found definite evidence for ordering from a neutron diffraction study of (NiV)σ (FeV)σ and (MnCr)σ. On the basis of these results, combined with those of the X-ray studies on (MnMo)σ (35) (CoCr)σ (36) and (FeCr)σ (10), Kasper and Waterstrat (31) proposed the following generalisation about the nature of the order in binary σ-phases containing first long row elements and also molybdenum.

It is recalled that elements to the left of manganese (V,Cr,Mo) are designated A and those to the right (Fe,Co,Ni)B. The generalisation in terms of crystallographic position of the unit cell is,

Site	Atoms per site	Coordination No.	Atom types
AI	2	12	A
BII	4	15	B
CIII	8	14	Mixed
DIV	8	12	A
EV	8	14	Mixed

Although there did not appear to be any complete correspondence of a position with a kind of atom for all positions for any given σ-phase, there was correspondence generally for positions I, II and IV. The accommodation of varying proportions of the component atoms in positions III and V explains the existence of a wide range of composition. The authors also made the interesting point that there is a correlation of the scheme of ordering with coordination number. The B atoms (I and IV) occupy those positions of lowest coordination, namely 12, which corresponds to a slightly distorted regular icosahedra; the A atoms occupy the positions of highest coordination 15 and the two positions of intermediate coordination number, 14, have mixed occupancy.

Fig. (11) lists the order schemes which have been detected experimentally for various σ-phases. The Kasper scheme, which applies to most of the σ-phases excepting (CrRe) suggests the importance of the chemical nature of constituent atoms in σ-phase order, but because of the characteristic variation of atomic size associated with the transition elements of each long period, the importance of the size effect in ordering becomes very apparent.

Spooner and Wilson (37) have surveyed the nature of ordering associated with each crystallographic site. To avoid confusion A and B type atoms will be termed X and Y

Ordering Schemes for σ Phases

Phase				Composition		Site *A*		Site *B*		Site *C*		Site *D*		Site *E*		Ref.
r_A	A	B	r_B	At.-% A	At.-% B	A	B	A	B	A	B	A	B	A	B	
(1·35)	V	Ni	(1·24)	69	31	0·3	1·7	3·9	0·1	7·5	0·5	1·1	6·9	7·9	0·1	1
(1·35)	V	Ni	(1·24)	64	36	0·2	1·8	4	0	6·5	1·5	0·7	7·3	7·9	0·1	1
(1·35)	V	Ni	(1·24)	61	39	0·3	1·7	4	0	5·6	2·4	1·0	7·0	7·5	0·5	1
(1·35)	V	Fe	(1·28)	60	40	0·3	1·7	4	0	6·5	1·5	1·2	6·8	6	2	1
(1·28)	Cr	Mn	(1·35)	25	75	0	2	1	3	3	5	0	8	3·5	4·5	1
(1·28)	Cr	Co	(1·25)	53	47	0	2	4	0	8	0	0	8	4	4	2
(1·28)	Cr	Fe	(1·28)	40	60	0	2	4	0	0	8	0	8	8	0	3
(1·40)	Mo	Fe	(1·28)	50	50	0	2	3	1	6	2	0	8	6	2	4
(1·40)	Mo	Mn	(1·35)	37	63	0	2	4	0	3	5	0	8	4	4	5
(1·40)	Mo	Co	(1·25)	60	40	0	2	4	0	7	1	0	8	7	1	6
(1·40)	Mo	Re	(1·37)	33	67	0	2	2	2	4	4	0	8	4	4	7
(1·40)	Mo	Re	(1·37)	45	55	0	2	3	1	4	4	1·5	6·5	5	3	7
(1·47)	Nb	Os	(1·37)	60	40	0	2	4	0	8	0	0	8	6	2	8
(1·47)	Nb	Ir	(1·35)	60	40	0	2	4	0	7	1	0	8	7	1	8
(1·47)	Nb	Re	(1·37)	45	55	0	2	4	0	4·75	3·25	0	8	4·75	3·25	8
(1·40)	Mo	Os	(1·37)	65	35	0·5	1·5	4	0	7·5	0·5	0·5	7·5	7	1	8
(1·40)	Mo	Ir	(1·35)	72	28	1	1	4	0	8	0	1·5	6·5	7	1	8
(1·28)	Cr	Re	(1·37)	40	60	1·5	0·5	1	3	2·5	5·5	4	4	3	5	8
(1·35)	V	Mn	(1·35)	19	81	0 0	2 0	1·8	2 2	1·2	6·8	0·0	8·0	2·7	5·3	9
(1·28)	Cr	Mn	(1·35)	20	80	0·2	1·8	1·4	2 6	1·2	6·8	0·4	7·6	2·8	5·2	9
(1·28)	Cr	Fe	(1·28)	46	54	0·6	1·4	2·2	1 8	3·6	4·4	2·8	5·2	4·0	4·0	9
(1·28)	Cr	Co	(1·27)	61	39	0·7	1·3	3·8	0·2	6·8	1·2	3·0	5·0	4·0	4·0	9

Note: Waterstrat and Kasper[10] claim that Os-Cr, Re-Cr, and Ru-Cr are disordered.

1. J. S. Kasper and R. M. Waterstrat, *Acta Cryst.*, 1956, **9**, 289.
2. G. J. Dickins, A. M. B. Douglas, and W. H. Taylor, *ibid.*, 1956, **9**, 297.
3. B. G. Bergman and D. P. Shoemaker, *ibid.*, 1954, **7**, 857.
4. C. G. Wilson and F. J. Spooner, *ibid.*, 1963, **16**, 230.
5. B. F. Decker, R. M. Waterstrat, and J. S. Kasper, *Trans. Amer. Inst. Min. Met. Eng.*, 1954, **200**, 1406.
6. J. B. Forsyth and L. M. d'Alte da Viega, *Acta Cryst.*, 1963, **16** 509.
7. C. G. Wilson, *ibid.*, 1963, **16**, 724.
8. F. J. Spooner and C. G. Wilson, *ibid.*, 1964, **17**, 1533.
9. S. H. Algie and E. O. Hall, *ibid.*, 1966, **20**, 142.
10. R. M. Waterstrat and J. S. Kasper, *Trans. Amer. Inst. Min. Met. Eng.*, 1957, **209**, 872.

Fig. 11

respectively in the ensuing discussion.

Site A (000); CN12 : occupied mainly by Y atoms except for (MoIr)σ and (CrRe) ; $r_x > r_y$ except for (CrMn)σ and (CrRe)σ; independent of n_e.

Site B (x,x,0); x = 0.3981; CN15 : occupied mainly by X atoms except for (MnCr)σ and (CrRe)σ and (MoRe)σ; $r_x < r_y$ for (CrMn)σ and (CrRe)σ.

Site C (x,y,0); x = 0.4632, y = 0.1316; CN14 : occupied by X and Y atoms but X atoms predominate except when Y = Mn or Re; domination by X increases with n_e; site equally divided when Y = Mn or Re.

Site D (x,y,0); x = 0.7376, y = 0.0653; CN12 : occupied mainly by Y atoms; $r_x > r_y$ except for (CrRe)σ and (CrMn)σ.

Site E (x,x,z); x = 0.1823; z = 0.2524; CN14 : occupied by X and Y atoms, Y atoms predominate for large n_e.

The fact that A and D sites are usually filled by Y atoms having smaller radii suggests the ordering requirements of size and chemical nature. Similar factors govern the filling of the larger B sites. In particular when the larger atom is a Y-type as happens in (CrMn)σ and (CrRe)σ, the majority of B sites are filled by Y atoms. The size factor is not apparent in filling up the intermediate C and E sites,

except for large values of n_e. (The total number of valency electrons in s and d shells of the binary constituents.)

The phases containing Mn or Re are always distinguished by the mixed nature of the filling in C and E sites. Wilson (38) has pointed out that the exceptional phases (CrMn)σ (MoMn)σ (MoRe)σ and (CrRe)σ in which the X and Y atoms come from groups VI and VII of the periodic table show marked similarities in their ordering schemes. However, this aspect is much less apparent for σ-phases whose atoms come from different groups of the periodic table. Spooner and Wilson (37) have also pointed out that the effect of an increasing valance electron contribution per atom can be estimated by considering the following series of σ-phases.

1. NbRe (6.1) ; VFe (6.2) ; NbOs (6.2) ; NbIr (6.6), VNi (7.1)
2. MoRe (6.55) ; CrMn (6.75) ; MoIr (6.85) ; MoFe (7.0) ; MoCo (7.2).

In series 1 the X atom has 5 valence electrons and in series 2 it has 6 valence electrons. The average number of valency electrons per atom of the unit cell is given in brackets. As the number of valency electrons per atom increases in each series the order approaches the simplest form in which Y atoms fill A and D sites only and X atoms

fill B, C and E sites only. Wilson and Spooner (37) concluded from these results that a complex scheme, taking into account, size effect, the electronic factor and the chemical factor, governs the ordering of sigma phases. As already pointed out the stability of the phase and its composition range would also seem to depend upon satisfying the ordering requirements since the only σ phases reported as being randomly ordered are (CrOs) (CrRe) (52) and (CrRe) (52,26). Waterstrat and Kasper (52) suggest that the random distribution in these three alloys is due to the opposing influences of atomic size and electronic structure which serve to disrupt the entire ordering tendency. If atomic size determines the occupancy of the sites it would be expected in (CrRu)σ and (CrOs)σ that the smaller atom chromium would be found in the CN12 positions. But if Ru or Os should be found in these sites a periodic relationship would be dominant since both are in the iron group.

Spooner and Wilson (37) disagree with the Kasper and Waterstrat random ordering scheme for (CrRe)σ and their ordering scheme is shown in Fig. (11). Furthermore they offer an explanation of the random ordering in (CrOs)σ and (CrRu)σ as follows.

Since $r_{Cr} = 1.28\overset{o}{A}$ and $r_{Os} = 1.34\overset{o}{A}$ the Y atom is larger

than the X atom so that normal requirements (smaller atom and type Y) for filling A and D sites cannot be satisfied. In this respect it is similar to the (CrRe)σ order scheme of Spooner and Wilson (37). Using this scheme as a model, the B sites would be filled by Y and X atoms and since the number of valence electrons per atom is only 6.6 for the composition used ($OsCr_2$), it is expected that C and E sites would have mixed occupants. Thus the presence of order might be difficult to detect and in fact Kasper and Waterstrat (52) state that their measurements were not accurate enough to detect small amounts of ordering. Similar arguments apply to (CrRu)σ since Ru and Os belong to the same group in the periodic table.

There have been several reports that an order-disorder transformation takes place in some sigma phases. Pearson and Hume Rothery (47) report a heat of transition in (MnCr) at 998°C. Kasper and Waterstrat (31) confirmed that the high temperature (1100°C) degree of ordering in (MnCr) was less than that in specimens annealed at 850°C. However it was not confirmed that an order-disorder transition occurred. Marcone and Coll (23) detected changes in hardness, electrical resistance and volume in (CoV) at ~550°C. They point out that the ratio between the postulated disordering temperature and the melting temperature is found

to be 0.53 which is in reasonably close agreement with the prediction of Oriani (48) when an order-disorder transformation is observed.

Electronic structure

Measurements of specific heat (21) and electrical resistance (22,23,24) indicate that the σ-phase is likely to be an almost full zone structure. Theoretical support for this viewpoint comes from Rocher and Friedel (54), whose model of the electronic structure predicts a very high electronic density at the Fermi level for a d-band filled up to more than one-third. Also the Brillouin zone treatment indicates the existence of a full first zone able to accommodate 1.72 electrons per atom (20), and a second zone able to accommodate 6.97 electrons per atom (10). Bergman and Shoemaker (10) point out that it is doubtful if the average valence of the metal atoms in the σ-phase can be as high as 6.97. Instead, they suggest that the actual valence is closer to 5.76 (a value obtained by treatment of inter-atomic distances (10)) than it is to 7 and that the second zone remains incompletely filled.

Specific Heat

Hoare and Matthews (21) have deduced from specific heat measurements of (FeCr)σ that the density of states at the

Fermi level is of the order of 5.7 per electron volt per atom. They measured the heat capacity of both the alpha (bcc) and σ-phase in a 44.1% FeCr alloy between 1.8 and 2.4°K. The interpretation of the results is based on the assumption that the lattice and electronic contributions to the specific heat are proportonal to T^3 and T respectively. It follows that

$$C_V = \underset{\text{electronic}}{\gamma T} + \underset{\text{lattice}}{\beta T^3}$$

and that a plot of $C_V/T : T^2$ should give a straight line; from the intercept the value of γ, the electronic heat coefficient, may be determined, while the slope yields θ_D, the Debye temperature.

The results for the FeCr bcc phase and also pure iron are shown in Fig. (12a). The graphs indicate that the lattice contribution to the specific heat is small, and that the difference between the pure iron and alloy in the phase is only slight.

For the σ-phase material, the method usually employed to distinguish between the electronic and lattice components cannot be used since similar treatment of the results produces a $Cr/T : T^2$ curve with a negative slope and therefore negative values of the Debye temperature Fig. (13). Hoare

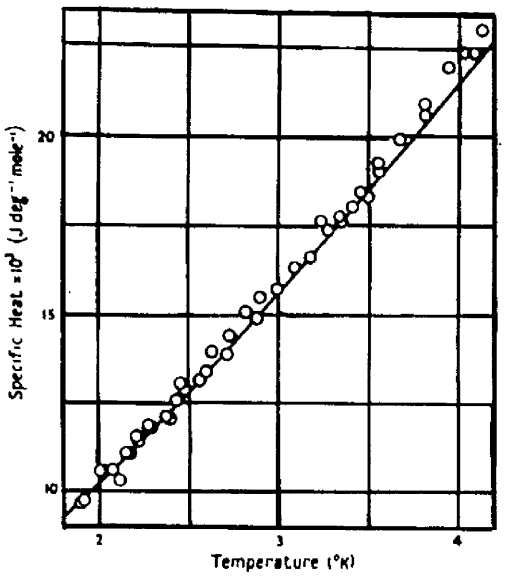

a. Measured specific heat of iron–chromium alloy in alpha phase. The full line represents results of Keesom and Kurrelmeyer (1939) for pure iron.

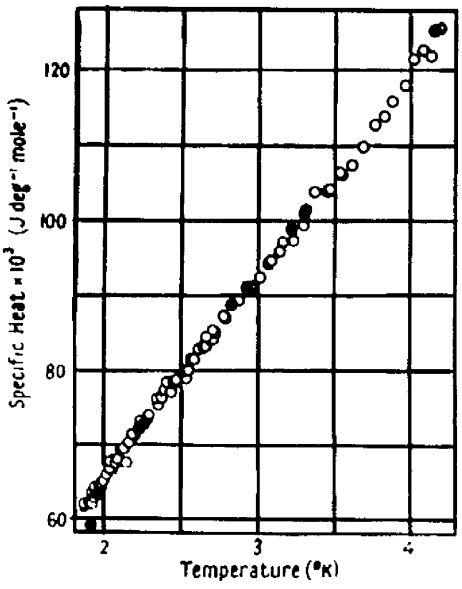

b. Measured specific heat of same iron–chromium alloy as for figure a when transformed to the sigma phase. Open circles, results using helium as initial exchange gas, full circles, check results using hydrogen as initial exchange gas.

Fig. 12

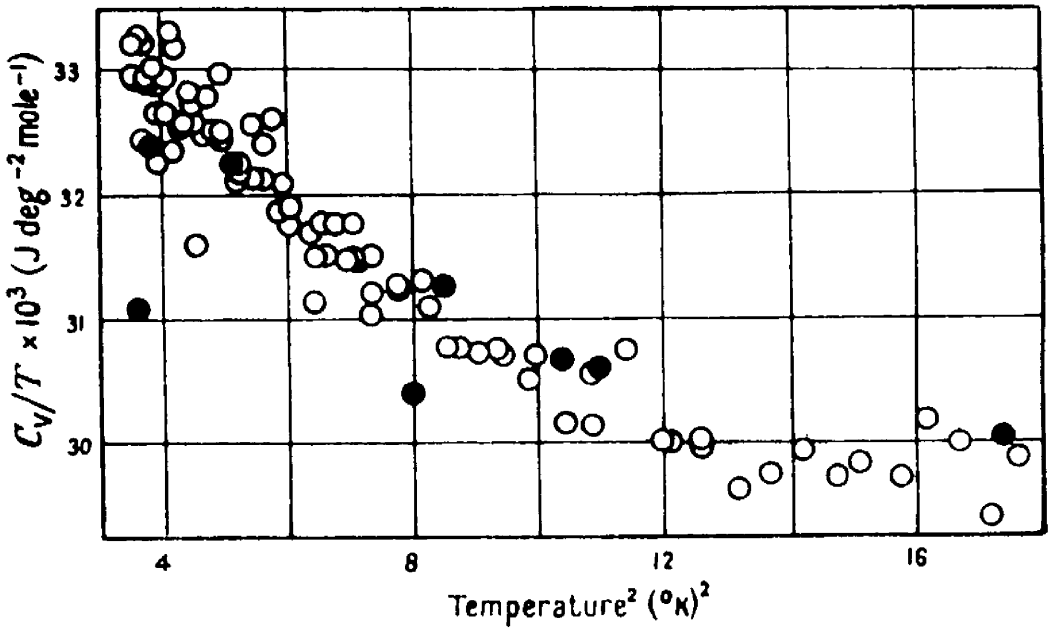

Plot of C_v/T against T^2 for sigma phase alloy.

Fig. 13

and Matthews (21) point out that if it is assumed that the whole of the observed specific heat is electronic in origin, then its magnitude is greater than has previously been observed for any metal or alloy.

Further progress in the understanding of the band structure of the sigma phase must depend to some extent on an explanation of the high density of states, and the departure from linearity of the $C_V/T:T^2$ plot observed by Hoare and Matthews.

Electrical resistance

Kasper (22), Kazanstev (24), and Marcone and Coll (23) have reported that σ-phases have high values of resistance at room temperatures and also a negative temperature coefficient of resistance. At very low temperatures some sigma phases become superconducting and Fig. (14) summarises the current data; the σ-phases are labelled F (ferromagnetic), S (superconducting) and N (normal to 1°K).

The relationships between the critical temperature (Tc) and (a) number of valence electrons per atom, (b) mean atomic volume and (c) density of electrons are shown as Fig. (16).

The Tc versus average valence electron/atom plot shows a pronounced maximum at 6.7 and all σ-phases except

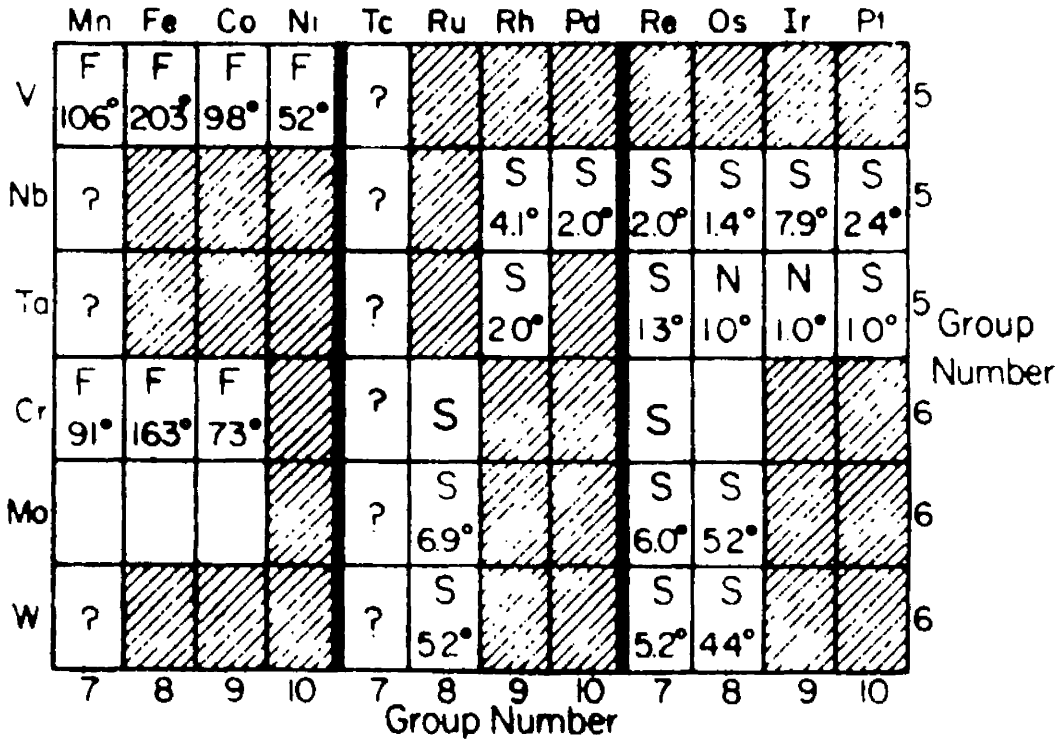

Sigma phases tested for superconductivity.

Fig. 14

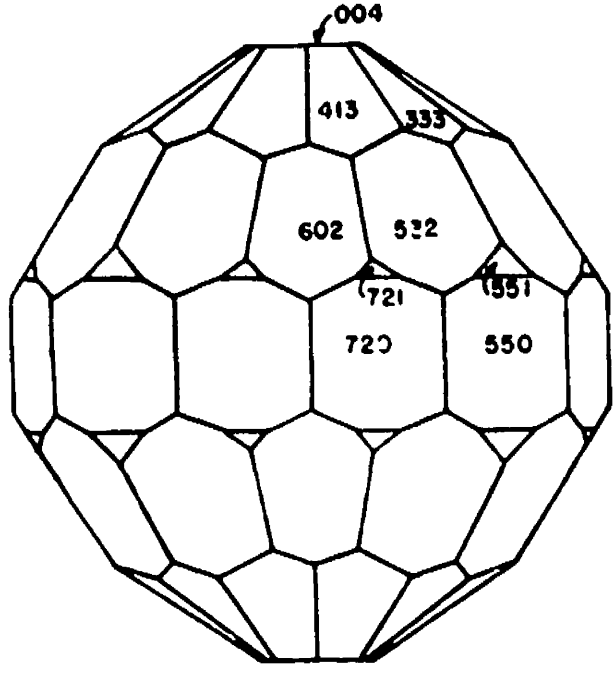

Second Brillouin-zone polyhedron. (Bergman and Shoemaker.)

Fig. 15

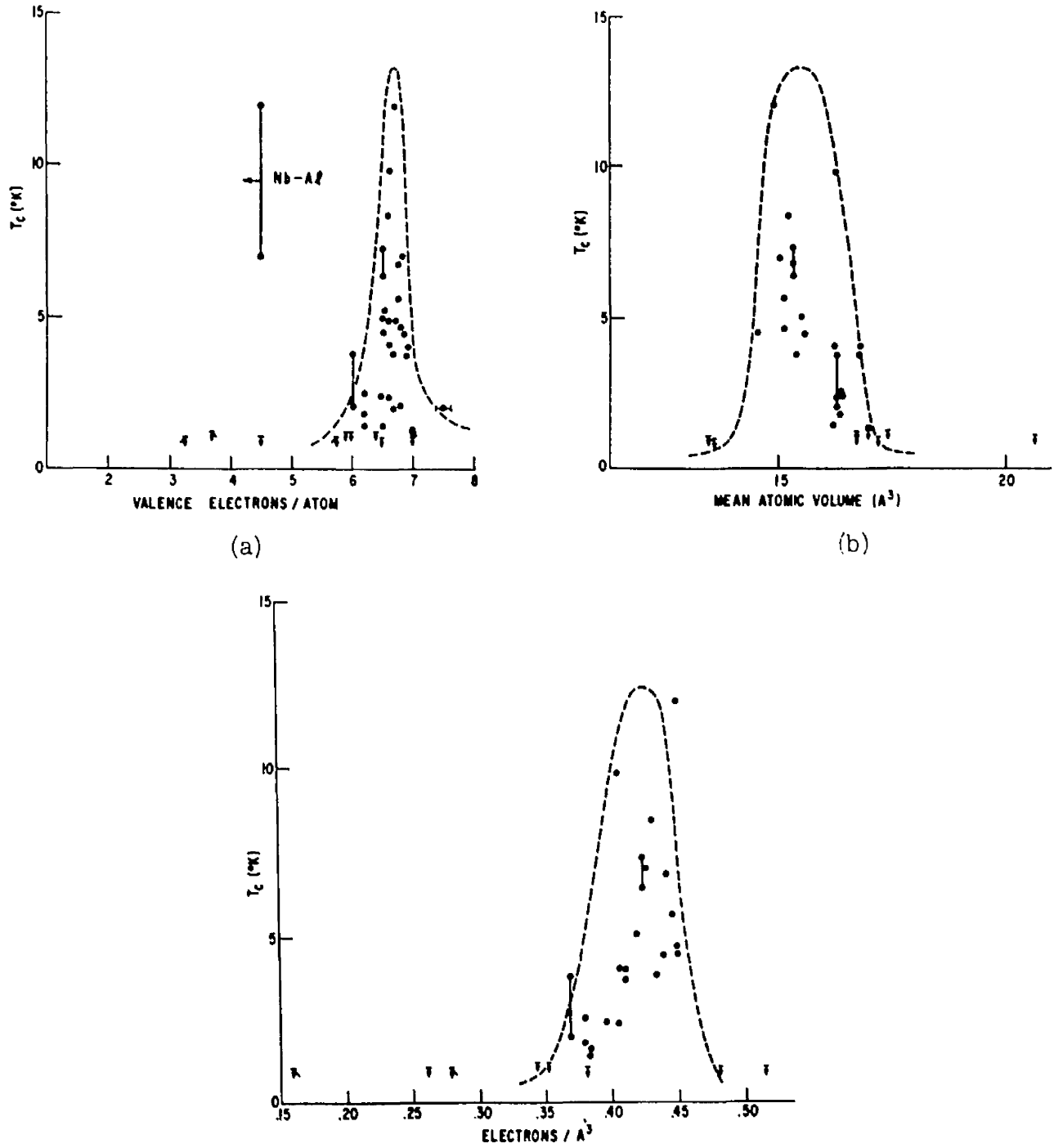

Critical temperature data for $D8_b$ (σ-phase) compounds: (*a*) versus number of valence electrons per atom, (*b*) versus mean atomic volume, and (*c*) versus density of electrons.

Fig. 16

(2NbAℓ)σ, which is reported as having a broad superconductive transition (55), fall in the vicinity of this maximum. The plot of Tc versus mean atomic volume shows a broad dependence centering upon 15Å^3 to 16Å^3 per atom. The combined parameter of volume and valence Fig. (16c) shows a range of 0.37 to 0.45 electron/Å with the higher Tc associated with the larger values.

It has been suggested (62) that the existence of a peak at 6.5 in the Tc versus e/a plot is connected with existence of a peak at this electron concentration in the density of states at the Fermi surface. Theoretical support for this viewpoint has been put forward by Rocher and Friedel (54) who suggest that the superconductivity of the σ-phase is due to a high density of electron states.

Magnetic properties

At room temperature all σ-phases are non-magnetic but at low temperatures some become ferromagnetic. Nevitt and Beck (25) measured the Curie temperatures of all the binary and several ternary sigma alloys formed by first long period transition elements. Fig. (17) shows the graph of Curie temperatures of binary alloys containing Cr and V plotted against atomic number of the other component element in each alloy. The dashed curve expresses the variation of saturation magnetic moment with the average atomic number for

the ferromagnetic elements of the first long period and their alloys. The similarity of these curves is in agreement with the relationship between Curie temperature; Θ, and saturation magnetic moment, I_0, for ferromagnetic substances; $\Theta \alpha I_0$ (27).

The ternary alloy data of Nevitt and Beck (25) does not conform to this simple correlation since there is a general lowering of the Curie temperature when a third element is added to any one of the binary alloys (see Figs. (18,19)). Nevitt and Beck interpret this behaviour in terms of a relationship proposed by Bethe (27) which predicts that the alignment of magnetic moments of neighbouring atoms is parallel or anti-parallel depending on the extent of the overlap of the charge distributions of the partially filled d-shells of the transition metals. The overlap of the adjacent 3d shells is changed when one transition element is substituted for another on a particular site. The possibilities for ferromagnetic coupling in a given lattice can be analysed qualitatively, when the interatomic spacings are known, by substituting Néel's values for the 3d shell diameters of the elements into the Néel criterion for positive exchange coupling: $d-2r \geqslant 1.05\text{Å}$ where d is the distance between atom centres and 2r is the average diameter of the 3d shell.

Nevitt and Beck (25) deduce that the substitution

of manganese atoms for iron atoms on certain of the lattice sites in (FeV)σ and (FeCr)σ results in a decrease in the number of positive exchange couplings in the lattice, because positive Fe-Fe interactions are replaced by antiferromagnetic Fe-Mn, Mn-Mn and Mn-V couplings. Although this is a satisfactory explanation for manganese additions it does not explain the depression of the Curie temperatures when the ternary addition has a smaller 3d-shell than the original atom. Such a depression is observed when Co is added to (FeV)σ, (FeCr)σ (MnV)σ and (MnCr)σ, and Ni to (CoV)σ. Analysis of these additions in terms of the Neel criterion suggest that there is an increase rather than a decrease in number of possible positive 3d-shell exchange interactions; a result which is contrary to experiment.

An alternative explanation based on previous work by Shull (29) on hexagonal (CoCr) solid solutions has been proposed by Nevitt and Beck (25). A transfer of electrons among certain atoms is supposed to take place in sigma alloys and the resultant decrease in magnetic moment of the structure is reflected in a decrease in Curie temperature.

Nevitt and Beck (25) also investigated the Curie temperatures of (FeCrMo)σ and (CoCrMo)σ as a function of composition. They found that the Curie temperature depended on the concentration of Fe and Co which suggests

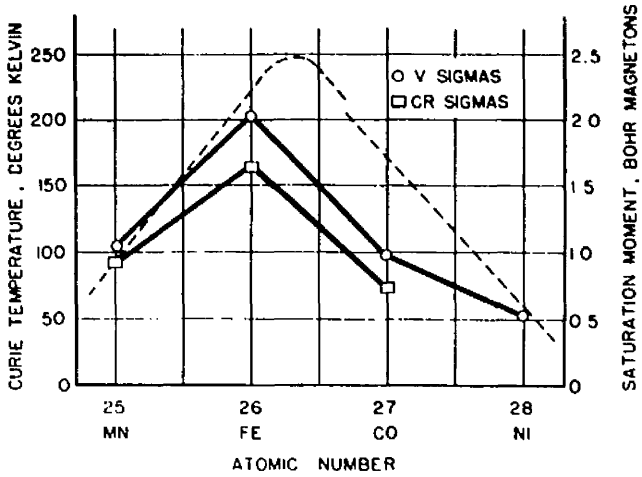

Curie temperatures of binary alloys containing chromium and vanadium are plotted against the atomic number of the other component element in each alloy.

Fig. 17

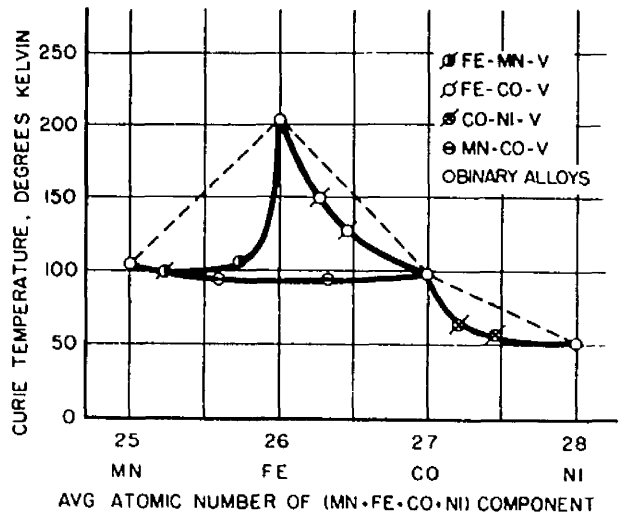

Curie points of ternary σ alloys containing vanadium are plotted against the weighted average atomic number of the other two alloy components.

Fig. 18

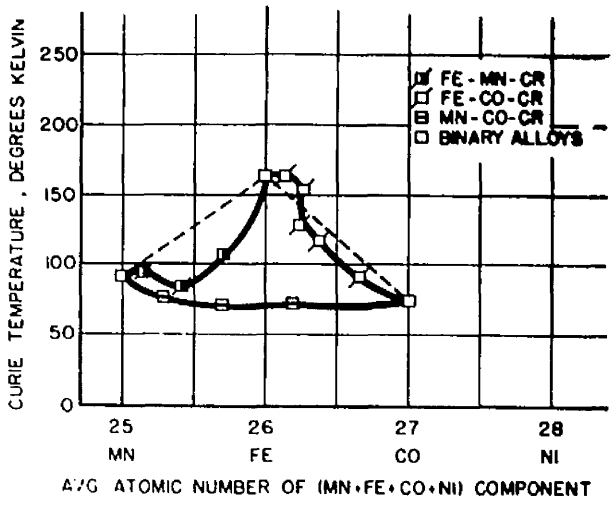

Curie points of ternary chromium σ alloys are plotted against the weighted average atomic number of the other two alloy components.

Fig. 19

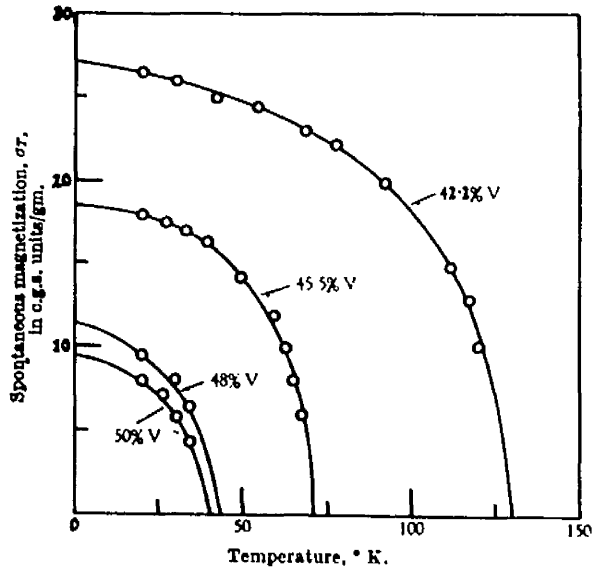

Variation of spontaneous magnetization, σr, with temperature for the four iron-vanadium sigma phase alloys

Fig. 20

that the number of ferromagnetic atoms in the structure is an important factor. Furthermore the lattice expansion caused by the addition of Mo had no effect on the Curie temperature. The authors propose that Mo additions produce two mutually compensating effects: an increase in the number of positive interactions due to the increased interatomic distances and a decrease in the number of positive interactions due to the substitution of strongly negative Fe-Mo, Cr-Mo and Mo-Mo interactions for some of the positive Fe-Fe, Fe-Cr and Cr-Cr 3d shell exchange couplings.

Parsons (30) has measured the mean magnetic moment per atom P_B of (FeV)σ and its variation with composition. The results (Fig. 20)) show that there is a decrease in magnetic moment and Curie point with increasing vanadium content, hence confirming Nevitt and Beck's postulate that the magnetic moment increases with increasing concentration of the magnetic element, in this case Fe. Parsons also points out that a linear extrapolation of the curve of magnetic moment versus composition goes to zero moment at a composition corresponding to about 53%V although the composition limit of (FeV)σ is about 57%V. Frank and Kasper (31) have also reported that a 60%V (FeV)σ showed no ferromagnetism even at 4.2°K.

Two interpretations of these results are proposed by Parsons. Firstly, if the magnetic moment of the σ-phase is due to a net unbalance of positive and negative spins in a common d band, then there is a redistribution of spins in the band as the composition changes, leading to a balance of spins at 53%V; the phase does not however cease to be stable at this point. Secondly, there is a ferrimagnetic arrangement of magnetic ions in the structure which alters with composition. Parsons favours this interpretation as more probable since the curves of inverse susceptibility against temperature above the Curie point are slightly concave to the temperature axis.

Mechanical Properties

The work of Bain and Griffiths (2) not only showed the existence of the σ-phase but also described many of its characteristic features. Chief among these are the extreme hardness of the σ-phase itself and the embrittlement associated with its presence.

Lena (32) has reviewed the occurrence and effects of σ-phase formation in commercial alloys. He points out that the magnitude of the effect which the σ-phase may have on the mechanical properties of stainless steels is greatly dependent not only on the amount present, but also on the particle size and distribution. In general, sigma

increases the notch sensitivity of all stainless steels and the impact test is a more sensitive indicator of its presence than any other mechanical property. When sigma envelopes grain boundaries, the ductility at room temperature is greatly reduced, but at elevated temperatures it is not so pronounced. Levin et al (56)(57) have observed above 450°C to 500°C a sharp increase in the plasticity of (FeCr)σ, a condition which often permits the use of sigma containing steels at high temperatures. Well dispersed sigma may increase tensile strength but the possibility of using sigma as a matrix strengthener for high temperature service has been discounted because it causes cracking and decreases both fatigue and creep strength.

It has been suggested (33) that the high hardness and brittleness of (FeCr)σ is due to the difficulty in nucleating and generating glissile dislocations. This difficulty is said to arise from the work that the dislocations may have to overcome due to the ordering forces between the atoms. More recently Kitchingman (34) has discussed the brittleness of the σ-phase and the ductility of the structurally similar β-uranium in terms of the ordering and coordination numbers of the atomic positions in the sigma structure. Both of the above viewpoints are discussed in detail in Chapter II.

The hot hardness behaviour of (FeCr)σ has recently been investigated by Tedmon and Westbrook (58). The hardness minimum seen in Fig. (22) is commonly found in compounds existing over a wide range of compositions since the stoichiometric composition represents a minimum concentration of structural defects. But in the case of the highly complex sigma structure three of the five crystallographic sites have a definite preference for one type of atom whereas the remaining two sites may accommodate either atom types. Consequently, Tedmon and Westbrook suggest that no structural reason is apparent for the observed hardness minimum. Two other possible explanations are proposed by these authors.

Firstly the fault structure observed by Marcinkowski and Miller (33) may act in an analogous way to domain hardening in simpler structures and an explanation may be found if the size of the fault structure or its energy are composition dependent.

Secondly, the structure or mobility of dislocations in the σ-phase may be affected by electronic factors which will be composition dependent.

The point which lies significantly off the curve in Fig. (22) represents an alloy which has a higher carbon

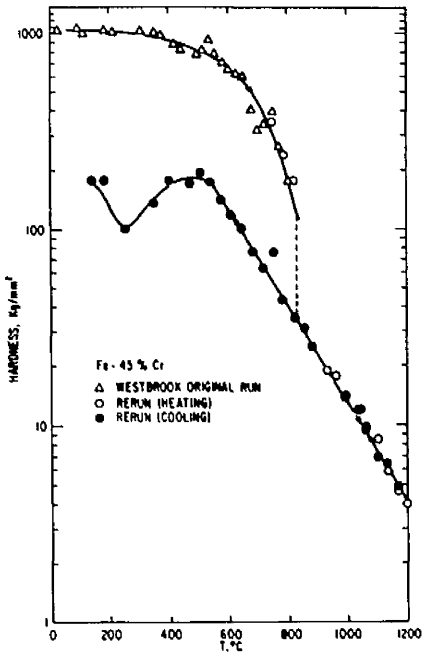

Log hardness vs temperature for Fe-45% Cr alloy, first tested in sigma condition by Westbrook, then retested (this study), in both sigma and alpha condition.

Fig. 21

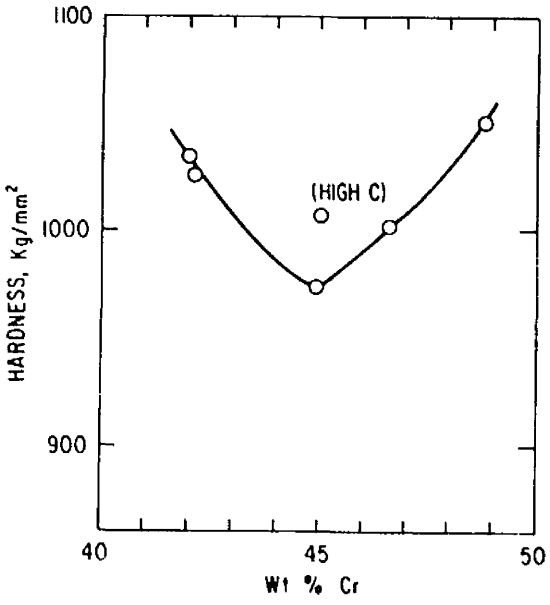

Room-temperature hardness (linear scale) vs composition for alloys in sigma phase condition.

Fig. 22

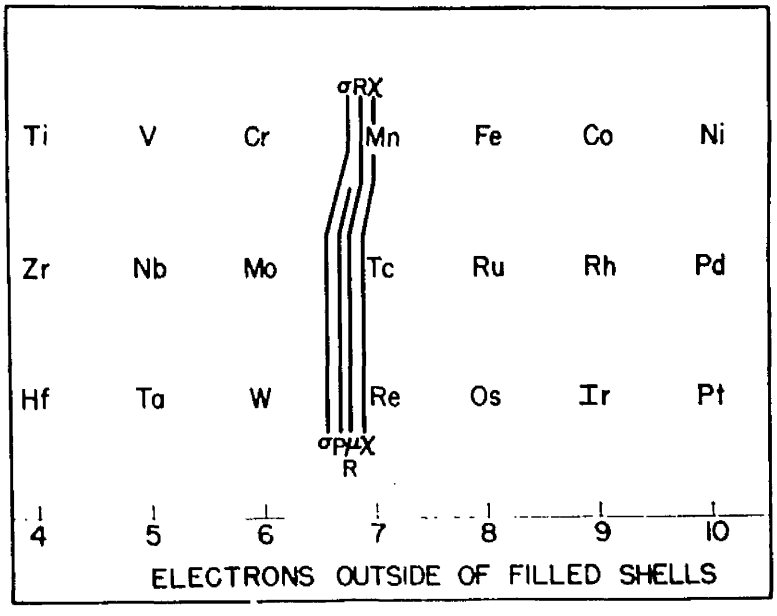

Schematic arrangement of σ, P, μ, R, and χ phases in order of increasing electron concentration.

Fig. 23

level than the others. Tedmon and Westbrook suggest that it might be due to hardening by interstitial carbon atoms.

Several authors (59)(60) have observed some temperature dependent structural changes in the σ-phase which in most cases have been attributed to a change of order. Although Fig. (21) also shows an anomalous behaviour in hot hardness the effects were not reproducible and Tedmon and Westbrook proposed that this behaviour arises from the mechanical anisotropy of the material and not the state of order.

In the same investigation slip markings were observed at the edges of some indentations Figs. (24,25) suggesting conventional deformation modes can operate in the usually brittle sigma structure. The operative deformation mode or modes were not identified since the orientation of the crystals showing deformation patterns could not be found.

Radiation damage

Spooner and Wilson (61) have investigated the effect of fast neutron bombardment on the structure of some σ-phase alloys. Radiation damage consisting of (i) line broadening (ii) changes in unit cell dimensions and (iii) disordering was observed. The magnitude of the effects depended on the total fast neutron dose.

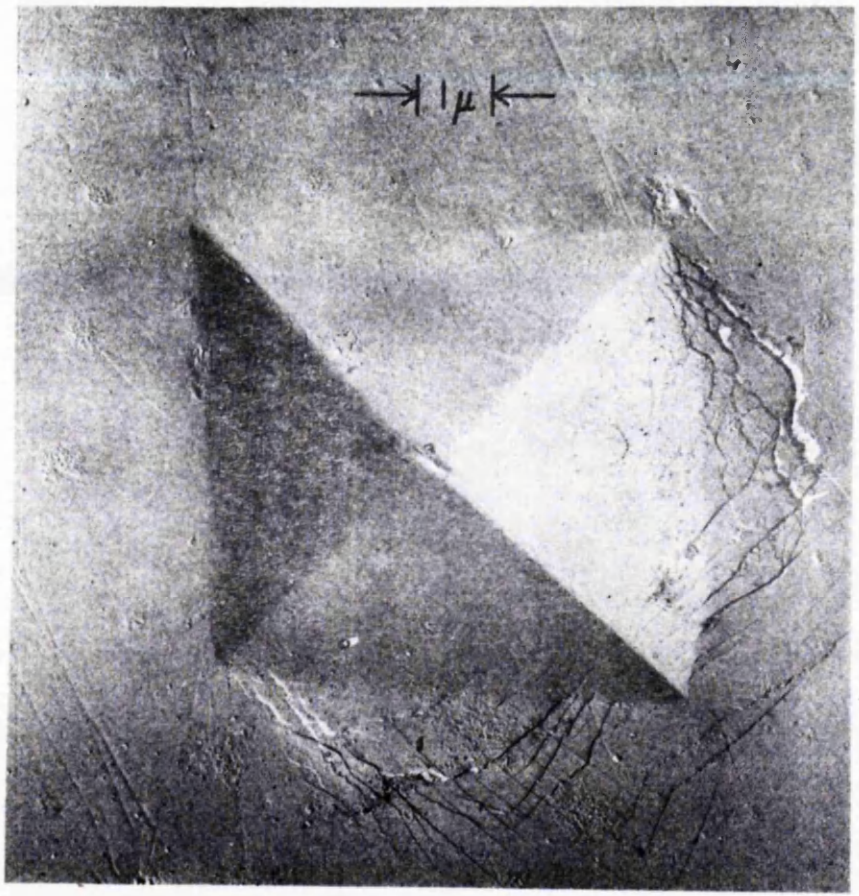

Electron micrograph of a hardness impression on an Fe-44% Cr alloy. The alloy is sigma phase and the deformation was carried out at room temperature.

Fig. 24

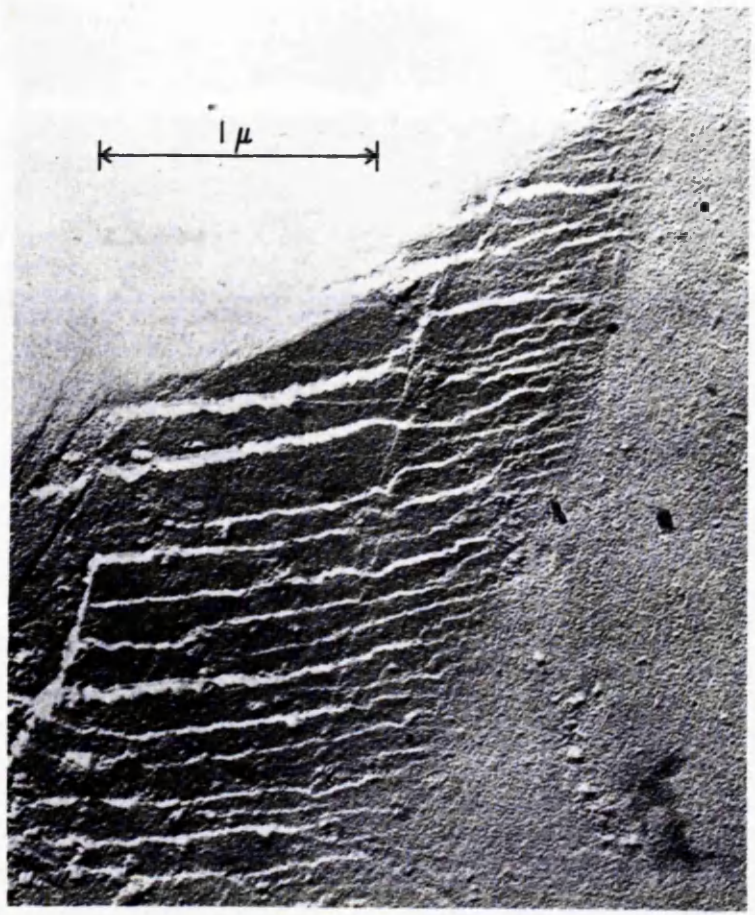

High-magnification electron micrograph of strained region adjacent to hardness indentation. The center of the hardness impression lies above and slightly to the left of the slip traces, with the right corner of the indentation visible in the upper-right corner of the micrograph. This sample is an Fe-44% Cr alloy, tested at room temperature, in the sigma condition.

Fig. 25

The line broadening is attributed to clusters of point defects and the changes in unit cell dimensions to disordering of atoms of different radii.

Theories of Sigma Phase Formation

Several attempts have been made to rationalise the occurrence of sigma phases in transition metal systems, on the basis of the regularity of the occurrence of the phase, and of the systematic shifts in composition. Most investigators have attributed these regularities to either electronic effects (39,40,41) or close packing of spheres (42,43,51). On the other hand Haworth (44) concludes that the occurrence of σ-phase cannot be predicted from normal intermediate phase considerations.

That σ-phases might be electron compounds was first suggested by Sully and Heal (45). Sully (39) later published a qualitative formulation taking as a basis Pauling's theory of the electronic structure of the transition metals. He proposed that an exchange of electrons can occur between bond and atomic orbitals so the latter are filled to the extent permitted. Since the number of vacancies varies from one transition metal to the next, the ratio of atoms to electrons in excess of those required to fill the 3d vacancies varies with composition. Two electron : atom ratios were calculated depending on whether or not the

4s electrons contributed to the bonding. When 4s electrons were included in the bonding the excess electron to atom ratio was 2.25 and without 4s electrons was 1.7.

Whereas Sully used binary sigma phases Rideout and Beck et al (16) approached the correlation of sigma phase boundaries in ternary alloys. They used a slightly different approach and proposed that the important factor in σ phase formation is the number of electron vacancies per atom.

The electron vacancy numbers, N_V, were originally taken from the Pauling theory, but were later modified empirically in order to bring about better agreement with data for the phase in certain ternary systems. For alloys, N_V was calculated from the electron vacancy numbers of the components as follows;

$$N_V = 4.66\ (Mo+Cr+V)+3.2(Mn)+2.2(Fe)+1.7(Co)+1.6(Ni)$$

where the symbols Cr, Mn etc, stand for the atomic fractions of the corresponding elements in the alloy. On this basis, a reasonably constant value of $N_V = 3.4$ was obtained for all the sigma phases studied.

Rideout and Beck et al (16) have pointed out that the two approaches of themselves and Sully may be related quite simply. That is, the number of electron vacancies and the

number of excess bonding electrons are virtually the same criterion, and hence draw comparable conclusions. Almost simultaneously Bloom and Grant (40) showed that a similar criterion can be developed without making reference to the Pauling theory. Their treatment is based on the assumption that the σ-phase compositions are largely determined by a preferred electron number of 210 electrons per unit cell or seven per atom.

All these early attempts to show that the σ-phase might be understood as an electron compound were substantiated by experimental results obtained with the transition elements of the first long period. As the new sigma phases were discovered between transition elements of the three long periods, the theoretical interpretation became confused. Greenfield and Beck (7) carried out an extensive investigation to provide the necessary experimental data for a revaluation of the electron compound theory. Firstly they assigned to the elements of the second and third long periods electron vacancy numbers corresponding to those of the first long periods but found no correlation between theory and experimental results. Secondly, they assigned different electron vacancy numbers to the second and third series on the basis that there is no complete analogy among the elements of the three transition series, but again found no correlation.

The electron compound concept using Pauling's theory has been seriously weakened by the fact that it does not apply to a large number of the presently known σ-phases. Furthermore, studies of the Curie temperatures (25,30) of these phases do not support the electron compound hypothesis, and Nevitt and Beck (25) conclude that the sigma structure cannot be assigned a Pauling sub-band of its own with a characteristic number of electrons independent of composition. The problem of the σ-phase has been further complicated by the discovery of (NbAℓ)σ and (TaAℓ)σ (49) which demonstrates that the phase is not restricted to systems in which both components are transition metals having partially filled d-electron levels. Also there are absences of the sigma phase in certain systems. However, Knapton (8) has pointed out that searches for the phase may have failed to detect it and that surveys on annealed specimens (7) may actually relate to alloys in a non-equilibrium condition.

The extent to which packing considerations in contrast to other factors determine the choice of structure cannot be readily ascertained. Frank and Kasper (43) claim that packing considerations are of primary importance, and that electronic factors may be operative in selecting between alternative structures that satisfy the packing requirements.

The problem concerning the association of different component

elements with the different coordination or ordering is well known in the case of the Laves phase structures, but in the sigma phase there are varying degrees of order according to the combinations of elements and no direct correlation with the usual atomic radii can be made. However it has been shown that the lattice parameters and interatomic distances may be calculated to a good approximation by considering the σ-phase in terms of close packing of spheres.

It is recalled that the interatomic distances in the horizontal layers of the sigma lattice, which determine the a-parameter are mostly governed by the sizes of the individual atoms. The distance between atoms in the E sites, which form the vertical rows is given by $d_{EE} = c/2$. It is a characteristic feature of the σ-phase that this distance is much less than the sum of the radii of the atoms in these sites. The nature of this E bond, between E-E atoms, is unknown but it is extremely important in determining the value of c.

Stuwe has demonstrated that the lattice parameters are simply related to the average atomic radius of the component atoms by the following equations,

$$a = 6.85 r_{average} \quad : \quad c = 3.57 r_{average}$$

The variation of the a-parameter with composition fits the above equation well except in the case of σ-phases containing Si: Stuwe suggests that electronic interaction may be responsible for this effect. The c-parameter and its variation with concentration can be better described by giving atoms in the E-positions an "effective" coordination number 4 instead of 14 which would mean that they are in direct contact only with each other.

More recently Shoemaker and Shoemaker (51) have shown that interatomic distances may be calculated to a good approximation as the sum of the characteristic atomic radii. Two radii, one for major ligands and one for minor ligands are specified for each atom except in the case of CN12 where only a minor ligand radius is specified. The equation formulated enables interatomic distances to be predicted within 0.01Å.

$$r = 0.1\,(CN) - 0.2\Delta$$

where CN is the coordination number (12, 14, 16) and $\Delta = 1$ for major ligands and $= 0$ for minor ligands.

Although this rule can also be applied to other intermetallic compounds (P, R, γ and μ phases) as well as the Laves and β-tungsten phases better agreement is achieved using the modified rule of Shoemaker and Shoemaker (51). The modification is to consider the radii as linear functions of the weighted

average of the Pauling CN12 radius of the two kinds of atoms, with the radii weighted according to the overall chemical composition of the alloy. For example,

$M_m N_n$ ...: $\bar{R} = (m.\ RCN12^M + n.RCN12^N + ...)/(m+n+...)$.

The interatomic distances may be predicted to within $0.06\mathring{A}$ with this modified rule.

Although these two relationships are of a purely empirical nature they are a consequence of geometric considerations involved in the packing of atoms of somewhat different sizes. Furthermore this treatment gives explicit recognition to the idea that major and minor radii for a given atom can be expected to be different and also that this difference may have some connection with features of electronic structure, such as existence of strong bonds in the major-ligand direction (50).

Sigma phase stability has been discussed so far in terms of (a) the valence electron concentration (VEC); (b) the electrochemical factor, strongly related to the transfer of electrons; (c) the size factor or geometrical factor.

With the valence electron concentration concept the question of which valencies have to be applied arises. Several systems have been proposed besides the usual chemical valencies. "Metallic" valencies have been put

forward by Pauling on the one hand and by Trost (80) and Engel (81) on the other (see Fig. 26). In some cases the valencies deduced have different meanings dependent on the combining element concerned. Thus, the normal valencies refer to compounds with hydrogen or oxygen, while the metallic valencies are established mainly on the interaction of atoms within the element in the solid state itself, or in metallic solutions taking into account the magnetic behaviour (Pauling) or the orbital constructions of the bands (Trost).

That geometrical arrangement alone does not lead to a definite conclusion has already been noted (Frank and Kasper). This is not unexpected since it is known that solid noble gases have the same structure as typical metals, a cubic or hexagonal close packing and besides the different atomic size there is a marked difference in the nature of the chemical bond.

Phases related to Sigma

The σ-phase can be considered as one of a sequence of alloy phases closely related in structure and occurring in a relatively narrow electron concentration range between the chromium group and the manganese group. The sequence, comprising the structure types σ, P R μ and χ(αMn) is arranged schematically in Fig. (23) from left to right in

Valences of Elements

Valence electrons	1	2	3	4	5	6	7	8	9	10	11	12
Metallic valences (Pauling)	1	2	3	4	5	6	6	6	6	6	5.6	4.6
Net bonding electrons (Trost)	1	2	3	3.9	5	6	7	7	4.57	3.76	3	2
Net bonding electrons (Engel)	1	2	3	4	5	6	6.8	6.4	6	5.4	4.1	2

Fig. 26

order of increasing average electron concentration.

The chi (χ) phase is isomorpous with alpha manganese and is body centred cubic with 58 atoms per unit cell. Coordination polyhedra corresponding to CN12, 15 and 16 occur in the structure. The phase appears in 17 binary systems of transition metals and in every case the A component is from the scandium, titanium, vanadium or chromium group, whereas the B component is either technetium or rhenium in 15 of the systems, and osmium in the remainder. Experimental studies (63,64) of ordering in the χ phase have provided support for the hypothesis (65,66) that the atom having the larger radius, invariably an A atom, is found in sites surrounded by 16 fold coordination polyhedra (large volume) whilst the smaller B atom occupies the sites CN12 and CN15 (small volume).

The (MoCr Ni) P-phase (67) is primitive orthorhombic with 56 atoms per unit cell; it resembles a sigma phase cell with an almost doubled b axis. As expected, the large molybdenum atoms exhibit a preference for sites of higher coordination. They share the CN14 sites with chromium but seem to be the sole occupants of CN15 and CN16 sites. The CN12 sites are occupied by nickel atoms in definite preference to chromium atoms (68).

The (MoCrCo) R phase (69) has rhombohedral symmetry with 53 atoms per cell. As in the P phase 12,14,15 and 16 fold coordination polyhedra occur. The sites having the larger volumes CN14, CN15 and CN16 are favoured by molybdenum atoms. Shoemaker (68) has recently applied neutron diffraction techniques to (MoMnFe) R to determine the extent of ordering in the CN12 position. Only a slight preference is shown by iron atoms for these sites in competition with manganese atoms.

The μ phase structure contains 13 atoms in a rhombohedral cell. As in the P and R phases, 12,14,15 and 16 fold coordination occur. Kasper (70) reports that iron or cobalt atoms are found in positions with CN 12 (icosahedral surroundings) while the larger tungsten or molybdenum atoms have the higher CN values.

Rideout and co-workers (16) have found the μ phase to occur over an extended range of compositions in the ternary systems (FeCoMo) (FeNiMo). The delta (δ) phase was discovered in the MoNi system by Ellinger (71). It has recently been assigned an orthorhombic structure with space groups, P2,2,2..(68). The ordering of the phase has not been studied up to now.

II THE FERRITE → SIGMA TRANSFORMATION

Introduction

Most sigma phases form by either a peritectic or peritectoid reaction (see Fig. (27)). In the case of (FeCr)σ and (FeV)σ, however, the phase forms from a body centred cubic solid solution. Although both of these alloy systems have received considerable attention from many investigators there is a dearth of information about the bcc → σ transformation in FeCr and almost none in FeV. Consequently the present investigation has been devoted to the factors affecting the formation and stability of the sigma phase in these two alloy systems.

The equilibrium diagrams of FeCr and FeV (Figs. (28,29) are similar; a continuous series of solid solutions exist as the α phase at high temperatures; a closed γ loop extends to 12% Cr and 1.2% V; a sigma phase field, centred on the equiatomic ratio with a peak at ~815°C FeCr and 1234°C FeV, is stable down to room temperature. The only fundamental difference is the recent report by Williams (72,73) that (FeCr)σ undergoes an eutectoid transformation to α + α'-a chromium rich solid solution (see Fig. (30)). This viewpoint has recently received theoretical support from Kubaschewski and Chart (74) who assessed the known

B \ A	V	Nb	Ta	Cr	Mo	W	Tc	Re
Mn	S δMn 1050°			P 1310°	D ?		?	?
Fe	S bcc 1200°			S bcc 815°	P 1540° D 1180°	?	?	?
Co	P 1420°			?	P 1585° D 1250°	?		
Ni	P 1270°							

Tc				?	?	?		
Ru				P 1600°		P 2300° D 1667°		
Rh		P 1660°	P 2110°					
Pd		P 1650°	P 2350° D 1575°					

Re	P 2490° D 1500°	P 2450° D 2400°	P 2740° D 2460°	P 2350°	P 2645° D 1200°	P 2900°		
Os		?	P 2500° D 1200°	P_d 1670° D 975°	P 2430°	P 2945°		
Ir		P 2060°	P 2475°		P 2095° D 1975°	P 2800° D 1800°		
Pt		P 1900°	?					
Au			?					

P - Peritectic
S - Solid State
D - Decomposes
P_d - Peritectoid
? - Unconfirmed report
Temperature °C

Fig.27

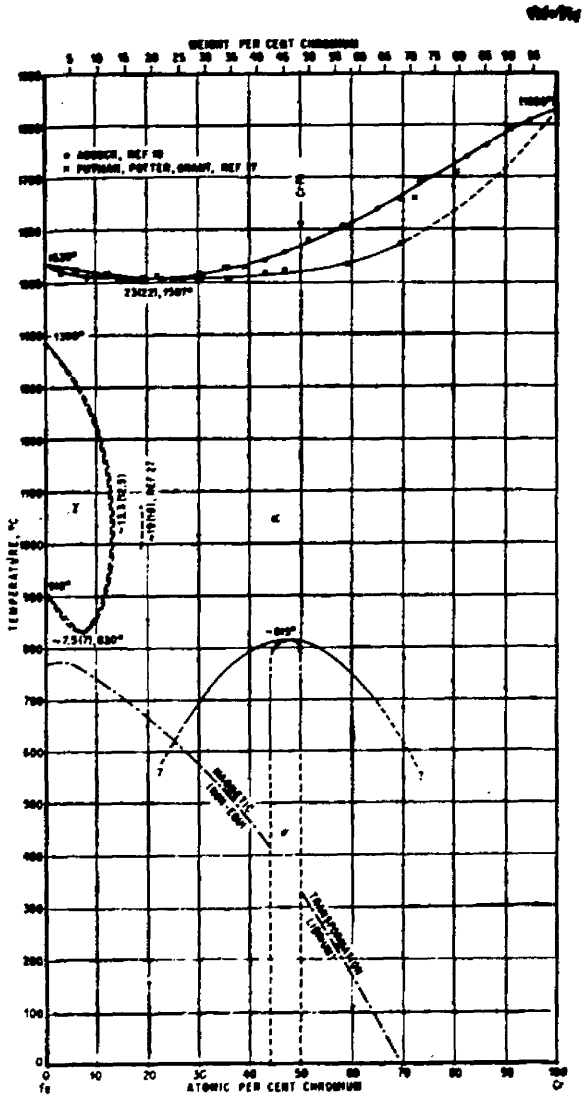

Cr-Fe

Fig. 28

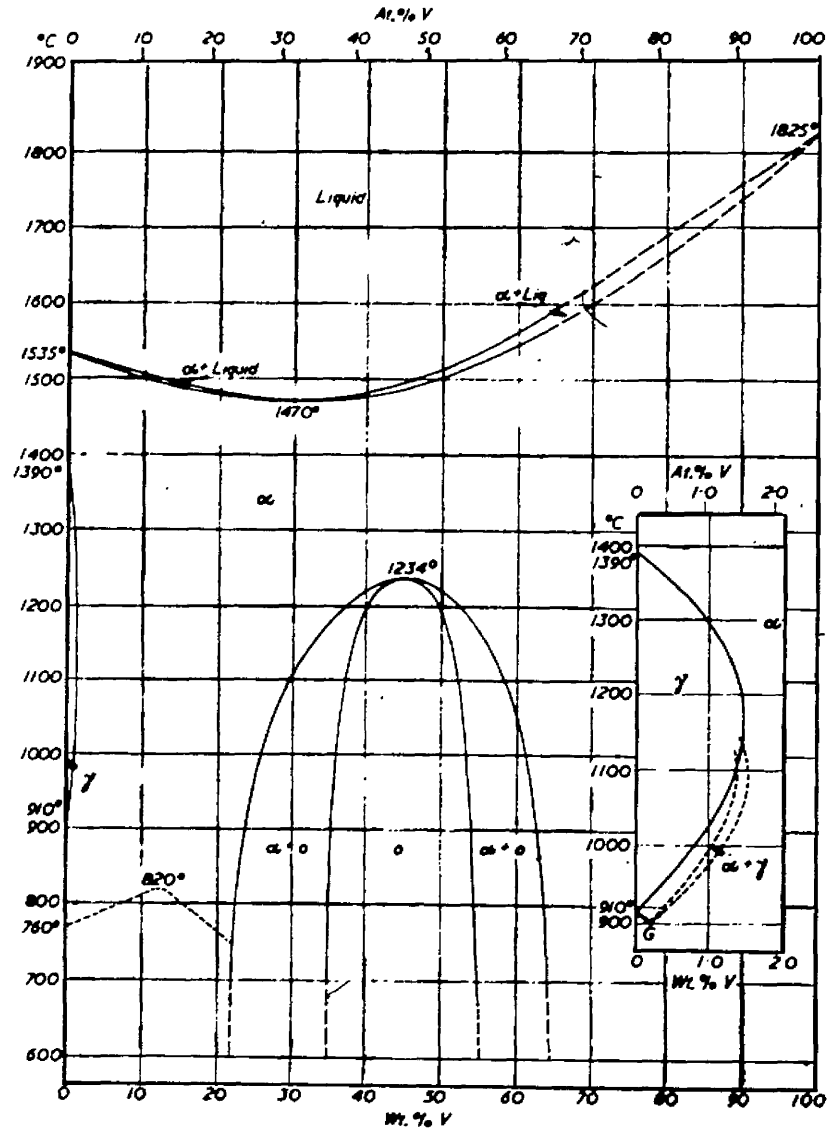

Fe-V

Fig. 29

thermochemical data on the formation of α and σ phases in FeCr and arrived at a eutectoid decomposition of 460° ± 50°C which is in fairly good agreement with the measured value of Williams ~520°C. In the light of this work it is not unlikely that the (FeV)σ might undergo a similar type of decomposition.

An important point to note about the FeV system is that due to the intense reactivity of vanadium at high temperatures some of the details in the equilibrium studies may not be representative of pure binary alloys. Pearson(75) has reviewed the effect of impurities on vanadium and these will be discussed later in terms of the transformation studied.

Kinetics

The α → σ transformation in pure FeCr alloys is very sluggish. Jette and Foote (76) report that a 49.4% chromium alloy in powder form, with no prior cold work, took 225 hrs. at 600°C to transform but the same powder after being cold worked in an agate mortar transformed to sigma after only 24 hrs. at 600°C. In the case of FeV alloys the transformation times are much shorter, the σ-phase forming in a matter of minutes.

The effects of composition, temperature and cold working on the rate of formation of σ-phase in iron-chromium alloys

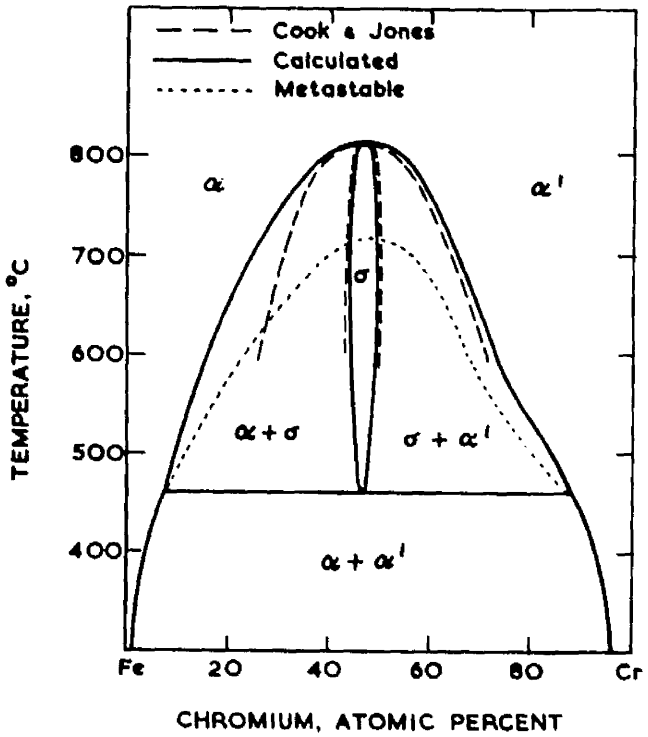

Part of the equilibrium diagram of the system iron–chromium

Fig. 30

Percent Sigma Transformed Versus Time at Various Temperatures. The "S" shape indicates a reaction taking place by nucleation and growth.

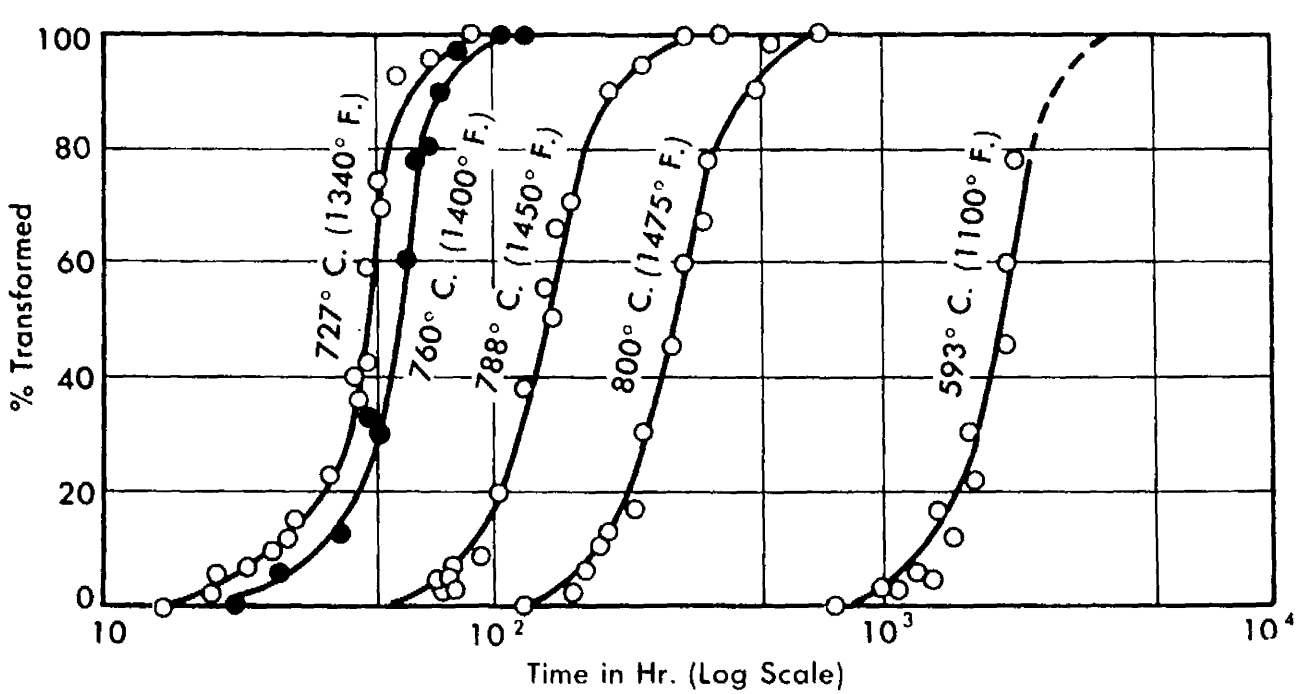

Fig. 31

have been investigated by Duwez and Martens (77) using magnetic and electrical resistance techniques.

An Fe 55.3% Cr alloy, which is located at the centre of the σ-phase field, was used to study the effect of temperature. The results are shown as Fig. (31), the percentage sigma transformed plotted against time at various temperatures. Duwez and Martens conclude from the "S" shape of the curves that the reaction is taking place by nucleation and growth. When the results are plotted as time necessary for 50% transformation versus the reciprocal of the absolute temperature it can be seen that at 725°C the time for half transformation is a minimum increasing sharply as the temperature approaches the equilibrium temperature for α and σ (820°C).

Isothermal transformations were also carried out on 20% and 95% cold worked samples. The results are compared with the stress free samples in Fig. (32). They have nearly the same shape as the curve for the annealed specimens but are displaced vertically. Thus the main effect of cold work is to accelerate the formation of sigma but not to change the temperature at which the formation is a maximum (725°C).

From a practical point the time necessary for half

of the α phase to transform to σ is about 45 hrs. for annealed alloys, 4 hrs. at 20% and 20 mins. for 95% cold work. Values of the heat of activation for the transformation were calculated from the slope of the straight line portion of the curves in Fig. (32).

α(annealed) → σ 80,000 cal. per mol.
α(20% cold work) → σ 63,600 cal. per mol.
α(95% cold work) → σ 42,700 cal. per mol.

The inverse transformation (from sigma to alpha) was also studied by Duwez and Martens (77). Their results, which are shown in Figs. (32) and (34), also lead them to conclude that the transformation is by nucleation and growth and that the reaction is relatively fast; at 850°C (30°C above eqlb. temperature), it takes only about 3 mins. to reach 50% transformation.

A range of alloys was isothermally treated at 650°C to establish the effect of chromium concentration on the transformation. Similar curves of percentage transformed versus log time were obtained to those in Fig. (32). Fig.(33) shows the time to 50% transformation versus chromium content for both annealed and cold worked samples. The top curve in Fig. (33) indicates clearly that the rate of formation is a maximum when the alloys contain from 43.5

Time Necessary to Convert Half the Alpha Structure Into Sigma Phase in a 44.7% Cr, 55.3% Fe Alloy.

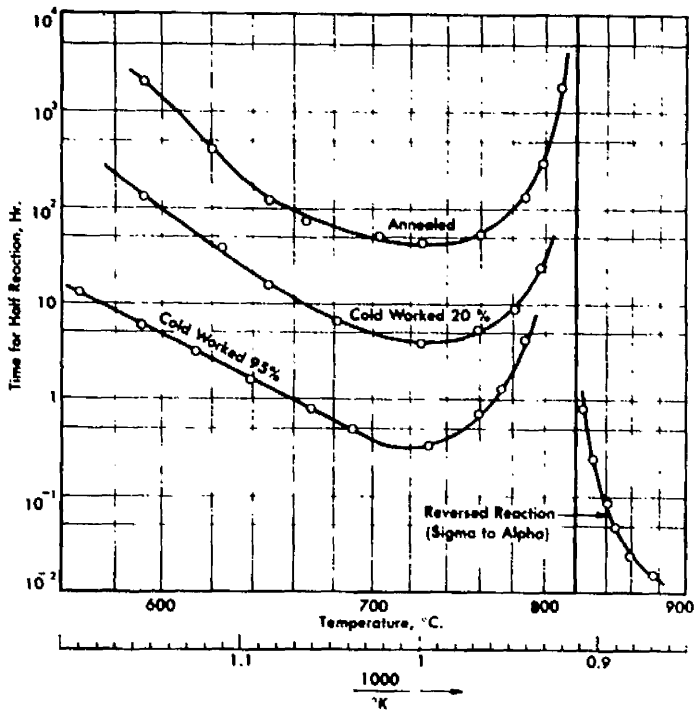

Fig. 32

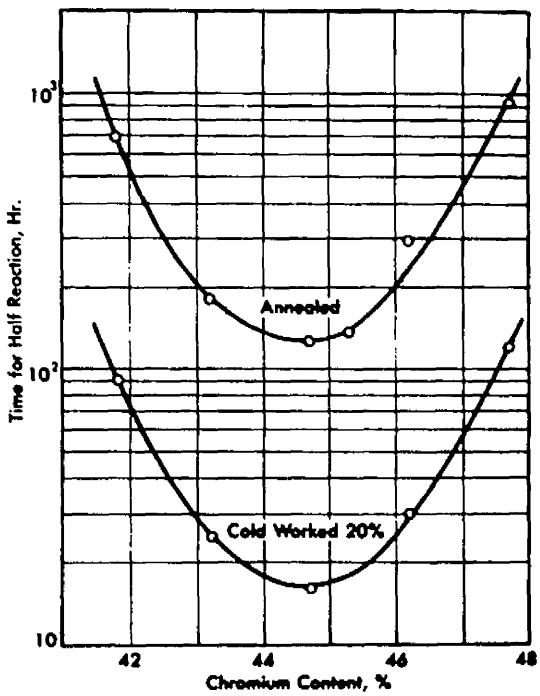

Time Necessary at 650° C. to Convert Half the Alpha Into Sigma in Cr-Fe Alloys With Varying Chromium.

Fig. 33

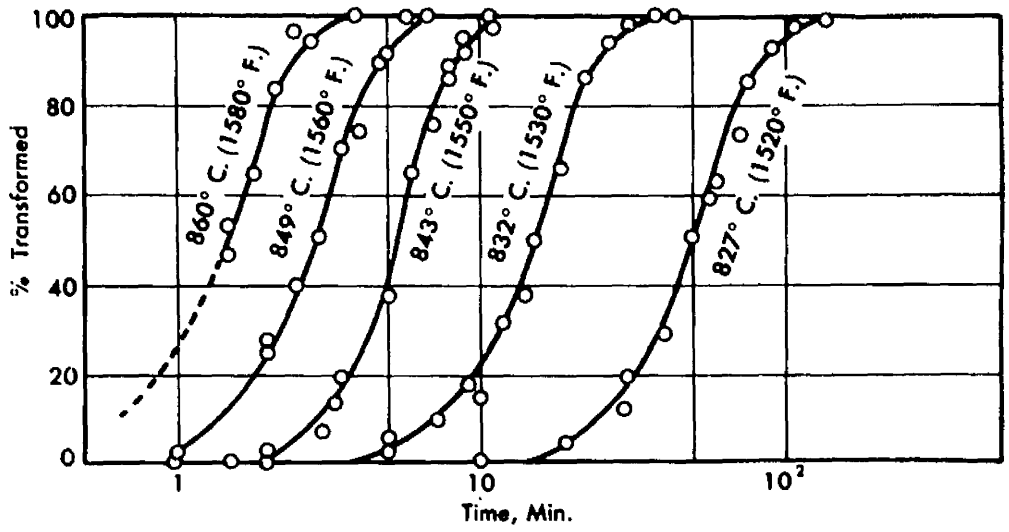

Percent Sigma Transformed Into Alpha Versus Time at Various Temperatures.

Fig. 34

to 45.5% chromium and decreases very rapidly as the chromium is either decreased or increased.

A more detailed study of the $\alpha \rightarrow \sigma$ transformation in iron-chromium alloys was made by Bastien and Pomey (78,79,82) (see Fig. (36)). They used several techniques to study the transformation including hardness, dilatometry, electrical resistance and magnetic measurements. They noted that the α phase increased in hardness prior to the formation of any σ -phase. This was attributed to ordering in the solid solution. Although unable to confirm this interpretation by X-ray methods, the structure factors are too close, other experimental techniques lead to a similar conclusion. Two reactions were distinguished (see Fig. (35)).

$$\alpha_d \rightarrow \alpha_0 \quad 480°C$$

$$\alpha_0 \rightarrow \alpha_d \quad 600°C$$

Isothermal studies of the $\alpha \rightarrow \sigma$ transformation revealed three reactions;

(i) α_d (quenched 1100°C) $\rightarrow \sigma$ 750 - 650°C, Q = 25 Kcal. per mol.

(ii) α_d (quenched 1100°C) $\rightarrow \alpha_0$ (partially ordered) $\rightarrow \sigma$ 550 - 650°C Q = 70 Kcal. per mol.

(iii) α_d (quenched 1100°C) $\rightarrow \alpha_0 \rightarrow \sigma$ 475 - 500°C Q = 30 Kcal. per mol.

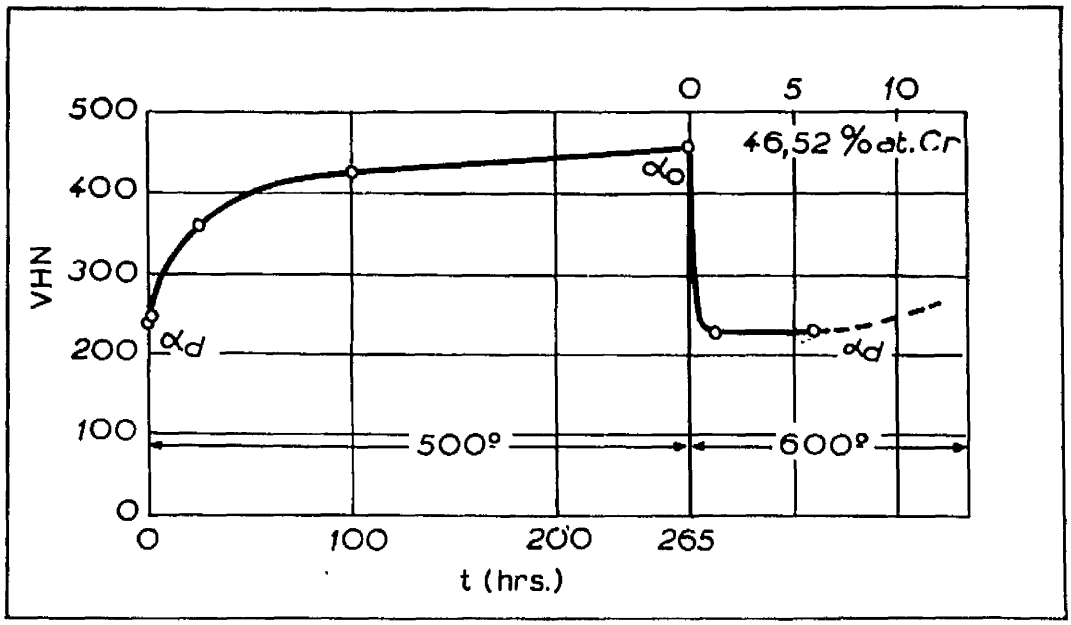
0 5 10
46,52 % at. Cr
500
400
300
200
100
0
VHN
α_o
α_d
α_d
500°
600°
0
100
200
265
t (hrs.)

Fig. 35

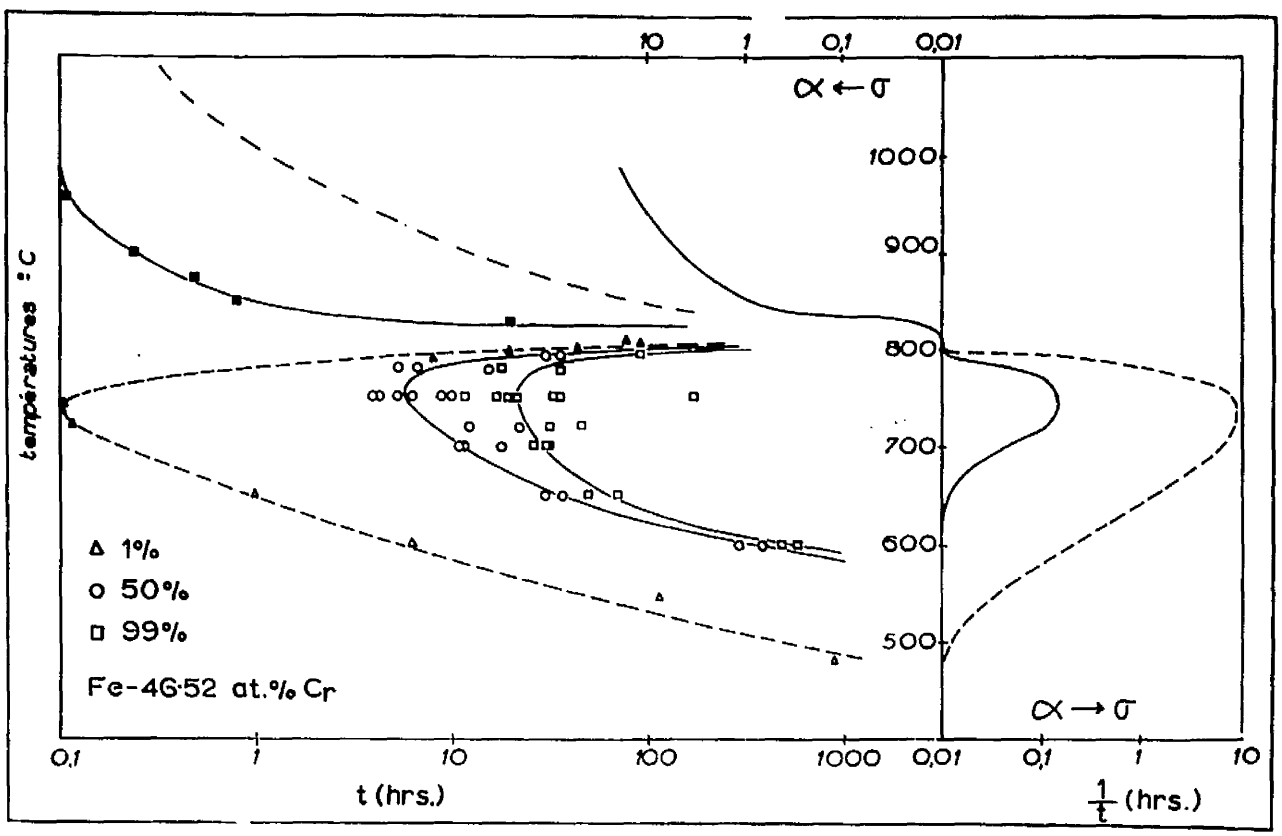
10 1 0,1 0,01
$\alpha \leftarrow \sigma$
1000
900
800
700
600
500
temperatures °C
Δ 1%
o 50%
□ 99%
Fe-46·52 at.% Cr
$\alpha \rightarrow \sigma$
0,1 1 10 100 1000
t (hrs.)
0,01 0,1 1 10
$\frac{1}{t}$ (hrs.)

Fig. 36

A metallographic investigation showed that the sigma tends to form at the grain boundaries and only occasionally in the middle of a grain. No difference was noted in the shape of precipitate formed by the three different reactions.

By traversing the α/σ boundary Pomey (79) was able to show that α and σ grains have the same composition and consequently there is no long range diffusion during the transformation. It was also noted that cracks form in the sigma phase during the transformation from the alpha phase. More cracks form on prolonged annealing but when reannealed at 1100°C in the alpha phase the cracks seal up.

Anderson and Jette (83) have investigated the microstructure of iron-chromium alloys with silicon additions which accelerate the $\alpha \rightarrow \sigma$ transformation. In slowly cooled alloys, well within the $\alpha + \sigma$ boundary the σ occurs in patterns suggesting a eutectic. Fig.((37) (1)) shows the 'eutectoid' to be partly coarsely laminated and partly globular mottled. In other annealed and slowly cooled alloys, the laminated structure is entirely absent and the sigma appears in an irregular distribution of sharply cornered elongated areas Fig. (37(2)). These areas all contain a more or less mottled structure.

Quenched and aged specimens, whose compositions are

located near the phase boundary between the α and α + σ regions have structures not unlike martensite Fig. (37(3)). Anderson and Jette also noted that alloys in the sigma phase were hard to etch but when deeply etched produced a distinctive corrugated structure with rarely any indication of grain boundaries. Occasionally the corregations form a distinct rectangular Widmanstatten structure Fig. (35(5,6)).

In the case of the iron-vanadium system Beck and Phillip(84) have noted that the body centred cubic phase orders before practically any of the stable sigma is formed. Using chromium radiation three super-lattice lines were observed $(100)_{\alpha}$, $(111)_{\alpha}$ and $(210)_{\alpha}$. It was also noted that there is a slight decrease in the lattice parameters when the phase is ordered. No other work has been published on the α → σ transformation in iron-vanadium alloys.

The effect of alloying additions on the formation of (FeCr)σ and (FeV)σ

Carbon, Nitrogen and Boron: These elements do not show any appreciable solubility in the sigma phase. Instead they form carbides, nitrides and borides with the element having the lower atomic number in a given transition series. This is in accordance with the assumption (85,86) that bonding strength between a transition metal (Me) and one of the non-metals carbon, nitrogen or boron (X) decreases with

1

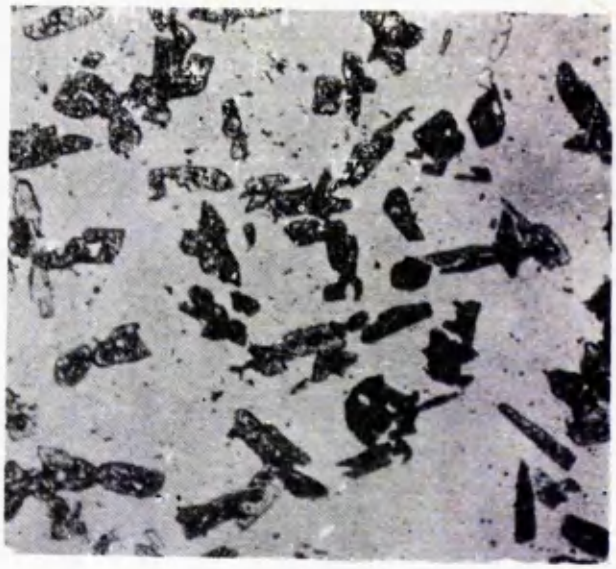

2

3

4

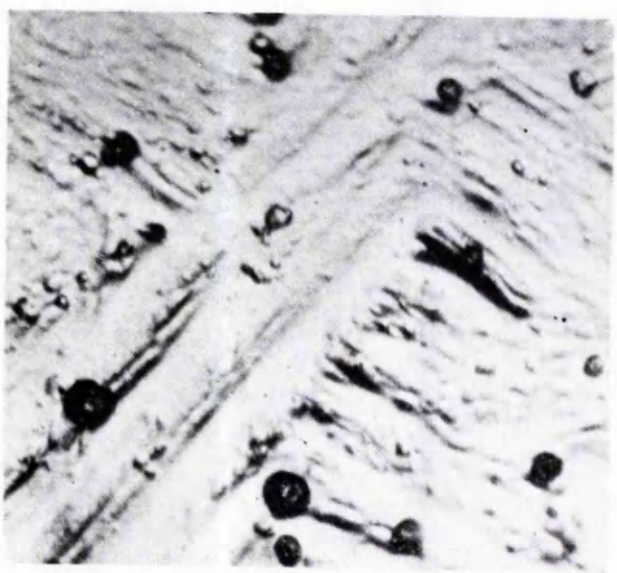

5

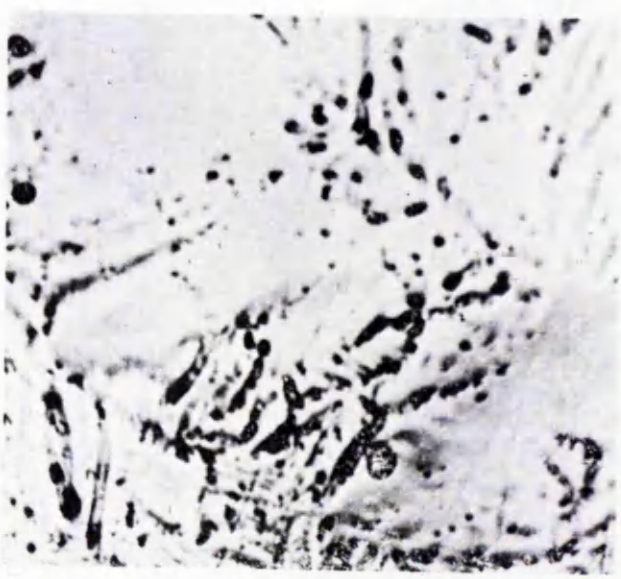

6

Fig 37

increasing atomic number of the transition metal in a given transition period.

In the metal rich part of the FeCrC system 15 - 43 wt%Cr Shortsleave and Nicholson (87) found that Cr - rich $(CrFe)_{23}C_6$ carbide is formed thereby lowering the amount of Cr available for σ formation. The higher the carbon content of the FeCrC alloy the higher the total Cr content which is necessary for (FeCr)σ to be formed. The effect of nitrogen on sigma formation in FeCrNi steels is analagous, Cr - rich nitrides being formed (65)(83). Aronsson and Asselius (89) have shown that a Cr - rich boride $(CrFe)_2B$ is formed when boron is added to FeCr, and that above 8%B no sigma is formed. Lattice parameter measurements of an FeCr 54/46% alloy with increasing boron concentration show that the 'a' axis of (FeCr)σ decreases and the 'c' axis increases. Aronsson and Asselius suggest that the differences in lattice parameters are not due to solubility of boron in (FeCr)σ but due solely to the variations in iron content caused by chromium being used to form borides.

There are no reports of any studies of the effect of non-metals on (FeV)σ formation. However, it is probable that the results described for (FeCr)σ are applicable to (FeV)σ and that V - rich carbides, nitrides and borides are formed which

have the effect of lowering the amount of vanadium available for sigma formation.

Silicon :

Following the work of Jette and Foote in 1937 (76), several investigators have studied the influence of silicon on the formation of σ phases. The indications are that silicon shows an extensive solid solubility in binary sigma phases of 3d elements and extends the stability range of the sigma phase.

Anderson and Jette (90) carried out an X-ray investigation of the FeCrSi diagram. They established that up to 9 or 10 wt%Si was soluble in (FeCr)σ. No lattice parameters were calculated since the structure was unknown but a list of observed $\sin^2\theta$ values was published.

More recently Aronsson and Lundstrom (91) have confirmed the results of Andersen and Jette and shown that (FeCr 10%Si) is stable up to the melting point and that when the solubility limit (17%Si at 900°) is exceeded Cr - rich Cr_3Si and Fe - rich α phase with about the same silicon content are formed, see Fig. (38).

Only small changes in lattice parameters with varying silicon concentrations were observed Fig. (39). The 'a' values decrease and the 'c' values increase. The unit cell

volume decreases by 0.03% per atomic %Si which is about half the decrease when small amounts of silicon (10%) are dissolved in iron (92). The axial ratio increases from 0.5181 to 0.5220 for an increase of 0 → 14% silicon.

That the cell volume and 'a' dimension decrease is important since the Goldschmidt radius 1.34Å for silicon CN12 is greater than both iron and chromium. However, it has been pointed out (93) that results from structure determinations of silicides and from the solid solubility of silicon in transition metals with unfilled d-shells indicate an apparent Si-radius of 1.20Å. If the revised estimate of atomic radius of silicon is used the cell shrinkage is quite understandable.

From X-ray diffraction measurements on single crystals Arronson and Lundstrom (91) propose that silicon behaves as a B type metal occupying mainly IV (D) positions. Also they propose the following distribution of atoms in (FeCrSi) assuming that the metal atoms are ordered in the manner suggested by Kasper and Waterstrat (31).

I	A	mainly Fe
II	B	mainly Cr
III	C	Fe + Cr + perhaps little Si
IV	D	3Si + 5Fe
V	E	Fe + Cr + perhaps little Si.

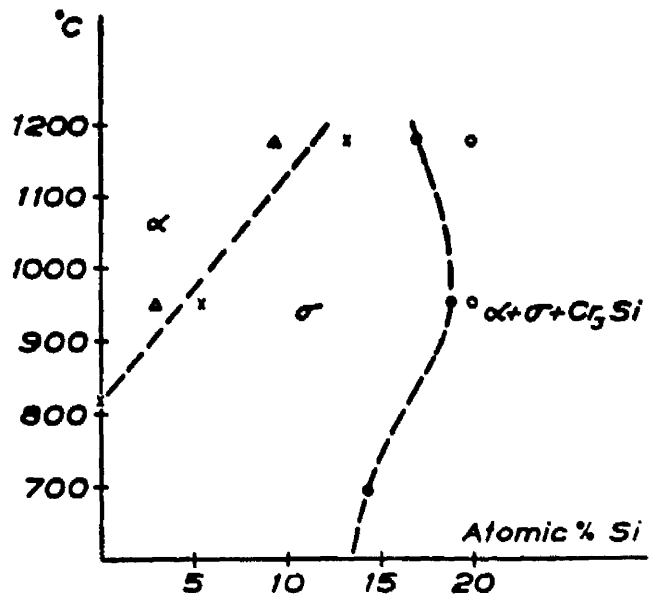

Sigma region in the section FeCr-Si of the Fe-Cr-Si system.

△ Powder photographs showing α-phase
X » ——— » ——— » σ-phase
○ » ——— » ——— » α+σ+Cr_3Si
● Solubility limit of sigma phase, determined from lattice dimensions.

Fig. 38

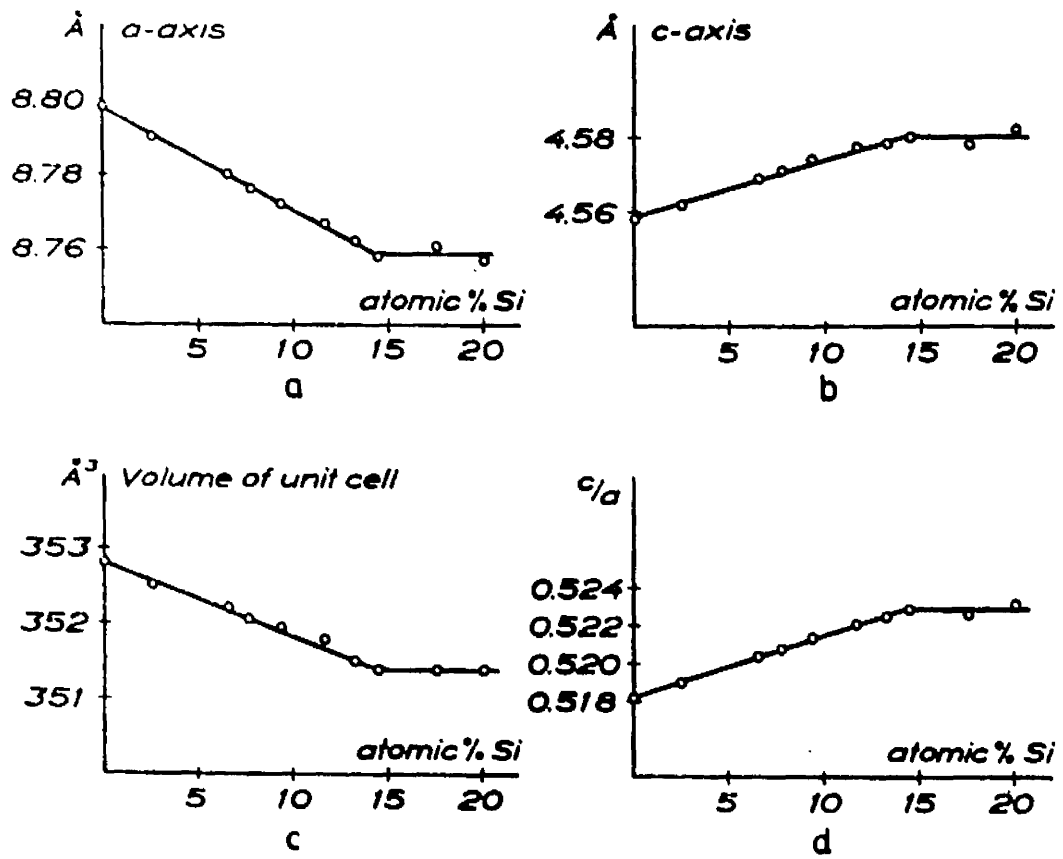

Lattice parameters of σ-FeCrSi as functions of Si-content at 690°.

Fig. 39

That silicon behaves as a B metal is in accordance with the following facts; the solubility of silicon is greater in iron (26%) (92) than in chromium (<14%) (94); the highest coordination number of silicon in any other known silicide structure is 12.

Aronsson and Lundstrom make the interesting point that no silicon atoms are found in position I which is also CN 12. However, if more than 2 Si-atoms are placed in the unit cell the IV positions alone permit a more even distribution of the Si-atoms in the structure than does a combination of I and IV positions. If Si-Si contacts are to be avoided, a maximum of four Si-atoms per unit cell can occupy the positions having CN 12 and this can only be achieved if IV positions alone are occupied. It is recalled that the solubility limit corresponds to about 4Si-atoms per unit cell.

Aronsson and Lundstrom also remark on some interesting features common to both sigma and βW (A15) structures. In both of these structures straight rows of metal atoms with close contact are found. These rows are most easily formed by the transition metals of the Va and VIa groups. They are also found in a number of silicide structures which indicates that silicon might have some beneficial effect on the stability of these rows.

Additions of silicon to FeV have a similar effect as

on FeCr. Beck et al (95) have observed that at least 7% Si is soluble in (FeV)σ and that silicon tends to stabilise the σ-phase. Lattice parameter measurements (Fig. (43) show a similar trend to the (FeCrSi) results; increasing silicon content tends to increase 'c' decrease 'a' and to decrease the volume of the unit cell. It was also noted that with increasing silicon content new X-ray diffraction lines appeared and became progressively stronger. These intensity variations were accounted for by assuming that all Si-atoms occupy the IV (D) sites in the σ-structure.

Phosphorus :

Phosphorus has been found to have an effect comparable to silicon in FeCr and FeV. In the FeVP system the σ-phase single field was found to contain as high as 4%P at 1050°C (96). The effect of phosporus on the CrNi system has been investigated (97) and results show a similar behaviour to silicon in FeCr. For a constant CrNi ratio an increase in phosphorus content causes a decrease in the 'a' dimension while within the limits of experimental error the 'c' dimension is unaltered. There is also a contraction of the unit cell. Again, as in the case of silicon, it is surprising that the unit cell contracts when the Goldschmidt radius for phosphorus is 1·09Å. Studies of phosphides and the solid solubility of phosphorus in iron point to an apparent phosphorus

radius of less than 1.20Å. Since phosporus has a more pronounced effect on lattice parameters than silicon it is probable that phosporus might be smaller than silicon.

Aluminium :

Aluminium tends to destabilise the σ-phase in relation to the body centred cubic α phase. In the FeCr system Tagaya and Nenno (98,99) found that in alloys up to 30% Cr, 0.3% Aℓ or less increased the amount of σ-phase but a greater amount reduced it. In 35% Cr alloys the σ-phase could be completely suppressed by the addition of 1.25% Aℓ.

Similar results were found by Beck et al (95) in the FeV system. Less than 0.5%Aℓ is sufficient to suppress the σ-phasecompletely at 1175°C. No lattice parameters have been published and no ordering systems have been proposed.

Inspection of Figs. (40,41) reveal the extreme nature of the two opposite effects of aluminium and silicon on binary σ-phases. Beck et al (95) have discussed the nature of the effect of aluminium and silicon on the basis that the σ-phase may be a full zone structure. They suggest that the addition of silicon results in an increased tolerance of the σ phase for strongly electropositive elements such as vanadium and chromium; this may be due to the relatively electronegative nature of silicon. Beck et al go on to suggest that the

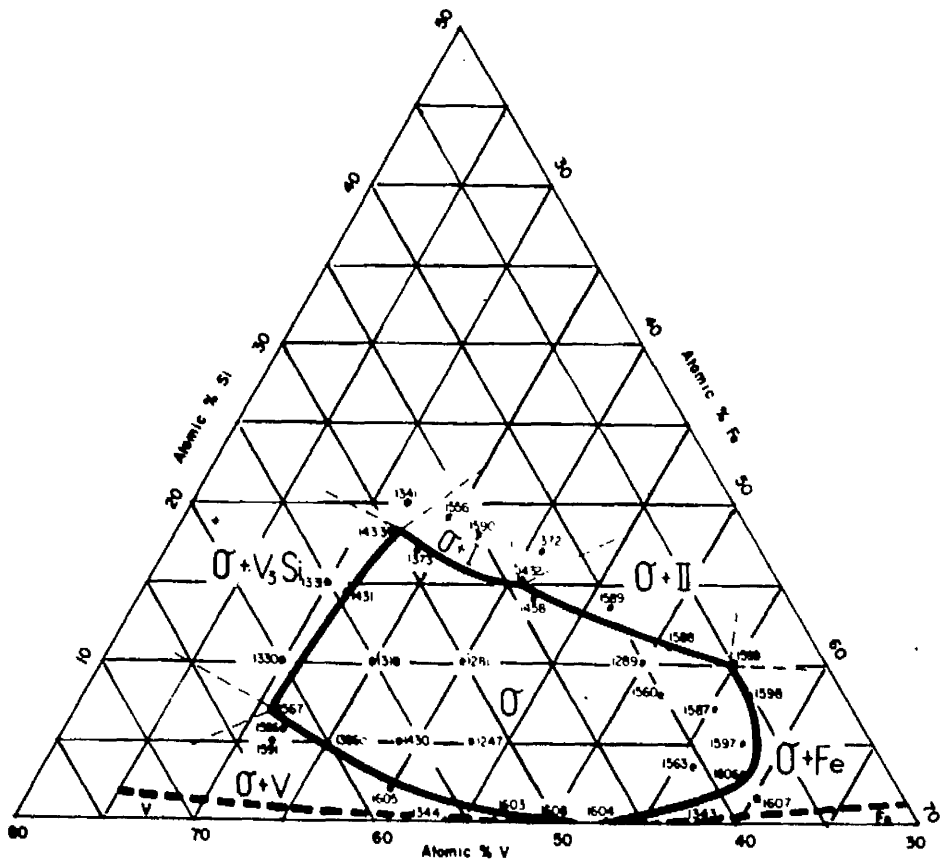

-Sigma phase in the 1175°C isothermal section of V-Fe-Si ternary phase diagram.

Fig. 40

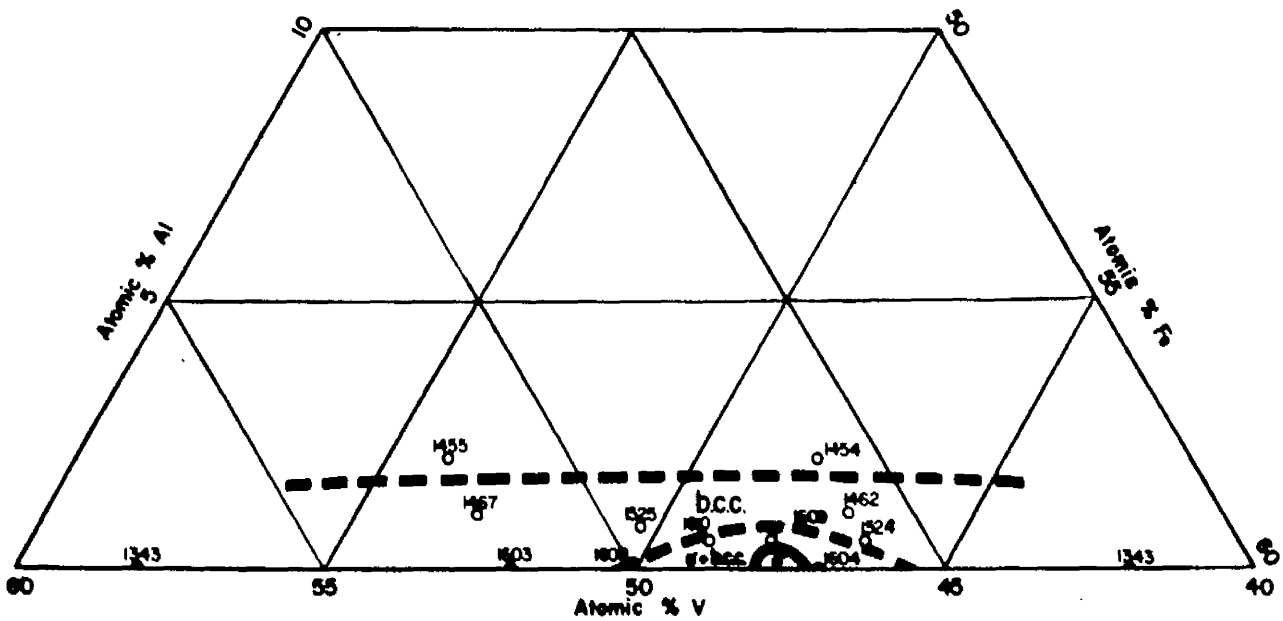

-Sigma phase in the 1175°C isothermal section of V-Fe-Al ternary phase diagram.

Fig. 41

silicon atoms may act here as "acceptors" of the extra electrons contributed to the system by the increased number of vanadium or chromium atoms. Conversely, the effect of aluminium in suppressing the α-phase may be due to its greater electropositive nature.

Manganese and Nickel :

The effect of manganese on iron-chromium alloys of commercial purity has been studied by Burgess and Forgeng (100). They noted that manganese accelerates the formation of the σ-phase and furthermore the temperature range in which the σ-phase is stable is appreciably widened by the presence of manganese.

45% chromium 0.78% manganese α→σ 7 hrs. 700°C

44% chromium 5.34% manganese α→σ 1 hr.700°C

Additions of up to 4.6% manganese were made to iron-chromium-silicon alloys by Jette and Andersen (101). The effect on the lattice parameters is small, which is due in part to the similar atomic sizes of iron, chromium and manganese and also to the low concentrations. The amount of sigma formed seemed independent of the concentration of manganese. Up to 2.0% nickel additions were also investigated with similar conclusions as those drawn for manganese, namely no effect on lattice parameters or rate of formation

Time Necessary for Half Transformation in an Alloy With 3% Tungsten, in Comparison With a Corresponding Alloy With None.

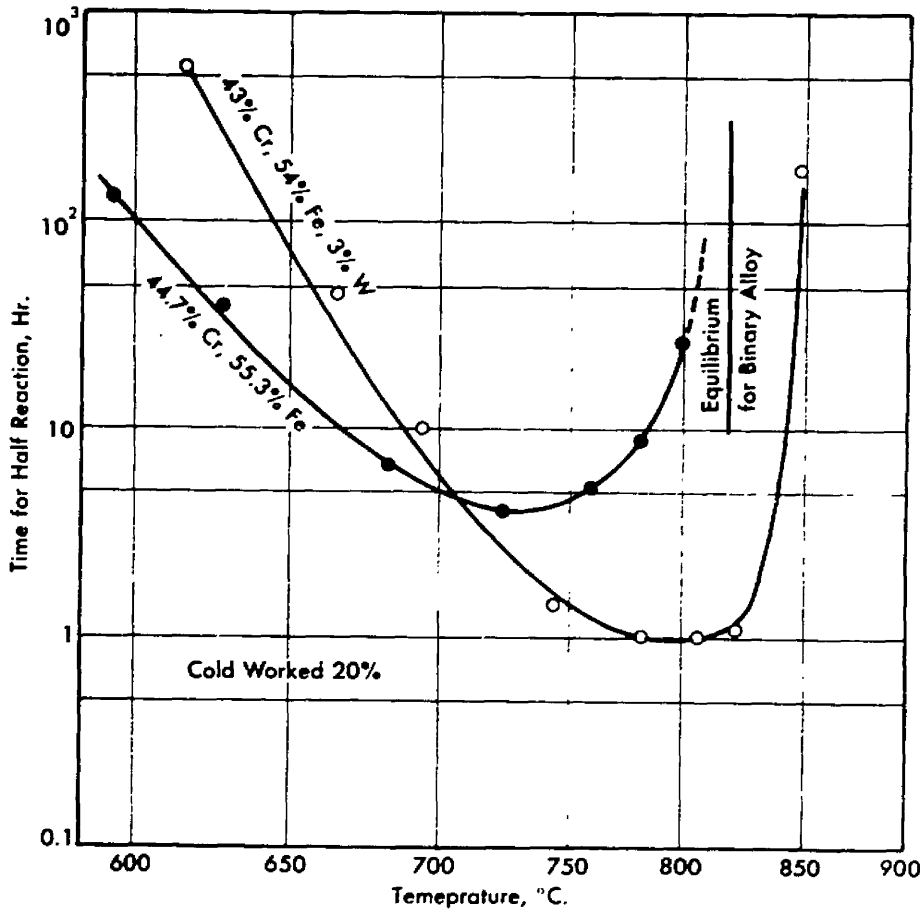

Fig. 42

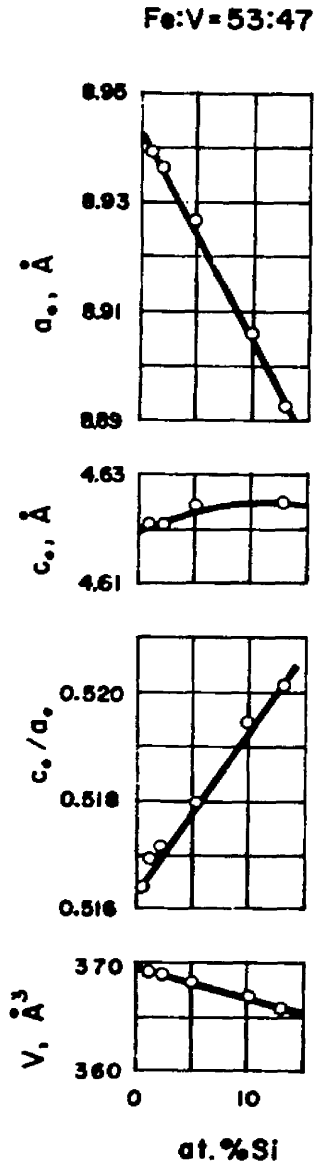

Fig. 43

of sigma phase.

Tungsten :

Duwez and Martens (77) have investigated the isothermal behaviour of a ternary alloy containing 43% chromium, 54% iron, 3% tungsten. The curves obtained at various temperatures for percentage transformed versus time had a typical S shape but were not as steep as the binary alloys shown in Fig. (42).

The addition of tungsten to iron-chromium alloys raises the temperature at which α and σ are in equilibrium and also raises the temperature at which the rate of sigma formation reaches a maximum. At temperatures below the maximum rate, sigma forms more rapidly in the binary alloy.

Atomic Mechanism

Kitchingman (34) has recently proposed an atomic mechanism of the body-centred cubic to sigma phase transformation based on the concept of kagomé tiling.

It is recalled that the sigma phase may be regarded as a simple layer structure of two hexagonal nets (Band C) at right angles, each supported by a diamond net (A); the stacking sequence is ABACAB. Following the conventions of Frank and Kasper (43) such a layer structure may be described in terms of the stacking of sheets of kagomé-tiling.

Fig. (44) illustrates the arrangement of atoms within each single sheet of tiling and also the three sheets superimposed.

The body-centred cubic may be regarded as a hexagonal structure with its c axis along one of the cube diagonals Fig. (45). The structure may now be interpreted in terms of three layers in the $[11\bar{1}]$ bcc direction; the stacking sequence being ABCABC. The three layers, ABC produce one layer of the sigma structure by a telescopic movement in the $[11\bar{1}]$ bcc. The atoms at the centre of the hexagonal nets so formed are removed to give the diamond net of the A layer of the sigma structure shown in Fig.(46). The crystallographic relations are

$$(11\bar{1}) \;||\; (001) \text{ sigma}$$
$$(1\bar{1}0) \;||\; [140] \text{ sigma}$$

In order to complete the sigma structure it is necessary to turn alternate hexagonal layers at right angles such that the top of a kagomé in the C layer is placed at the centre of a kagomé in the B layer.

Fig. (46) shows a network of four kagomés formed from a sequence of A, B and C layers of the bcc structure.

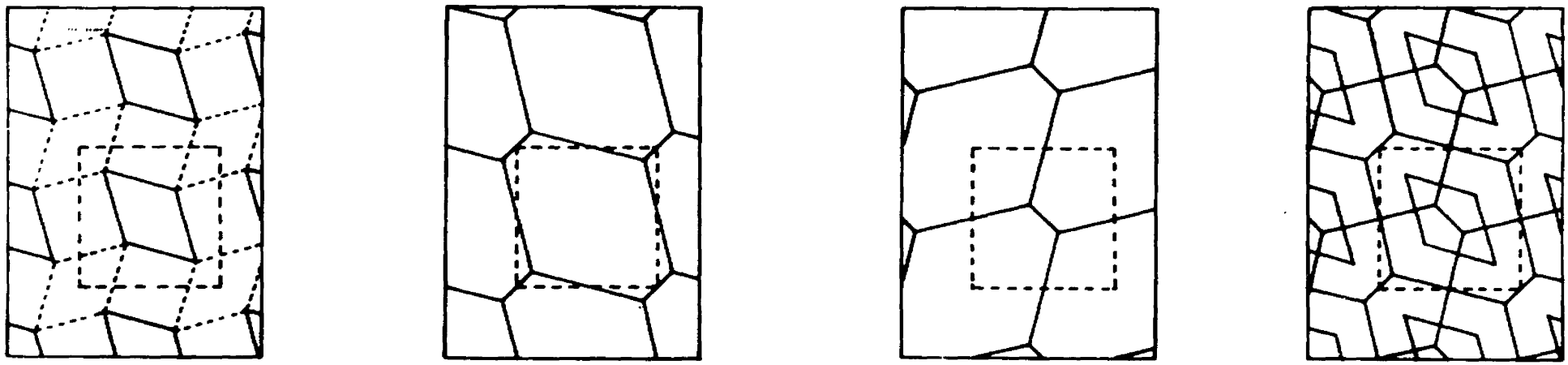

Fig. 44

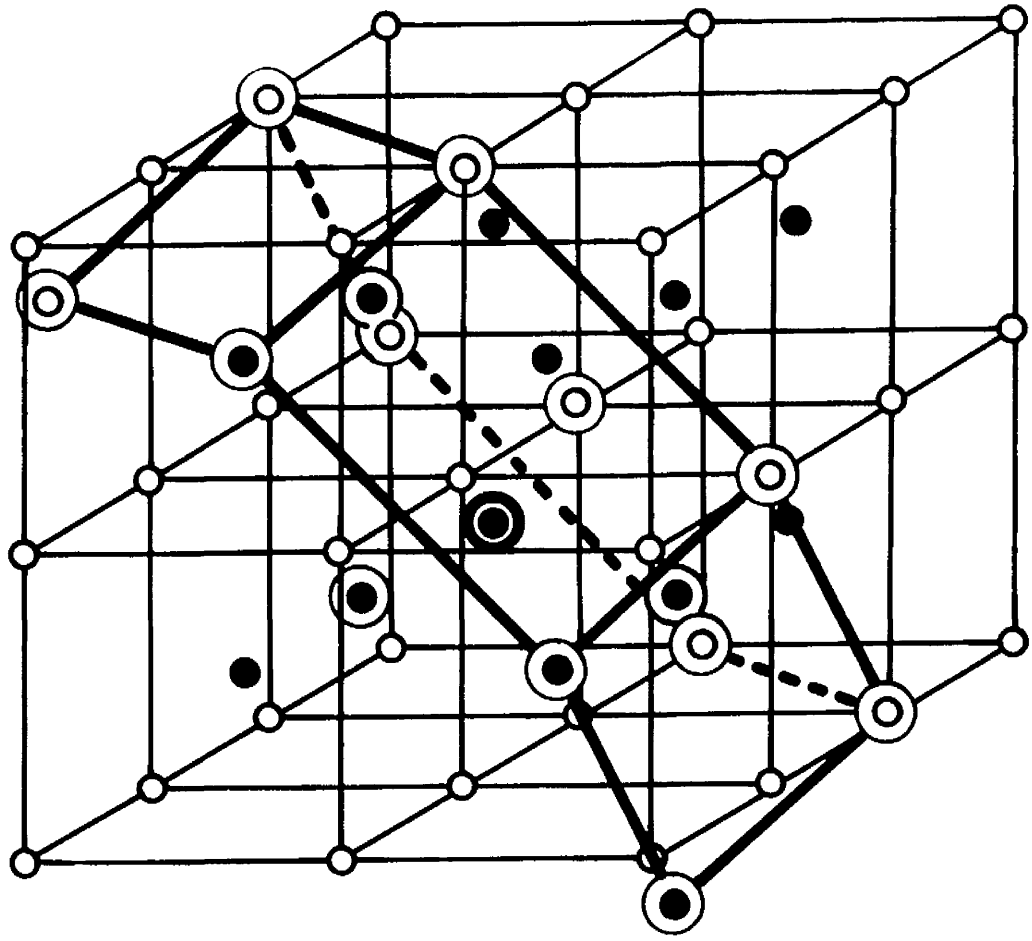

Fig. 45

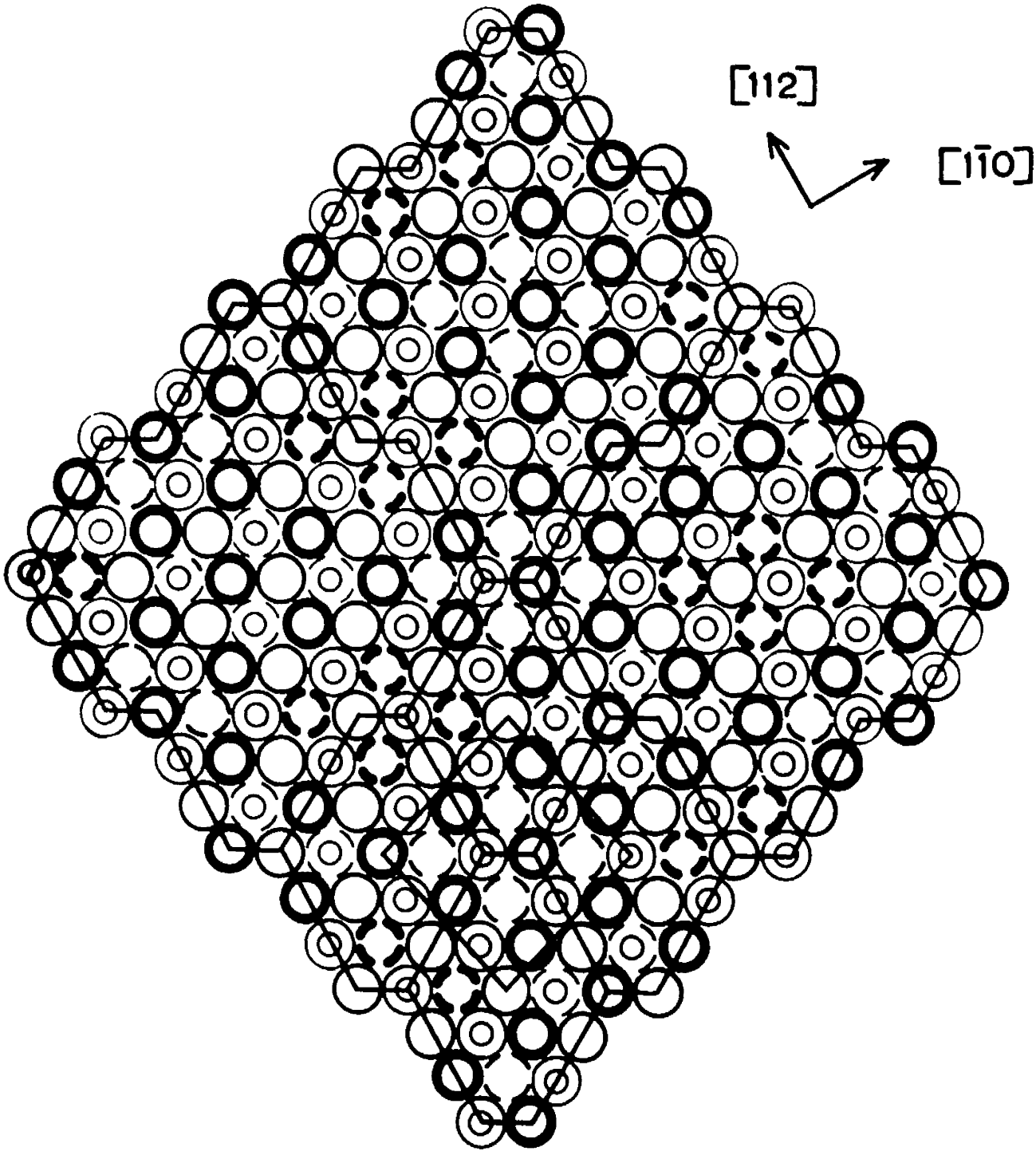

◎ $\frac{z}{c} = 0$ ○ $\frac{z}{c} = \frac{1}{3}$ ● $\frac{z}{c} = \frac{2}{3}$

Fig. 46

Three different groups of atoms may be removed from each layer as shown in Fig. (47). C is the obverse of B and A is a symmetrical group formed of a half C and B. Three such kagomé groups, (i.e.) twelve kagomés, fit together so that their border atoms are coincident. The whole structure consists of such groups of twelve kagomés, connected together as in Fig. (48). The contribution from any one layer in the bcc structure (see Fig. 47b), shows that in each layer certain groups of four neighbouring atoms, the dashed atoms, associate together to form the diamond nets connecting agomés, shown by the dashed nets in Fig. (44). Three layers below this there is a similar group of four atoms which are nearest neighbour atoms in the bcc structure. It is recalled that the distance between these atoms which fill the median voids between the crossed hexagons and form threads through the structure is much less than the sum of the radii of the atoms in these sites. Kitchingman also points out that in the disordered body centred cubic this nearest neighbour distance is the sum of the respective atomic radii, but in the ordered body centred cubic structure it is reduced compared with the sum of the radii.

The formation of the sigma phase commences with atoms of the diamond nets bonding with their counterparts, nearest neighbours in the body centred cubic, in successive layers.

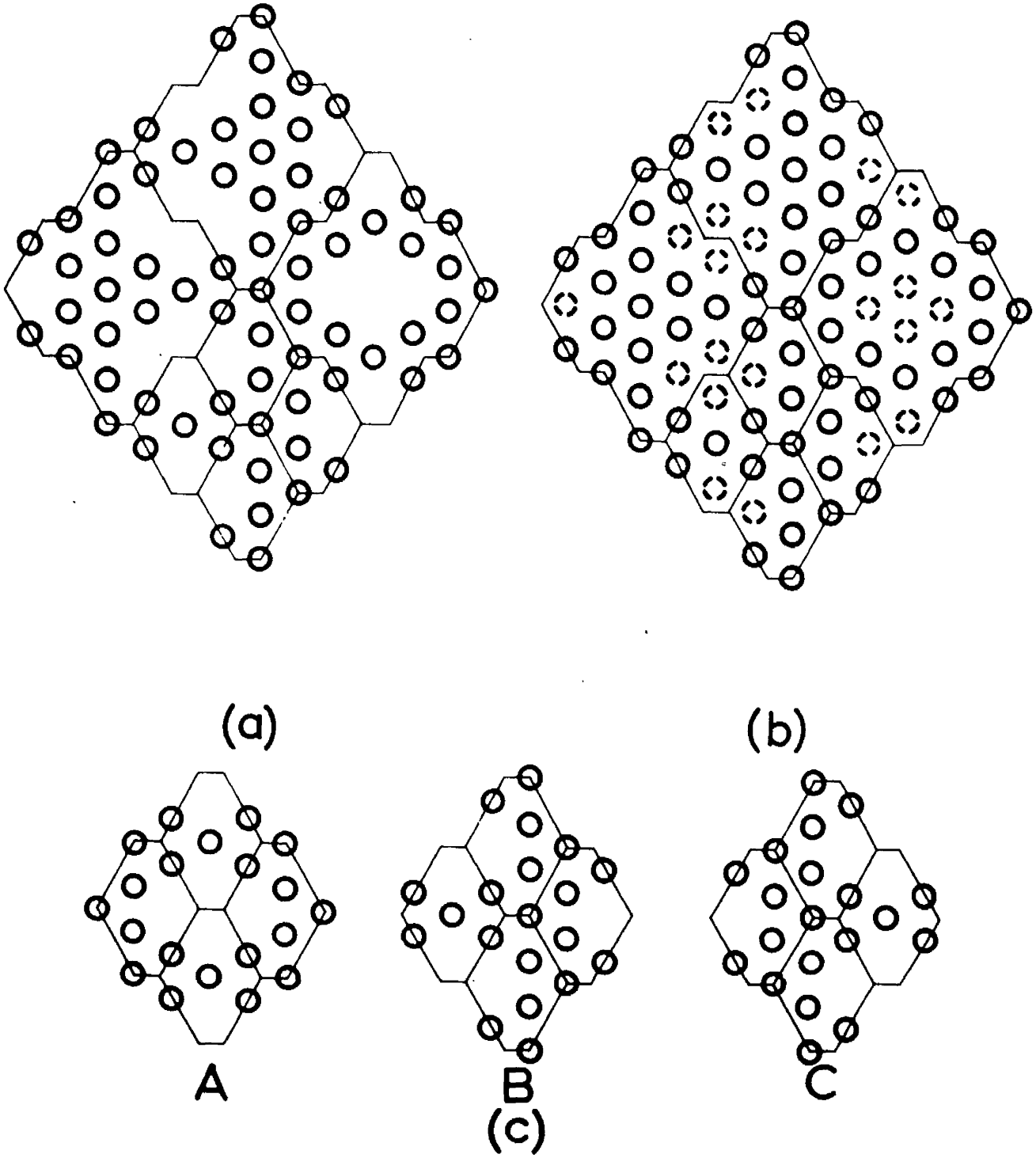

Fig. 47

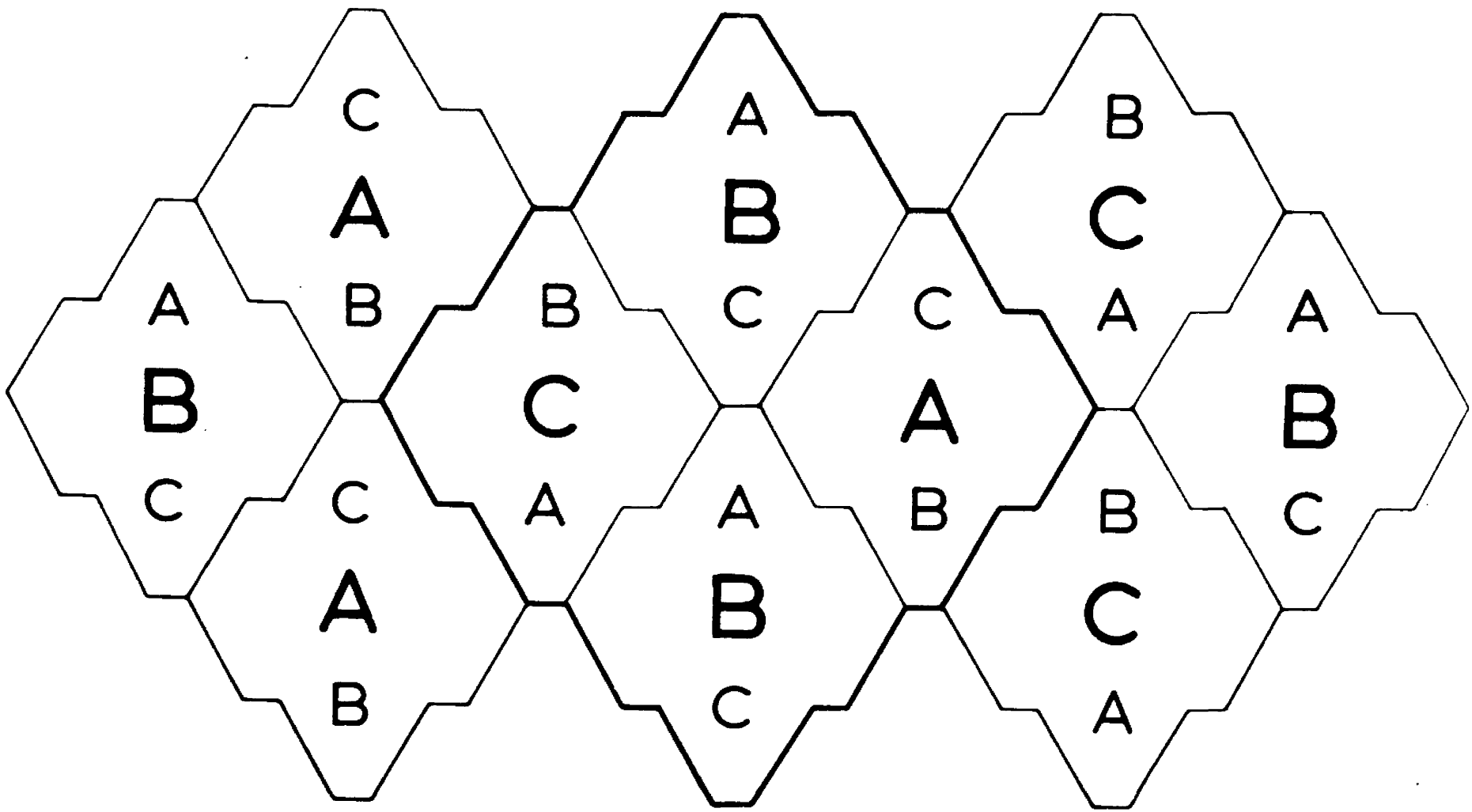

Fig. 48

This is followed by their movement in the $[11\bar{1}]$ bcc direction. In the final sigma structure these will form the vertical rows of E-type atoms. The transformation is completed by the remaining atoms in the body centred cubic layer combining to form the kagomés of the B and C layers of the σ-phase. In the case of the B layer kagomés this only involves movements of atoms in the $[111]_{bcc}$ direction. In the case of C layer kagomés the atoms must not only move in the $[111]_{bcc}$ direction but also rotate to occupy the positions of closest packing between the hexagons of the B layers.

Kitchingman describes the method of rotation and motion in the $[11\bar{1}]$ direction in the bcc by imagining lines of hexagons throughout the structure similar to the zones which Kronberg (102) used to describe slip in β-uranium. The hexagons rotate within these zones as the atoms move in the $[11\bar{1}]_{bcc}$ direction; atoms on opposite sides of the zone boundary move in opposite directions. This mechanism is shown in Fig. (49). It is clear that the rotation can only take place from one zone to the next as each kagomé at right-angles is formed.

In Kronberg's model a similar rotation of kagomés was brought about by the interchange of atoms from superimposed hexagons. However, Kitchingman points out that this was necessary since Kronberg's mechanism described the transition

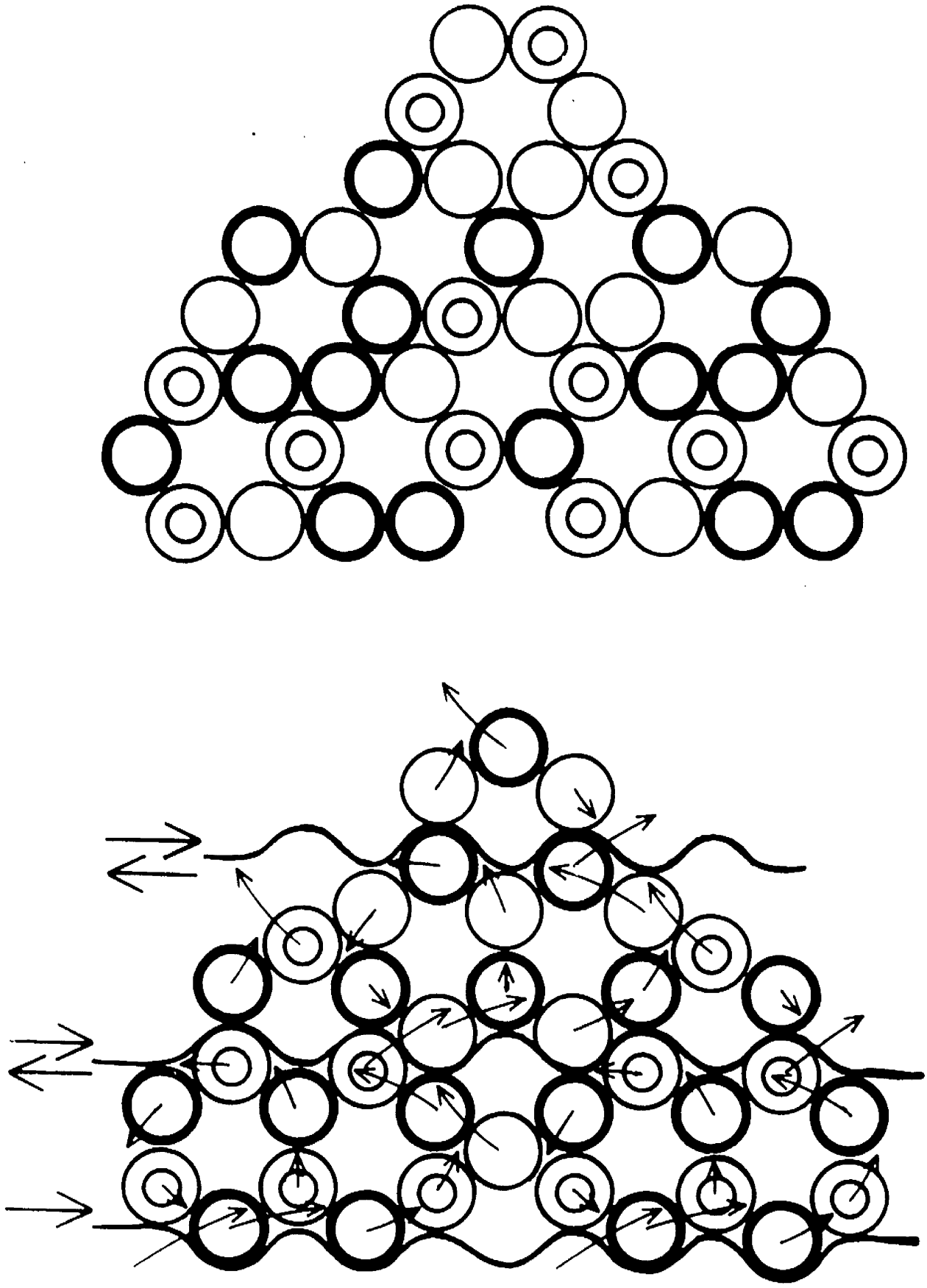

Fig. 49

from sigma to slipped sigma but in this model it is not necessary since the atoms in the body centred cubic structure are already displaced perpendicular to the hexagons in the $[11\bar{1}]_{bcc}$ direction and the rotation takes place as they move from the positions of more open packing of the body centred cubic structure to the closer hexagonal packing. The mechanism is equivalent to a shearing and displacement of kagomé nets and both mechanisms bring about the same rearrangement of atoms in the hexagonal planes.

Fig. (50) shows the movements in groups of twelve kagomes relating the atom positions in the bcc strucuture to those in the sigma phase structure based on the mechanism of Fig. (49). The partial long range order in the bcc structure just before transformation to the sigma phase may be deduced from the partial long range order of the sigma phase shown in Fig. (51).

Kitchingman has also discussed the reasons why the σ -phase is brittle when β-uranium which has a similar structure is ductile.

It has been established that sigma phase alloys show partial long range order characteristic of their composition. Fig. (51), which is adopted from Kronberg's model for slip in β-uranium and shows the ordered positions

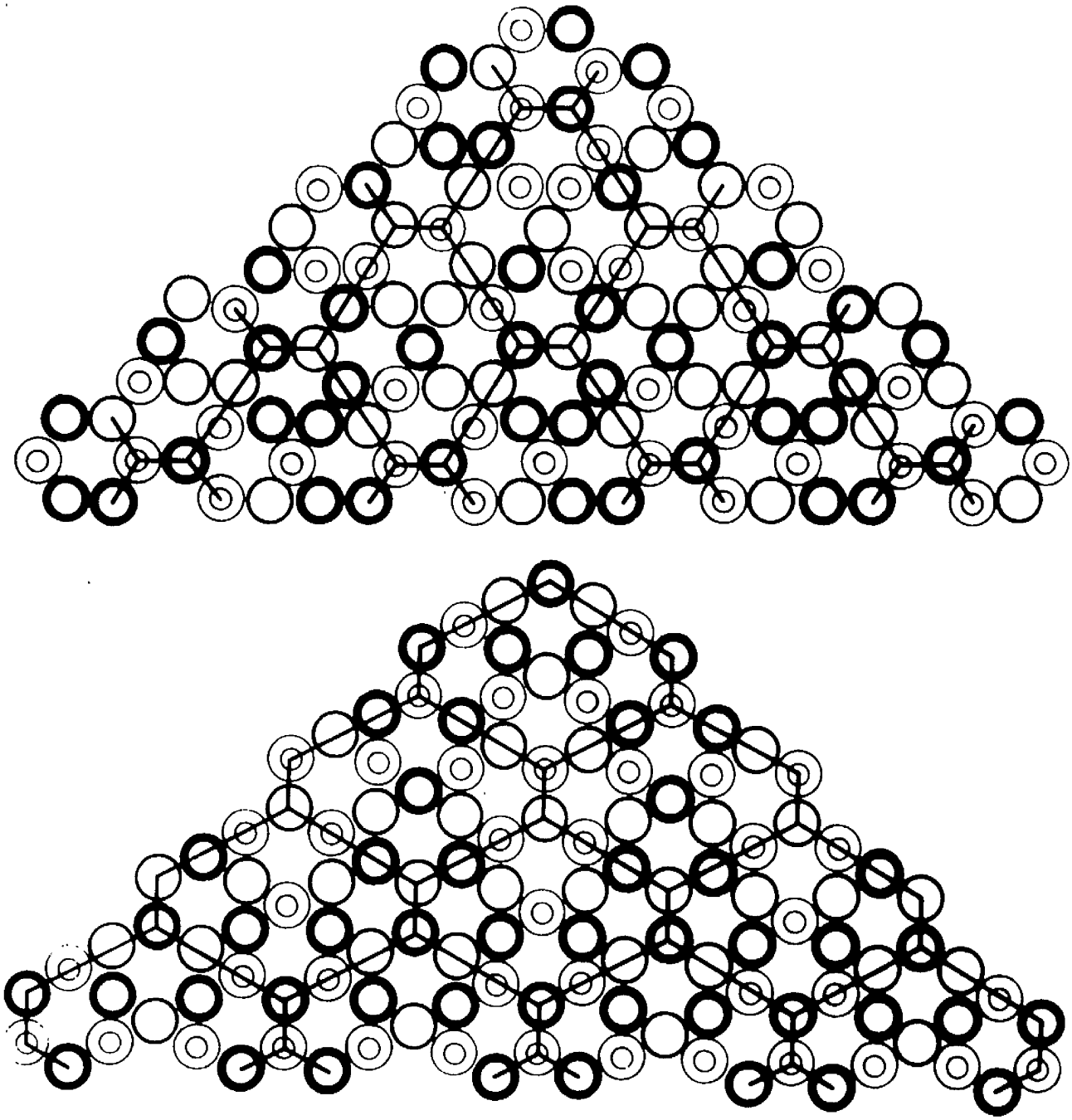

Fig. 50

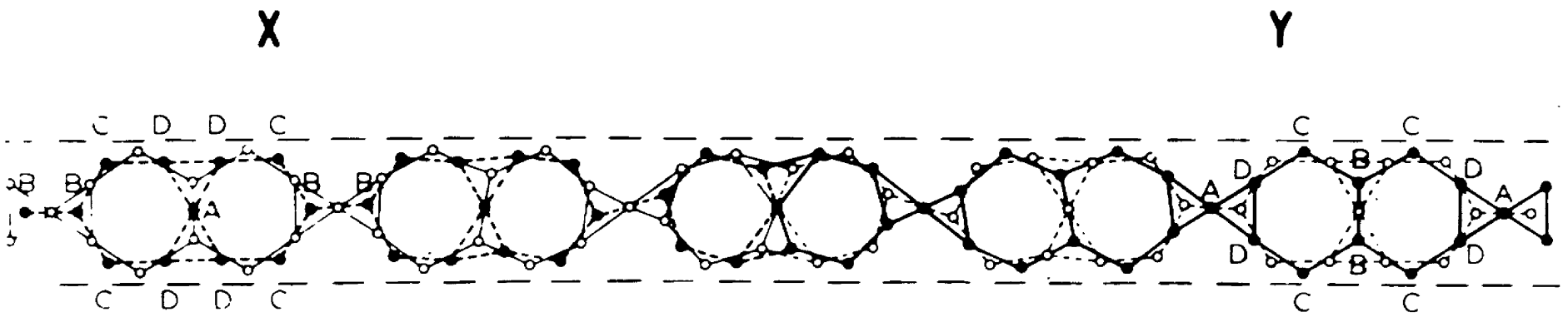

POSITION	COORD. NO.	ATOM	
A	12	Fe	Al
B	15	Cr	Nb
C	14	Fe/Cr	Al
D	12	Fe	Nb
E	14	Fe/Cr	Nb

INTERCHANGE	C.N. CHANGE
B → D	15 → 12
D → B	12 → 15
C → D	14 → 12
D → C	12 → 14
A → A	12 → 12

Fig. 51

of the iron and chromium atoms together with their coordination numbers. The slip zone XY and the rotation of hexagons within the slip zone is also shown. That atoms in the hexagonal nets play no part in the slip other than acting as central supports for the hexagons which rotate about them is in agreement with Kitchingman's model in which the diamond nets are more strongly bonded than those in hexagonal nets.

When slip takes place, in the case of β-uranium, rotation of the hexagons merely replaces uranium atoms with uranium atoms; uranium being present with all three coordination numbers, 12, 14 and 15 according to the definition of Frank and Kasper (43).

In the case of FeCr, rotation leads to an incompatibility with respect to ordering since in the case of the atom replacement B, D an iron atom CN 12 is replacing a chromium atom CN 15, in other positions both atoms show CN 14. The case of 2Nb Aℓ is analogous, incompatibility occurs in the replacement C D since Aℓ atoms of CN 14 must be replaced by Nb atoms CN 15. Again, both atoms show CN 12 but Aℓ does not show CN 15.

Kitchingman then proposes that uranium can exist in this structure in three different states characterised by coordination numbers 12, 14 and 15. Similarly niobium has

three states of CN 12, 14 and 15, iron two of CN 12 and 14, chromium two of CN 14 and 15 and Aℓ two of CN 12 and 14. Consequently Kitchingman suggests that these states may be associated with slightly different sizes and probably different outer electronic structures. It has been previously suggested by Mott and Stevens (103) and Lomer and Marshall (104) that iron may exist in two different electron states in alloys in order to explain certain magnetic properties of iron alloys.

Chapter II

THEORETICAL CONSIDERATIONS

I PHASE TRANSFORMATIONS IN METALLIC SYSTEMS

Introduction

Previous investigators have described the α→σ transformation as a nucleation - and - growth process. Duwez and Martens have noted that the kinetics are similar to those found by Borelius (105) in the ordering of equiatomic gold-copper alloys. It has also been noted that the α-phase orders to a CsCℓ structure prior to the formation of any σ-phase. The reaction product σ has been shown to have the same composition as the α-phase which suggests that there is no long range diffusion during the transformation. The growing crystals of α-phase frequently cross the prior grain boundaries of the parent phase Fig. (52). The theoretical model of the atomic mechanism suggests a type of shear mechanism brought about by the movement of zonal dislocations.

Since the mechanism of the α→σ transformation is not fully understood it is useful at this stage to review the different mechanisms by which phase transformations take place.

Modes of Transformation

In nucleation - and - growth transformations the new phase grows at the expense of the old by the relatively

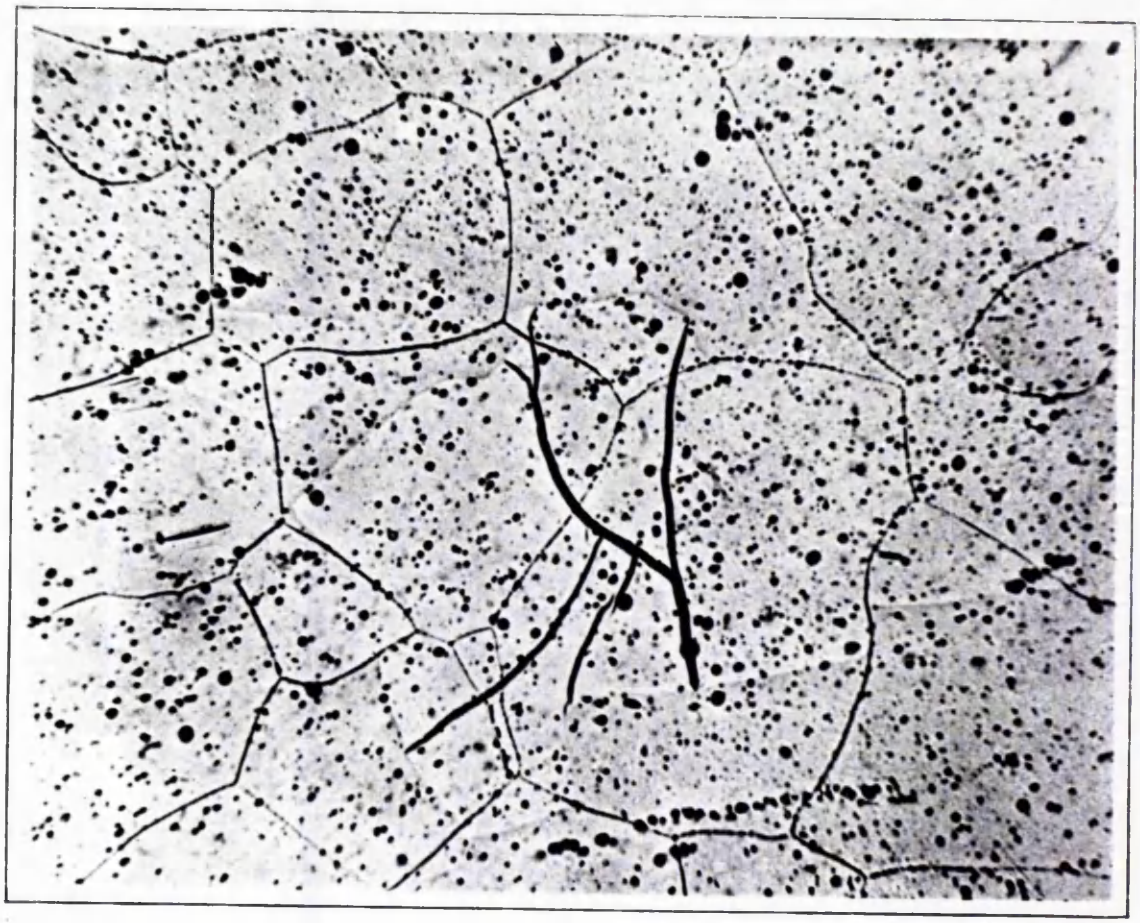

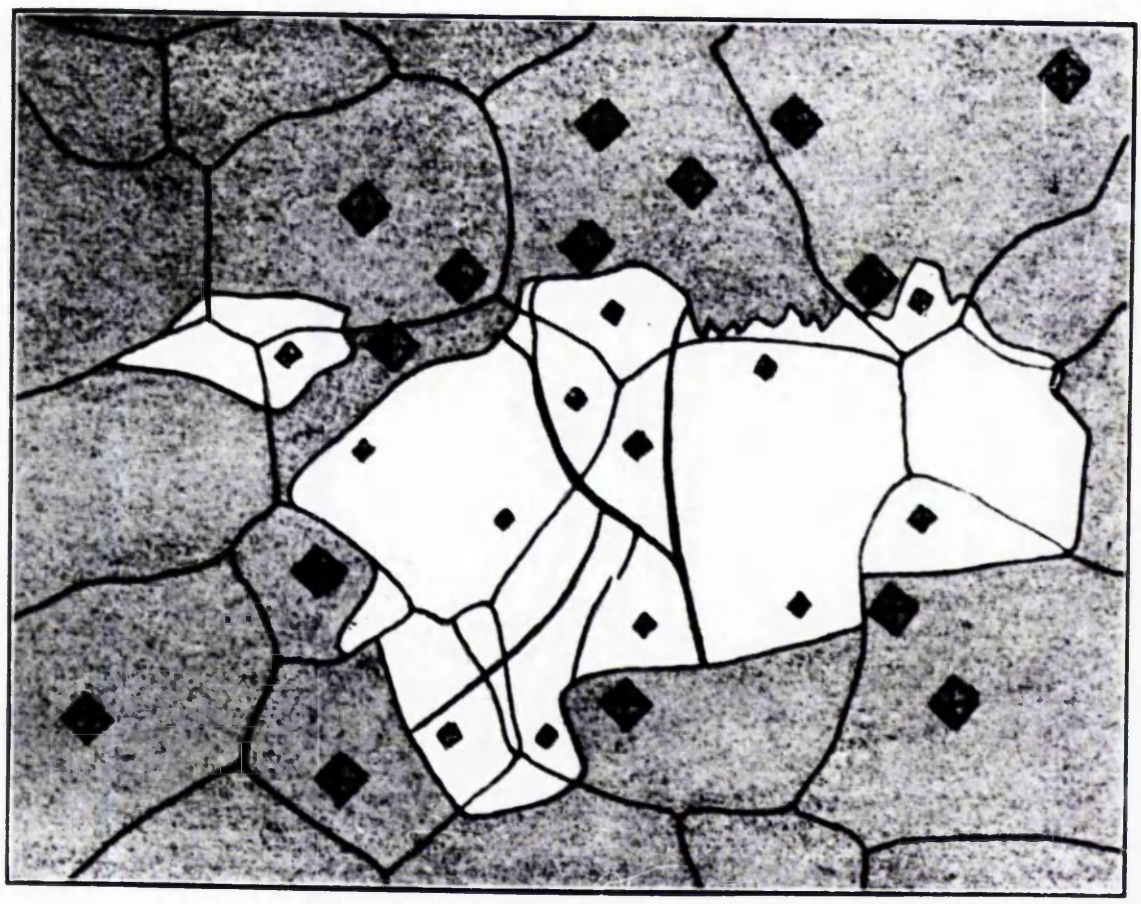

Fig 52

slow migration of the interphase boundary, and growth results from atom by atom transfer across this boundary. The atoms move independently at a rate which varies markedly with temperature. At a given temperature, the transformation proceeds isothermally the amount of new phase formed increasing with time. The volume of a transformed region differs in general from its original volume but its shape is unaltered. The transformation may be accelerated by cold working the parent phase. Possible explanations for this effect are that the activation energy for diffusion may be lowered and that the diffusion rate will temporarily increase as a result of the temporary increase in the number of vacant lattice sites.

It is evident that thermal activation and diffusion play an important role in nucleation and growth processes. However, martensitic transformations do not involve diffusion and are dependent only slightly, if at all, on thermal agitation; accordingly they are designated athermal transformations.

The amount of transformation is virtually independent of time. On cooling, transformation begins spontaneously at a fixed temperature (M_s) and as the temperature is changed, more and more material transforms

until the temperature (M_f) is reached at which the reaction is complete. The fraction transformed at any time during the cooling is characteristic of the temperature providing that other variables such as grain size are constant.

At any temperature a number of single crystals of a new phase form rapidly within an original grain. On cooling to another temperature these crystals usually do not grow but new crystals are formed.

Plastic deformation at any temperature in the transformation range usually increases the amount of transformation. Deformation above M_s may also result in the formation of martensite even though the temperature is too high for spontaneous reaction. The highest temperature at which martensite may be formed under stress is the M_d. If the original phase is worked in a temperature range where it is stable, above M_d, the resultant deformation often inhibits the transformation; the M_s is depressed and the amount of transformation at any temperature is reduced.

Despite the fact that volume changes are often, though not invariably, small the transforming material changes its shape; a feature which is usually recognised by the disturbances produced on an originally flat polished surface.

Although most martensitic transformations exhibit the characteristics described there are some exceptions. For example, certain martensitic transformations form isothermally at a low rate whilst some nucleation and growth transformations proceed with surprising rapidity. Consequently a change of shape has become the sole criterion of the martensitic transformation.

Further examples of the classification difficulties, unless shape change is taken as the sole criterion, occur in transformations in which diffusion controls the process, but which nevertheless conforms to the basic geometry of a martensitic change. The most common case is the bainite transformation in steels which forms by a slow shear-like transformation. It has the features of martensite yet it cannot proceed unless the driving force of the transformation is increased by an accompanying precipitation of carbides in the new phase. The precipitation, which is related to the diffusion of carbon, controls the rate of growth.

In the order-disorder transformation in equiatomic copper-gold alloys the long-period superlattice forms from the disordered cubic phase by a process of nucleation - and - growth. However, the orthorhombic phase grows in the form of pyramidal plates, and is accompanied by the production of

surface relief effects in the manner of martensitic transformations (106,107). Similar reactions occur in the majority of b.c.c. β phases based on the noble metals Cu, Ag, and Au (108). The β phases formed by these metals with divalent Zn, Cd, Mg, and Hg occur in the region corresponding to 50-50 atomic percent of solvent and solute. They order rapidly into the C_sCl structure during slow or even fast cooling followed by a martensitic transformation (108).

The β phases formed by the noble metals with trivalent (Al, Ga, Tl, In) and quadrivalent (Sn, Pb, Si) elements have a lesser tendency to form ordered structures on cooling, and when ordering does take place it is of the Fe Al type, the Heusler-alloy type, or a more complex type. Accordingly, the martensitic transformation in these phases involve several complexities. In the Cu - Ga (109) system in particlar the microconstituents, which invariably consist of shapeless areas with very jagged and irregular boundaries, are described as massive.

The word "massive" was first used by Greninger in 1939 (110) to describe the appearance of the microstructure obtained after quenching the high temperature b.c.c. β phase in a Cu - 9.3% Al alloy. Other examples of massive volumes of a low temperature phase formed from a high temperature phase of the same composition have been reported in alloy

systems of Cu, Ag, Fe, Zr (109,112,118).

Recently there has been some discussion (113) as to whether the word massive may be applied to classify a type of transformation. Massalski (109) has defined a massive transformation as one which is essentially diffusionless but in which, unlike the martensitic transformation, there is no shape change or surface relief. However, Owen considers that the word massive is a poor description of the transformation envisaged since it gives the impression of the in situ transformation of large volumes of parent phase whereas the atom transfer must occur across an interface which moves through each crystal separating the massive and parent phase. Consequently he confines the application of the word massive to descriptions of optical microstructures.

All massive structures are not formed by the same transformation mechanism. Two extremes have been recognised: those formed by short range diffusion (SRD) across an incoherent or possibly semi-coherent interface with no resulting shape change and those produced by a martensitic process involving shear.

In the SRD transformation the massive grains grow by the movement of incoherent grain boundaries which are not restricted or impeded by the boundaries of the parent grains through which they move (see Fig. 53b,c). The surface

of specimens transformed by SRD have been examined but no evidence of surface shears or other irregularities has been found (118).

The other extreme, the martensitic transformations, has been shown to occur in some iron alloys notably iron-nickel alloys containing between 10 and 29.5% Ni (118). It was shown that over a wide range of cooling rates these alloys transformed from γ to α of the same composition. Complete transformation was not observed in alloys with the highest nickel content but in those with lower nickel contents the γ to massive α was complete. It is an important feature of this transformation that the change can go to completion leaving no "retained austenite" if the cooling is continued through the necessary temperature range. Owen and Gilbert (111) and Yeo (114,115) have noted from the surface relief structure that the masses of α are made up of packets containing a large number of parallel or in some places interlacing shear plates. Consequently the transformation is martensitic and the product is designated "massive α'". The shear plates do not cross the austenite phase grain boundaries Fig. (53 d) and the volumes of α are smaller than the volume of a γ grain but otherwise the masses of α are not related to the parent grain.

Although there was little doubt that the masses of

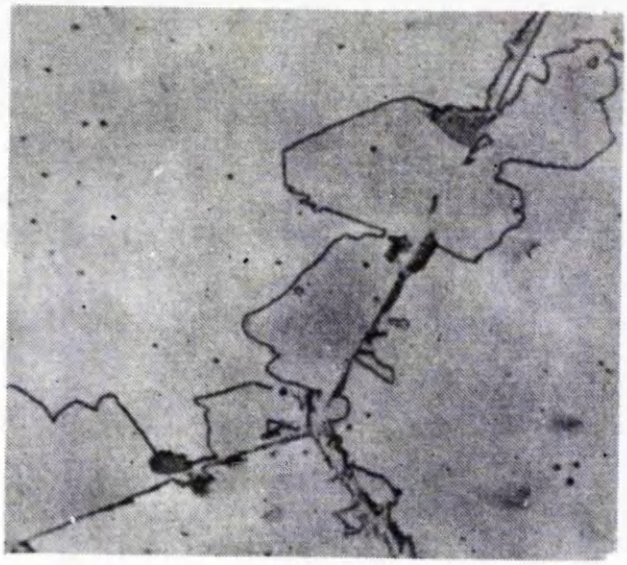

a

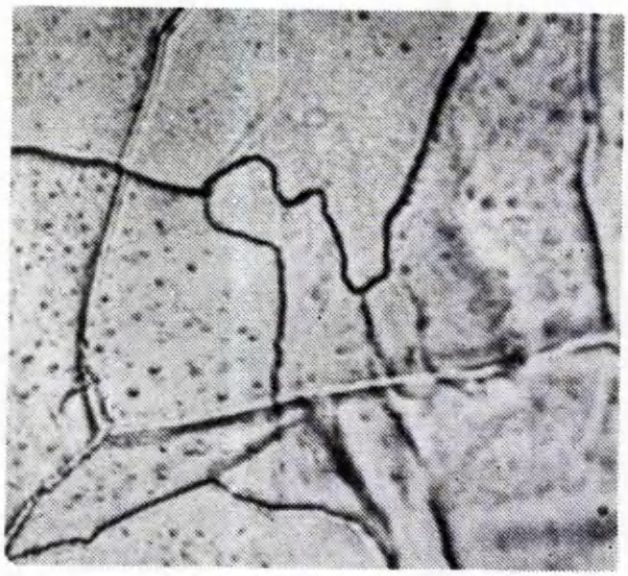

b

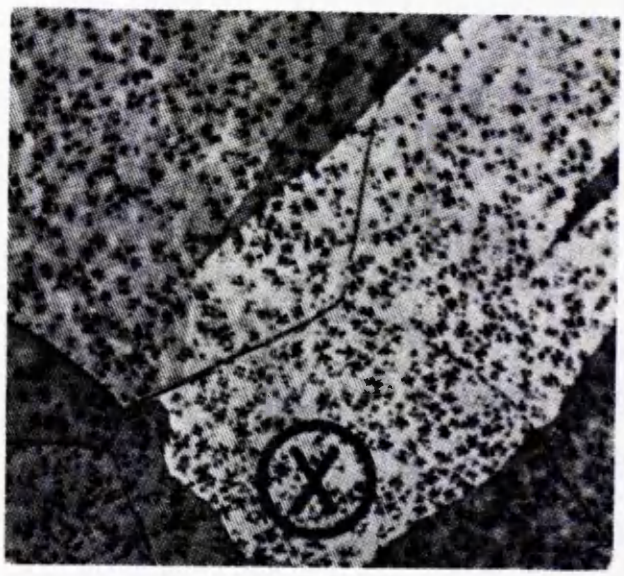

c

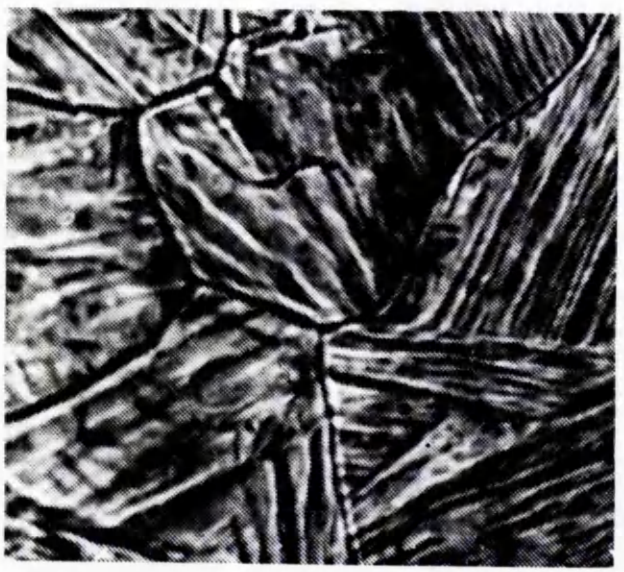

d

e

Fig 53

α are made up of shear plates, the individual plates could not be revealed by the conventional etching techniques. Owen (113) points out that the microstructural appearance of this type of martensite is strikingly different from the more familiar acicular forms of martensite which consist of single or connected lenticular martensite plates embedded in a matrix of retained parent phase. To distinguish between the two general forms of martensite Owen (113) has introduced the terms massive martensite and acicular martensite.

The short straight lengths of boundary observed in optical microstructures, suggesting the possibility of the existence of a martensitic transformation by the movement of a planar semi-coherent interface, was first studied by Hull and Garwood (112). They found that the planar facets enclosing massive α grains grown in the β phase of a Cu - 39% Zn alloy to be parallel to matrix planes of simple indices such as $(100)_\beta(100)_\beta$ or $(112)_\beta$ and sometimes also coincident with the martensitic habit planes $(155)_\beta$ to $(166)_\beta$. From these observations it was suggested that a "dislocation mode of growth" might operate during the growth of massive α.

Owen and Wilson (113) have suggested that it seems most likely that the planar boundaries develop because during the growth of the massive constituent, segments of the low energy, relatively immobile interface develop and become

progressively more extensive because they move more slowly than the adjacent high angle boundary.

In some alloy systems the massive microconstituent can be produced by either an SRD or martensitic transformation depending upon the composition of the parent phase, the annealing temperature,(and hence the grain size of the high temperature phase) and the cooling rate. Since the SRD transformation is isothermal on continuous cooling a specimen may transform partially by this mechanism and then at some low temperature complete the transformation martensitically.

II EMPIRICAL KINETICS

From experimental studies of the kinetics of a transformation at a number of different constant temperatures, a complete isothermal transformation diagram may be drawn. This time - temperature - transformation (T-T-T) diagram gives the relation between the temperature, T, (plotted linearly) and the time, t, (plotted logarithmically) for a fixed fraction transformed y. Normally only three curves of T against log t_y are plotted, $t_{0.05}$, $t_{0.5}$ and $t_{0.95}$. The values $t_{0.05}$ and $t_{0.95}$ are plotted in preference to t_0 and t_1 since the beginning and end of a transformation cannot be measured accurately.

When both nucleation and growth rates are temperature

dependent, the isothermal transformation rate will not be a simple function of the temperature. In many reactions the nucleation rate, which is determined by a Boltzmann type equation, decreases more than linearly with temperature (116). This gives a rapidly increasing nucleation rate as the undercooling increases. The growth rate, in contrast, is controlled by an activation energy which is nearly independent of temperature, and hence the rate decreases as the temperature decreases. These opposing factors result in the characteristic C-shape curves of the T-T-T diagram; the transformation rate first increasing and then decreasing as the temperature falls. At sufficiently low temperatures, the nucleation rate may be so large that the nucleation sites saturate early in the reaction. The overall reaction rate is then controlled only by the growth rate.

Isothermal reaction curves are usually interpreted in terms of an equation due to Avrami (117), which has been shown to be a good approximation in all modes of transformation (116).

$$y = 1 - \exp - (kt^n) \qquad - 2(i)$$

where, $3 \leq n \leq 4$

y = volume fraction transformed

t = time

k = reaction constant.

For most transformations, the value of n is independent of temperaure over appreciable temperature ranges and may be found by plotting log log $(\frac{1}{1-y})$ versus log t, the slope giving n. Since n depends only on the growth geometry it should only change when this geometry changes.

The rate of transformation is found by differentiating equation (2(i)),

$$\frac{dy}{dt} = nk\ (1-y)\ t^{n-1}$$

where (1-y) is the impingement factor and $nk\ t^{n-1}$ gives the rate law in the absence of impingement.

In the early stages of the transformation the reaction rate is often assumed to be controlled by two different activation energies, one for the formation of critical nuclei ΔG_c and the other for their subsequent growth E_A. As already pointed out, at sufficiently low temperatures $\Delta G_c << E_A$ and consequently the reaction rate is controlled by the growth rate alone.

To calculate a meaningful value of E_A it is necessary to make its determination independent of the empirical function f(y). Since y and t are functionally related it is possible to choose t instead of y as the dependent variable. The general rate equation.

$$\frac{dy}{dt} = k\ f(y)$$

may be rewritten

$$dt = k^{-1} f^{-1}(y)dy$$

The time t_Y, required for a specified fraction $y = Y$ to transform is,

$$t_Y = k^{-1} \int_{y=0}^{y=Y} f^{-1}(y)dy$$

The time t_Y to transform to the chosen value of y is measured at a series of temperatures with all other variables maintained constant. If the function f(y) does not vary in the temperature range studied, the integral has a constant numerical value.

Hence, $t_Y \propto k^{-1}$

But the temperature dependence of the reaction rate obeys an Arrhenius type equation,

$$k = A_A \exp\left(\frac{-E_A}{KT}\right)$$

where A_A may be identified with the frequency factor for the basic atomic events, K is the Boltzmann constant, and T is the absolute temperature.

Thus, $t_Y \propto A_A^{-1} \exp\left(\frac{E_A}{KT}\right)$

and $$\ln t_Y = \text{const.} - \ln A_A + \frac{E_A}{K}\left(\frac{1}{T}\right)$$

A graph of log t_Y versus 1/T is linear if E_A and A_A are independent of temperature, the slope being $\frac{E_A}{2.3K}$.

Chapter III

APPLICATION OF X-RAY DIFFRACTION TECHNIQUES TO THE STUDY OF METAL CRYSTALS

Diffraction of X-rays by the Crystal Lattice

The phenomenon of diffraction arises from the interaction of waves in a periodic structure. A crystal is built on a three dimensional pattern formed by an ordered repetition of a specific arrangement of atoms. The diffraction of X-rays may be observed and then interpreted in terms of the crystal structure.

The essential condition which must be met if diffraction is to occur was formulated by Bragg and is known as the Bragg Law. Since the rigorous derivation may be found in several publications (108,119) only the Bragg equation is given and its particular application to the derivation of lattice parameters.

$$\lambda = 2d_{hkl} \cdot \text{Sin } \theta \qquad - 3(i)$$

where λ is the wavelength of radiation used, d is the interplanar distance of the planes of atoms of indices hkl, and θhkl is the direction in which the diffracted maximum will occur.

The interplanar distance d for a particular structure

can be related to the parameters of the structure. The relation is dependent on the form of the crystal structure.

For a cubic system it is:

$$d = \frac{a}{\sqrt{(h^2+k^2+l^2)}}$$

Combining this with the Bragg equation,

$$\sin^2\theta = A(h^2+k^2+l^2) \qquad - 3(ii)$$

where $A = \frac{\lambda^2}{4a^2}$. Likewise, similar expressions are derived for the other symmetry groups.

For the tetragonal system,

$$\sin^2\theta_{hkl} = A(h^2+k^2) + C\,l^2 \qquad - 3(iii)$$

where $A = \frac{\lambda^2}{4a^2}$, $C = \frac{\lambda^2}{4c^2}$

The Powder Method for the Determination of Lattice Parameters

In this method a powder of small crystals of the specimen, produced by either filing or grinding, is packed into a thin walled beryllium glass capilliary tube and set at the axis of a cylindrical camera. The specimen is then rotated in a collimated beam of monochromatic X-rays.

The random orientations of the individual crystals in the powdered specimen are equivalent to the rotation of a single crystal about all possible axes during X-ray exposure.

For each set of planes a cone of diffracted X-rays is produced (see Fig. (54) and a series of lines corresponding to the diffraction from different sets of crystal planes is produced on the film surrounding the specimen. Each diffraction line is made up of a large number of spots, each from a separate crystal particle, the spots being so close they appear as a continuous line.

A Phillips camera, 11.46 cm. diameter, was used for the work described in this thesis. The method of film loading and measurement is shown in Fig. (54). The point X ($2\theta = 180°$), where the incident beam entered, is half way between the measured positions of lines 4, 4, and 3,3; similarly, the point Y ($2\theta = 0°$) where the transmitted beam left, is half way between lines 1,1, and 2,2. The difference between the positions of X and Y gives L, and θ is found by proportion:

$$\frac{4\theta}{\pi} = \frac{S_1}{L}$$

For the high angle lines,

$$\frac{2\phi}{\pi} = \frac{S}{L}$$

where $\phi = (180° - 2\theta)$ is the back reflection angle. Hence asymmetrical loading provides for the film shrinkage correction without calibration.

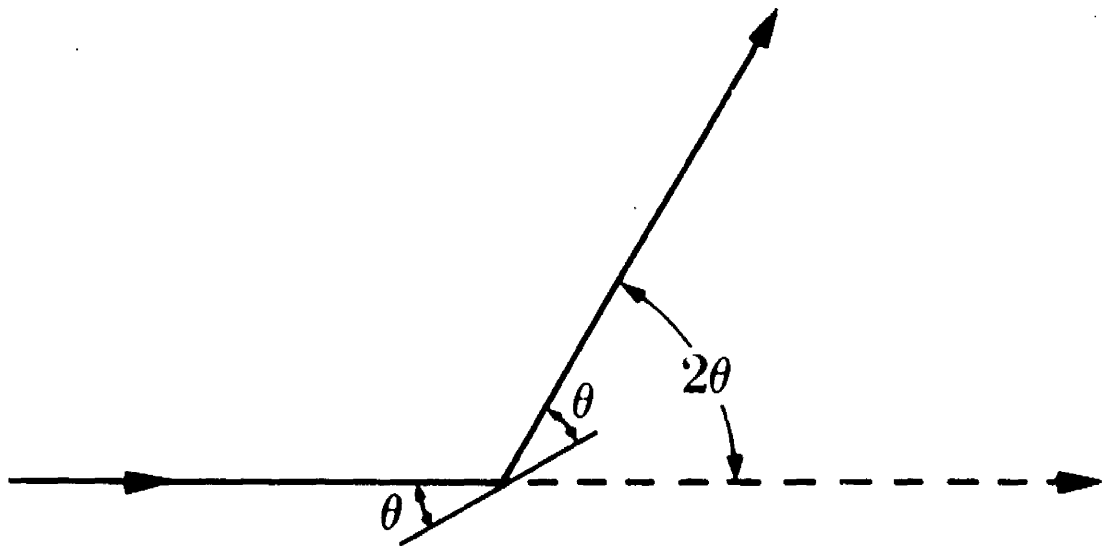

(a)

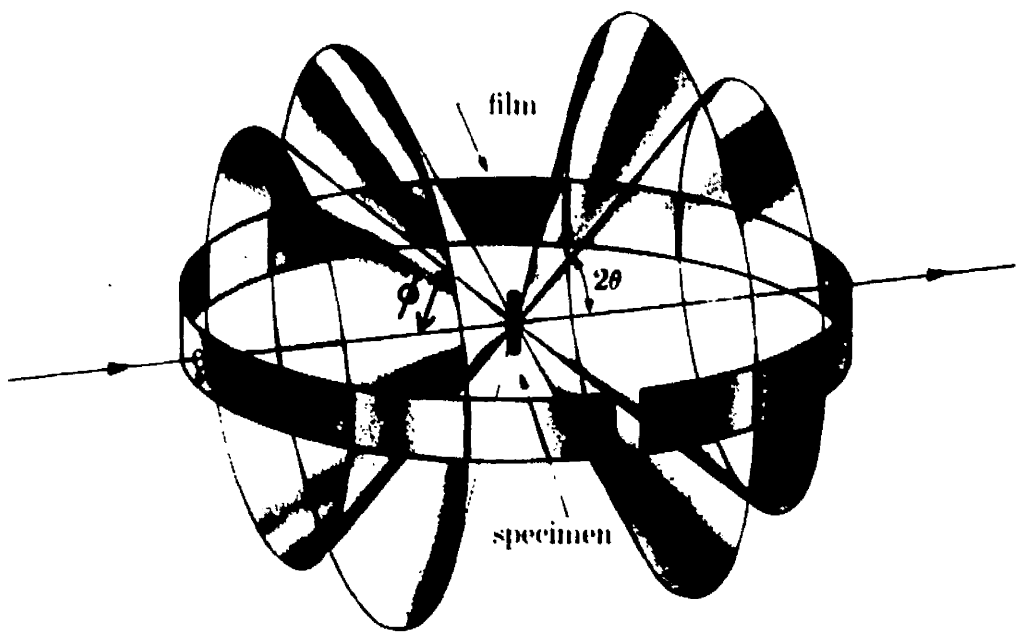

(b)

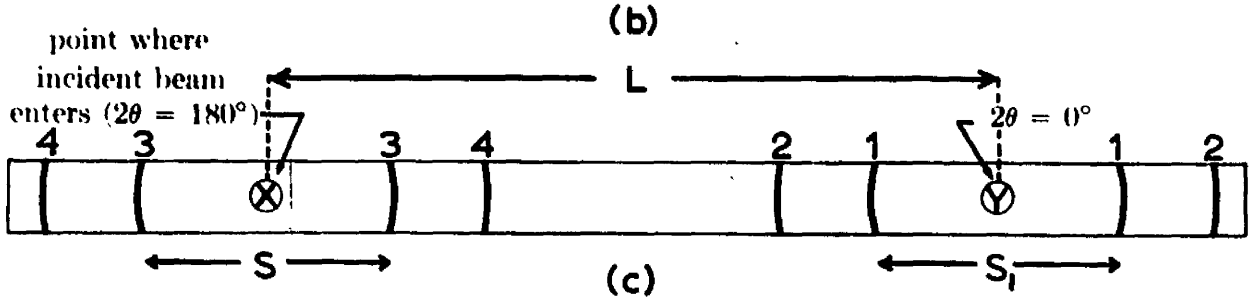

(c)

Debye-Scherrer powder method: a) diffraction of X-ray beam; b) relation of film to specimen and incident beam; c) appearance of film when laid out flat.

Fig. 54

Thus from the measured position of a diffraction line on the film, θ the Bragg angle can be determined, and knowing λ, the spacing d of the reflecting lattice planes, which produced the line, can be calculated. From equation 3(ii) it is seen that the lattice parameters for a cubic crystal system may be calculated for every line on the film provided that the Miller indices are known. The values calculated for each reflection are not found to be the same and this is attributed to two types of error, random and systematic. The random errors decrease as θ increases and tend to a minimum as $\theta \rightarrow 90°$. The systematic errors show a definite dependence on θ and also tend to a minimum as $\theta \rightarrow 90°$. The sources of error in the Debye-Scherrer photographs are film shrinkage, incorrect camera radius, specimen eccentricity absorption and beam divergence. Good technique can largely overcome or correct for the first two errors, but the main sources of systematic error can only be accounted for in practice by an extrapolation technique.

The simplest method is to plot values of lattice parameter against $\cos^2\theta$ and extrapolate the straight line graph obtained back to $\theta = 90°$ to obtain the correct value of the lattice constant. A more rigorous analysis carried out independently by Taylor and Sinclair (120) and Nelson and Riley (121) has shown that a plot of parameter versus

$$\frac{\cos^2\theta}{\sin^2\theta} + \frac{\cos^2\theta}{\theta}$$

holds quite accuratley down to very low values of θ and not just at high angles. Consequently it provides a satisfactory correction for the main sources of error.

Whilst the above procedure is straightforward in the case of cubic lattices the lattice constants of two and three parameter structures can only be calculated for every line by use of assumed axial ratios.

In the case of tetragonal structures, equation 3(iii) may be solved for 'a' if a sufficient number of reflections (hko) are available by using the Taylor-Sinclair extrapolation function. The parameter 'c' may also be calculated in a similar manner from (001) reflections. Usually there are insufficient reflections of this type to carry out the calculation in which case a method of successive approximations is used in equation 3(iii). A value is assumed for the axial ratio, 'a' and 'c' are calculated for all the high angle lines and extrapolation graphs prepared. The values of lattice parameter obtained in this manner are then used to evaluate a new axial ratio and the operation is repeated using this new axial ratio. The process is continued until the values of 'a' and 'c' give the same axial ratio as that assumed in order to calculate 'a' and 'c'

Although this method is widely used it is subject to considerable error and final values of 'a' and 'c' obtained are strongly dependent on the initial value which is assumed for the axial ratio. This can be a major problem in establishing the effect of a small addition of a third element on the axial ratio of a binary alloy.

A useful analytical extension of the graphical methods has been proposed by Cohen (122). In this method the solution of the normal least squares equation yields explicit expressions for the lattice constants. The form of the normal equations in this method also enables the standard deviations, and hence the standard errors of the lattice constant to be calculated (123). Furthermore Cohen (122) noted that, using his method of calculation, the Debye camera becomes an absolute instrument, even with respect to film shrinkage, if the angles that are measured on the photographs are the anlges $\phi(180-2\theta^{\circ})$ between the incident and reflected beams.

To treat the systematic errors, Cohen proposed modifying the Bragg relationship to,

$$\lambda/2d = \sin(\theta+\Delta\theta) = \cos 1/2\ (\phi+\Delta\phi)$$

where ϕ is the diffraction angle measured experimentally and $\Delta\phi$ is the small angle, due to the net effect of all the

systematic errors which must be added to ϕ to make their sum $\phi+\Delta\phi$ fulfill the Bragg relation. Then by squaring, expanding the right hand term by Taylor's theorem, and neglecting all powers of the small angle $\Delta\phi$ excepting the first, Cohen obtained,

$$\frac{\lambda^2}{4d^2} = \cos^2 \tfrac{1}{2}\phi - \tfrac{1}{2}\Delta\phi.\sin\phi \qquad - 3(iv)$$

$$\therefore \quad \frac{\lambda^2}{4d^2} + \tfrac{1}{2}\Delta\phi\sin\phi = \cos^2 \tfrac{1}{2}\phi = \sin^2\theta \qquad - 3(v)$$

as the general modified form of the Bragg relationship applicable to experimentally measured diffraction angles.

Next Cohen expressed $\Delta\phi$ in the analytical form appropriate to the camera used. For the back-reflection Debye-Scherrer camera $\Delta\phi = K_1\phi$, where K_2 is the Drift Constant.

From equation 3(iii) the specific observation equation becomes

$$\sin^2\theta = A\,\alpha + B\beta + D\delta \qquad - 3(vi)$$

where $\alpha = (h^2+k^2)$, $\beta = l^2$, and $D\delta$ is the correction for the systematic errors; D is the drift constant and δ is the extrapolation function which can either be those already discussed or the $\phi\sin\phi$ function suggested by Cohen.

If there were no random errors in the measurement of each line U_i would equate to zero in equation 3(viii),

$$A\alpha_i + B\beta_i + D\delta_i - \sin^2\theta_i = U_i \qquad - 3(viii)$$

where the subscript i indicates that there is an equation for each line. The least squares principle states that the best values of A, B and D are obtained when the residual in $\sin^2\theta$, $\sum_i U_i^2$, is a minimum. It can be shown that this condition is satisfied by the solution of the normal equations,

$$A\sum\alpha_i^2 + B\sum\alpha_i\beta_i + D\sum\alpha_i\delta_i = \sum\alpha_i\sin^2\theta$$

$$A\sum\alpha_i\beta_i + B\sum\beta_i^2 + D\sum\delta_i\beta_i = \sum\beta_i\sin^2\theta$$

$$A\sum\alpha_i\delta_i + B\sum\beta_i\delta_i + D\sum\delta_i^2 = \sum\delta_i\sin^2\theta$$

Thus by combining all the data for lines above 60°, accurate values of the lattice parameters may be determined without making any initial assumption as to the axial ratio. Cohen's method is completely satisfactory to correct for all systematic errors provided that the angles measured experimentally are ϕ's not θ's.

Modifications of the Cohen procedure have been suggested by Hess (124) and Lawn (125). These workers stress the need for the inclusion of a weighting function in the Cohen least squares equations.

Hess pointed out that Cohen's method violates the least squares principle of minimising the sum of the weighted squares of the residuals of the quantities actually measured. Thus the sum of the squares of the residuals of the line diameters must be minimised.

The Hess modified form of the normal equation 3(iii) for tetragonal structures, may be written in terms of the ring diameters s_i and the camera diameter D.

$$\frac{\lambda^2}{4}\left(\frac{h^2+k^2}{a_0^2} + \frac{l^2}{c_0^2}\right) + K_0 \frac{s}{2D} \cdot \sin \frac{s}{D} = \cos^2 \frac{s}{2D} \qquad - 3(viii)$$

where $\frac{s}{D} = \phi$ and $K_0 = 1/2\ K$. This equation may then be brought to the form

$$F = A_0\alpha + B_0\beta + K_0\delta - \gamma \qquad - 3(ix)$$

by the following substitutions

$$A_0 = 1/a_0^2 \quad , \quad B_0 = 1/c_0^2$$

$$\alpha = \tfrac{1}{2}\lambda^2(h^2+k^2) \; ; \quad \beta = \tfrac{1}{2}\lambda^2 n^2 l^2 \; ; \quad \delta = {}^{s}/_{D} \cdot \sin {}^{s}/_{D}$$

$$\gamma = 1 + \cos \frac{s}{D} = 2\cos^2 \frac{s}{2D}.$$

The equation 3(ix) is non-linear in terms of the ring diameter and the more common techniques of least squares computation are not adequate for the derivation of the

appropriate normal equations. Deming (126), however, has generalised the Gauss solution of the non-linear least squares problem to include the case where parameters are present.

Basically, Deming's method consists of linearising the observation equations by rewriting them as Taylor series in terms of parameter residuals, employing approximate values of the unknown parameters, and then neglecting all powers of these residuals higher than the first. All derivatives in the expansion are likewise evaluated with the approximate parameters. Therefore in choosing the approximations to be used for the parameters care must be exercised that the approximations are reasonably good, or else higher orders of the parameter residuals may not be truly negligible. The effect of this analysis in the case of a back-reflection Debye camera is to attach an inherent weight of $\mathrm{cosec}^2\phi$ to each measurement.

In addition to the modification of the Cohen procedure described by Hess a further source of variation occurs in lattice constant data in systems other than cubic, and this arises from the choice of planes whose reflections are to be used in the calculations. This was first pointed out by Jette and Foote (123), and a weighting procedure to make allowance for this source of error has been suggested by

Lawn (125).

Thus the normal equations may be weighted with

$$w_i = \underset{\text{Hess}}{w(\theta)} \cdot \underset{\text{Lawn}}{w_a(hkl)}$$

for each line measured, and the normal equations in the parameter rsiduals, ΔA, ΔB, ΔK are

$$\Delta A\sum\alpha^2 w_i + \Delta B\sum\alpha\beta w_i + \Delta K\sum\alpha\delta w_i = \sum\alpha F_0 w_i$$

$$\Delta A\sum\alpha\beta w_i + \Delta B\sum\beta^2 w_i + \Delta K\sum\beta\delta w_i = \sum\beta F_0 w_i$$

$$\Delta A\sum\alpha\delta w_i + \Delta B\sum\beta\delta w_i + \Delta K\sum\delta^2 w_i = \sum\delta F_0 w_i$$

The analytical methods of calculation can therefore be fundamentally more rigorous than graphical methods, but the graphical methods have the advantage that they can supply an overall representation of the accuracy of the results and allow those measurements of individual reflections which appear inconsistent with the majority of the data to be weighted accordingly when preparing the graphs. However a similar procedure can be incorporated in the analytical calculations by rejecting those data for which $\sin^2\theta$ residuals are greater than an amount which is estimated from the accuracy of the experimental measurements.

Indexing of Powder Photographs

The indexing of powder patterns of cubic structure does

not normally present any problems, but the indexing of two and three parameter patterns is more difficult. The various graphical charts can be very helpful in indexing hexagonal and tetragonal patterns. However, using graphical methods it is not always possible to index all the high angle lines uniquely and fit must be refined by numerical calculation of the lattice parameters.

In cases where both the crystal class and the approximate values of the lattice parameters are known, the problem is relatively straightforward and amounts to selecting values of h, k and l for each reflection, which when substituted in the appropriate Bragg equation yield values of $\sin^2\theta_{calculated}$ which agree with values of $\sin^2\theta_{observed}$, obtained from film measurements. A tolerance of 0.002 between observed and calculated values of $\sin^2\theta$ is usually adopted to allow for both systematic and random errors in measurement of observed $\sin^2\theta$ values.

The Computer Programme

A computer programme has been written by Hoff and Kitchingman (127) to calculate accurate lattice parameters using the different methods already described.

The data supplied to the computer consist of the approximate lattice parameters and the measured line

diameter of all the diffraction lines on the powder photograph, together with the camera constants, the wavelength of the radiation and the code numbers. From these data, the indexing routine carries out a straightforward comparison procedure between the observed $\sin^2\theta$ values and those calculated from the approximate lattice constants using integer values of hkl. After the first indexing of the pattern the assumed lattice parameters are automatically refined by an application of Cohen's least squares method to the low angle data. The whole pattern is then re-indexed using these refined constants. The programme then carries out a Cohen least squares analysis on the high angle ($\theta > 45°$) data to further refine the lattice constants and the whole pattern is re-indexed a second time. After each indexing of the diffraction pattern the indices, Bragg angle, and input measurement of each diffraction line are printed out together with the difference between observed and calculated values of $\sin^2\theta$ for each indexed line. After the pattern has been finally indexed the lattice parameters are calculated from a least squares analysis of the high angle data, and the programme then proceeds to the calculation of the lattice parameters using the weighting functions of Hess and Lawn.

The Cohen least squares routine in this programme

incorporates the Taylor-Sinclair or Warren (128) extrapolation function to correct for systematic error. This routine also includes a set of conditions which test the overall agreement between the measurements on all lines and which progressively reject inaccurate or erroneous data as the acceptable tolerance between the observed and calculated values of $\sin^2\theta$ is reduced from 0.045 in $\sin^2\theta$ in steps of 0.0005 to 0.0005. The calculated lattice parameters and their associated standard errors are printed out after each application of the least squares routine.

When the indices of the diffraction lines are known these may be supplied with the input data and in this case the lattice parameters are first calculated from the high angle ($\theta<45°$) data using the Cohen least squares procedure described above. This and subsequent sections of the programme are followed both when the indices are calculated by the computer and when the indices are supplied with the input data.

In the next stage of the calculation the parameters obtained by the Cohen method are used as approximate parameters in the calculation of the parameter residuals using the weighting function suggested by Hess (124). The Deming (126) method is used for the solution of the non-

linear least squares problem in the manner already described. The lattice parameters derived by this procedure and their associated standard errors are printed out.

The final use of the least squares method in the computer programme again involves the use of the Hess method of calculation but with the additional weighting function suggested by Lawn (8). The lattice parameters and their associated standard errors are printed out.

The last stage of the programme calculates and prints out the coordinates of the lattice parameter versus Taylor-Sinclair function extrapolation graphs, so that if required, a graphical representation of the overall accuracy of the results is available, and moreover, the parameter values derived by the application of the three least squares methods may be compared with those derived using a standard graphical procedure. To determine the coordinates of these extrapolation graphs the values of 'a' and 'c' in the tetragonal system derived from the final application of the least squares method yield the assumed axial ratios.

Chapter IV

EXPERIMENTAL DEVELOPMENT AND PROCEDURE

Introduction

The kinetics of a phase change are studied experimentally by observing the change of some property that is a function of concentration of one of the phases. The most common techniques employed are electrical, magnetic and volume measurements. The phase transformation investigated in this study lends itself to any of these three techniques; the volume change is 0.6%; the alpha phase is ferromagnetic and the sigma phase is non-magnetic; the electrical resistance of the two phases differs considerably.

In the present study it was decided to use electrical resistance measurements to investigate the kinetics of σ-phase formation, and use metallographic, hardness and X-ray techniques to identify the transformation products and measure the lattice parameters.

Preparation of Specimens

The following series of alloys were prepared by melting in an arc furnace under an argon protective atmosphere Fig. (55).

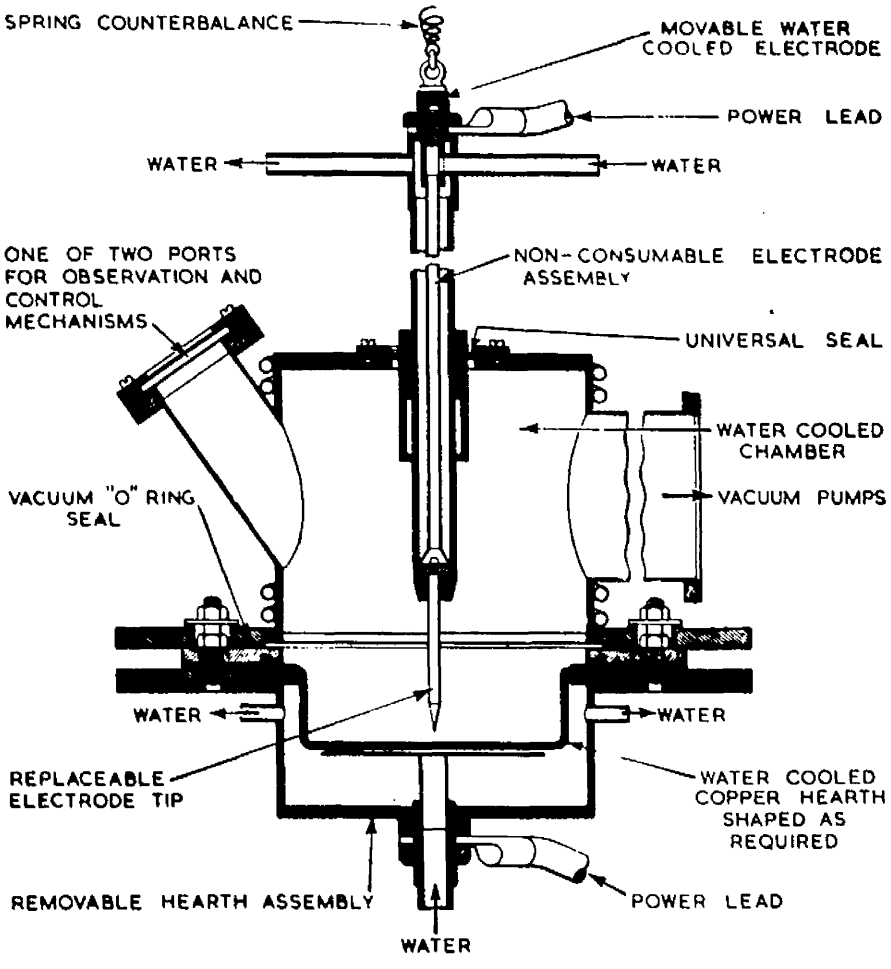

ARGON-ARC FURNACE.

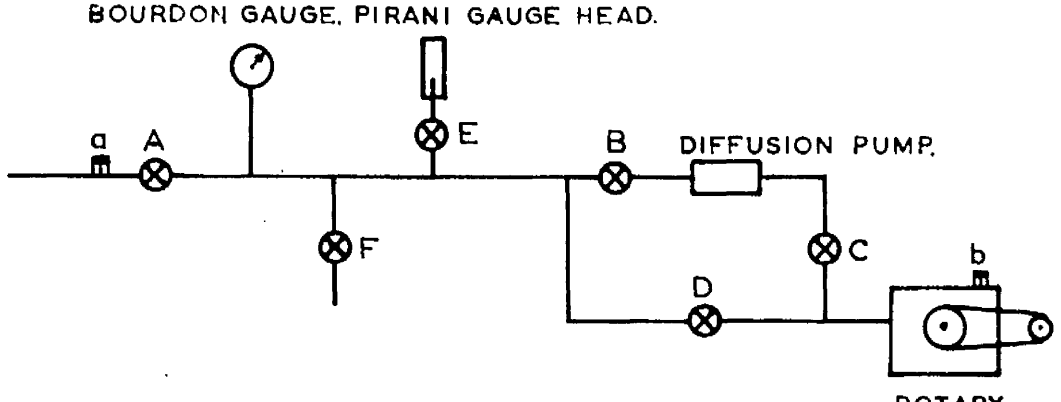

a, b – AIR ADMITTANCE VALVES.

A, FURNACE ISOLATION VALVE, B, BAFFLE VALVE, C, BACKING VALVE, D, ROUGHING VALVE, E, GAUGE VALVE, F, ARGON INLET VALVE.

ARC FURNACE VACUUM LINE.

Fig. 55

Alloy	Atomic % Fe	V	X
FeCr	50	50	
FeV	50	50	
FeVAl	-	-	-
FeVMn	48.33	48.33	3.33
FeVRe	48.33	48.33	3.33
FeVSi	-	-	-
FeVTa	48.33	48.33	3.33
FeVW	48.33	48.33	3.33
FeVZr	48.33	48.33	3.33

Materials supplied:

Iron lumps 99.95% Koch-Light Laboratories Ltd.

Element	P.P.M.
Cu	2
Mg	<10
Mn	40
Ni	<10
P	4
Si	42
S	67
C	48

Vanadium granules Johnson, Matthey & Co. Ltd.

Element	P.P.M.		
Si	400		
Fe	200	Oxygen	0.09%
Mo	50	Nitrogen	0.05%
Al	40	Carbon	0.05%
Mn	20	Hydrogen	0.01%
Cr	10		
Ni	8		
Mg	1		
Cu	1		

Chromium lumps 99.999% Koch Light Laboratories Ltd.

Manganese flakes " " " " "

Zirconium rod (iodide Zr) AEI Ltd.

Aluminium ingot Johnson Matthey & Co. Ltd. (spectrographically pure)

Rhenium powder " "

Tantalum rod " "

Tungsten rod " "

In the argon arc melting process a low voltage high current electric arc is struck from a non-consumable tungsten electrode onto the metal to be melted. The

melt is contained in a water cooled copper hearth and the furnace is encased in a vacuum tight chamber.

The furnace is first evacuated to 5×10^{-4}mm. Hg. and then filled with argon (99.995%) to 12 cm. Hg.. A maximum of 20 gms. of metal could be melted satisfactorily with adequate fluidity for a homogeneous button. To further purify the argon atmosphere a 20 gms. zirconium "getter" button was melted before each sample.

Preparation of the iron-vanadium alloys was carried out by a straight forward process of melting the constituent metals into a button, and after each melt inverting and remelting for a period of three minutes using a current of 300 amps. In all, six such treatments of the buttom were carried out, the arc being circulated continually to facilitate mixing.

To produce an ingot which would require the minimum machining a further process was necessary. The buttons were remelted in a trough $3"\times\frac{1}{4}"\times\frac{3}{8}"$, again with inversion after each run of three minutes, until a sound ingot was obtained.

Preparation of the ternary alloys required special treatment. The ternary additions were graded into two types, (i) melting points above FeV (50/50 At% - 1500°C) and (ii) melting points below 1500°C.

Elements of the first type were melted with small pieces of vanadium to form a master alloy which was then diluted to the appropriate concentration by adding small pieces of iron between melts. The rest of the process was as described for the binary alloys.

Additions of the second type were added to small pieces of the already prepared binary alloy and a sound ingot produced by the method already described for the binary alloys.

In the case of the FeVRe alloy the rhenium powder was first compressed to a small billet prior to melting since the force of the arc tended to disperse the powder.

The FeV$A\ell$ and FeVSi alloys were difficult to prepare and despite adding excess aluminium and silicon to counteract losses during melting the chemical analysis showed less than 0.1% for each alloy. Consequently neither was used in the present study. It is probable that powder techniques could be used successfully in these cases.

Chemical analysis of the ternary FeVX_y alloys was complex since the vanadium tended to mask the analysis of the X addition, and normal procedures could not be adopted. Although three analytical laboratories were

tried none was prepared to analyse the titanium and rhenium alloys. However, as the analysis of the other alloys agreed with the prepared compositions it was assumed that these alloys also had the same values.

The ingots produced in the arc furnace were homogenised in the annealing furnace for 24 hrs. at 1350°C and 10^{-5}mm. Hg.

Annealing Furnace

A furnace capable of annealing specimens at high temperatures (1500°C) and high vacuums (10^{-5}mm.Hg.) with a quenching arrangement was designed and built Fig. (56).

An alumina tube 4.6 cms. diameter and 110 cms. long was fitted with specifically designed brass couplings at each end Fig. (57). At the top end of the tube a ground glass flange was fitted. A brass plate with a groove for a nitrile 'O' ring made the vacuum seal with the glass flange. Two Wesley-Coe lead-throughs set in the plate enabled a fuse wire to be put in circuit with a switch and 12-volt lead-acid battery. A fan was placed just above the furnace to keep the brass coupling cool.

At the lower end of the alumina tube a flanged copper tube was fitted with access to a Penning gauge and a Genevac rotary and oil diffusion pump. The copper flange had

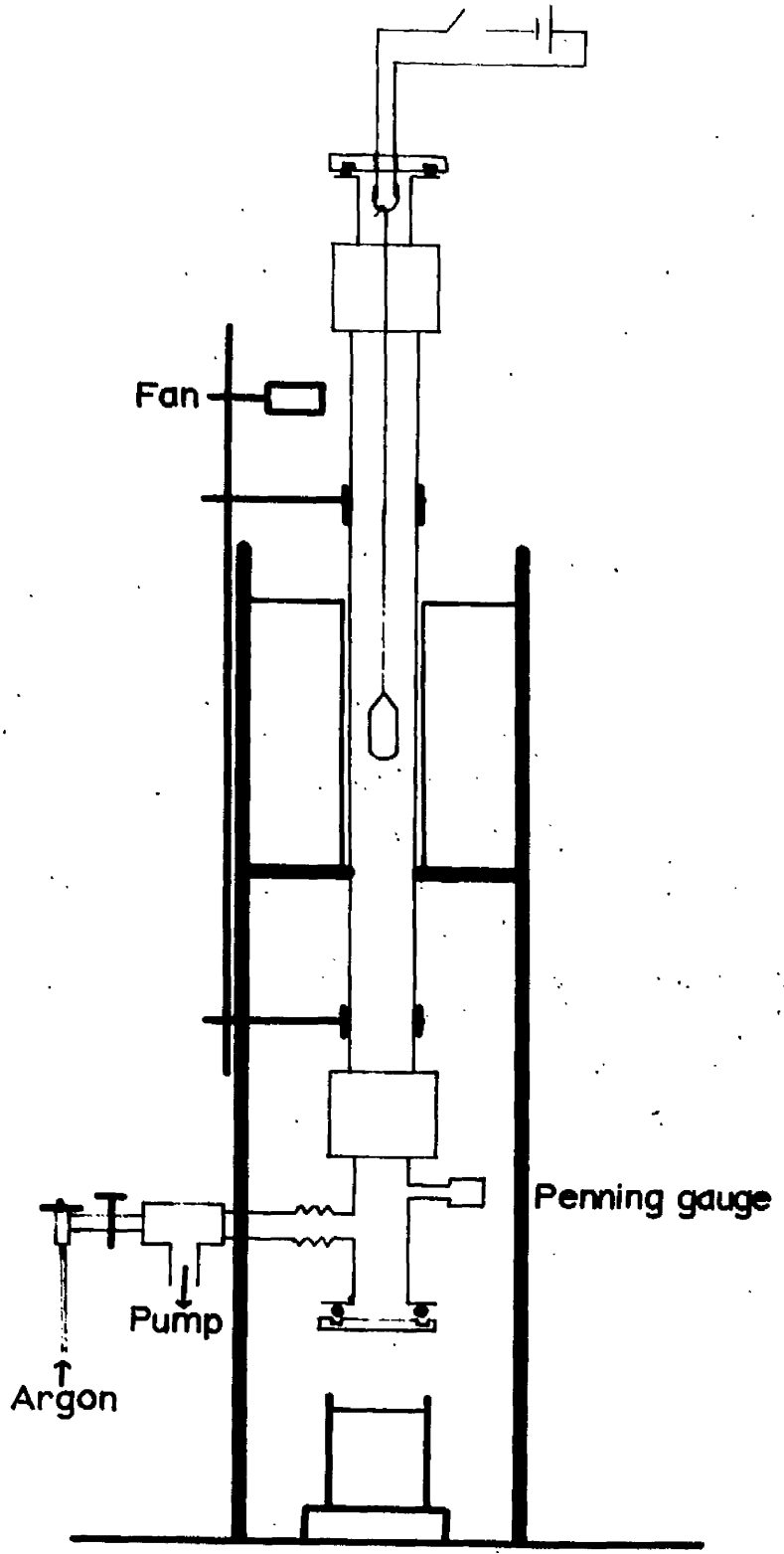

ANNEALING FURNACE

Fig 56

a recess for an 'O' ring, against which a flat brass plate fitted to make the vacuum seal. The furnace was controlled to $\pm$ 5°C by an Ether controller.

The specimen was suspended on the fuse wire and the whole system evacuated to 5×10^{-5} mm. Hg.. After raising the furnace temperature and annealing for the requisite time at the high temperature, argon (99.995%) was bled into the system through a preset leak valve and hand valve, when the system was filled with argon to atmospheric pressure the bottom plate fell away; the suspension wire was fused and the specimen dropped into the quenching medium. The time interval from the introduction of the argon to the specimen reaching the quenching medium was approximately 40 secs.

Specimen Fabrication

After the ingots had been homogenised at 1350°C for 24 hrs. and quenched into a mixture of ice and water, they were machined to 4 mm. diameter and 4 cm. length. The turnings were used for chemical analysis and lattice parameter measurements.

Normally specimens in the form of a wire are used for resistance methods, but in the case of iron-vanadium alloys cold swaging was unsuccessful probably because of the embrittlement by nitrogen. Precipitation of brittle σ-phase

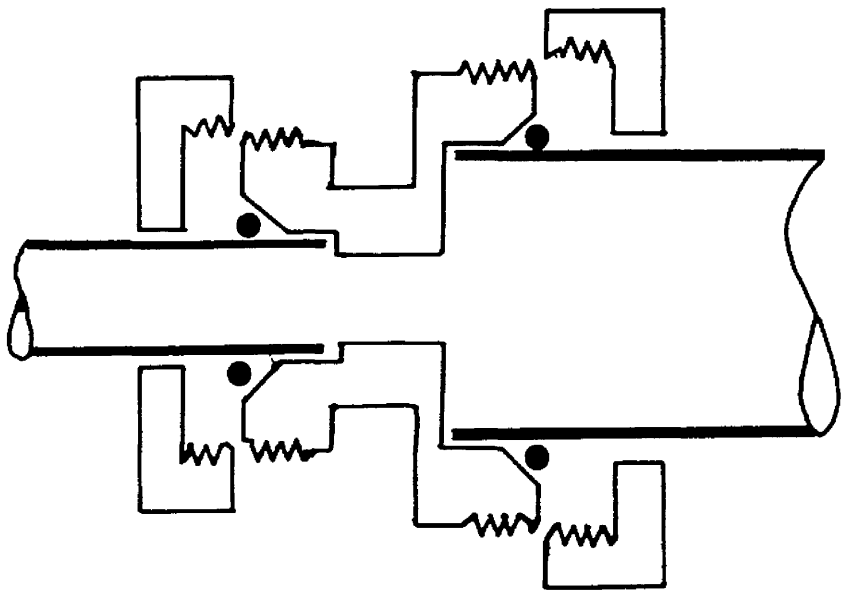

VACUUM COUPLING

Fig. 57

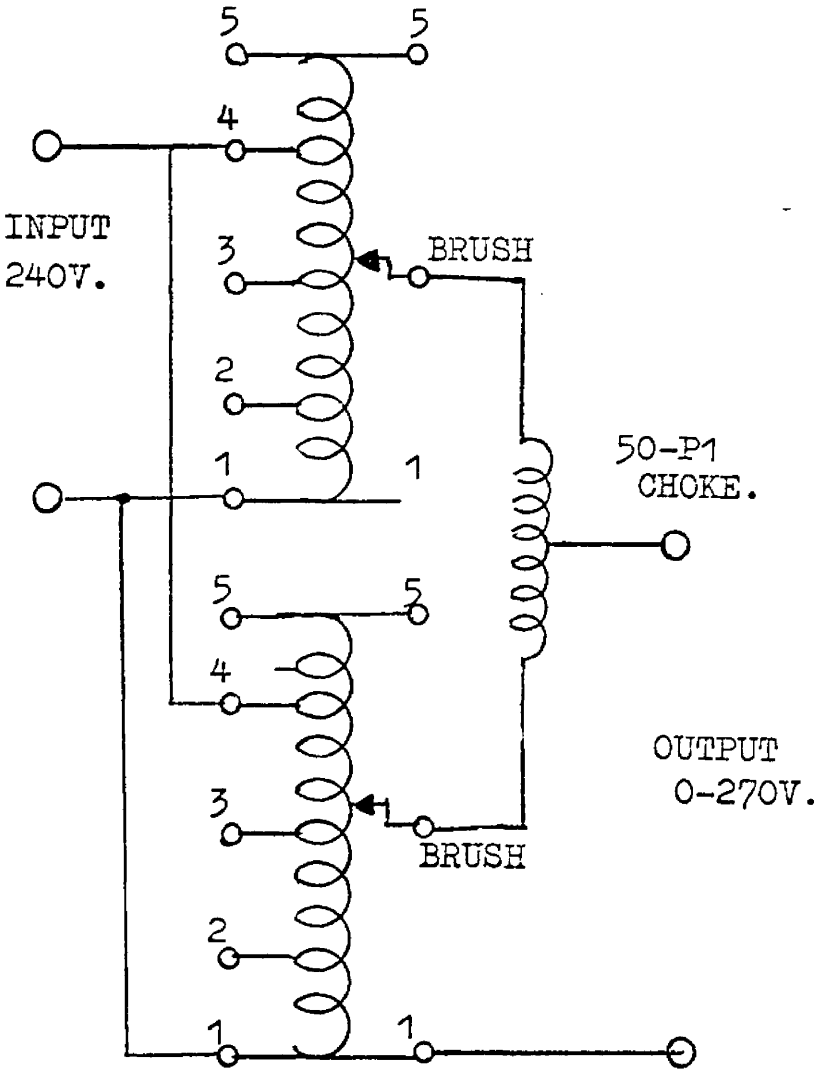

Fig. 58

prevented hot swaging. Spark machining appears to be the only technique to obtain wire but no facilities were available. On the other hand no difficulties were encountered when cold swaging the iron-chromium alloys.

The Potential Fall Method

In this method a constant current is passed through the specimen mounted in series with a standard resistance. The potential drop across the specimen is recorded continuously and the stability of the current is checked by reference to the potential across the standard resistance.

The specimen assembly is shown as Fig. (59). The platinum wires used for the current (DC, 0.75 mms. diameter) and potential leads (P, 0.5 mms. diameter) were spot welded to each end of the specimen. The temperature was measured by a Pt./Pt. 13% Rh. thermocouple (Tc) spot welded to the specimen. These six leads were sheathed in alumina tubes and taken out of the furnace through a brass plate via Wesley-Coe lead-throughs. The plate had a recess for a nitrile 'O' ring, and fitted against a ground glass flange to make a vacuum tight seal. The flange was connected to the alumina tube, 65 mm. diameter and 160 cms. long, by an aluminium coupling of the type shown in Fig. (57). At the other end of the alumina tube a similar aluminium coupling joined the system to a rotary and oil diffusion

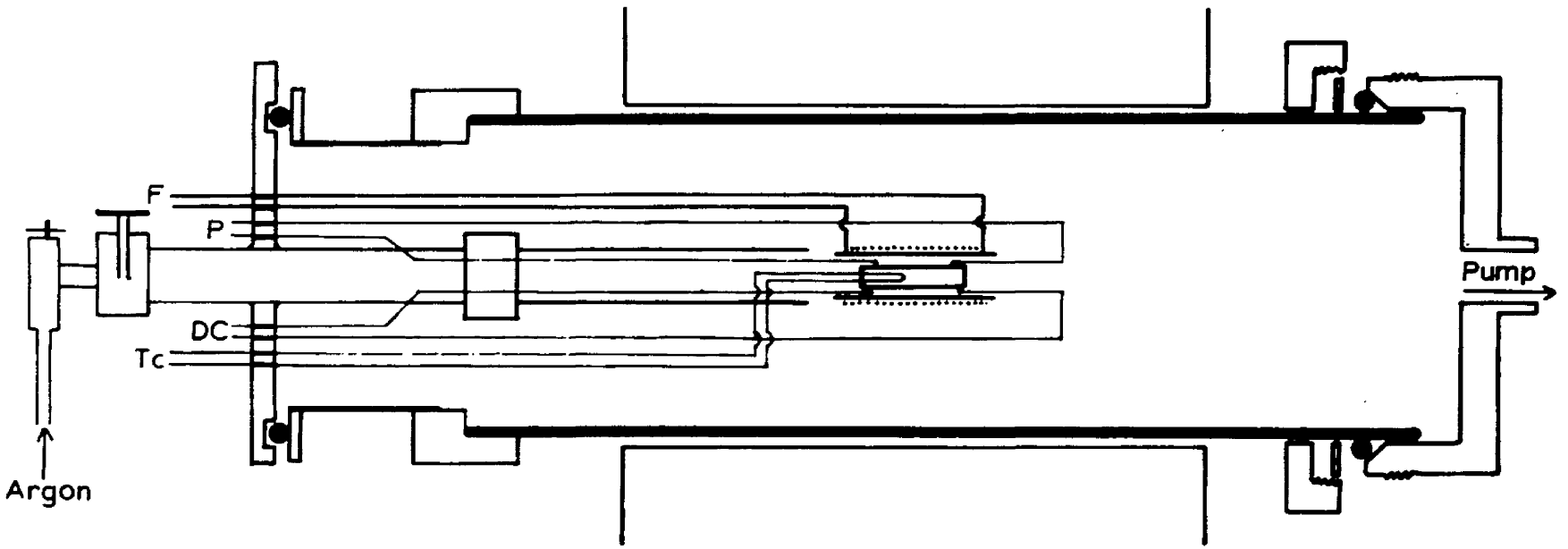

SPECIMEN ASSEMBLY

Fig. 59

pump which enabled the system to be evacuated to 10^{-4} mm. Hg. measured by a Penning gauge.

The lower part of the isothermal curves was established by placing the specimen assembly into the furnace which was preset at the required reaction temperature. Early experiments showed that a down-quench method was necessary to establish the upper part of the curve and a method of annealing and quenching to the reaction temperature 'in situ' was devised.

The technique usually adopted for investigating fast reactions is to have the specimen in wire form heated directly by an AC current so that the specimen will reach the ambient furnace temperature within a few seconds of quenching (93). In this case it was not possible to manufacture a wire specimen for reasons already discussed. Consequently a small heating coil was made of Pt, 13% Rh, wire (0.35 mm. diameter) wound on a small alumina tube (0.25" diameter). This device enabled specimens to be annealed up to 1350°C within the furnace. The quenching was achieved by switching off the heating coil and then passing argon (99.995%) through a preset leak valve and tap, whilst still pumping. The argon passed through the copper and mullite tubes directly onto the specimen and heating coil. The details of this assembly are shown in Fig. (59). This

system was sufficient to retain the alpha phase and to achieve the ambient furnace temperature within four minutes.

The potential drop across the specimen was recorded continuously as a function of time, on a Kipp and Zonen potentiometric recorder. The instrument was capable of operating with full scale deflections of 0.05, 0.1, 0.25, 1.0 and 2.5 mv. in any preselected range. This was achieved by opposing the potential fall across the specimen by a known potential generated within a standardised potentiometer circuit. Under such conditions any range of potential could be selected, the excess being recorded as an out of balance potential. The ink trace thus gave the potential in the first case from the moment the specimen was placed in the furnace, and in the second case from the moment of quench to the final equilibrium state.

The salient problem in resistance techniques is the elimination of stray emfs, in particular from the specimen-lead junctions. Consequently in the lower temperature range specimens were set at right-angles to the main alumina tube to ensure that there was no temperature gradient across the specimen. Furthermore before each series of runs a dummy run was recorded to check for such effects. Experimental conditions were simulated exactly, though no current was allowed to flow in the potential circuit. Any potential generated would then have been due to the thermoelectric

power of the junctions alone.

The currents used, ranging from 1.5 - 2.0 amps., were initially generated by four 12-volt lead-acid batteries in parallel, but at later stages of experimentation were superseded by a transistorised circuit described in the next section.

The standard resistance was maintained at a uniform temperature in an oil bath. No change in temperature could be detected by the passage of two amps.. Thus within experimental error the resistance remained constant. However absolute values of resistance were not required, so checks on the current were to ensure that potential changes across the specimen were due to the phase change alone. Consequently it was unnecessary to determine the resistance of the standard resistance or the dimensions of the specimen.

Constant Current Source

The constant current generated by the four 12v. lead-acid batteries (48 amps./hr.) was stable for approximately six hours after each charging. This time was increased to twelve hours by putting a 12v lead-acid battery in series with two 6v. Nife cells (75 amp./hr.) in parallel. A further improvement was obtained by incorporating a circuit due to Booth (129) Fig. (60a). More recently Booth (129) has

designed a constant current source to operate from the mains supply with an output of 2 amps. at 0.30 volts (Fig. 60b).

In each of Booth's circuits the standard technique of comparing the voltage across a small series resistor with that across a silicon voltage-reference diode is employed; the potential difference being used to effect control. In the battery operated version, both comparison and control are performed by the compounded transistors. The transistor power dissipation is restricted by a series-connected rheostat. The mains operated device requires increased stabilisation and this is obtained from the voltage-reference diode which is powered from a subsidiary current regulating network. The use of the compound-complementary connection for the comparison and control transistors enables much of the power in these components to be transferred to a shunt resistor, without serious impairment of the overall stabilisation.

By changing the resistance R to the appropriate value, currents between 0 and 2 amps. may be obtained. At 2 amps. the potential across the standard resistance showed a variation of less than 1%.

A significant feature of the mains operated circuit is that transformations of any length of time may be investigated continuously.

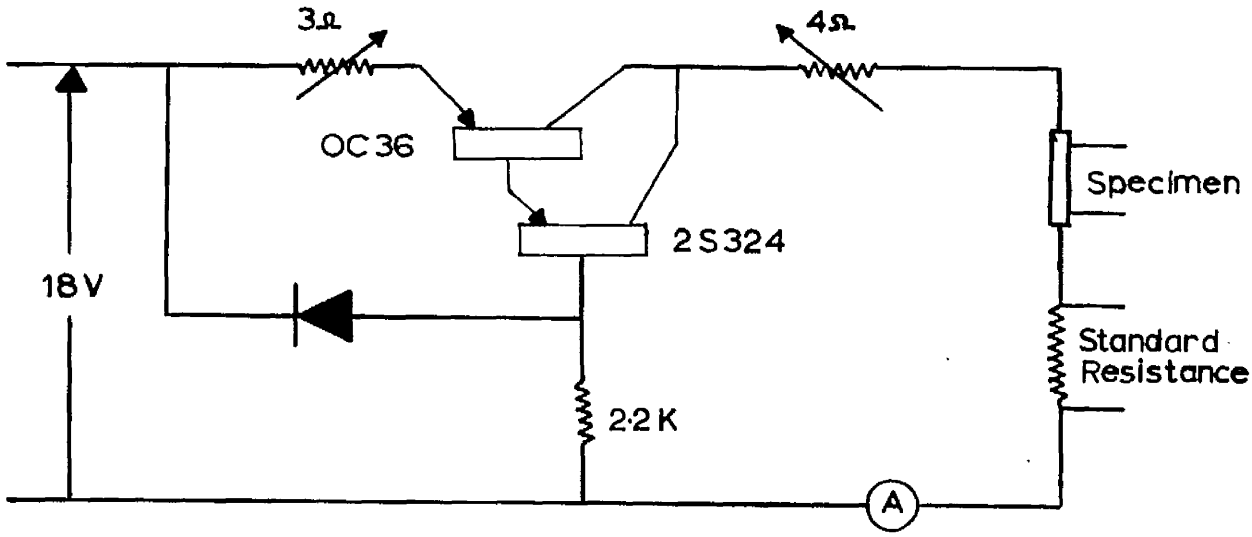
3Ω
4Ω
OC36
2S324
Specimen
18V
Standard Resistance
2·2K
A

(a)

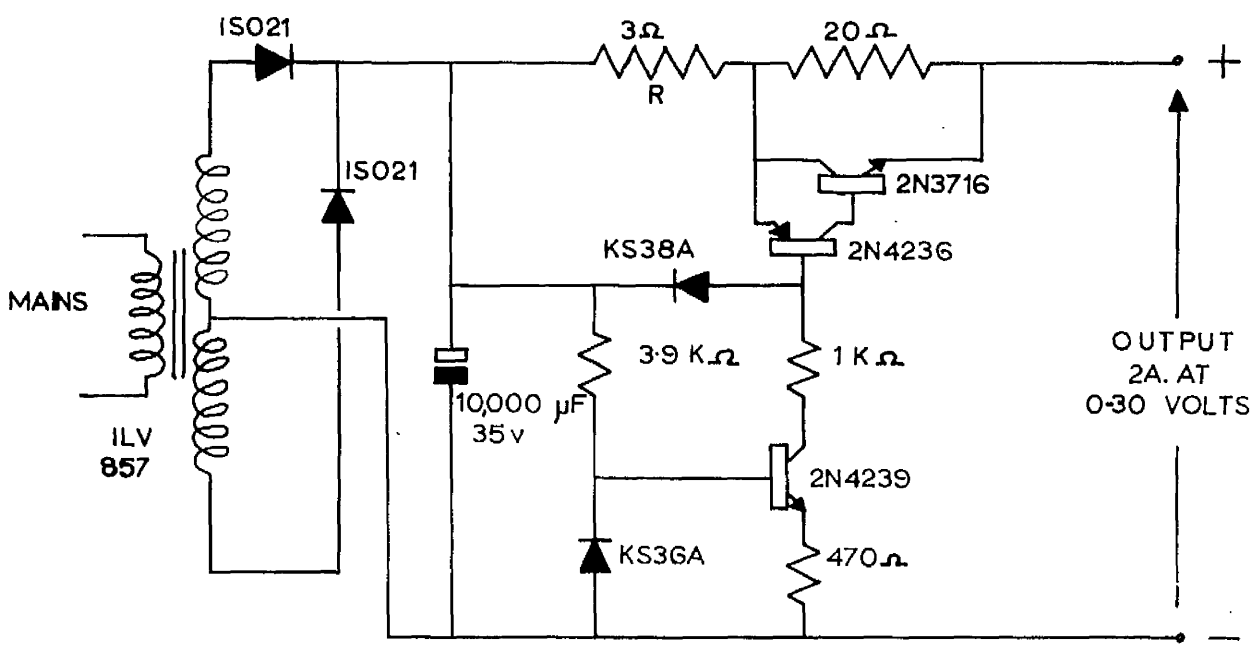
IS021
3Ω
R
20Ω
+
IS021
2N3716
2N4236
KS38A
MAINS
3·9 KΩ
1 KΩ
OUTPUT
2A. AT
0-30 VOLTS
10,000 μF
35 v
ILV
857
2N4239
KS3GA
470Ω
—

(b)

Fig. 60

Furnace Circuits

The circuits of the furnace and control systems are shown in Figs. (61,62). The effects of stray emfs have already been discussed. To reduce these emfs a furnace was built with three separate windings (0.35" diameter Pt. 13% Rh.) each independently supplied from three variable transformers A, B and C Fig. (61) to give a uniform temperature zone of 6".

The central winding was incorporated in a standard temperature control system due to Cairns (130), capable of controlling to $\pm$ 0.1°C. A transitrol Ether controller normally 40 mV f.s.d. was sensitised by removal of resistances in the input circuit to give f.s.d. of 4 mV. By opposing the thermocouple emf, inserted near the furnace windings, with that from a standardised potentiometer circuit any excess deliberately allowed for would actuate the controller. Selected tappings off the potentiometer threfore result in control over any range of temperature desired. Further stability was achieved by the use of a two-position mercury switch which actuated a high or low current to flow through the furnace.

For temperatures up to 950°C a T_1T_2 thermocouple was used, controlling the furnace temperature to $\pm$ 0.25°C, and at temperatures above 950°C at Pt./Pt. 13% Rh. thermocouple

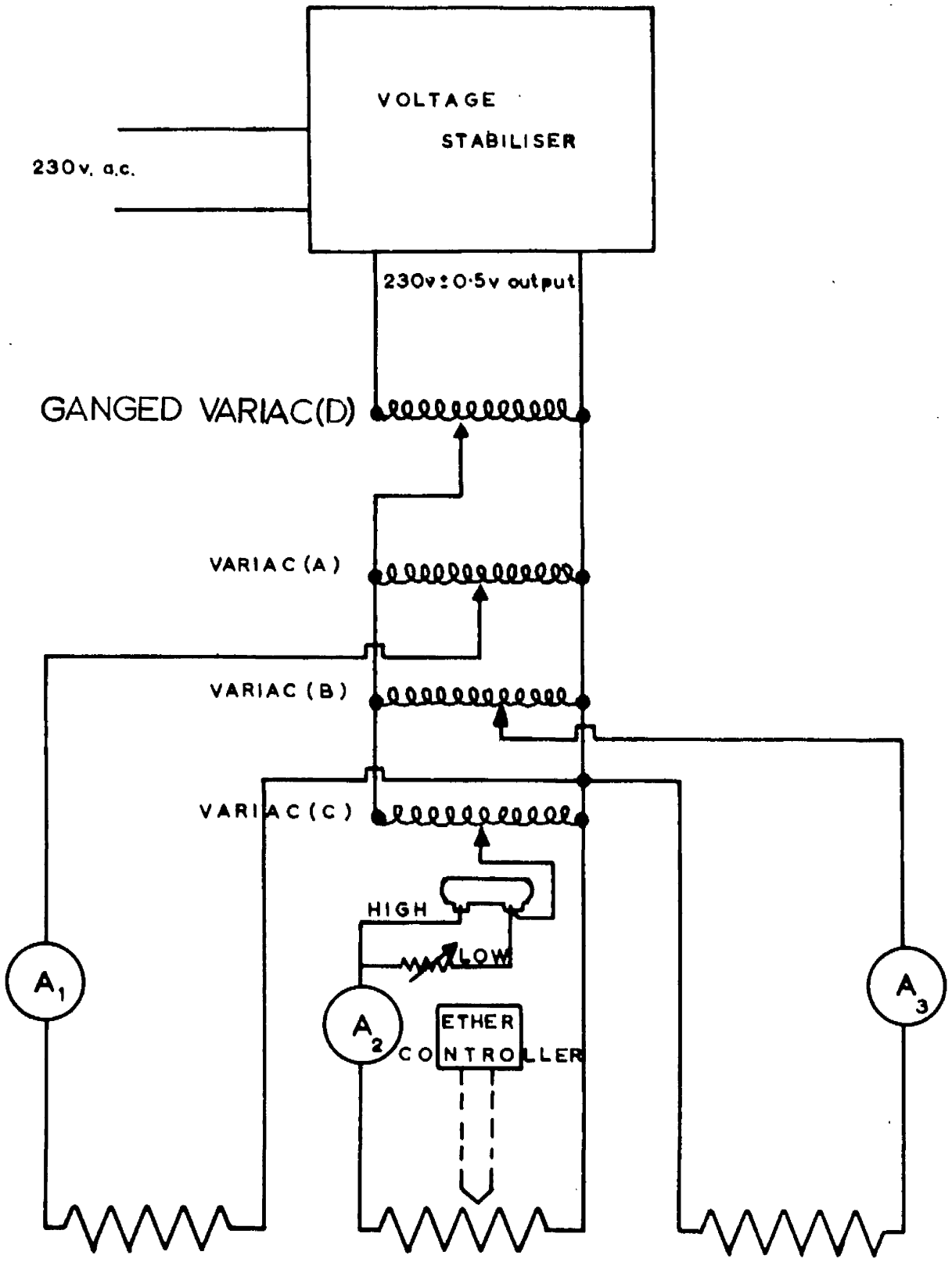
VOLTAGE
STABILISER
230v. a.c.
230v ± 0·5v output
GANGED VARIAC(D)
VARIAC (A)
VARIAC (B)
VARIAC (C)
HIGH
LOW
A1
A2
A3
ETHER
CONTROLLER
FURNACE WINDINGS

Fig. 61

FURNACE CONTROL CIRCUITS.

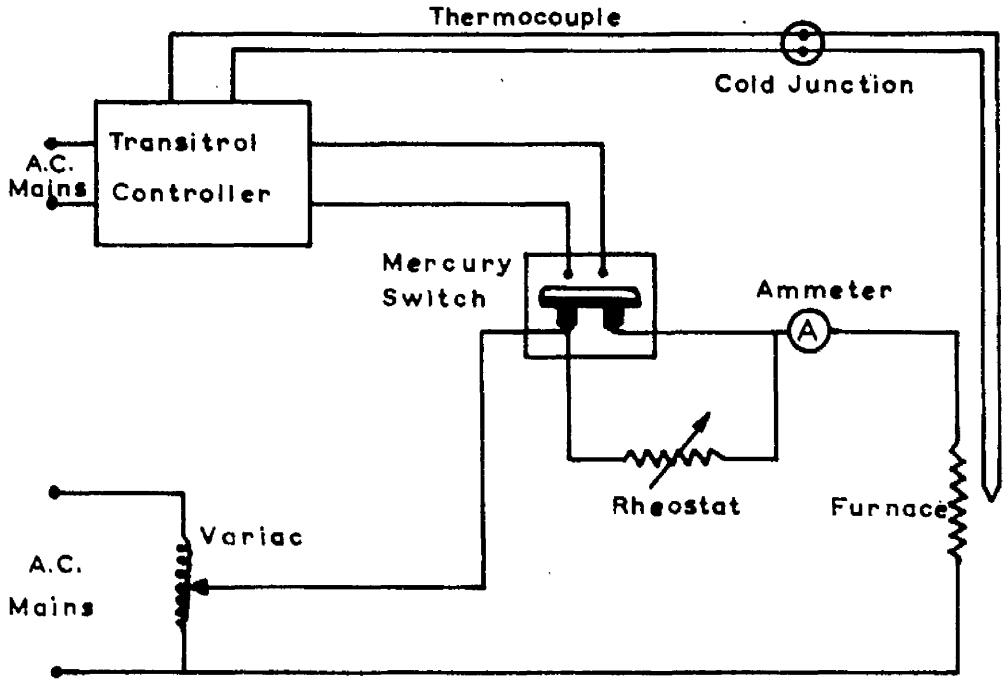

a. High-Low Control.

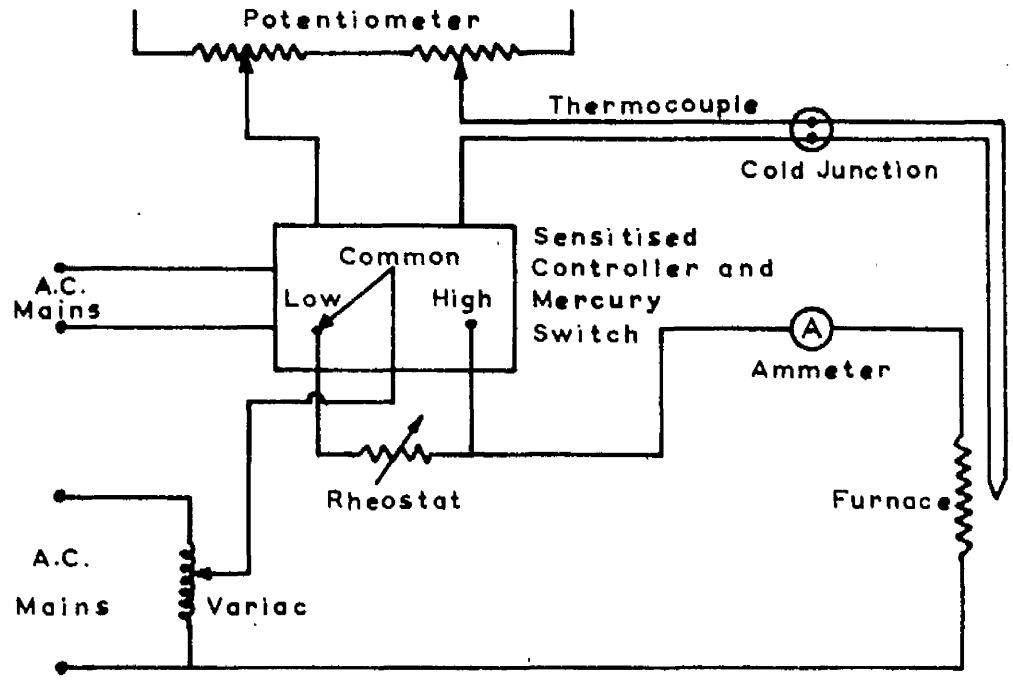

b. Sensitised High-Low Control.

Fig. 62

controlled the furnace to ± 1°C. The current/temperature characteristics of the outer furnace windings were calibrated to enable the furnace to be used successfully.

For continuous heating and cooling experiments use was made of the ganged variac D Fig. (58) which effects a simultaneous increase or decrease in variacs A, B, and C.

The mains input to the ganged variac was stabilised to ± 0.5 volts by a Claude Lyons Voltage Stabiliser Type BM 17000.

Experimental Procedure

(a) The variation of electrical resistivity with temperature was determined under conditions of continuous cooling at rates of 2.5 and 5.0°C per minute in the temperature range 1210°C - 1070°C.

(b) The temperature coefficient of resistance of both the α and σ-phase was investigated in the temperature range 100°C - 1270°C. A specimen was quenched from 1350°C to retain the α-phase and then placed in the furnace Fig. (59). The furnace was then set at the requisite temperature and the specimen annealed. Times of annealing varied, longer times being used at the lower temperatures (2 hrs. 300°C, 1 hr. 800°C, 1/4 hrs. 1200°C). At each temperature the

specimen potential was measured three times. Firstly with no current flowing to ascertain the thermal emf generated and secondly with the current flowing and thirdly with the direction of the current reversed.

(c) The kinetics of the $\alpha \rightarrow \sigma$ phase change were investigated, in the binary and six ternary alloys, using electrical resistivity changes to indicate the progress of the transformation.

For each isothermal transformation investigated the following procedure was adopted.

The specimen was annealed at 1350°C for 12 hrs. and quenched into iced water. The leads were spot welded at each end of the specimen. The furnace was set at the temperature required and evacuated to 10^{-3} mm. Hg.; the open end being sealed with a blank plate. Argon (99.995) was then bled into the system to atmospheric pressure and the plate removed. With the dc current flowing and the recorder set the specimen assembly was put into the furnace which was then evacuated. At the end of the reaction argon was again introduced into the system and the specimen withdrawn and quenched into water.

In the high temperature range, the specimen assembly was

put into the furnace at room temperature and the furnace evacuated to 10^{-4} mm. Hg.. The temperature of the furnace was then raised to the transformation temperature. The heating coil was switched on and controlled at 1300°C by the thermocouple spot welded to the specimen. After annealing for 30 mins. in the α-phase the heating coil was switched off and argon forced into the system whilst it was still being evacuated. The reaction was then followed on the Kipp and Zonen recorder.

Metallography

Iron-vanadium alloys in the α-phase may be polished mechanically using conventional techniques. Specimens can be ground on wet silicon carbide papers and polished finally with diamond paste. Alloys in the σ-phase tend to be friable. They need careful grinding and a much longer polishing time to prepare surfaces suitable for etching.

The most effective etching reagent used was nitric acid diluted with an equal volume of water. All micro-structures shown in this thesis were etched in this solution. For single phase sigma alloys it was found that no grain structure could be revealed. An attempt to show the structural details of sigma phase was made using electrolytic techniques. A Disa-electropol machine was used and two electrolytes tried.

Electrolyte	A2	Oxalic acid
Pre-grinding	no. 400	no. 600
Flow rate	4	4
Polishing	20 secs.	30 secs.
Current	1.8 amps. (40V)	0.2 amps.
Etching	3 secs. (0.05A)	-

where the code number of emery papers corresponds to the Lunn wet-grinding method.

Although both of these electrolytes revealed the structural details of the α-phase no details of the σ-phase could be distinguished other than cracks.

Specimens used for the investigation were the end pieces from the ingot prepared in the arc furnace, and were approximately 5×5×4 mm. The high temperature treatment (1200°C - 1350°C) was carried out in the annealing furnace described earlier. For the low temperature annealing specimens were placed in a silica tube coupled to a small rotary and oil diffusion pump. A furnace, controlled to $\pm$ 1/2°C, was mounted on rails which enabled the silica tube to be evacuated and the furnace brought up for the requisite annealing time and then withdrawn.

Using the reaction times derived from the TTT curves

of the binary and six ternary alloys the products of partially transformed specimens were investigated as well as the single phase structure of the alpha and sigma phases.

X-ray Powder Photography

In each case when a powder photograph was to be taken the following procedure was adopted. The turnings from each ingot were transformed to the σ-phase by an annealing at 900°C and cooling under vacuum. The turnings were then ground in a mortar and pestel and sieved through a 300 B.S. mesh. The powder which passed through the mesh was then ready for powder photography of the σ-phase or for annealing and quenching in the bcc phase.

The powder was packed into small tubes of beryllium glass, diameter 0.3 mm., to a depth of 1 cm. and sealed off with a very small gas flame at about 1.5 cm. The specimen was accurately positioned in an 11.46 cm. camera, its axis being set as close as possible to that of the camera by observation on rotation. The cameras were fitted with fluorescent screens to assist alignment in the X-ray beam.

A Phillips fully rectified PW 1010 X-ray set was used with a chromium target operated at 30 kv and 8 mA. Three types of film were tried in the early stages of the investigation, G, B and CX. The G and B types tended to

show too much background at the high angle end of the films. CX film was found to be the most suitable requiring a 24 hrs. exposure.

After exposure the films were processed and the line diameters on the powder photographs measured using a vernier travelling microscope. In the course of the work films were measured twice and in some cases a second film was also taken and measured. The σ-phase data was then computed using the programme (127) already described. The α-phase bcc structure parameters were calculated by hand.

CHAPTER V

RESULTS

Resistivity Results

1. The isothermal transformation of alpha to sigma was studied in the range 730 - 800°C and 1090 - 1120°C in an equiatomic iron-vanadium alloy and six ternary alloys. On the assumption that the electrical resistivity is a linear function of the decomposed fraction, the fractional transformation of alpha to sigma was calculated from the recorded specimen potential drop, as follows,

$$f(y) = \% \text{ transformation} = \frac{V_s - V_t}{V_s - V_f}$$

where V_t, V_s and V_f are the potential drops across the specimen at time t, at the start and end of the reaction, respectively. The resulting reaction curves of fraction transformed against log time are shown in Appendix III.

2. The results of the resistivity experiments were expressed in the form of TTT diagrams, 5% transformation constituting the start of the reaction and 95% the end, as shown in Figs. (63,65,67,69,71,73,75) for the respective systems.

3. The reciprocal rate curves have been plotted, Figs. (64,66,68,70,72,74,76) and the activation energy for

the reaction derived from the gradients in the manner described in Chapter II.

4. An equiatomic iron-vanadium alloy has been investigated under conditions of continuous cooling. Fig. (77) shows the variation of potential drop across the specimen as a function of temperature.

5. Values of the resistivity of the alpha and sigma phases determined under equilibrium conditions in the range 100 - 1250°C are shown in Fig. (81).

6. The values of the σ-phase lattice parameters obtained by the three methods of calculation described in Chapter III are listed with the standard errors in Table (IX). The values of the bcc lattice parameters are shown in Table (XI).

Errors

Isothermal transformations: The determination of accurate incubation periods for reaction at any temperature will depend firstly on the degree of temperature stability prior to transformation and secondly on the sensitivity of the measuring instrument. Variation of ±1.0°C prior to transformation causes a variation of ±0.0008 mv, a value derived from Fig. (81). Therefore the error in the incubation period due to a temperature fluctuation is equal to ±0.08% per °C per millivolt of specimen potential. Since

order of ±2 - ±10%. It will be greatest at high temperatures (low PD change) and decrease with falling temperatures. General limits of total experimental error in the observed reaction times can therefore be set between the limits ±4 - ±12% for the transformation ranges 700 - 800°C and 1090 - 1110°C.

It is expected that the derived activation energies should lie within the above limits, though the graphical representation will probably result in an additional error, and the derived values can be considered representative of the data within the range ±10 - ±15%.

Lattice parameters: The standard errors printed at the side of each parameter value in Table (IX) represents the minimum experimental error associated with the results. The magnitude of random and systematic errors is shown by the plot of lattice parameter against the Taylor-Sinclair function Fig. (79). From the small gradient of the graph it is seen that the systematic error is small and the scatter of points indicates that the random errors of measurement are also small.

Only two high angle lines could be measured on the bcc films and 0.005 is the estimated minimum experimental error of the lattice parameters shown in Fig. (XI).

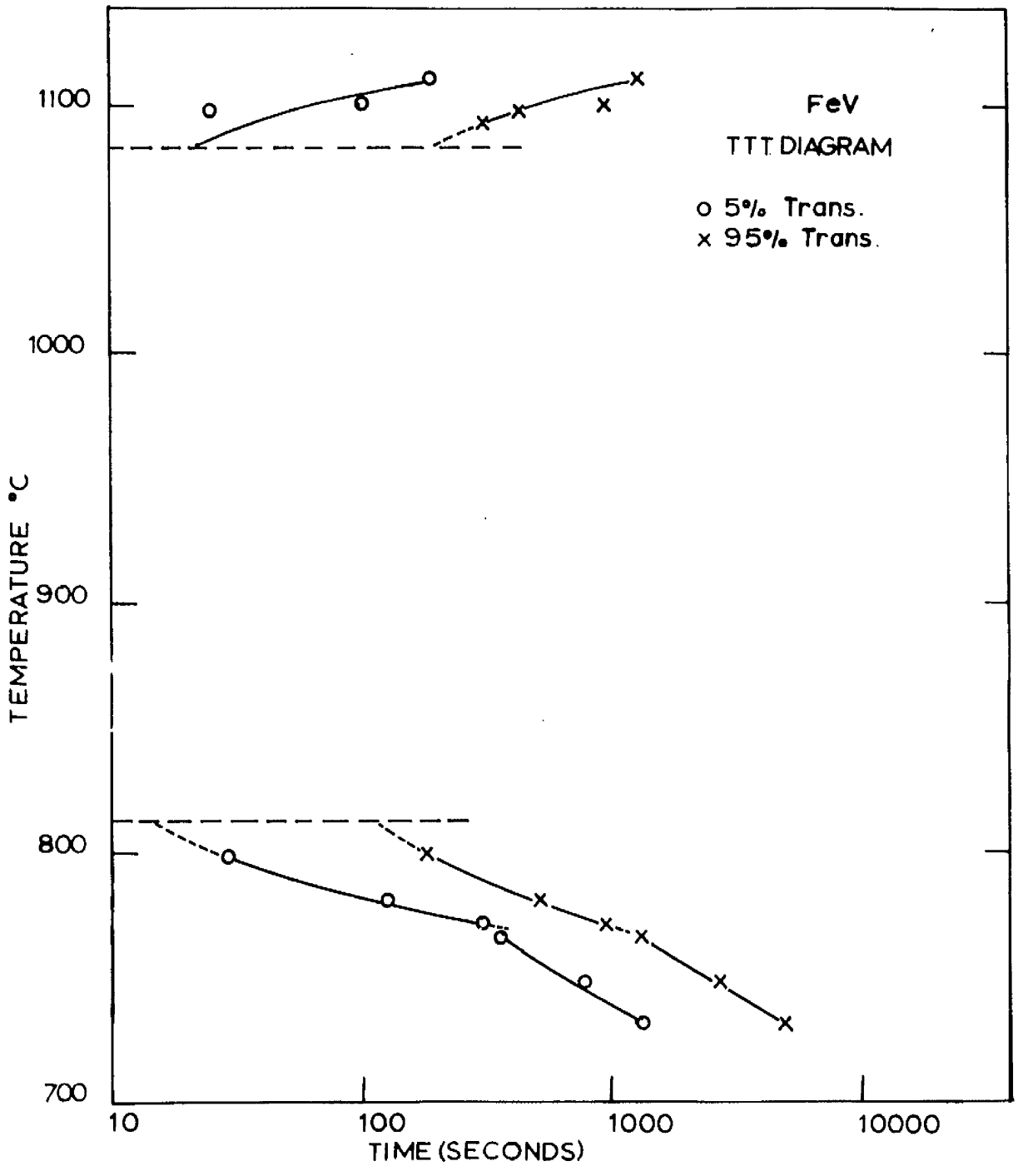
FeV
TTT DIAGRAM
o 5% Trans.
x 95% Trans.
1100
1000
900
800
700
TEMPERATURE °C
10
100
1000
10000
TIME (SECONDS)

Fig. 63

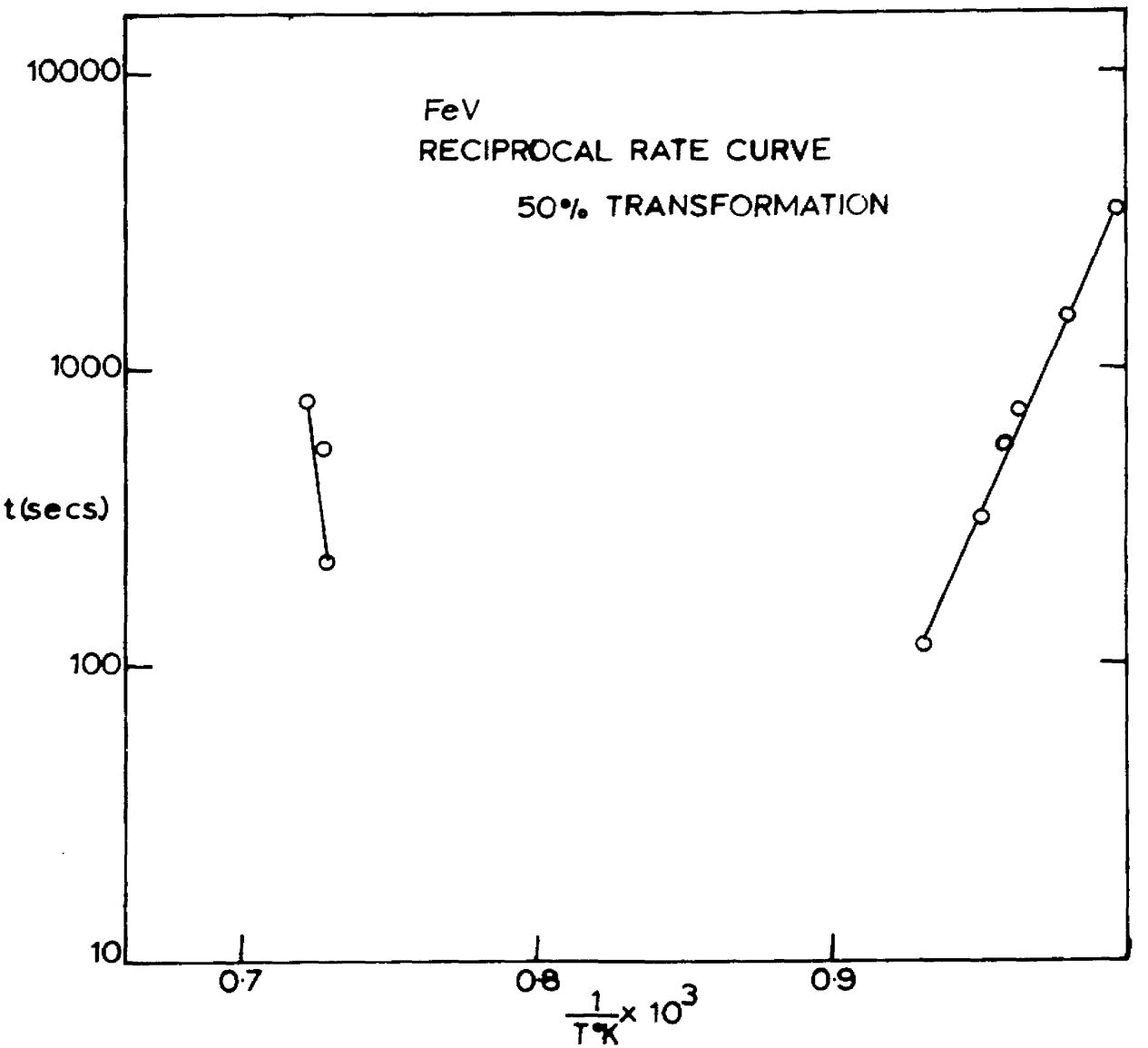
FeV
RECIPROCAL RATE CURVE
50% TRANSFORMATION
10000
1000
100
10
t(secs)
0·7
0·8
0·9
$\frac{1}{T°K} \times 10^3$

Fig 64

TABLE I

Fe-V

Temp. °C	$\frac{1}{T°K} \times 10^3$	PERCENTAGE TRANSFORMED 5% t (secs)	5% log t (secs)	50% t (secs)	50% log t (secs)	95% t (secs)	95% log t (secs)
731	0.996	1320	3.121	3475	3.541	4910	3.691
747	0.980	785	2.895	1500	3.176	2675	3.427
765	0.963	360	2.556	735	2.866	1325	3.122
770	0.959	300	2.477	560	2.748	960	2.982
780	0.950	125	2.097	315	2.498	515	2.712
798	0.934	14	1.461	113	2.053	178	2.250
1094	0.732	-	-	-	-	310	2.491
1098	0.729	25	1.398	220	2.342	430	2.633
1099	0.729	120	2.079	535	2.728	940	2.973
1113	0.722	185	2.267	770	2.886	1280	3.107

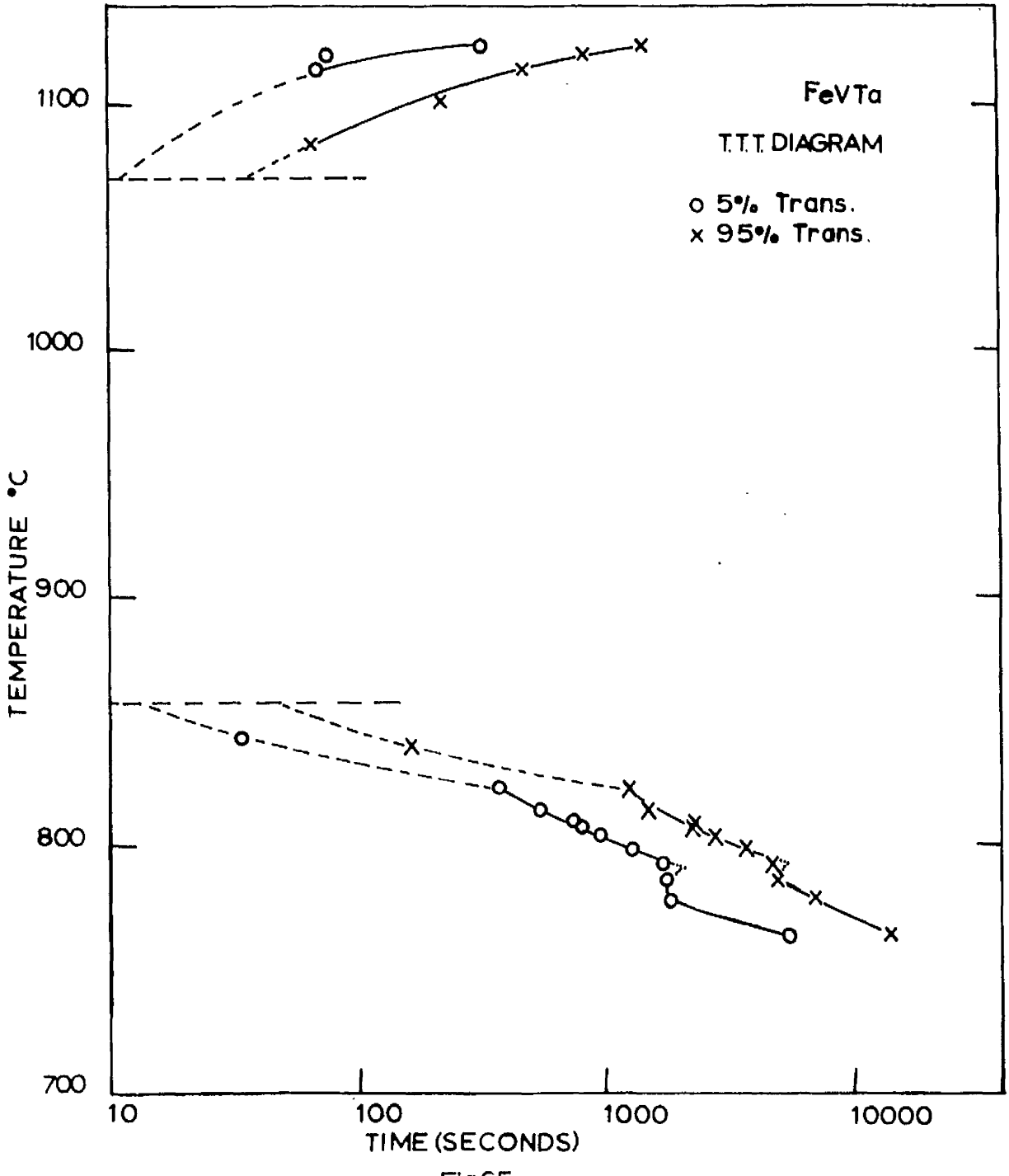
FeVTa
T.T.T. DIAGRAM
o 5% Trans.
x 95% Trans.
1100
1000
900
800
700
TEMPERATURE °C
10
100
1000
10000
TIME (SECONDS)

Fig 65

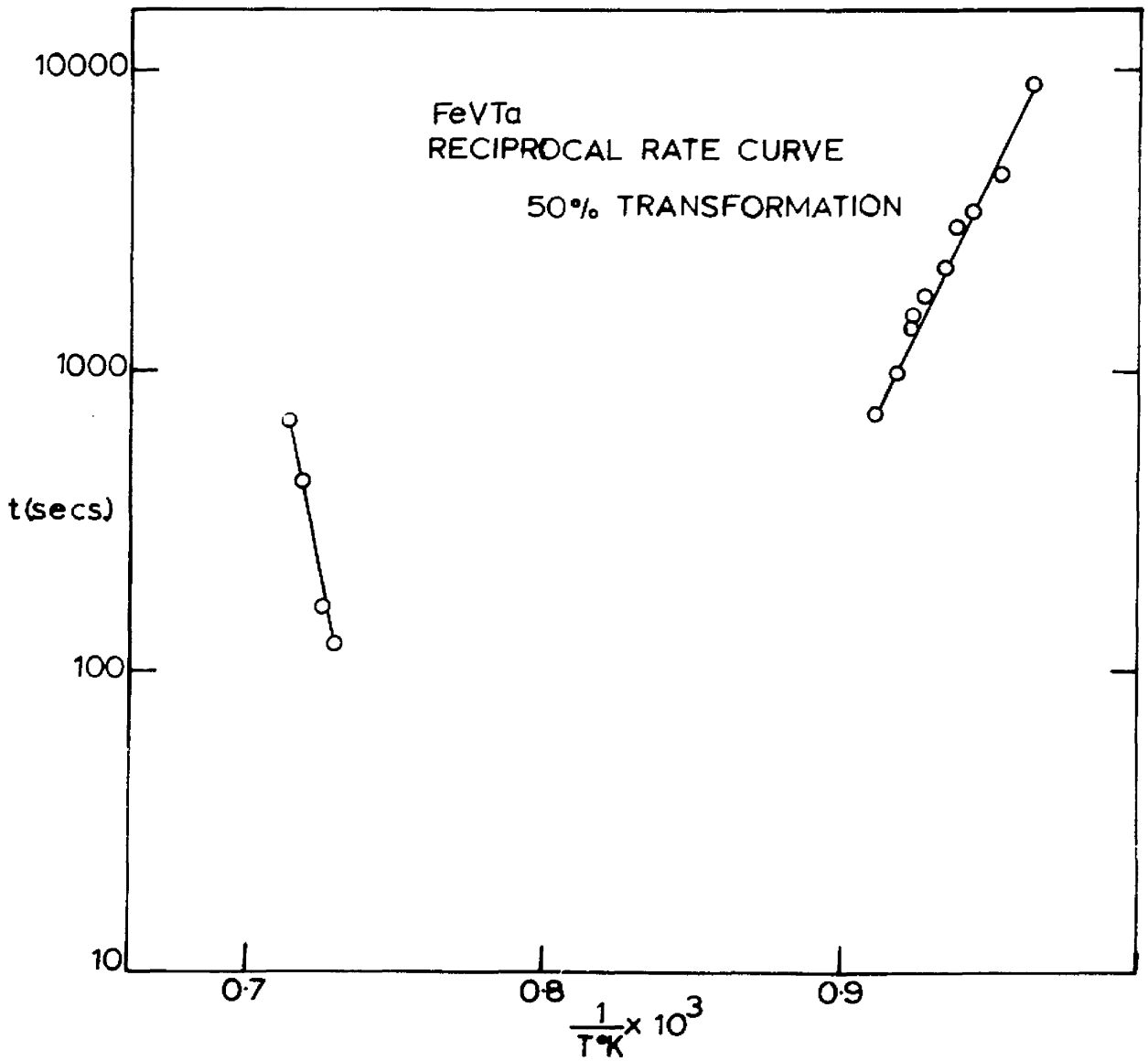
FeVTa
RECIPROCAL RATE CURVE
50% TRANSFORMATION
10000
1000
100
10
t(secs)
0·7
0·8
0·9
$\frac{1}{T°K} \times 10^3$

Fig.66

TABLE II

Fe-V-Ta

PERCENTAGE TRANSFORMED

Temp. °C	$\frac{1}{T°K} \times 10^3$	5% t (secs)	5% log t (secs)	50% t (secs)	50% log t (secs)	95% t (secs)	95% log t (secs)
764	0.964	5380	3.731	9020	3.955	13340	4.125
777	0.952	2675	3.247	4560	3.659	6745	3.829
786	0.944	1710	3.233	3400	3.532	4855	3.686
792	0.939	1670	3.220	3080	3.489	4690	3.671
798	0.934	1235	3.092	2190	3.340	3665	3.564
804	0.929	918	2.963	1790	3.253	2680	3.428
807	0.926	775	2.889	1490	3.173	2170	3.337
809	0.924	730	2.863	1445	3.160	2255	3.353
814	0.920	528	2.723	995	2.998	1440	3.158
823	0.912	360	2.556	720	2.857	1235	3.092
843	0.896	34	1.532	78	1.892	163	2.212
1084	0.737	-	-	-	-	65	1.813
1102	0.727	-	-	120	2.079	225	2.352
1114	0.721	70	1.845	160	2.204	475	2.677
1120	0.718	75	1.880	420	2.623	825	2.920
1124	0.716	320	2.505	670	2.826	1450	3.161

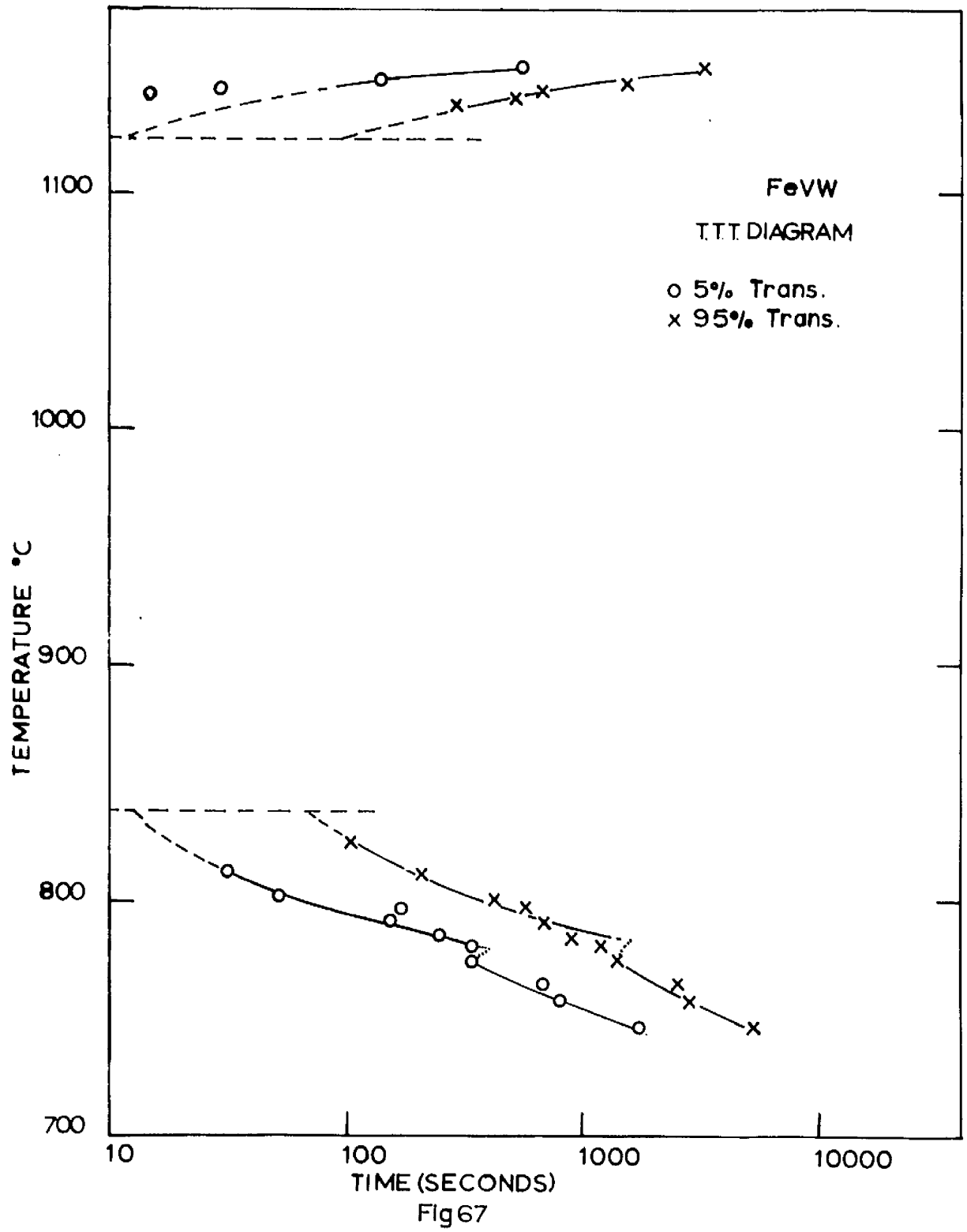
FeVW
T.T.T. DIAGRAM
o 5% Trans.
x 95% Trans.
1100
1000
900
800
700
TEMPERATURE °C
10
100
1000
10000
TIME (SECONDS)
Fig 67

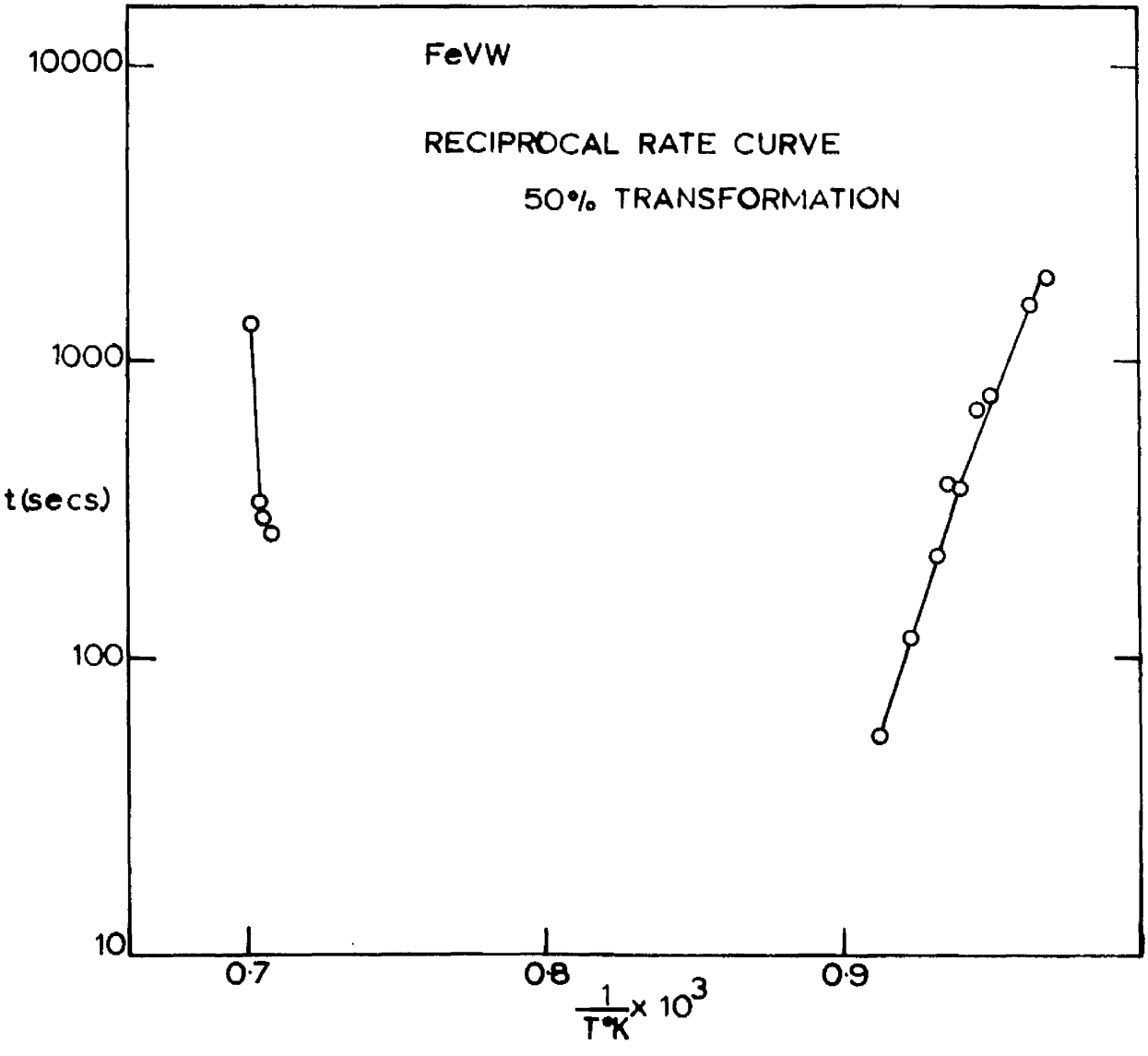
FeVW
RECIPROCAL RATE CURVE
50% TRANSFORMATION
10000
1000
100
10
t(secs)
0·7
0·8
0·9
1/T°K x 10³

Fig.68

TABLE III

Fe-V-W

Temp. °C	$\frac{1}{T°K} \times 10^3$	PERCENTAGE TRANSFORMED 5% t secs.	5% log t (secs)	50% t secs.	50% log t (secs)	95% t secs.	95% log t (secs)
747	0.980	1950	3.290	3548	3.550	6075	3.784
758	0.970	890	2.949	1920	3.283	3350	3.505
765	0.963	755	2.878	1495	3.175	2835	3.453
774	0.955	380	2.580	600	2.778	1560	3.193
780	0.950	390	2.591	760	2.881	1320	3.121
785	0.945	278	2.443	698	2.844	993	2.997
791	0.940	165	2.218	375	2.574	750	2.875
796	0.935	185	2.267	385	2.586	635	2.803
800	0.932	58	1.763	218	2.338	465	2.658
810	0.923	35	1.544	115	2.061	225	2.352
823	0.912	-	-	55	1.740	115	2.061

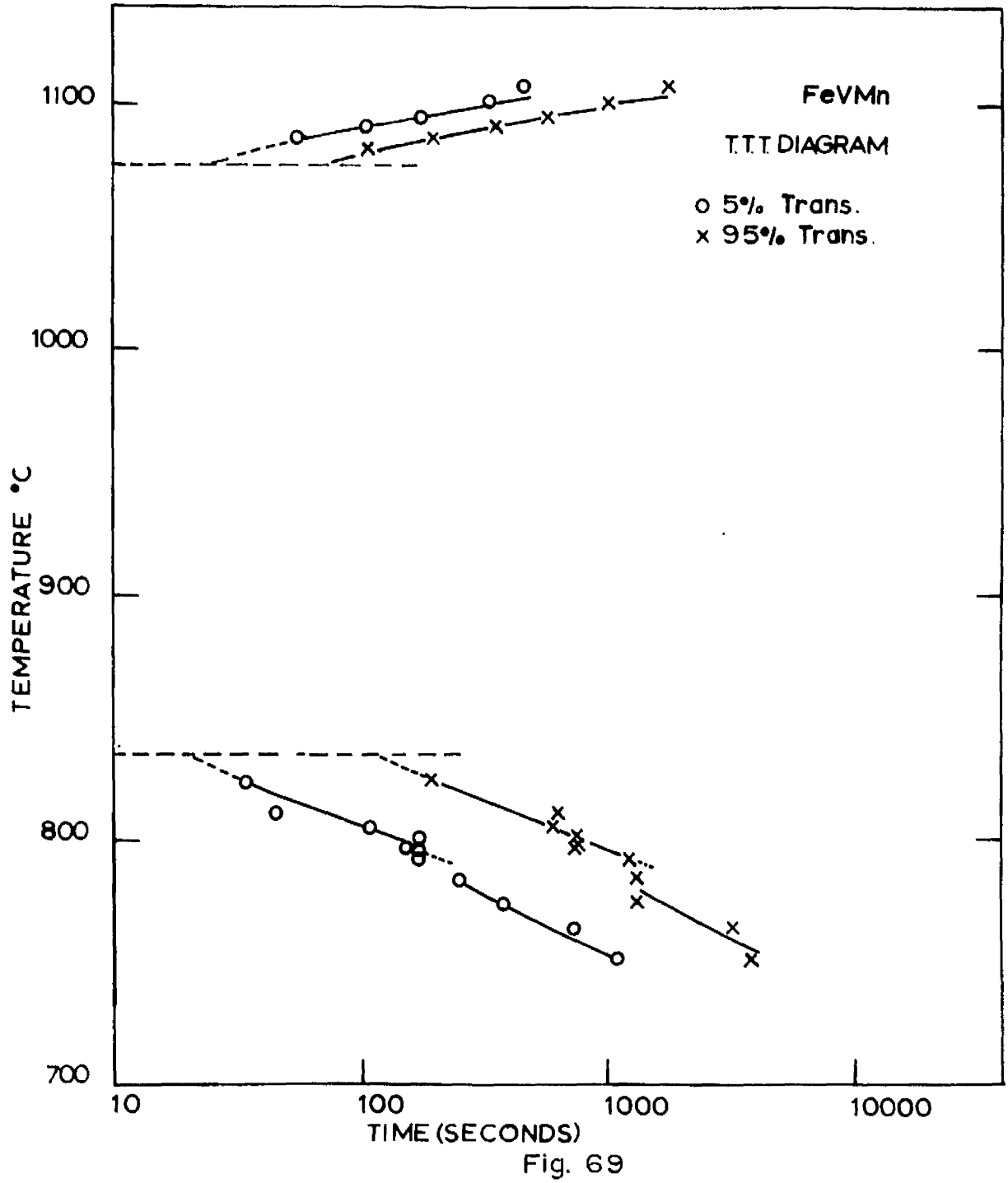
FeVMn
T.T.T. DIAGRAM
o 5% Trans.
x 95% Trans.
1100
1000
900
800
700
TEMPERATURE °C
10
100
1000
10000
TIME (SECONDS)
Fig. 69

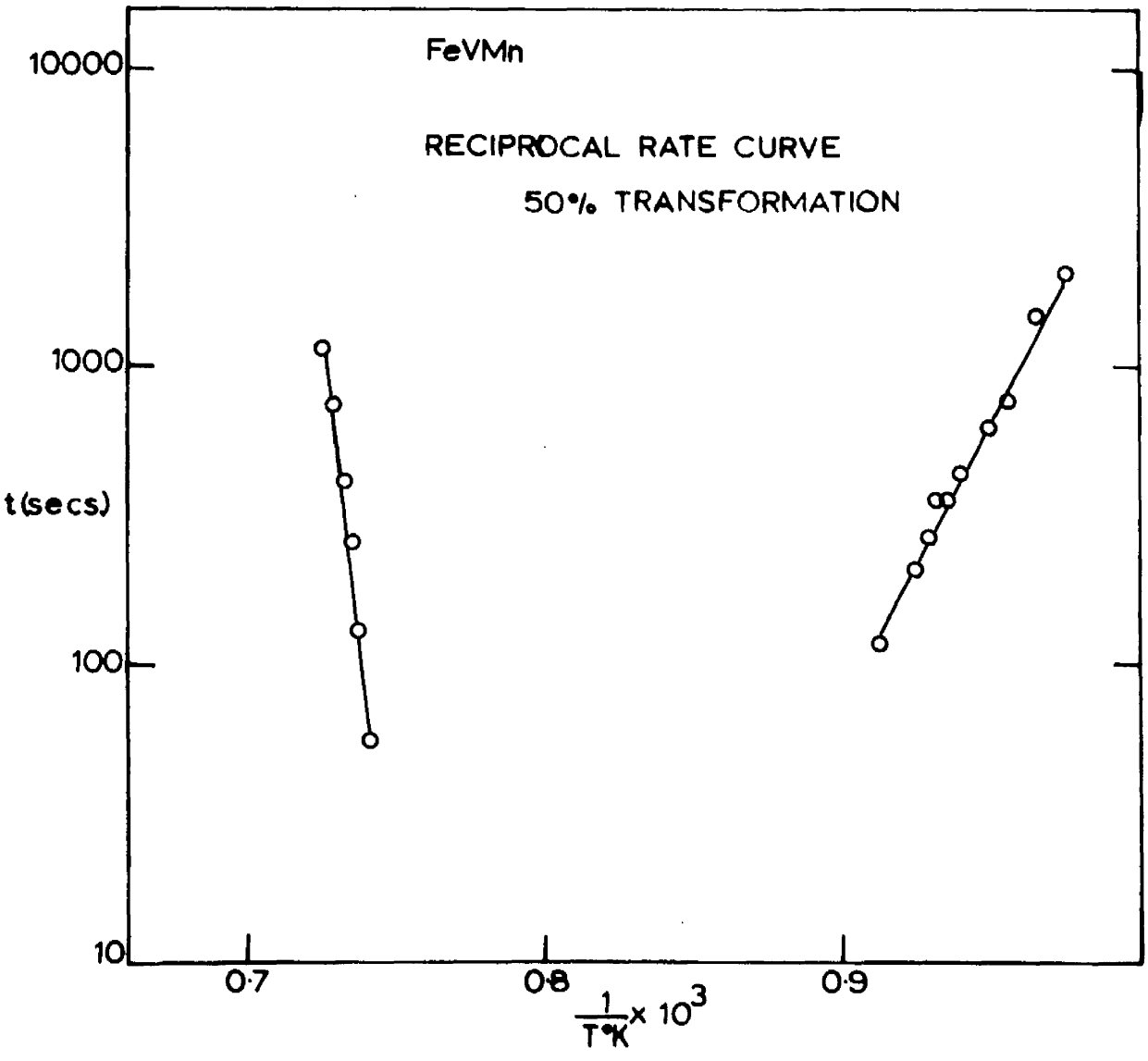
FeVMn
RECIPROCAL RATE CURVE
50% TRANSFORMATION
10000
1000
100
10
t(secs)
0·7
0·8
0·9
1/T°K x 10^3

Fig.70

TABLE IV

Fe-V-Mn

PERCENTAGE TRANSFORMED

Temp. °C	$\frac{1}{T°K} \times 10^3$	5% t (secs)	5% log t (secs)	50% t (secs)	50% log t (secs)	95% t (secs)	95% log t (secs)
752	0.975	1090	3.037	2075	3.317	3810	3.581
764	0.964	725	2.860	1430	3.155	3070	3.487
774	0.955	375	2.574	745	2.872	1273	3.105
784	0.946	245	2.389	595	2.775	1285	3.109
792	0.939	170	2.230	430	2.633	1215	3.085
796	0.935	168	2.225	350	2.544	718	2.856
797	0.935	165	2.175	370	2.568	730	2.863
801	0.931	170	2.230	350	2.544	740	2.869
805	0.928	108	2.031	260	2.410	605	2.782
811	0.923	45	1.653	170	2.230	635	2.803
823	0.912	35	1.544	115	2.061	188	2.273
1072	0.743	-	-	-	-	20	1.301
1081	0.739	5	0.699	55	1.740	110	2.041
1085	0.736	55	1.740	125	2.097	195	2.290
1090	0.734	105	2.021	250	2.398	355	2.550
1093	0.732	175	2.243	400	2.602	570	2.756
1100	0.728	330	2.519	725	2.860	1030	3.013
1107	0.725	460	2.663	115	3.044	1790	3.253

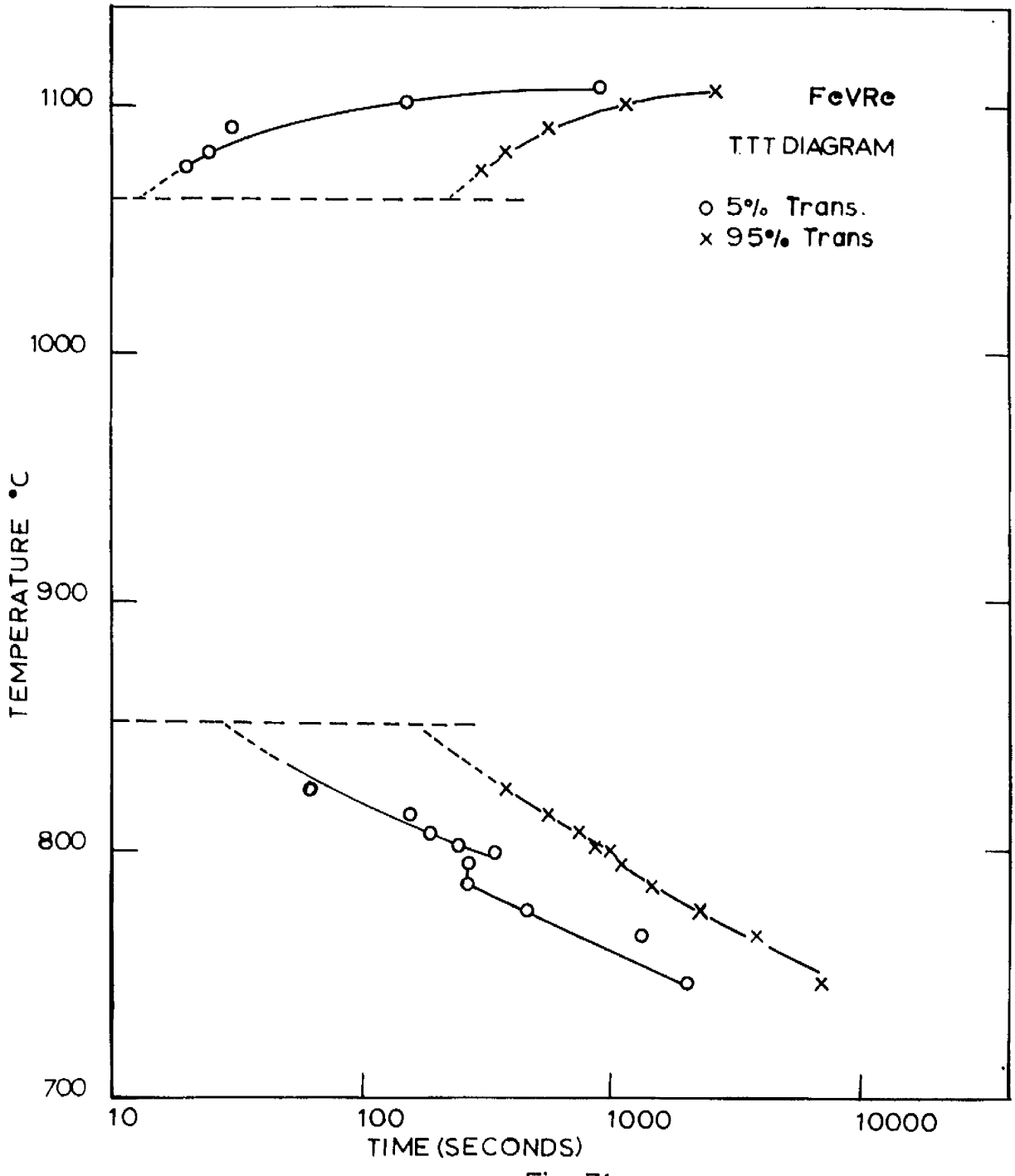
FeVRe
TTT DIAGRAM
o 5% Trans.
x 95% Trans
1100
1000
900
800
700
TEMPERATURE °C
10
100
1000
10000
TIME (SECONDS)

Fig. 71

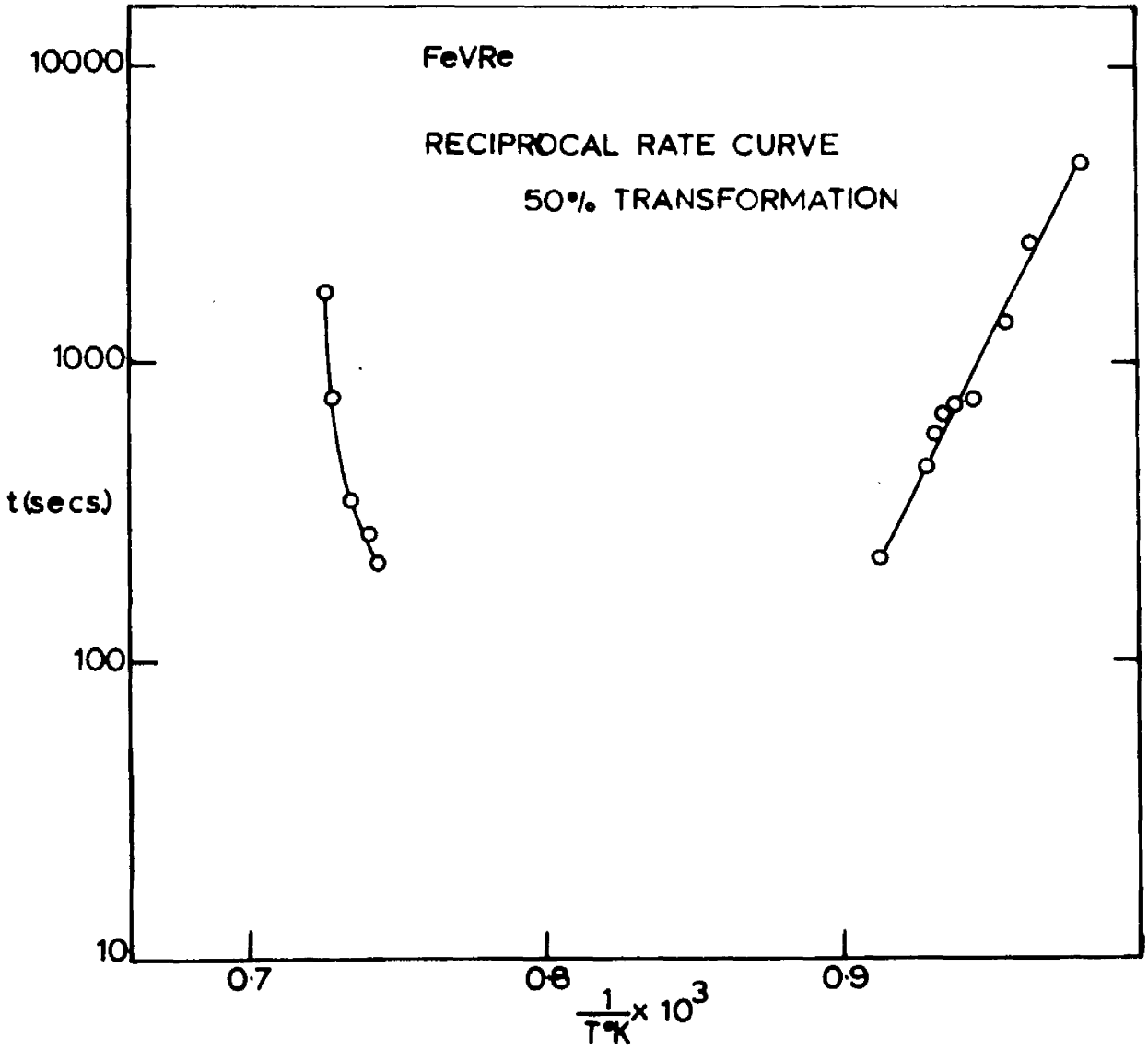
FeVRe
RECIPROCAL RATE CURVE
50% TRANSFORMATION
10000
1000
100
10
t (secs)
0·7
0·8
0·9
$\frac{1}{T°K} \times 10^3$

Fig. 72

TABLE V

Fe-V-Re

PERCENTAGE TRANSFORMED

Temp. °C	$\frac{1}{T°K} \times 10^3$	5% t secs.	5% log t (secs)	50% t secs.	50% log t (secs)	95% t secs.	95% log t (secs).
746	0.981	2065	3.315	4630	3.666	6950	3.842
765	0.963	1150	3.061	2530	3.403	3900	3.591
774	0.955	475	2.677	1350	3.130	2328	3.366
785	0.945	260	2.415	743	2.871	1515	3.180
793	0.938	340	2.532	710	2.851	1130	3.053
798	0.934	343	2.535	648	2.811	1010	3.004
801	0.931	245	2.389	507	2.730	880	2.942
813	0.921	158	2.199	365	2.736	585	2.763
823	0.912	65	1.813	220	2.342	368	2.565
843		-	-	-	-	170	2.230
1073	0.743	20	1.301	210	2.322	305	2.484
1079	0.740	25	1.390	260	2.415	375	2.574
1089	0.734	30	1.477	340	2.532	560	2.748
1100	0.728	150	2.176	750	2.875	1110	3.045
1105	0.726	890	2.949	1715	3.233	2560	3.408

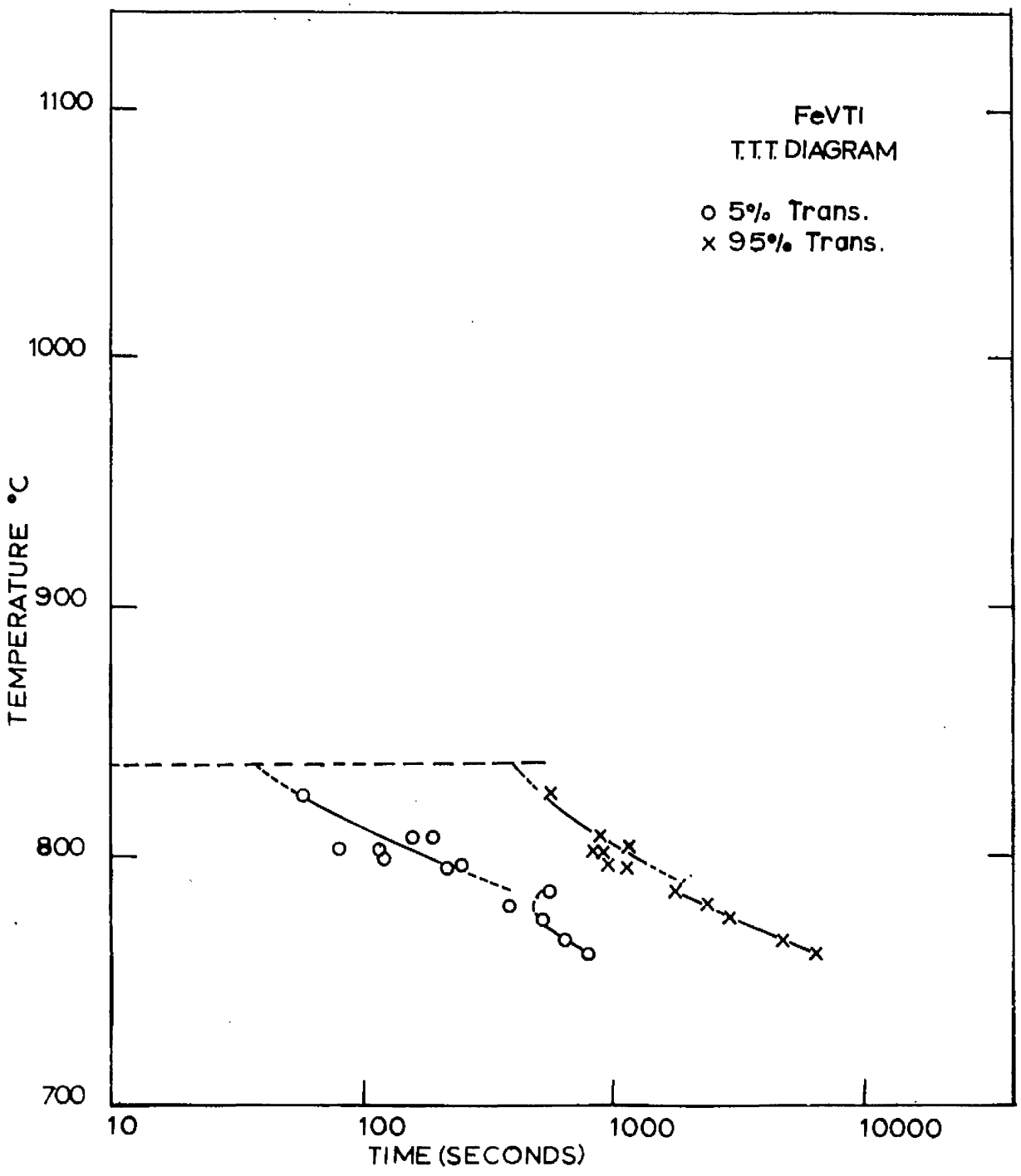
FeVTI
T.T.T. DIAGRAM
o 5% Trans.
x 95% Trans.
1100
1000
900
800
700
TEMPERATURE °C
10
100
1000
10000
TIME (SECONDS)

Fig. 73

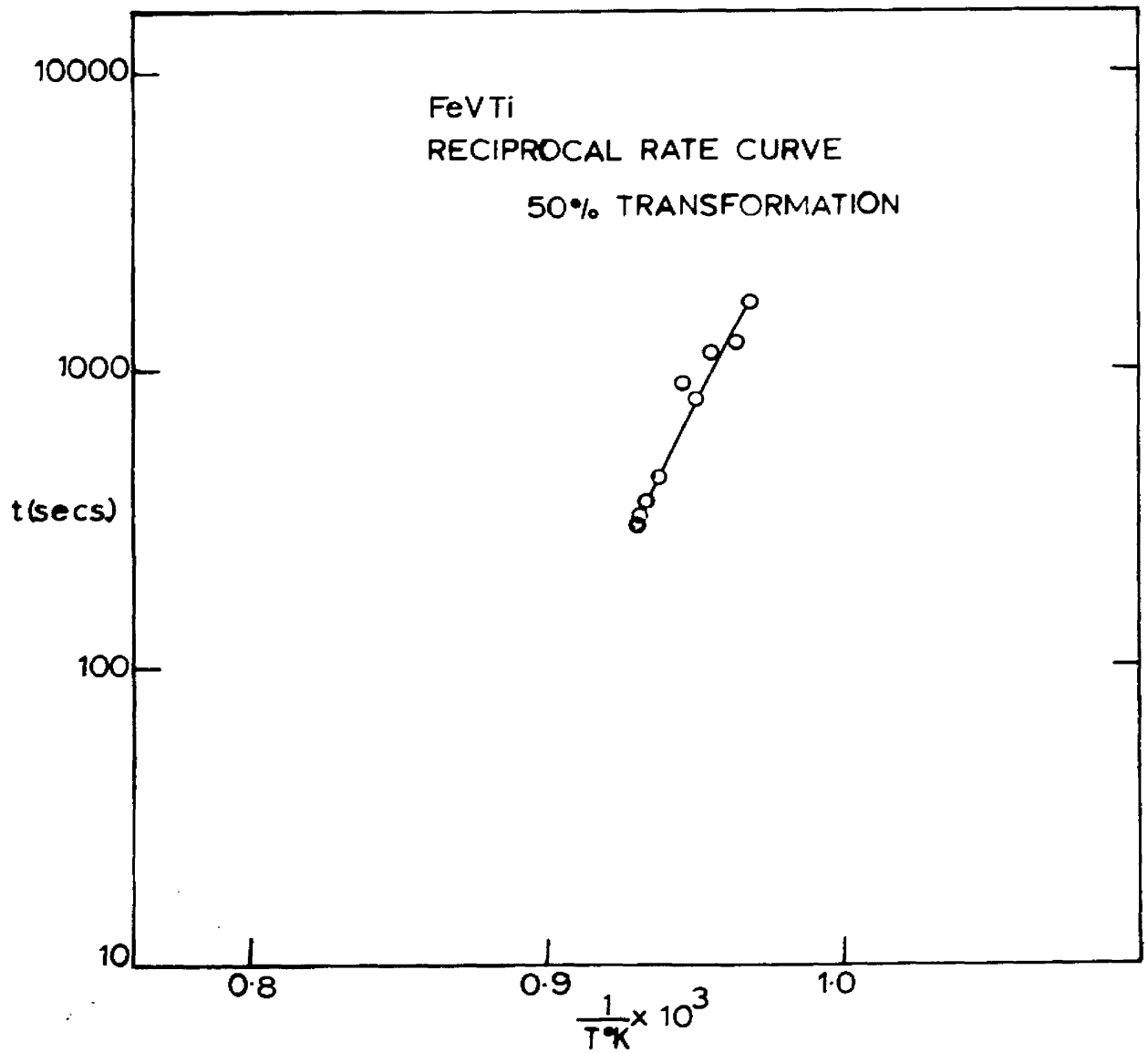
FeV Ti
RECIPROCAL RATE CURVE
50% TRANSFORMATION
10000
1000
100
10
t(secs)
0·8
0·9
1·0
$\frac{1}{T°K} \times 10^3$

Fig.74

TABLE VI

Fe-V-Ti

TEMP°C	$\frac{1}{T°K}\times10^3$	PERCENTAGE TRANSFORMED 5% t secs.	5% log t secs.	50% t secs.	50% log t secs.	95% t secs.	95% log t secs.
760	0.968	770	2.887	1778	3.250	6405	3.809
765	0.963	630	2.799	1300	3.114	3800	3.579
774	0.955	513	2.710	1163	3.066	2785	3.445
780	0.950	375	2.574	820	2.914	2370	3.374
785	0.945	553	2.742	955	2.980	1725	3.237
794	0.937	213	2.327	460	2.663	1125	3.051
795	0.936	248	2.394	443	2.646	950	2.978
798	0.934	120	2.079	370	2.568	900	2.954
801	0.931	115	2.061	340	2.532	655	2.816
802	0.930	80	1.903	315	2.498	1140	3.057
806	0.927	160	2.204	413	2.616	880	2.944
823	0.912	58	1.763	223	2.347	560	2.750

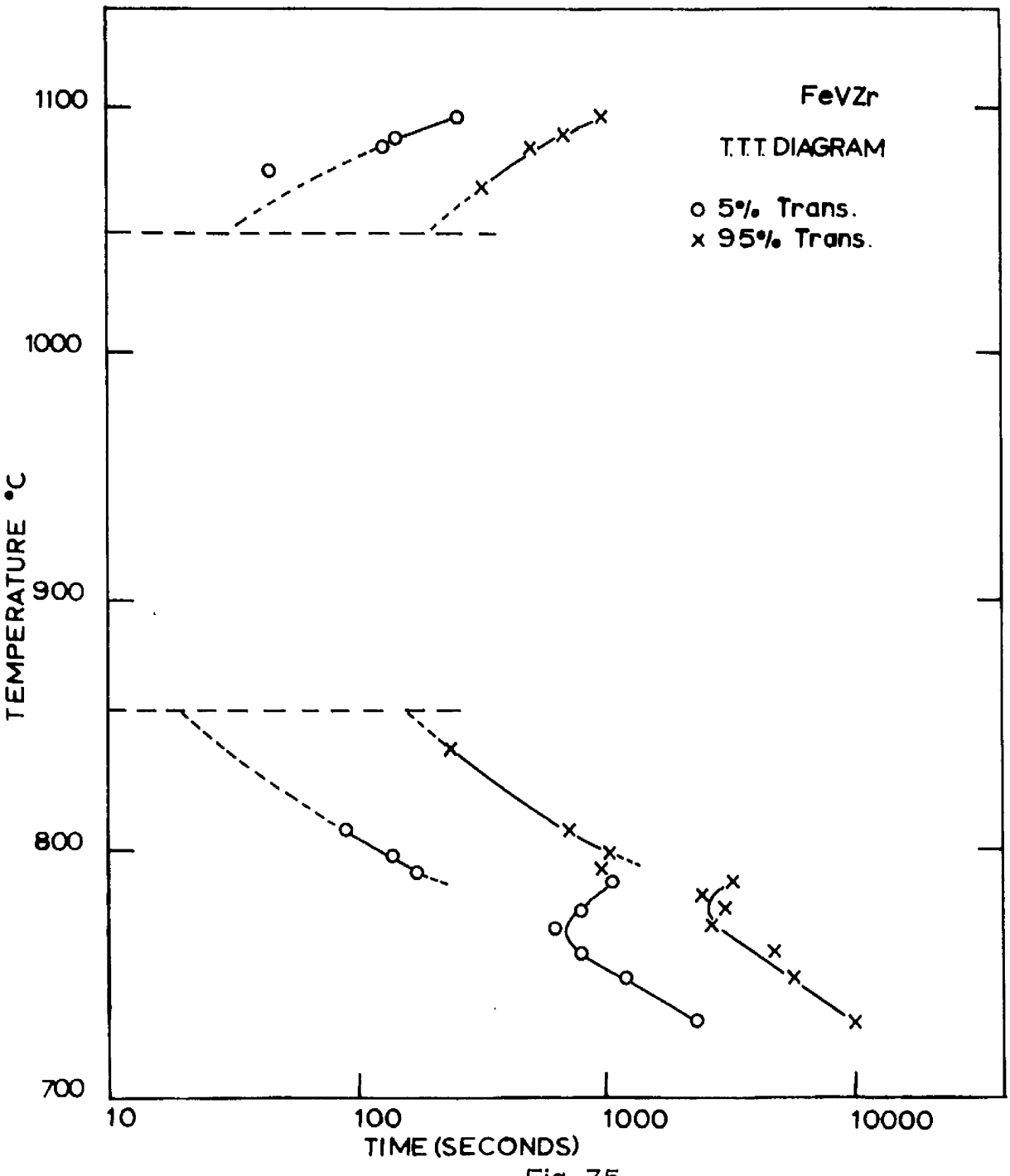
FeVZr
T.T.T. DIAGRAM
o 5% Trans.
x 95% Trans.
1100
1000
900
800
700
TEMPERATURE °C
10
100
1000
10000
TIME (SECONDS)

Fig. 75

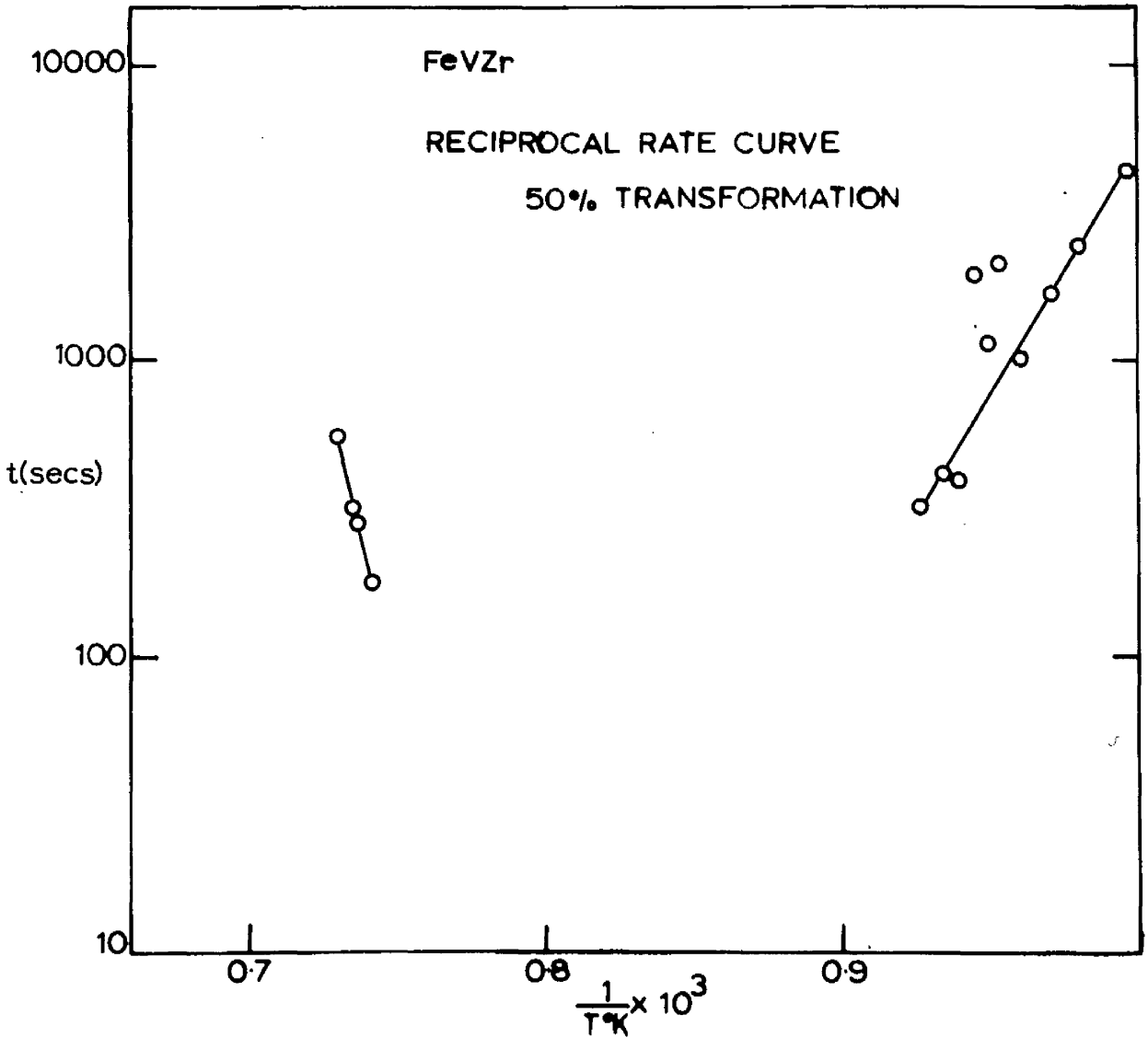
FeVZr
RECIPROCAL RATE CURVE
50% TRANSFORMATION
10000
1000
100
10
t(secs)
0·7
0·8
0·9
1/T°K x 10^3

Fig.76

TABLE VII

Fe-V-Zr

PERCENTAGE TRANSFORMED

Temp. °C	$\frac{1}{T°K} \times 10^3$	5% t (secs)	5% log t (secs)	50% t (secs)	50% log t (secs)	95% t (secs)	95% log t (secs)
730	0.997	2280	3.358	4570	3.660	8085	3.908
747	0.980	1230	3.090	2515	3.400	5620	3.750
757	0.971	631	2.800	1738	3.240	4893	3.690
768	0.961	633	2.801	1005	3.015	1663	3.221
775	0.954	793	2.899	2133	3.329	3075	3.488
780	0.950	140	2.146	1072	3.030	2468	3.392
785	0.945	1068	3.029	1978	3.295	3243	3.511
791	0.940	170	2.230	398	2.600	985	2.993
796	0.935	137	1.370	418	2.621	1035	3.015
806	0.927	90	1.954	333	2.522	670	2.826
823	0.912	-	-	-	-	245	2.389
1065	0.747	-	-	-	-	324	2.511
1074	0.742	44	1.644	183	2.263	418	2.621
1083	0.737	128	2.107	287	2.458	513	2.710
1086	0.736	145	2.161	318	2.502	678	2.831
1095	0.730	253	2.403	553	2.743	980	2.991

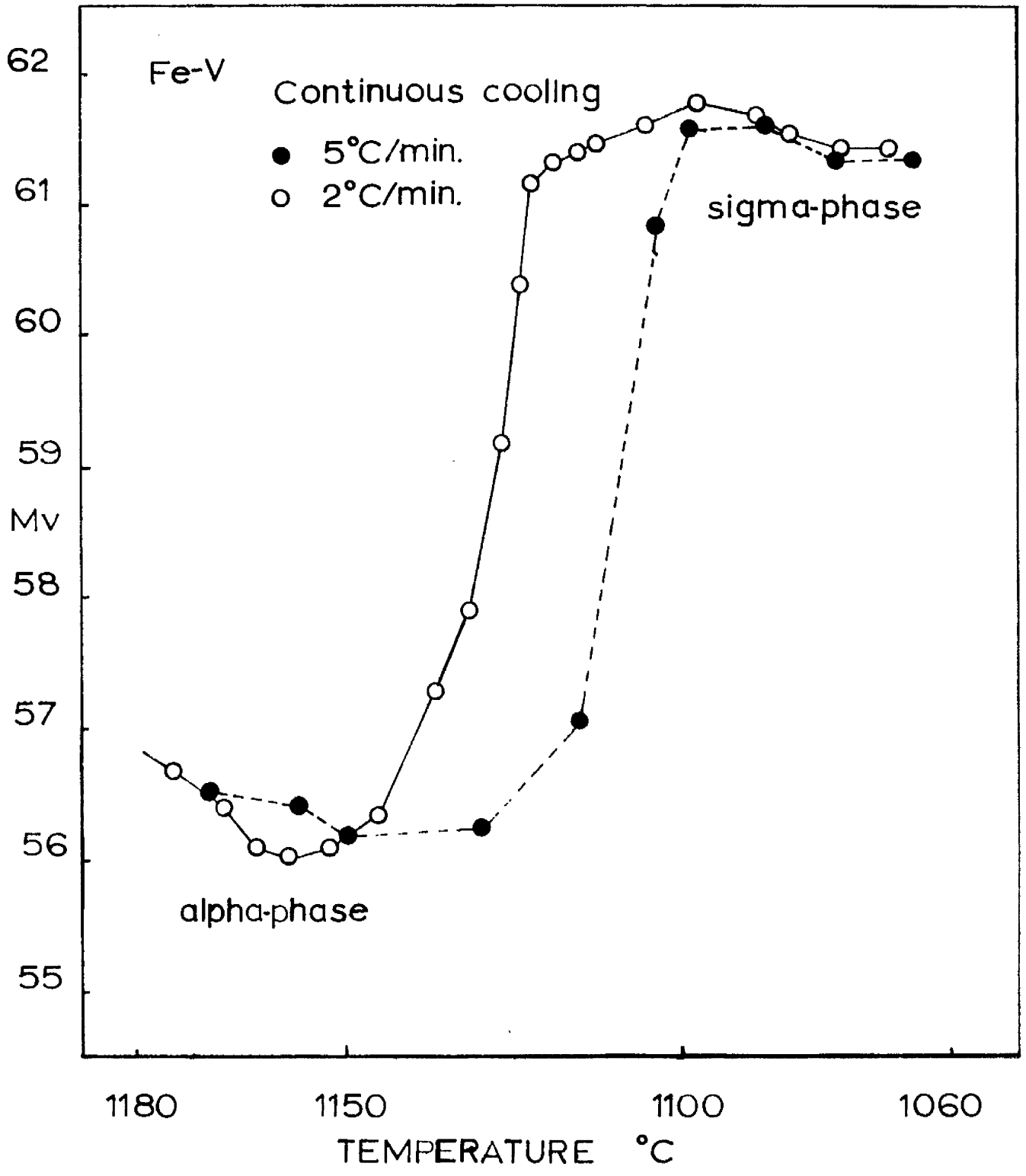
Fe-V
Continuous cooling
● 5°C/min.
o 2°C/min.
sigma-phase
alpha-phase
62
61
60
59
Mv
58
57
56
55
1180
1150
1100
1060
TEMPERATURE °C

Fig. 77

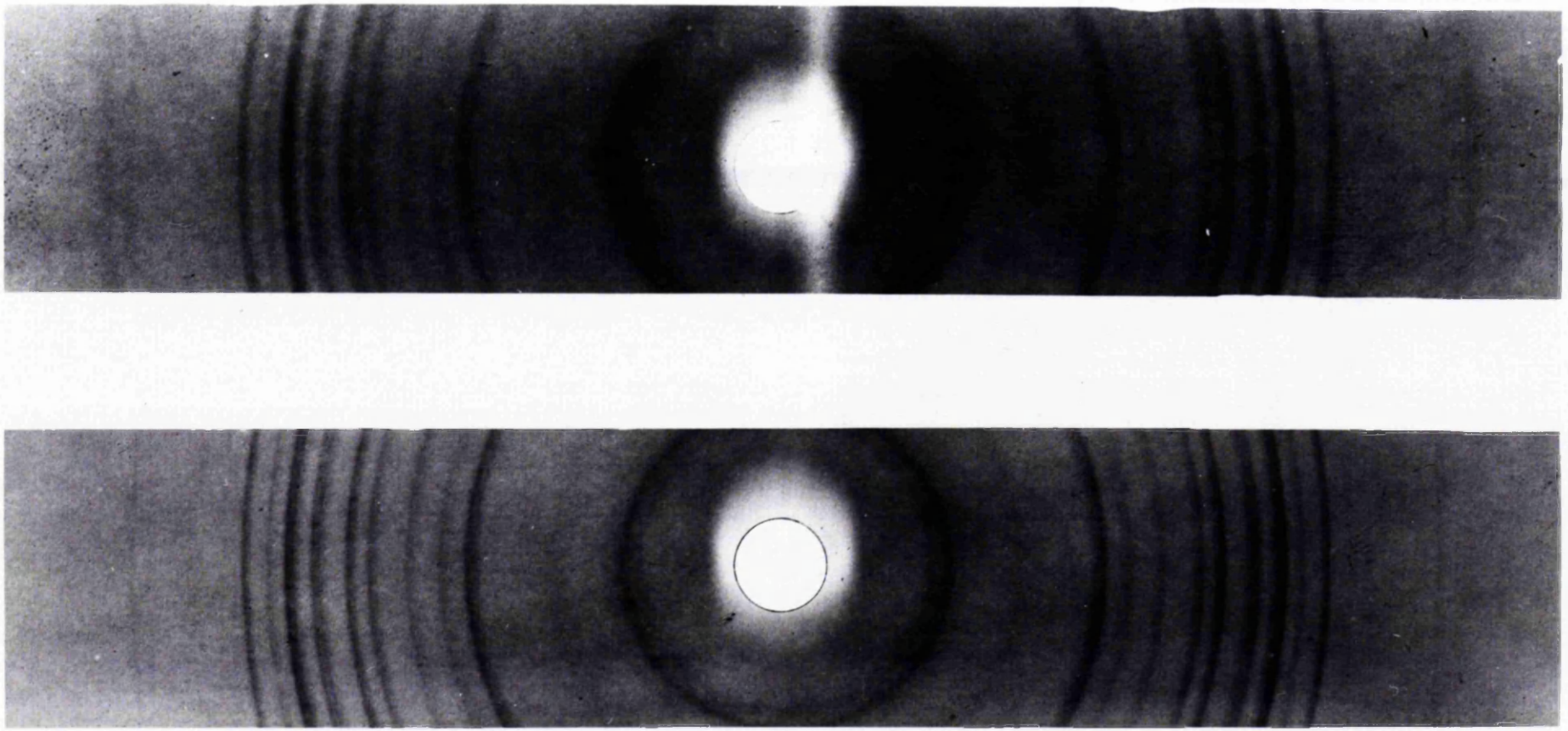

Fig 78

TABLE VIII Line indices for σ-phase

Fe-V		Fe-V-Zr	
θ	hkl	θ	hkl
28.4110	131	16.2563	011
29.7767	002	17.8837	111
31.8727	112,140	29.7078	002
32.9457	330	31.8027,	112,140
33.9437	022	32.8276	330
34.9316	122,240	33.8600	022
35.6845	141	34.8274	122,240
36.6900	331	35.5924	141
37.8905	222	36.5198	331
39.7864	050,132,340	37.7672	222
63.5974	070,352	39.6696	050,132,340
64.8510	170,550	42.5194	232
65.7359	143	43.1793	051,341
67.0566	333	63.3920	070,352
68.6698	270	64.5044	170,550
69.7729	171,243,551	65.5318	143
71.4312	262	66.8092	333
73.1520	452	68.4016	270
74.6252	271	69.4415	171,243,551
82.2863	004,362	71.3264	262
		72.9138	452
		74.1987	271
		81.8691	004,362

TABLE IX σ-phase Lattice parameters

Alloy	"a" parameter	standard errors	"c" parameter	standard errors	Method of calculation
FeV	8.9482_3	0.0011	4.6216_0	0.0008	Cohen
	8.9489_3	0.0011	4.6217_1	0.0009	Hess
	8.9490_8	0.0012	4.6218_7	0.0011	Hess & Lawn
FeVMn	8.9520_0	0.0016	4.6255_6	0.0014	Cohen
	8.9528_1	0.0014	4.6260_0	0.0015	Hess
	8.9528_5	0.0013	4.6233_9	0.0024	Hess & Lawn
FeVRe	8.9600_1	0.001	4.6259_3	0.0005	Cohen
	8.9609_2	0.0007	4.6258_3	0.0003	Hess
	8.9610_5	0.0008	4.6257_3	0.0002	Hess & Lawn
FeVTa	8.9807_4	0.002	4.6355_8	0.0006	Cohen
	8.9809_7	0.001	4.6360	0.0003	Hess
	8.9801_2	0.001	4.6361_5	0.0003	Hess & Lawn
FeVTi	8.9647_4	0.001	4.6278_9	0.0005	Cohen
	8.9647_9	0.001	4.6281_9	0.0002	Hess
	8.9639_6	0.0009	4.6282_7	0.0002	Hess & Lawn
FeVW	8.9553_2	0.0009	4.6242_1	0.0005	Cohen
	8.9550_6	0.0006	4.6236_6	0.0003	Hess
	8.9550_4	0.0008	4.6235_4	0.0001	Hess & Lawn
FeVZr	8.9634_1	0.0005	4.6255_6	0.0002	Cohen
	8.9634_6	0.0004	4.6254_6	0.0001	Hess
	8.9638_8	0.0005	4.6254_2	0.00006	Hess & Lawn

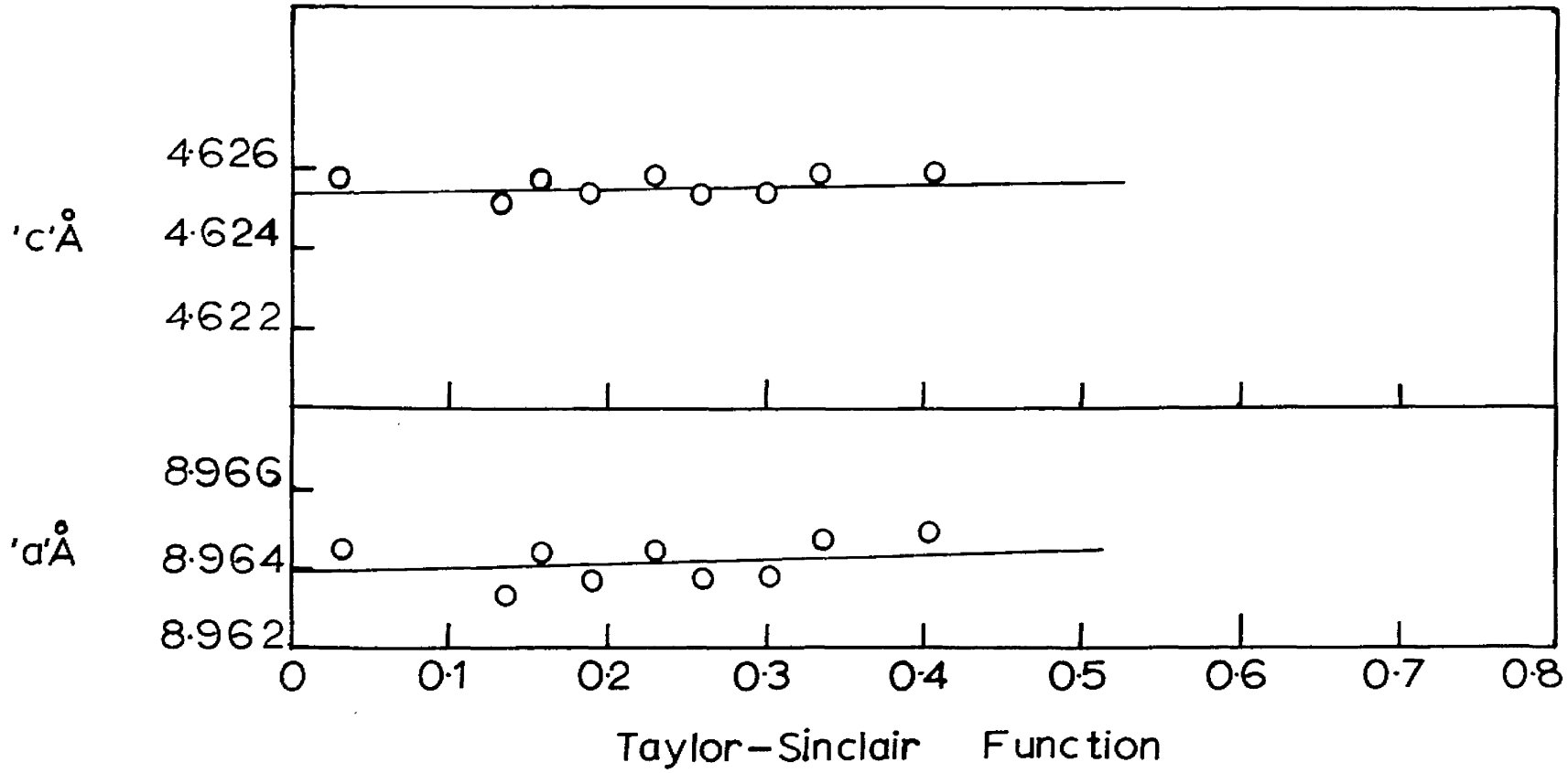
4·626
'c'Å
4·624
4·622
8·966
'a'Å
8·964
8·962
0
0·1
0·2
0·3
0·4
0·5
0·6
0·7
0·8
Taylor–Sinclair Function

Fig. 79

TABLE X

σ-phase Lattice parameters Fe-V-Zr

θ	hkl	"a" parameter	"c" parameter	Taylor-Sinclair Function
63.3920	352	8.9649_2	4.6259_6	0.4056_7
65.5318	143	8.9646_7	4.6258_2	0.3384_7
66.8092	333	8.9637_6	4.6253_6	0.3017_0
68.4016	270	8.9636_4	4.6252_9	0.2592_3
69.4415	171	8.9643_8	4.6256_8	0.2334_5
	551	8.9643_8	4.6256_8	0.2334_5
71.3264	262	8.9636_9	4.6253_2	0.1905_6
72.9138	452	8.9642_9	4.6256_3	0.1581_4
74.1987	271	8.9632_1	4.6250_7	0.1343_2
81.8681	004	8.9644_5	4.6257_1	0.0342_2

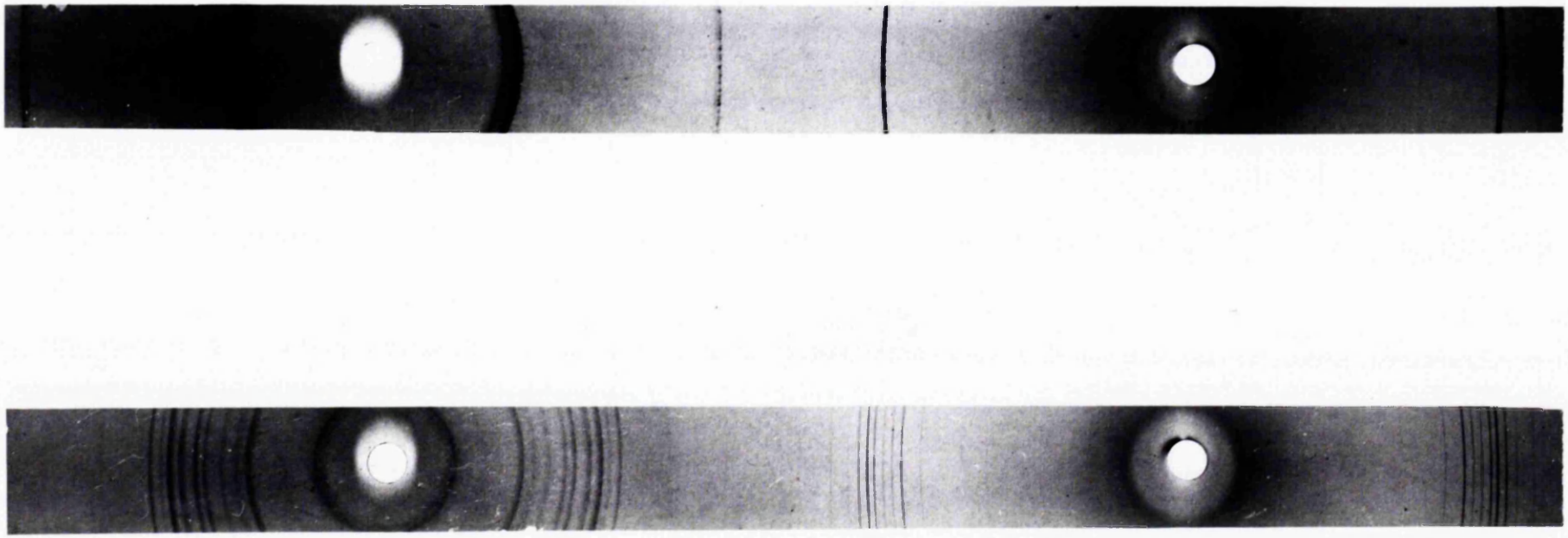

Fig 80

TABLE XI Lattice parameters of α-phase

Alloy	disordered	ordered
Fe-V	2.9145	2.8944
Fe-V-Mn	2.9150	-
Fe-V-Re	2.9238	2.9050
Fe-V-Ta	2.9298	-
Fe-V-Ti	2.9220	2.9021
Fe-V-W	2.9179	2.9022
Fe-V-Zr	2.9192	-

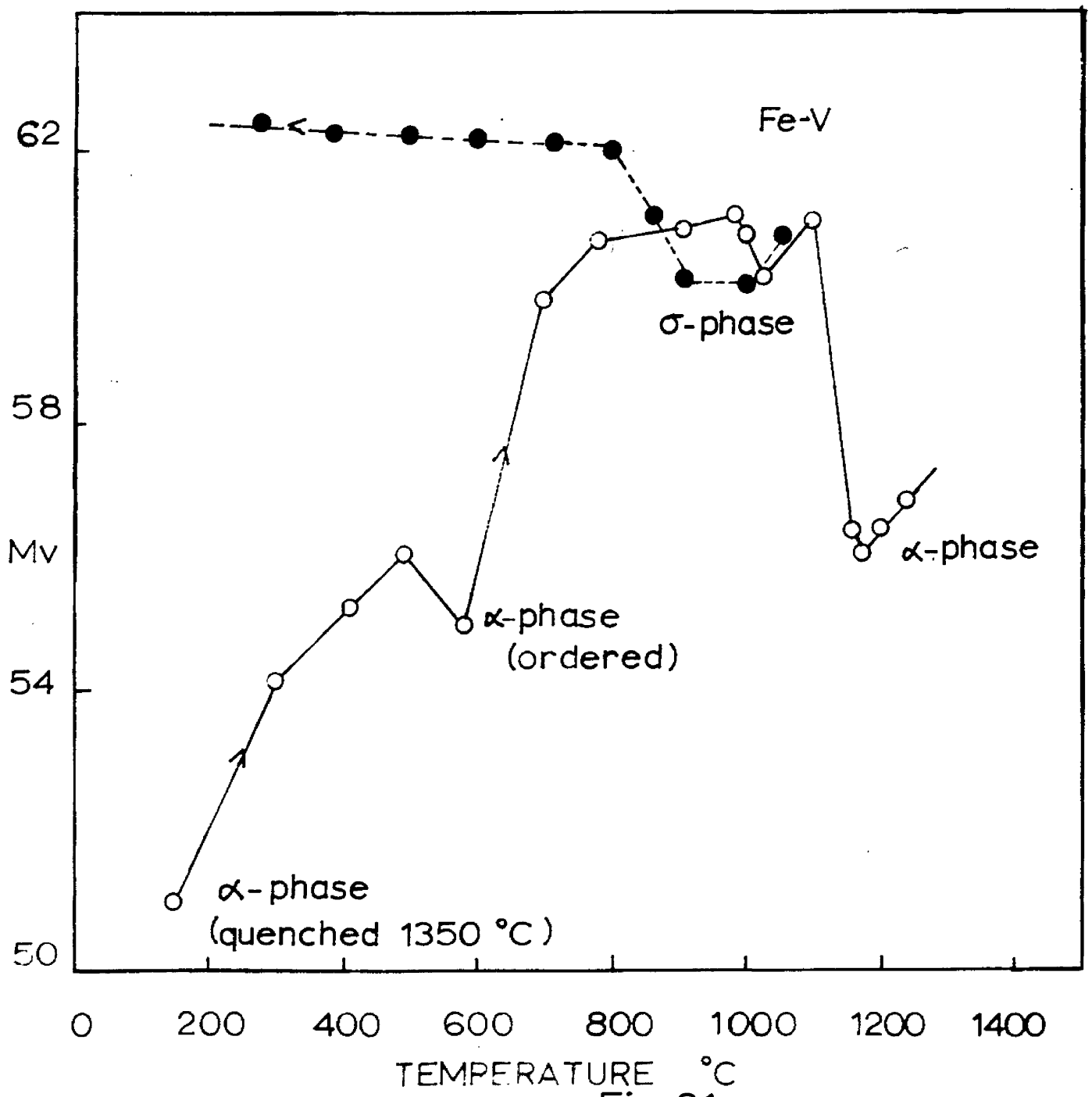
Fe-V
62
58
54
50
Mv
σ-phase
α-phase
α-phase
(ordered)
α-phase
(quenched 1350 °C)
0
200
400
600
800
1000
1200
1400
TEMPERATURE °C

Fig. 81

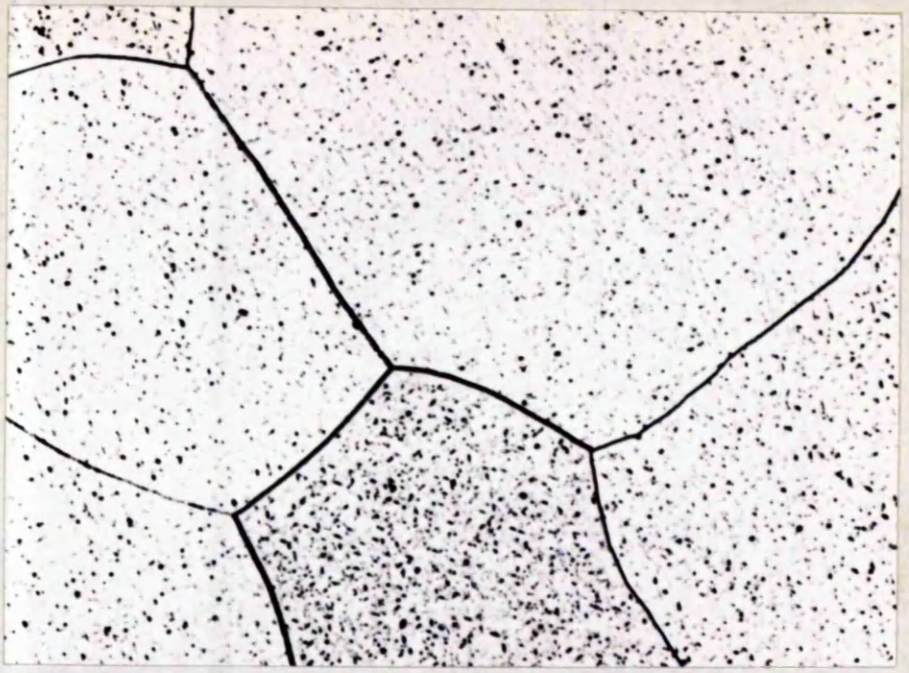

Plate 1. Fe-V, quenched from 1350°C. x 160.

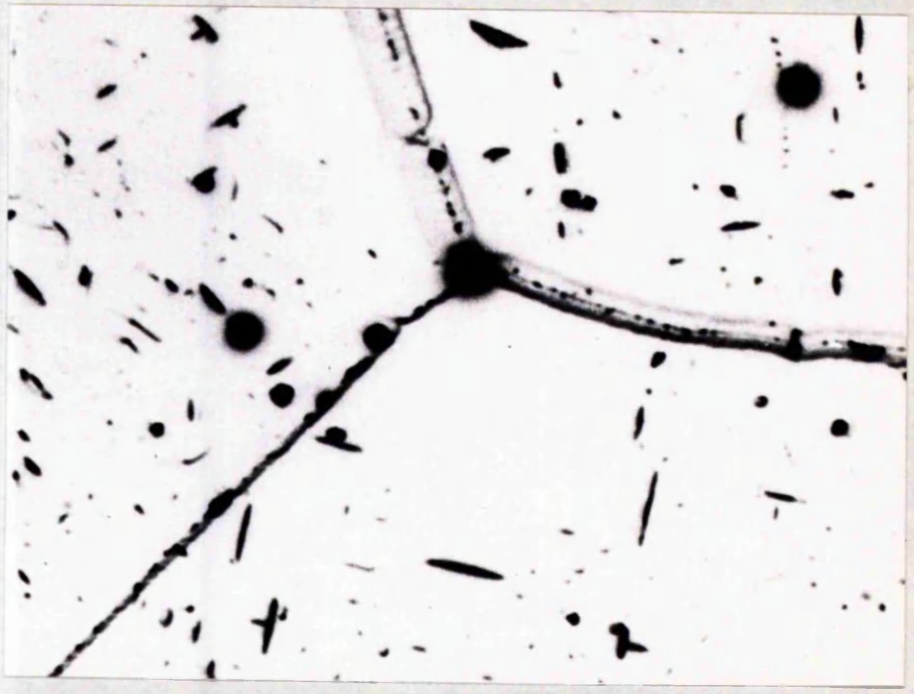

Plate 2. Fe-V, quenched from 1350°C. x 400.

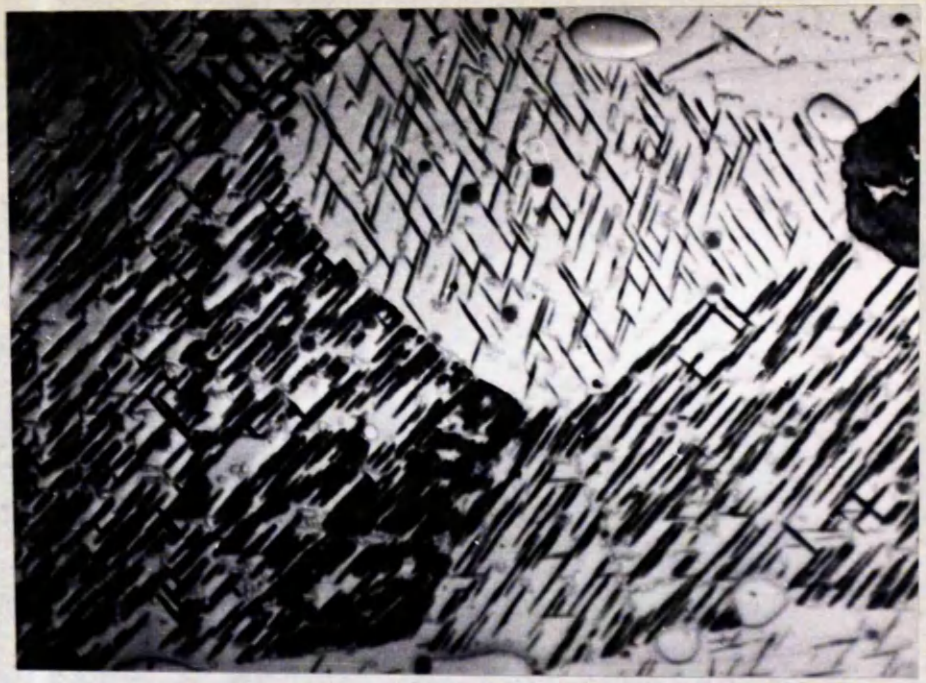

Plate 3. Fe-V, slow quench from 1250°C. x 160.

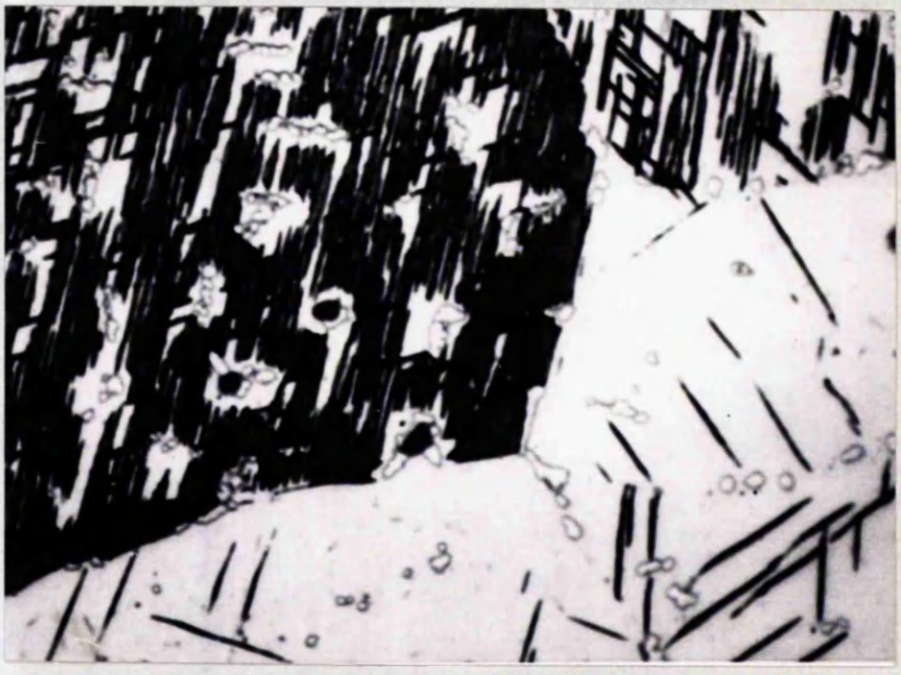

Plate 4. Fe-V, slow quench from 1250°C. x 400.

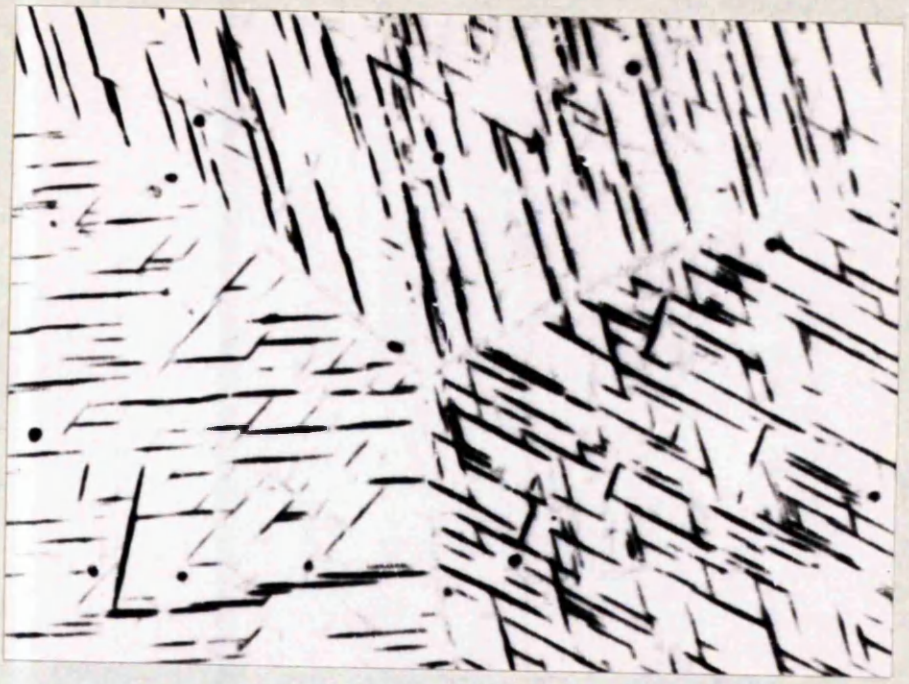

Plate 5. Fe-V, Slow quench from 1250°C. x 400.

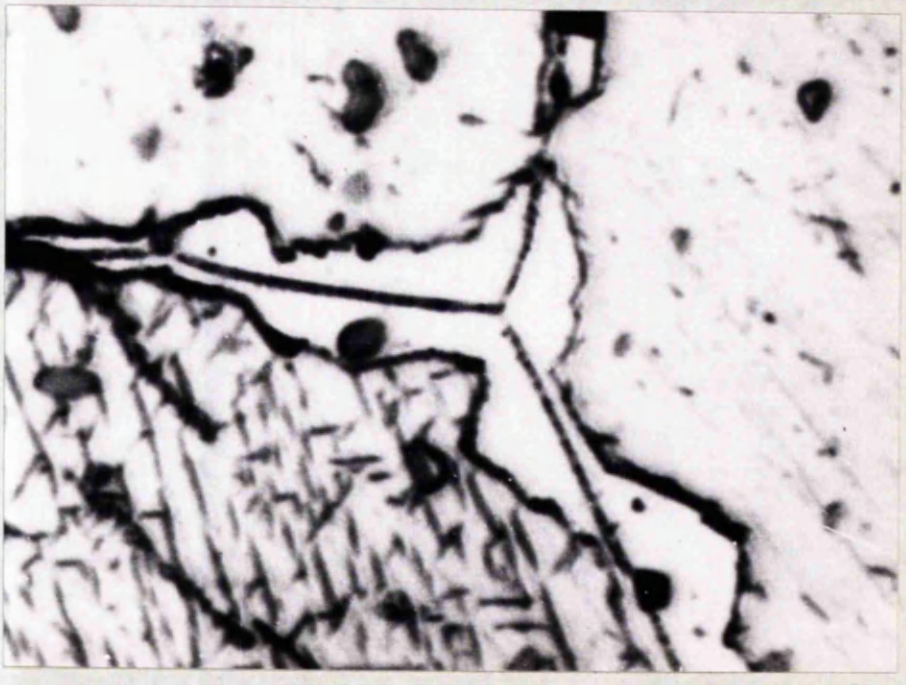

Plate 6. Fe-V, slow quench from 1250°C, and partially transformed at 780°C. x 400.

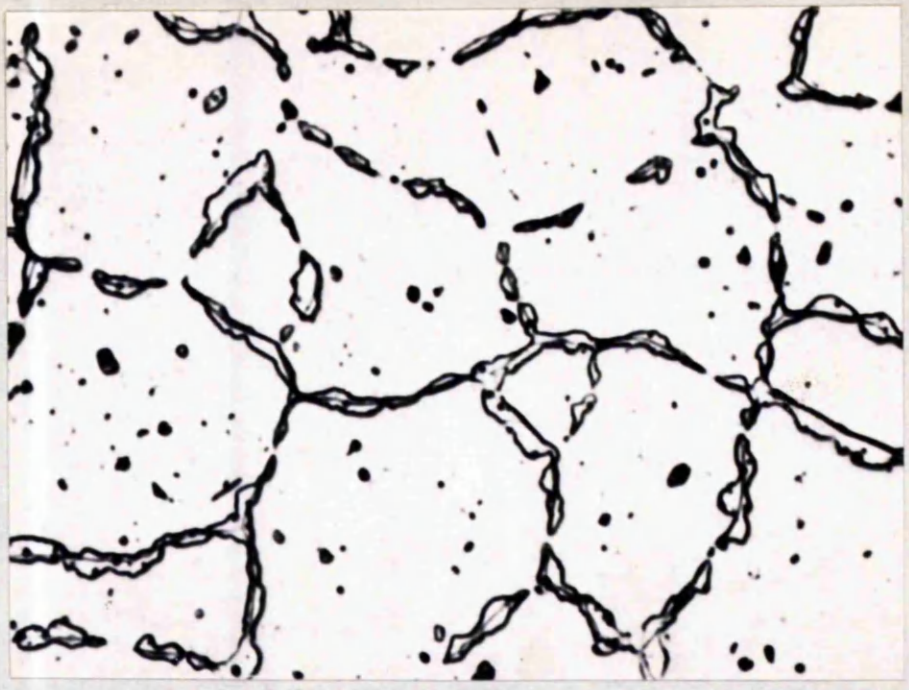

Plate 7. Fe-V-Mn, quenched from 1350°C, and partially transformed at 760°C. x 160.

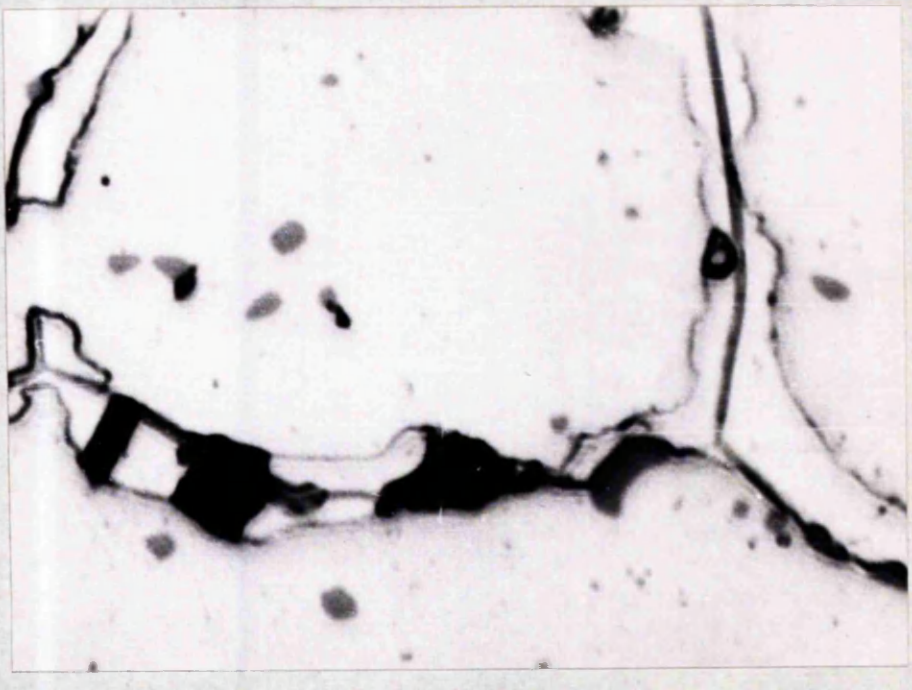

Plate 8. Fe-V-Mn, quenched from 1350°C, and partially transformed at 760°C. x 400.

Plate 9. Fe-V-W, quenched from 1350°C, and partially transformed at 760°C. x 160.

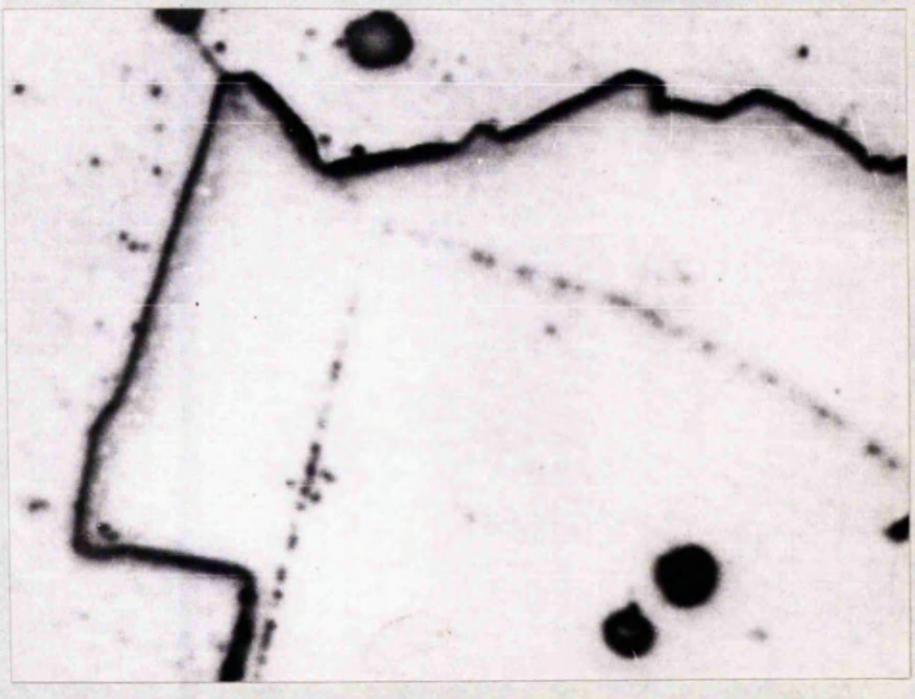

Plate 10. Fe-V-W, quenched from 1350°C, and partially transformed at 760°C. x 400.

Plate 11. Fe-V-W, quenched from 1350°C, and partially transformed at 760°C. x 400.

Plate 12. Fe-V-W, quenched from 1350°C and partially transformed at 760°C. x 400.

Plate 13. Fe-V, quenched from 1350°C and isothermally transformed at 850°C. x 25.

Plate 14. Fe-V, quenched from 1350°C, and isothermally transformed at 850°C. x 160.

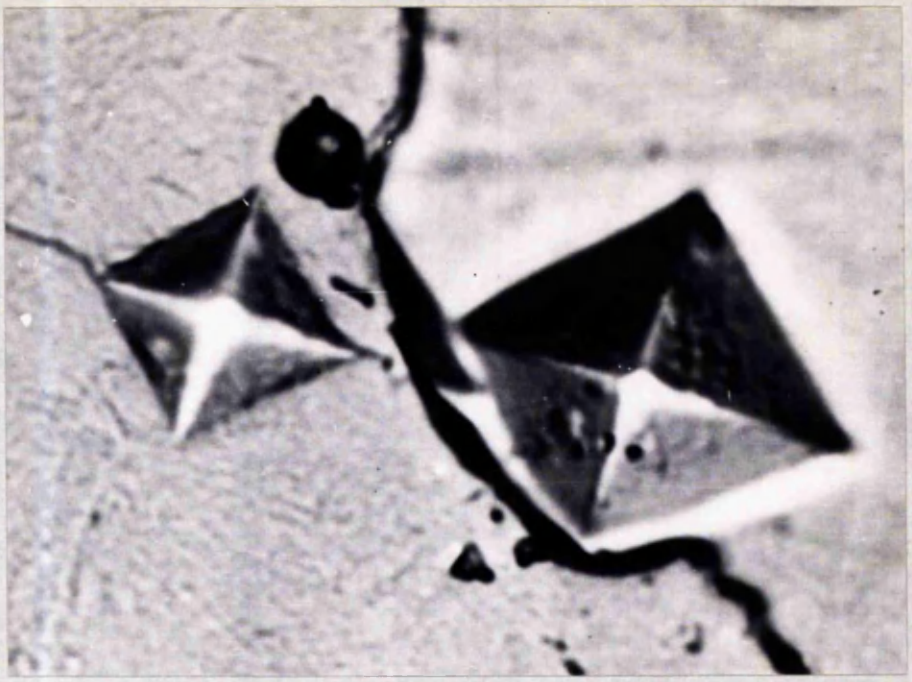

Plate 15. Fe-V-W, quenched from 1350°C and partially transformed at 760°C. x 640.

CHAPTER VI

DISCUSSION OF RESULTS

Isothermal Transformation Studies

The change in electrical resistivity during the $\alpha \rightarrow \sigma$ transformation, under isothermal conditions was used to determine the rate of formation of the sigma phase. By assuming that the electrical resistivity is a linear function of the decomposed fraction, the following equation may be applied

$$f(y) = \% \text{ decomposition} = \frac{V_t - V_o}{V_f - V_o}$$

where V_t, V_o and V_f are the potentials across the specimen at time t, after quenching and attaining the reaction temperature, and at the end of the transformation respectively. They are proportional to the specimen resistance, providing the measuring current remains constant.

Graphs of f(y) against log time for the binary and ternary alloys are shown in Appendix III. They exhibit a general sigmoidal form. This in itself is not thought to be significant of any mode of reaction, for it can be shown that any curve in which a function say x varies by equal increments from 0 at t = 0, will be sigmoidal in shape, when plotted against the logarithm of time.

The isothermal resistivity results are tabulated and summarised in the form of TTT curves. As discussed in Chapter II the TTT curves are expected to exhibit a C-shape. Values for the activation energies have been calculated from the linear portion of the reciprocal rate curves.

Fe-V

The results from the isothermal resistivity experiments are listed in Table (I). The beginning and end of the reaction is taken as 5 and 95% of the transformation. The fraction transformed against log time curves, which are characterised by a sigmoidal shape, are shown in Appendix III. In the lower temperature range the incubation periods decrease progressively from 1320 secs. at 731°C to 14 secs. at 798°C, and in the upper range from 185 secs. at 1113°C to 25 secs. at 1098°C. At temperatures in the range 800°C to 1090°C the reaction is too fast to measure with the present experimental arrangement. In the TTT diagram (Fig. (63), there is evidence of a cusp at about 780°C which might be attributed to another reaction mechanism.

Transformations at the lower temperatures showed a decrease in resistance prior to the increase in resistance caused by sigma phase formation. This decrease is attributed to the formation of an ordered CsCl structure noted in the X-ray diffraction studies. At higher temperatures and faster

reactions no such decrease in resistance was noted, as the effect is probably masked by the rapidly increasing resistance of the specimen heating up. If at these higher temperatures an ordered phase is still a prerequisite for sigma formation then the superlattice is capable of forming very quickly possibly by atomic rearrangement rather than by diffusion. However if the α-phase does not order before the σ-phase forms at these higher temperatures then the cusp in the TTT curve could be associated with a change of reaction in the manner noted by Pomey in the iron-chromium system, discussed in Chapter I (p.38).

The possible transformations are

$$\alpha_{\text{disordered}} \rightarrow \alpha_{\text{ordered}} \rightarrow \sigma$$

$$\alpha_{\text{disordered}} \rightarrow \alpha_{\text{partially ordered}} \rightarrow \sigma$$

$$\alpha_{\text{disordered}} \rightarrow \sigma$$

It was noted in Chapter II that a specimen cooled quickly might show two arrest points if there were two reaction mechanisms operating. The fastest cooling rate achieved with the present apparatus was 5°C/min. Fig. (77). This rate of cooling only indicates the complete transformation from $\alpha \rightarrow \sigma$ by one mechanism between 1130°C and 110C C. However a series of experiments are now in progress in which α-phase powder specimens are quenched after

very short anneals at temperatures above the cusp. If no order lines are detected prior to sigma formation then this will provide direct evidence in support of the proposed reactions.

A value of 82 Kcal/mole for the activation energy of the reaction has been derived from the reciprocal rate curve Fig. (64). This high value indicates that growth is thermally activated, a characteristic usually associated with the nucleation- and -growth type of transformation.

Metallography

Alloys quenched from 1350°C into iced water or oil show a single α-phase structure. Plates (1,2) show a specimen which has been quenched from 1350°C into iced water after annealing at 780°C in air for several hours. Within the α-phase grains there is a fine precipitate which can only be resolved at high magnification. When this specimen was

transformed to σ-phase some of the precipitate remained. The orientation between the needle-like precipitate within each grain is always 90° but the directions change at the grain boundaries. Typical structures are shown in Plates (13,14). It is probable that the needles are a nitride phase. As already mentioned no structural details of the σ-phase are revealed by the etching reagents used. However, the orientation of the nitride needles may be taken as a guide to the positions of the grain boundaries.

Alloys quenched from 1250°C show a distinct Widmanstätten precipitate. Plates (3,4,5) show this type of structure in a specimen slowly quenched from 1250°C. Most of the precipitate forms in one direction though some forms at approximately 90 and 45° to this direction. The orientation differs from grain to grain, Plate (5).

The concentration of precipitate varies from grain to grain over the entire specimen with no preferential positions. In some grains there were short plates forming a straight line of cross hatched precipitate across the grain. This is probably due to precipitation at low angle sub-boundaries. Small areas of σ-phase can also be seen in Plate (4). The region around the sigma is depleted of precipitate. It is also evident that the σ-phase is growing on particles which are probably of the nitride phase. The hardness of the grains

containing large amounts of precipitatewas indistinguishable from that of areas with very little precipitate. A powder specimen, contained in a small mullite tube was quenched from 1250°C into iced water. The resulting powder diffraction photograph showed a set of intense lines of indices (110) (200) (211) and also a set of less intense lines of a smaller bcc cell. Order lines at (100) and (111) were also present. Powder specimens quenched from 1350°C show only one set of lines corresponding to a single bcc structure.

Two possible explanations for the precipitate are proposed. Firstly the separated lines might be due to a distorted bcc structure, brought about by ordering to produce a tetragonal or orthorhombic structure during the quench. By considering how the planes of indices (110) (200) and (211) in a bcc cell would be affected by the formation of either of these structures, it can be shown that the lines (200) and (211) on the powder photograph would split into two lines for a tetragonal and three lines for an orthorhombic structure. The line (110) would split into two for each structure. This suggests that the precipitate would have a tetragonal structure. However an X-ray diffraction study of a single crystal would be necessary to confirm this proposal.

A second explanation might be that two bcc solid solutions exist in the iron-vanadium system as observed in

the iron-chromium system,Fig. (30). In the specimens investigated a phase with a smaller cell has precipitated which suggests that it is iron rich and is depleted of the larger vanadium atoms. If this is so the Widmanstätten pattern of plate-like particles could be the ordered phase.

The relative stability of a superlattice increases with increasing difference between the atomic diameter of the solvent and solute. The greater the lattice distortion the greater will be the tendency to relieve the strain by an atomic rearrangement. Consequently superlattice formation is not observed frequently since if the size factors are unfavourable the solid solution will never contain sufficient of the solute to form a superlattice. On the other hand if the size factors are too favourable the solute and solvent atoms may interchange so freely that the lattice distortion may be so small that a regular arrangement is scarcely more stable than a random structure. When the FeCr and FeV alloys are compared on this basis the chromium atom exhibits a smaller size than the vanadium atom and consequently there is a greater tendency to form a superlattice in FeV since the lattice strains are greater. It is possible that this is the reason why iron-chromium sigma formation is so sluggish compared with the iron-vanadium sigma phase since an ordered structure is a prerequisite for sigma formation.

A specimen quenched from 1250°C showing the Widmanstätten structure was partially transformed to sigma in the low temperature range, Plate (6). The precipitate took no part in the sigma growth which was mainly from grain boundaries and only occasionally from the centre of grains. When the sigma field grew across a grain containing precipitate the grain became devoid of any Widmanstätten precipitate.

In the high temperature range investigated by resistance methods no partially reacted samples were obtained for metallographic studies. This is due to the practical difficulties of quenching a partially reacted sample in a short reaction time and a narrow temperature range. However specimens were partially transformed in the low temperature range, Plate (7,9,10). The indications are that nucleation is favoured at grain boundaries and only occasionally within grains. Growth of the sigma phase is accompanied by cracks appearing in the newly formed phase. A typical example of this is seen in Plates (8,12) where the thick black line is a crack which traverses the sigma phase and terminates at the α/σ boundary.

Plate (15) shows the alpha and sigma phase fields distinguished by means of two microhardness impressions. The marked difference in the sizes of the two impressions

indicates that the sigma phase is much harder than the alpha phase. A fine crack can be seen at the edge of the smaller impression demonstrating the brittle nature of the sigma phase.

An inspection of the boundaries between the sigma and parent α-phase revealed that they consisted of irregular edges made up of straight sections, Plates (9,10,11). The irregular interface is presumably due to growth being halted at certain points by some kind of obstacle.

Mode of Growth

The atomic mechanism for the α→σ transformation proposed by Kitchingman (34) implies that growth is intrinsically a slow process because of the complexity of atom movements involved and necessitates an extensive reshuffling of atoms to accomplish the structural change. Growth involves the migration of an interface by means of the thermally activated movement of single atoms through distances comparable with the interplanar spacing, coupled with a considerable movement of atoms within alternate planes.

Ternary Additions

The details of the elements added to the equiatomic iron-vanadium alloy are summarised in the following table,

Element	Goldschmidt Atomic radius (CN 12)	Atom Type
Fe	1.27	B
V	1.36	A
Mn	1.31	B
Re	1.37	A or B
Ta	1.46	A
Ti	1.45	-
W	1.41	A
Zr	1.60	-

Following the nomenclature of Frank and Kasper (43) sites in the bcc structure are CN 14, and sites in the sigma phase are CN 12, CN 14 and CN 15. It is recalled that in the sigma phase the iron atoms occupy CN 12 sites and the larger vanadium atoms CN 15 whilst the CN 14 sites are mixed. The values for the Goldschmidt radii are given for CN 12 but the effective size may alter for sites of different coordination. With the exception of manganese all the ternary additions have a larger CN 12 radius than vanadium. Each ternary alloy contains approximately 3.3 At.% of the ternary addition which represents one atom per unit cell in the σ-phase, the remaining 29 sites being shared equally between iron and vanadium. The lattice parameters of both the alpha and sigma phases Tables (XI),(IX) have been measured to indicate whether the ternary addition has been taken into solution. The variation of lattice parameters indicates that this is so.

In the following discussion the additions have been considered under the categories:- (i) A-type elements (Ta,W) (ii) B-type elements (Mn). (iii) A/B type elements (Re) (iv) Non-sigma forming elements (Ti,Zr).

A-type elements (Ta,W)

Fe-V-Ta: Tantalum has the most pronounced effect on the transformation of all the additions, Fig. (65). The incubation periods in the upper and lower temperature regions are longer than those for the binary alloy but the reactions in the intermediate temperature range are still too fast to be measured with the present apparatus. There are two cusps in the TTT curve and these could be attributed to the reaction mechanisms already described for the iron-vanadium alloy. The activation energy for the reaction was found to be 79.4 Kcal/mole. A metallographic investigation of partially transformed specimens showed that they have the same characteristics as those observed in the binary alloy and no distinctions could be drawn between structures formed above and below the cusps.

During the preparation of the X-ray powder specimens it was noted that the Fe-V-Ta sigma alloy was much more difficult to grind than the binary alloy. The powder diffraction photographs of Fe-V-Ta sigma phase taken after the grinding process with no prior annealing showed broadened lines. After annealing

at 500°C for 24 hrs. broadened lines were still observed. However annealing at 970°C for 10 hrs. sharpened the lines such that no broadening was evident. Fig. (78) shows the high angle lines of the deformed and annealed specimens.

Line broadening may be attributed to the following,

(i) Particle size, and faulting

(ii) Strain

The effects due to strain and particle size in the bcc and fcc structures can be resolved by a detailed analysis of the line profiles obtained from X-ray diffractometer traces. In the case of the sigma phase structure no analysis of the broadened line profiles has been carried out and it is only possible to discuss whether the line broadening observed in Fe-V-Ta could be due to particle size resulting from sequence faults formed during sigma growth, or lattice strain.

It is recalled that Kitchingman (34) has discussed the effects of deformation in the sigma phase in terms of Kronberg's model for slip in β-uranium. To apply this model to alloy sigma phases it is necessary to take into account the coordination numbers associated with the particular positions in the sigma phase. Kronberg's model involves only the movement of atoms within the hexagonal B and C layers of the sigma phase structure. These are rearranged as shown in

Figs. (49,50) so that across the slipped region the kagomé-tile structure changes direction. Kitchingman has shown that this involves an atom in a CN 12 site replacing one in CN 15, Fig. (51). In the case of β-uranium the structure is ductile since a CN 12 uranium atom is replacing a CN 15 uranium atom. In alloy sigma phases such a replacement is more difficult. For example, in FeCr it involves substituting an Fe atom of CN 12 for a Cr atom of CN 15. Whilst Fe exhibits CN 12 and CN 14 it does not exhibit CN 15, similarly Cr only exhibits CN 15 and CN 14. Uranium, on the other hand, shows CN 15, CN 14 and CN 12. Kitchingman has proposed that each atom of different CN exhibits a different electronic structure associated with the size of the coordination position. Consequently two factors which are complementary or associated must be taken into consideration when deciding whether Fe CN 12 can move into the position of Cr CN 15.

(i) The atom size

(ii) The electronic structure.

If this is true, considerations of whether slip and hence deformation can take place must not only take into account the relative sizes of the replaced atoms but also how the electronic structure is compatible with the CN of the position.

In the case of deformation of FeV by grinding the alloy

is found to be extremely brittle and the X-ray powder diffraction lines show no broadening. The lines before and after annealing being equally sharp. In the Fe-V-Ta alloy the lines were broadened but on annealing they became sharp. It is evident that deformation has occurred and has subsequently been annealed out.

Tantalum is an A-type atom, that is, one would normally expect them to substitute the A-type vanadium atoms in the sigma structure, on the basis of size and similar atom type. If deformation takes place, it is expected, according to the model described above, that in the slipped areas some Ta atoms must move into sites formerly occupied by Fe atoms. The change A→B position, CN 15 → CN 12, must occur. Two factors operate against this. Firstly, the size of the atoms, since the Goldschmidt radius of iron is 1.27 and tantalum 1.46. Secondly the electronic structure, since iron is a B-type and tantalum is an A-type atom. Since both A and B type atoms show CN 14 and an electronic structure associated with this CN, it is possible, therefore, that the tantalum atom is tolerated in a CN 12 site with an electronic structure approximating to a CN 14 position. In doing so it would be operating against the deformation and it would be expected that this energetically unfavourable arrangement would return to the original ordered positions on annealing. Thus it is

concluded that tantalum prefers to behave as an A-type element of CN 15 or 14. Furthermore it is somewhat less "A like" than vanadium which will not enter a CN 12 site and consequently not act in any deformation.

Another explanation might be that tantalum goes into the CN 14 E positions of the sigma structure. In iron-vanadium the hexagons might be held from rotation by the bonding of the chains of E atoms. When tantalum enters the E sites the bonding might change and allow the rotation of hexagons around them. In the present study the amount of tantalum added is insufficient to detect whether any of these atoms are in the E sites.

Fe-V-W: The effect of tungsten on the transformation kinetics is similar to that already discussed due to tantalum. In the low temperature range the TTT curve (Fig. 67) has been displaced away from the temperature axis. A cusp is also evident though metallographic studies indicate no change in the morphology of the sigma phase from that observed in iron-vanadium. The TTT curve has been markedly raised in the high temperature region.

As in the case of Fe-V-Ta the Fe-V-W sigma phase is much tougher than the pure binary phase. X-ray powder diffraction patterns showed broadened lines which on subsequent annealing

at 970°C for 10 hrs. sharpened. Since the atomic radii of the A-type tungsten is greater than vanadium the same reasoning may be applied to explain the deformation as already described for tantalum. Either the tungsten moves into a CN 12 site with a CN 14 electronic structure or the tungsten moves into the central E position E 14 and disrupts the bonding enabling the hexagons to rotate.

B-type element (Mn)

Fe-V-Mn: The effect of manganese on the transformation kinetics may be discussed with reference to the TTT diagram Fig. (69). Manganese moves the TTT curve away from the temperature axis. Incubation periods and reaction times are consequently lower at the extremes of the curves compared with Fe-V. In the intermediate temperature range 800 - 1090°C the reaction is indistinguishable from the pure binary alloy. A cusp in the TTT curve is evident but not pronounced. It occurs at a slightly higher temperature than that in the iron-vanadium alloy.

The metallographic structures of partially transformed specimens were no different from those observed in the binary alloy. Specimens quenched from 1350°C showed a single α-phase structure and those quenched from 1250°C a Widmanstätten precipitate. The σ-phase was observed to grow mainly from the

grain boundaries and rarely from the centre of grains. A value for the activation energy of 87.7 Kcals/mole has been calculated from the reciprocal rate curve Fig. (70).

The lattice parameters of the bcc α-phase and σ-phase are shown in Tables (IX),(XI) respectively. As in the binary alloy specimens quenched from 1350°C and annealed at 600°C for 1 hr. showed superlattice lines. Those quenched from 1250°C showed two sets of lines corresponding to either two bcc structures or a distortion to a tetragonal structure.

Powder, prepared from the binary alloy by grinding in a mortar and pestel for X-ray diffraction studies showed sharp lines with no prior annealing. Powder specimens of the ternary alloy Fe-V-Mn similarly prepared showed line broadening. After annealing at 970°C for 2 days the lines remained broadened. The line broadening is possibly due to lattice strain associated with the addition of manganese.

The three positions in the σ-phase that manganese can occupy are CN 12, CN 14 and CN 15. To occupy the CN 15 position the manganese must replace the vanadium atoms. Since the manganese atom is only slightly smaller than the vanadium atom this replacement could be accommodated with no lattice strain. This would mean that a B-type element would be replacing an A-type, suggesting that manganese can exhibit

either A or B characteristics. However only technetium and rhenium have been found to act as either A or B elements in σ-phases.

If the B-type manganese atom replaces a B-type iron atom it would probably occupy CN 12 sites and possibly CN 14 sites. That the lines in the powder diffraction photograph remain broadened after extensive annealing suggests that the manganese has occupied a small CN 12 site, but in doing so has caused a certain amount of lattice strain. The change in lattice parameters is small since only one atom per unit cell is altered and no definite conclusions can be made to substantiate the above suggestion. Furthermore no ordering schemes for ternary alloys have been proposed which establish whether a larger atom of a certain species (A or B) occupies a site in the sigma structure by size factor alone, or whether there is some rearrangement in the electronic structure such that A atoms are always replaced by A atoms and B atoms by B atoms.

A or B-type elements (Re)

Fe-V-Re: The TTT diagram and reciprocal rate curve are shown in Figs. (71),(72) respectively. The effect of rhenium on the transformation is to move the TTT curve away slightly from the temperature axis. Incubation periods are longer in the upper and lower temperature ranges but in the intermediate

temperature range the reaction is too fast to follow with the present apparatus and no distinction could be drawn between the binary and ternary alloys. The activation energy was calculated as 86.8 Kcal/mode. The metallographic structures were identical with those of the binary alloys.

Rhenium, which has been shown to act as either an A or B element in sigma forming binary alloys, has a larger atomic radius than vanadium. It is expected, therefore, that the rhenium atoms would occupy the larger CN 15 sites and consequently be accommodated with no lattice strain. X-ray diffraction photographs of a powder ground in a mortar and pestel showed no line broadening.

Non-sigma forming elements (Zr,Ti)

FeVZr: None of the sigma forming binary alloys contain zirconium. When added to the binary alloy zirconium slightly displaces the TTT curve, Fig. (75), from the temperature axis. The curve in the low temperature region exhibits a cusp which is much more marked than in the iron-vanadium binary or any of the other ternary alloys investigated. The activation energy calculated from the gradient of the reciprocal rate curve Fig. (76) was found to be 76.5 Kcal/mole.

The metallographic structures were as found in the iron-vanadium alloy and there was no apparent difference

between those specimens partially transformed above the cusp and those below. The ordered structures found in both the metallographic and X-ray studies of iron-vanadium specimens quenched from 1250°C were also observed in the Fe-V-Zr alloy.

The lattice parameter measurements of the alpha and sigma phases are shown in Tables (XI) and (IX) respectively. If the size factor is the only criterion for site occupation, a possibility since zirconium is not classified as either an A or B-type atom, the most likely sites to be occupied by zirconium are the largest, the CN 15 sites, occupied by a vanadium atom in the pure binary alloy. If the zirconium atom was accommodated in a small CN 12 site replacing an iron atom the lattice would be strained. Powder specimens prepared by grinding, showed no line broadening indicating that there is no lattice strain as noted in the manganese ternary alloys.

Fe-V-Ti: No binary alloy containing titanium as one of the components has been found to form a σ-phase. The effect of titanium on the TTT curve, Fig. (73), cannot be readily ascertained since only the lower temperature range has been investigated. Incubation periods are longer than those measured for iron-vanadium at the same temperature, which is reflected in the position of the TTT curve in relation to the axes. The activation energy was found to be 88 Kcal/mole.

A cusp is observed in the low temperature region though it is not so well defined as that caused by the zirconium addition. As in the Fe-V-Zr alloy no different metallographic structures were observed in partially transformed specimens in the low temperature region. No partially transformed specimens were obtained in the high temperature region due to the experimental difficulties.

The lattice parameters of the alpha and sigma phases are shown in Tables (XI) and (IX) respectively. The location of the titanium atoms in the sigma structure may be discussed in a manner similar to that applied to the zironcium addition. The titanium atoms are considered to occupy the CN 15 sites which are the largest in the sigma structure. As in Fe-V-Zr no line broadening was observed in the Debye-Scherrer powder photographs even after extensive grinding in a mortar and pestel. It was also noted that the Fe-V-Zr and Fe-V-Ti alloy were just as friable as the binary alloy.

The indications are that size factor alone governs the sites occupied by non-sigma forming elements in the sigma structure.

Resistance-temperature studies

Fig. (81) shows the change in resistivity of the pure iron-vanadium alloy with temperature. The open circles are

values measured during heating up and filled circles those measured on cooling.

The resistivity of a metal may be expressed by $\rho = \rho_0 + \rho_T$ where ρ_0 is due to the variation of the periodic field in which the electrons move, and ρ_T is the resistivity due to thermal vibration of the atoms about the lattice sites. In general ρ_0 is independent of temperature whilst ρ_T is strongly dependent on temperature and in the case of many metals is a linear function. If ρ_0 were constant, then a linear relationship should exist between resistance and temperature.

In the case of the disordered α-phase a linear relationship exists between room temperature and about 300°C. At 300°C the slope changes, indicating that the specimen resistance is less than the value obtained by extrapolating the section of the graph attributed to the disordered α-phase. At about 600°C there is a sharp decrease in resistance which is probably due to the formation of the ordered α-phase noted in the X-ray studies. From 700 to 990°C the resistance shows veyr little change with temperature. This is followed by a drop in resistance at approximately 1000°C and a final increase in resistance prior to the formation of the α-phase.

On cooling, shown by the filled circles, the σ-phase does not follow the same path, although it exhibits the same

shape of curve. Between 900°C and 800°C there is a sharp increase in resistance indicating a negative coefficient of resistance. This is followed by a more gradual increase in resistance between 800°C and 300°C.

As mentioned above a linear relationship is expected between resistance and temperature. From the metallographic and X-ray studies it is apparent that the σ-phase transforms to an ordered α-phase at approximately 1200°C and this phase disorders at temperatures in the region of 1350°C. Consequently values of resistance of the high temperature ordered α-phase are much less than the extrapolated values of the low temperature disordered phase.

That the σ-phase has two different negative coefficients of resistance suggests that it may exhibit two forms which are possibly associated with an atomic rearrangement.

Conclusion

The present study has shown that the sigma phase forms more quickly in the iron-vanadium than in the iron-chromium system. From the cusps in the TTT curves it has been suggested that two reaction mechanisms and possibly a third might be involved in the formation of the sigma phase. At temperatures below the cusps it has been shown by both X-ray diffraction and resistivity studies that the alpha phase orders prior to

the formation of the sigma phase. At temperatures above the cusp no ordering has been observed though it has been suggested that the change in resistance due to ordering might be masked by the rapid increase in resistance during the heating up period. If it is assumed that no superlattice is formed before sigma formation at temperatures above the cusps then the following reactions might occur,

$$\underset{\text{(disordered)}}{\alpha} \rightarrow \underset{\text{(ordered)}}{\alpha} \rightarrow \sigma$$

$$\underset{\text{(disordered)}}{\alpha} \rightarrow \underset{\text{(partially ordered)}}{\alpha} \rightarrow \sigma$$

$$\underset{\text{(disordered)}}{\alpha} \rightarrow \sigma$$

The metallographic investigation showed no difference between structures formed above and below the cusp. The sigma phase nucleates at grain boundaries and only occasionally within the grains. The morphology of the sigma phase in partially reacted samples has been described as massive and the α/σ boundary is irregular but with straight interfaces. It has also been observed that the growth of the sigma phase is not impeded by grain boundaries. The microprobe analysis of Pomey (78) has shown that there is no change in composition of the parent and product phases in iron-chromium alloys which suggest that there is no long range diffusion during the formation of the sigma phase. Consequently the reaction is

described as of the massive type with short range diffusion (SRD).

The effect of the additions to the equiatomic iron-vanadium alloy has been shown to be only slight. All the TTT curves show a cusp in the low temperature region. The TTT curves are displaced away from the axes but so slightly that it is not possible to measure the reaction in the intermediate temperature range 800-1090°C. The morphology of partially transformed specimens has been found to be the same as those observed in the binary alloy.

The line broadening observed in the X-ray diffraction studies of some of the σ-phase ternary alloys has been discussed in terms of the sites occupied by the additions. It has been proposed that elements of the same type can replace each other and only deformation will alter this arrangement which will return on annealing. In the case of non-sigma forming elements it has been suggested that the atomic size is the overiding factor and the atoms fit into sites most suited to their size.

The temperature coefficient of both the alpha and sigma phases in an equiatomic iron-vanadium has been investigated. It has been observed that the sigma phase has two different values for the temperature coefficient of resistance, both negative. This has been attributed to an electronic change

associated with an atomic rearrangement.

Overall the sigma phase itself seems to be the result of an attempt at closer packing as the temperature falls in which the size and electronic structure of atoms in particular sites are closely linked. These two factors affect considerably the deformation characteristics of the structure.

Suggestions for Future Work

The rates of formation of the iron-vanadium sigma phase observed in the isothermal resistivity measurements indicate the necessity of using wire specimens heated directly by an AC current. This would serve to establish the complete TTT curves and furthermore would achieve fast rates of cooling required to determine whether there are two or more reaction mechanisms for the $\alpha \rightarrow \sigma$ transformation.

The deformation exhibited in the ternary sigma phases are of particular interest. An analysis of the line profiles obtained from X-ray diffractometer traces might help to resolve the effects of different additions and clarify the criteria of atomic size and electronic structure for site occupancy. The deformation in the sigma phase might also be investigated by electron microscopy.

The Widmanstätten precipitate observed in all of the alloys suggests the need for a detailed examination of the phase diagram in the equiatomic region.

BIBLIOGRAPHY

1. Bain, E. C., Chem. Met. Eng., 1923, 28, 23.

2. Bain, E. C., and Griffiths, W. E., Trans. Amer. Inst. Min. Met. Eng. 1927, 75, 166.

3. Adcock, F., J. Iron Steel Inst., 1931, 124, 147.

4. Wever, F., and Jellinghaus, W., Mitt. K. W. Inst. Eisenforsch., 1931, 13, 93 and 143.

5. Ericksson, S., Jernkontorets Ann., 1934, 118, 530.

6. Bradley, A. J., and Goldschmidt, H. J., J. Iron Steel Inst., 1941, 144, 273.

7. Greenfield, P. and Beck, P. A., Trans. A.I.M.E. 1956, 206, 265.

8. Knapton, A. G., J. Inst. Met. 1958, 87, 28.

9. Nevitt, M. V., "Electronic Structure and Alloy Chemistry of the Transition Elements" (edited by P. A. Beck), 1963, New York: Wiley.

10. Bergman, G. and Shoemaker, D. P., Acta Cryst. 1954, 7, 857.

11. Kasper, J. S., Decker, B. F. and Belanger, J. R., Abstract for A.C.A. Meeting, June, 1952.

12. Dickens, G. J., Douglas, A. M. B. and Taylor, W. H., Acta Cryst. 1956, 9, 297.

13. Arnfelt, H. and Westgren, A., Jernkontor. Ann. 1935, 119, 185.

14. Magneli, A. and Westgren, A., Z. anorg. Chem. 1938, 238, 268.

15. Henglein, E. and Kohsok, H., Rev. Metall. 1949, 46, 569.

16. Rideout, S., Manly, W. D., Kamen, E. L., Lement, B. S. and Beck, P. A. Trans. Amer. Inst. Min. (Metall.)Engrs., 1951, 191, 872.

17. Tucker, C. Acta Cryst., 1951, 4, 425.

18. Jones, H., Proc. Roy. Soc., 1934a A, 144, 225.
Jones, H., Proc. Roy. Soc., 1934b, A, 147, 396.

19. Pauling, L. and Ewing, F. J., Rev. Mod. Phys. 1948, 20, 122.

20. Douglas, A. M. B. Brit, J. Apply. Phys. 1951, 2, 305.

21. Hoare, F. E. and Matthews, J. C. Proc. Phys. Soc. 1958, 71, 220.

22. Kasper cited by reference (95).

23. Marconne, N. J., and Coll, J. A., Acta Met., 1964, 12, 742.

24. Kazanstev, V. Doklady. Akad. Navk. 1955, 101, 477.
Kazanstev, V. ibid, 1959,124,806.

25. Nevitt, M. V., and Beck, P. A., Trans. Amer. Inst. Min. Met. Engr., 1955, 203, 669.

26. Alte da Veiga, L. M., Portgal. Phys. 1966, 4, 205.

27. Bozorth, R. M., Ferromagnetism, 1951, New York. D. Van Nostrand.

28. Bethe, H., Handbuch der Physik, 1933, Part 2, p.595.

29. Shull, C. C., cited in Ref. (25).

30. Parsons, D., Nature, 1960, 185, 839.

31. Kasper, J. S. and Waterstrat, R. M. Acta Cryst., 1956, 9, 289.

32. Lena, A., Metal Progress 1954, 66(1), 86; (2), 94.

33. Marcinkowski, M. J., and Miller, D. S., Phil. Mag., 1962, 7, 1025.

34. Kitchingman, W. J. To be published.

35. Decker, B. F., Waterstrat R. M., and Kasper, J. S., J. Metals, 1954, 6, 1406.

36. Dickens, G. J., Douglas, A. M. B., and Taylor, W. M. Acta Cryst. 1956, 9, 297.

37. Spooner, F. J., and Wilson, C. G., Acta Cryst., 1964, 17, 1533.

38. Wilson, C. G., Acta Cryst., 1963, 16, 724.

39. Sully, A. H., J. Inst. Metals, 1951-52, 80, 173.

40. Bloom, D. S. and Grant, N. J., Trans. Amer. Inst. Min. (Metall.) Engrs., 1954, 197, 88.

41. Greenfield, P., and Beck, P. A., Ibid, 1954, 200, 253.

42. Stuwe, H. P., Ibid, 1959, 215, 408.

43. Frank, F. C., and Kasper, J. S., Acta Cryst. 1958, 11,184.
Frank, F. C., and Kasper, J. S., Acta Cryst. 1959, 12,483.

44. Haworth, C. W., J. Less Common Metals, 1960, 2, 125.

45. Sully, A. H., and Heal, T. J., Research, 1948, 1, 288.

46. Knapton, A. G., J. Inst. Metals. 1958-59, 87, 62.

47. Pearson, W. B., and Hume-Rothery, W., Ibid, 1952-53, 81, 311.

48. Oriani, R. A., Acta Met. 1954, 2, 343.

49. Gupta, K. P., Trans. Met.Soc. A.I.M.E., 1961, 221, 1047.

50. Shoemaker, D. P., and Shoemaker, C. B., Acta Cryst., 1960, 13, 1010.

51. Shoemaker, D. P. and Shoemaker, C. B., Trans. A.I.M.E., 1964, 230, 486.

52. Waterstrat, R. M., and Kasper, J. S., Trans. A.I.M.M.E., 1957, 209, 872.

53. Baen, S. R., and Duwez, P. Trans. AIME, 1951, 191, 331.

54. Rocher, Y. A., and Friedel, J., J. Phys. Chem. Solids, 1961, 21, 287.

55. Corenzwit, E. ibid 1959, 93, 9.

56. Levin, E. E. and Pivnik, E. M., Metallovedenie i Term, Obrabot Metallov. 1957, 2, 27.

57. Levin, E. E. and Pivnik, E. M. and Libman, P. M. ibid, 1959, 9, 17.

58. Tedmon, C. S. and Westbrook, J. H. To be published in Trans. Amer. Soc. for Metals.

59. Mima, G. and Imoto, S. Nippon-Kinz-Gak Shi, 1953, 17, 549.

60. Bungardt, K. and Spyra, W. Arch. Eisen. 1958, 29, 471.

61. Wilson, C.G. and Parselle M. H. Acta Cryst. 1965, 19, 9.

62. "Intermetallic Compounds" Ed. J. H. Westbrook, John Wiley and Sons.

63. Ageev, N. V. and Shekhtman, V. S. Proc. Acad. Sci. USSR 1959, 127, Pt. 5, 1011.

64. Kripyakevich, P. I., Tylkina, M. A. and Savitski, E. M. Proc. Inst. Higher Education: Ferrous Metall. USSR, 1960, 12, 1.

65. Tisinai, G. F., Stanley, J. K., and Samans, C. H. Trans. A.I.M.M.E. 1954, 200, 1259.

66. Beck, P. A. and Manly, W. D. Trans. A.I.M.E. 1948, 183, 354.

67. Shoemaker, D. P., Shoemaker, C. B. and Wilson, F. C., Acta Cryst., 1957, 10, 1.

68. Shoemaker, C. B., and Shoemaker, D. P. Annual Meeting Am. Crystall. Assoc. 1961 (Abs.).

69. Komura, T., Sly, W. G. and Shoemaker, D. P. Acta Cryst., 1960, 13, 575.

70. Kasper, J. S. "Theory of Alloy Phases", A.S.M. 1955.

71. Ellinger, F. H., Trans. A.S.M., 1942, 30, 607.

72. Williams, R. O., and Paxton, H. W. J.I.S.I. 1957, 183,358.

73. Williams, R. O. Trans. Met. Soc. A.I.M.E., 1958, 212, 497.

74. Kubaschewski, O. and Chart, T. G. J. Inst. Metals, 1964-5, 93, 329.

75. Pearson, W. B., J.I.S.I. 1950, 164, 149.

76. Jette, E. R. and Foote, F., "Metals and Alloys", 1936, 7, 207.

77. Duwez and Martens "Ductile Chromium", A.S.M. 1957, p.322.

78. Bastien, P. and Pomey, J., Compt. rend., 1954, 239, 1636.

79. Bastien, P. and Pomey, J., ibid p. 1797.

80. Trost, W. R., "Orbital Theory in the Transition Metals", Dept. of Mines and Technical Surveys, Ottawa, Mines Branch Research Rept. R. 42, 1958.

81. Engel, N., Powder Met. Bull. 1954, 8, 7.

82. Bastien, P. and Pomey, J. Compt rend., 1955, 240, 866.

83. Andersen, A. G. H. and Jette, E. R., Trans. A.I.M.E. 1938, p. 318.

84. Beck, P. A. and Phillip, T. V., J. of Metals, Oct. 1957, 1269.

85. Hägg, G. Z. Physik. Chem. 1929, 6 B 221.

86. Ehrlich, P. Z. anorg. chem. 1949, 259, 1.

87. Shortsleave, F. J. and Nicholson, M, E. Trans. Amer. Soc. Metals, 1936, 24, 375.

88. Tisinai, G. F., Stanley, J. K. and Samans, C. H. Trans. Amer. Inst. Min. Met. Engr. 1954, 200, 1259.

89. Aronsson, B. and Åsselius, J. Acta. Chem. Scand. 1958, 12, 1476.

90. Andersen, A. G. H. and Jette, E. R., Trans. Amer. Soc. Metals, 1936, 24, 375.

91. Aronsson, B. and Lundstrom, T., Acta. Chem. Scand. 1957, 11, 365.

92. Farquhar, C. M., Lipson, H., and Weill, A. R., J.I.S.I. 1945, 152, 457.

93. Pickwick, K. M. Ph.D. Thesis, Manchester University, 1964.

94. Boren, B., Arkir Kemi, Mineral, Geol. 1933, 11A, No. 10.

95. Gupta, K. P., Rajan, N. S. and Beck, P. A., Trans. Met. Soc. A.I.M.E. 1960, 218, 617.

96. Gale, B. Acta Met. 1959, 7, 420.

97. Lundstrom, T. Acta. Chem. Scand. 1962, 16, 149.

98. Tagaya, M. and Nenno, S. Technol. Rep. Osaka Univ. 1955, 5, 49.

99. Tagaya, M., Nenno, S. and Kawamoto, M. Nippon Kinzoku Gakkai-Si 1958, 22, 387.

100. Burgess, C. O. Forgeng, W. D. Trans. A.I.M.E. 1936, 131, 277.

101. Jette Anderson, ibid 1936, 131, p.303.

102. Kronberg, M. L., J. of Nuclear Materials 1959, p. 85.

103. Mott, N. F. and Stevens, K. W. H. Phil. Mag. 1957, 2, 1364.

104. Lomer, W. M. and Marshall, W. Phil. Mag. 1958, 3, 185.

105. Borelius, cited by Ref. 77.

106. Kuczynski, G. C., Hochman, R. F. and Doyama, M. J. Appl. Phys. 1955, 26, 871.

107. Smith, R. and Bowles, J. R. Acta. Met. 1960, 8, 405.

108. "Structure of Metals", Barrett, C. S. and Massalski, T. B. McGraw-Hill Inc.

109. Massalski, T. B. Acta Met., 1958, 6, 243.

110. Greninger, A. B. Trans. AIME, 1939, 133, 204.

111. Gilbert, A. and Owen, W. S. Acta Met., 1962, 10, 45.

112. Hull, D. and Garwood, R. D. Inst. of Metals Monograph and Report Series No. 18, 1955, 219.

113. Owen, W. S. "Physical Properties of Martensite and Bainite" Special Report 93. The British Iron and Steel Inst.

114. Yeo, R. B. G. Trans. AIME, 1962, 224, 1222.

115. Yeo, R. B. G. Trans. ASM, 1964, 57, 48.

116. Christian, J. W. "The Theory of Transformations in Metals and Alloys", Pergamon, New York, 1965.

117. Avrami, M. J. Chem. Phys. 1939, 7, 1103
ibid 1940, 8, 12
ibid 1941, 9, 177.

118. Owen, W. S. and Gilbert, A. J.I.S.I. 1960, 196, 142.

119. Cullity, B. D. 'Elements of X-ray Diffraction', Addison-W.

120. Taylor, A. and Sinclair, H., Proc. Phys. Soc. 1945, 57, 126.

121. Nelson, J. B. and Riley, D. P. Proc. Phys. Soc. 1945, 57, 1960.

122. Cohen, M. U. Rev. Sci. Inst. 1935, 6, 68.

123. Jette, E. R. and Foote, F., J. Chem. Phys. 1935, 3, 605.

124. Hess, J. B., Acta Cryst., 1951, 4, 209.

125. Lawn, B. R. Acta Cryst. 1963, 16, 1256.

126. Deming, W. E. Statistical Adjustment of Data, 1943 (New York: Wiley).

127. Hoff, W. D. and Kitchingman, W. J. To be published.

128. Warren, B. E. J. Appl. Phys. 1945, 16, 614.

129. Booth, C. W. To be published.
For theory of this type of circuit see M.Sc. Thesis, Manchester University, 1967.

130. Cairns, J. H., Ph.D. Thesis, Manchester University, 1958.

The author wishes to thank Dr. W. J. Kitchingman for permission to use Figs. (44-51) before publication and also to acknowledge the following sources of diagrams.

Fig. 4. "Theory of Alloy Phases" by J. S. Kasper published by ASM, Cleveland, Ohio, 1956.

Fig. 54. "Elements of X-ray Diffraction", by B. D. Cullity, published by Addison-Wesley.

Fig. 55. "Electric Furnaces" edited by C. A. Otto, published by George Newnes Ltd., London.

APPENDIX I

The Coordination Polyhedra of Atoms

The domain of an atom is defined as the space in which all points are nearer the centre of that atom than any other. It is a polyhedra, each face of which is the plane equidistant from that atom and a neighbour. If all the planes bisecting the lines joining the central atom to all other atoms are described, then the innermost polyhedron bounded by these planes is the domain of that central atom. Every atom whose domain has a face in common with the domain of that central atom is, by this definition, one of its neighbours. The number of neighbours is called the 'coordination number' of the central atom, and the set of neighbours its 'coordination shell'. The polyhedron whose edges are the lines joining all the atoms of the coordination shell which are also neighbours of each other are called its "coordination polyhedron". The coordination polyhedron and the domain stand in dual relationship, each having a vertex corresponding to each face of the other.

The term "coordination number" (CN) has been used in two ways in crystallography, one which is precisely defined in principle though seldom used with rigour, and another employed intuitively without exact definition. According to the first, the coordination number, Z, is the number of nearest neighbours to an atom. According to this definition, in hexagonal close packing Z is 6 unless c^2/a^2 is exactly $8/3$, in which case it is 12. The definition is rarely applied with rigour in this case: Z is generally regarded as 12. In the body-centred cubic lattice however, some authors probably the majority, count Z as 8 in accordance with the nearest neighbour definition but others prefer to regard it as 14. The definitions given by Frank and Kasper provide a rigorous basis for the second view-point according to which Z is unambiguously 12 in the hexagonal close-packed metals and 14 in a body-centred cubic metal. In the more complex structures of metals and intermetallic compounds this definition yields numbers such as 14 where the nearest neighbour definition would give 1 or 2.

Having discussed the coordination of atoms around a single atom the conditions imposed on complete structures are now considered. In the complete structure it is required that not only the atoms around one form a normal coordination, but that these atoms in turn are also surrounded by normal coordination shells. The two main principles which emerge from this

consideration are firstly the existence of a "major skeleton" and secondly the existence of planar, or approximately planar, "layers" of atoms, containing certain necessary pattern - motifs.

Sites of 12 - coordination are distinguished as "minor" and of more than 12 - coordination as "major". If an atom is at a minor site, it has no neighbour with which it shares 6 neighbours in common. If atom A is at a major site of coordination number Z, it has (Z - 12) such neighbours. If B is one of these, it follows that B has a neighbour (namely A) in its coordination shell, with which it has 6 neighbours in common. Therefore B is also a major site. The line joining A and B, or joining any pair of atoms which have 6 neighbours in common is a "major-ligand". Every major site of coordination number Z is the meeting point of (Z - 12) major ligands. This is at least 2, since the case Z = 13 does not exist. Hence the major ligands form one or more connected networks which in all is known as the "major skeleton" of the structure sites of Z14, Z15 or Z16 are the meeting points of 2, 3, or 4 major ligands which are in line, 120° apart in a plane, or in tetrahedral disposition respectively. Frank and Kasper go on to point out that the geometry is similar to that of organic chemistry in the absence of univalent elements. This absence corresponds to the absence of Z13. It has the consequence that each connected system of major ligands is infinite.

The major ligands may be shorter ligands than the average even though they connect sites of larger coordination number, mainly suited for larger atoms.

APPENDIX II

The Computer Programme

The computer programme used for the indexing of the powder diffraction patterns and for the lattice parameter calculations has two main routines;

(i) Routine INDEX

(ii) Routine LEAST SQUARES ANALYSIS (L.S.A.)

The procedure is summarised in a flow diagram and the programme given in the following pages.

Flow Diagram

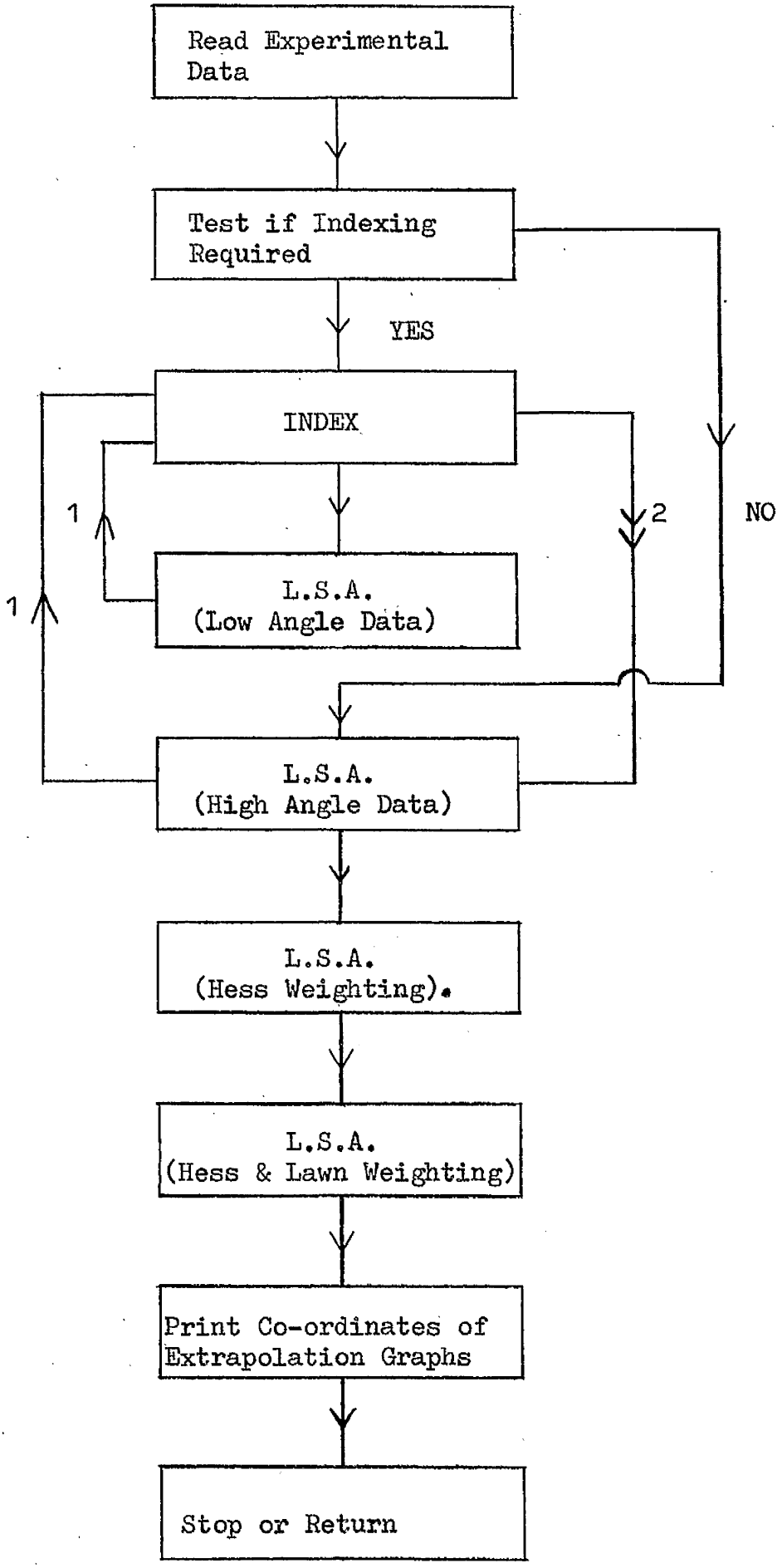

```
JOB
UTMT, BEDFORD 13/0
COMPUTING 25000 INSTRUCTIONS
OUTPUT
0 LINE PRINTER 2000 LINES
STORE 70/70
USE AB

compile array bound check

begin
real lambda, shrink, diameter, KE, A,B,C,D, AA,BB,CC,Ax,Bx,Cx,c
era,erb,erc,erax,erbx,ercx,Sa,Sb,Sc,a,b,c,aa,bb,cc,dd
integer n1,n2,n,ind,i,type,stage,CYCLE,N,I,j,limit
array Z(1:400), s(1:400), ZZ(1:400), ZH(1:400), R(1:400), W(1:400),
w(1:400), f(1:400)
integer array h(1:400), k(1:400), l(1:400), U(1:400)

routinespec index(realname A,B,C, arrayname Z,ZZ, integer n,type, c
integername N, integerarrayname h,k,l)

routinespec LEAST SQUARES ANALYSIS(integer I,type,stage, c
integerarrayname h,k,l,U, arrayname R,W,f, realname A,B,C,D,era,erb,erc)

switch JJ(0:3), LL(0:3), MM(0:3), NN(0:3)

comment For asymmetric camers supply the highangle diameters in c
decreasing order and the low angle diameters in increasing order, c
for 19cm cameras supply the dianeters from high angle end

1: newline; newline; newline
caption program start

read(type); if type<0 then ->2
read(limit)

read(lambda)
read(n1); read(ind); read(shrink); read(diameter)
unless diameter>18 then ->3
```

```
newline; caption 19cm ⌀ camera
read(KE)
n=n1;
cycle i=1,1,n
read(s(i))
if ind<0 then ->4
read(h(i)); read(k(i)); read(l(i));
\4: Z(i)=π/2-(s(i)*shrink +KE)/(2*diameter)
repeat
->5

3: newline; caption asymmetric ⌀ camera ⌀ of ⌀diameter
print(diameter,\3,3)
read(n2); n=n1+n2

cycle i=1,1,n1
read(s(i))
if ind<0 then ->6
read(h(i)); read(k(i)); read(l(i))
6: Z(i)=(shrink*s(i))/(2*diameter)
repeat

cycle i=(n1+1),\1,n
comment high angle data
read(s(i))
if ind<0 then ->7
read(h(i)); read(k(i)); read(l(i));
7:Z(i)=π/2-(shrink*s(i))/(2*diameter)
repeat

5:unless ind<0 then ->8
newline; caption indexing⌀ by⌀ sin2 ⌀ comparison
->MM(type)

MM(0): newline; caption cubic
read(a); A=lambda"/(4*a"); B=A; C=A;
->9
MM(1): newline; caption hexagonal
read(a); read(c);
A=lambda"/(3*a"); \C=lambda"/(4*c")
B=A
```

```
->9
MM(2): newline; caption tetragonal
read(a); read(c);
A=lambda^2/(4*a^2); C=lambda^2/(4*c^2)
B=A
->9
MM(3): newline; caption orthorhomb\\ic
read(a); read(b); read(c);
A=lambda^2/(4*a^2); B=lambda^2/(4*b^2); C=lambda^2/(4*c^2)

9:CYCLE=0

12: index(A,B,C,Z,ZZ,n,type,N,h,k,l\\)

if CYCLE>0 then ->35
newline; caption lows angles leasts squaress \\tos refines consts
newline
N=intpt(N/2); I=N
stage=0


cycle i=1,1,N
R(i)=(sin(ZZ(i)))^2
W(i)=1
f(i)=7-2*ZZ(i)
U(i)=1
repeat

->14

35:cycle i=1,1,N
U(i)=1
repeat
8:I=0
if ind<0 then ->10
N=n
cycle i=1,1,N
ZZ(i)=Z(i)
U(i)=1
repeat
10:I=0
```

```
cycle i=1,1,N
if ZZ(i)≤π/4 then ->13
I=I+1
ZH(i)=ZZ(i)
13:repeat

stage=0
cyclei=N-I+1,1,N
R(i)=(sin(ZH(i)))^4
W(i)=1
f(i)=(π-2*ZH(i))*(sin(π-2*ZH(i)))
repeat
comment WARREN FUNCTION USED ABOVE

14: LEAST SQUARES ANALYSIS(I,type,stage,h,k,l,U,R,W,f,A,B,C,D,era,erb,erc)

AA=0; BB=0; CC=0
18: if stage>0 then caption weighted$ procedure
A=AA+A
B=BB+B
C=CC+C
->JJ(type)

JJ(0): a=lambda/(2*sqrt(A))
newline; caption cubic$ parameter
Sa=a*era/(2*A)
print(a,1,8); print(Sa,1,8)
->15
JJ(1): a=lambda/sqrt(3*A)
c=lambda/sqrt(4*C)
newline; caption hexagonal$ parameters(a,c)
Sa=a*era/(2*A); Sc=c*erc/(2*C)
print(a,1,8); print(Sa,1,8)
print(c,1,8); print(Sc,1,8)
->15
JJ(2):a=lambda/(2*sqrt(A)); c=lambda/(2*sqrt(C))
newline; caption tetragonal$ parameters(a,c)
Sa=a*era/(2*A); Sc=c*erc/(2*C)
print(a,1,8); print(Sa,1,8)
print(c,1,8); print(Sc,1,8)
```

```
->15
JJ(3): a=lambda/sqrt(4*A); b=lambda/sqrt(4*B); c=lambda/sqrt(4*C)
newline; caption orthorhombic ß parameters
Sa=a*era/(2*A)\\; Sb=b*erb/(2*B); \\Sc=c*erc/(2*C)
newline; print(a,1,ð); print(Sa,1,ð)
newline; print(b,1,ð); print(Sb, 1,ð)
newline; print(c,1,ð); print(Sc,1,ð)

15: ifstage>0 then ->19
if ind>0 then ->16
CYCLE=CYCLE+1
unless CYCLE>2 then ->12

10: stage= 1
AA=A; BB=B; CC=C
cycle i=N-I+1,1,N
W(i)=1/(sin(ß-2*ZH(i)))^
w(i)=W(i)
repeat

cycle i=N-I+1,1,N
->LL(type)
LL(0): R(i)=AA*(h(i)^+k(i)^+l(i)^)-(sin(ZH(i)))^
->17
LL(1): R(i)=AA*(h(i)^+k(i)^+h(i)*k(i))+CC*l(i)^-(sin(ZH(i)))^
->17
LL(2): R(i)=AA*(h(i)^+k(i)^)+CC*(l(i)^)-(sin(ZH(i)))^
->17
LL(3): R(i)=AA*h(i)^+BB*k(i)^+CC*l(i)^-(sin(ZH(i)))^
17:repeat

LEAST SQUARES ANALYSIS(I,type,stage,h,k,l,U,R,W,f,A,B,C,D,era,erb,erc)

->18
19:if type=0 then ->30
if type=1 or type=2 then ->20
->21
20: cycle i=N-I+1,1,N
if type=2 then ->22
W(i)=w(i)*(4*(h(i)^+k(i)^+h(i)*k(i))/(3*a^))/((4*(h(i)^+k(i)^+h(i)*k(i))/
(3*a^))+l(i)^/c^)
->23
22\\: W(i)=w(i)*((h(i)^+k(i)^)/\\\\a^)/(((h(i)^+k(i)^)/a^)+l(i)^/c^)
23:repeat
```

```
LEAST SQUARES ANALYSIS(I,type, stage,h,k,l,U,R,W,f,A,B,C,D,era,erb,erc)

Ax=AA+A; erax=era/Ax
cycle i=N-I+1,1,N
if type=2then ->24
W(i)=w(i)*((l(i)^/c^)/((4*(h(i)^+h(i)*k(i)+k(i)^)/(3\\*a^))+l(i)^/c^))
->25
24: W(i)=w(i)*((l(i)^/c^)/(((h(i)^+k(i)^)/a^)+l(i)^/c^))
25:repeat

LEAST SQUARES ANALYSIS (I,type,stage,h,k,l,U,R,W,f,A,B,C,D,era,erb,erc)

Cx=CC+C
\\ercx=erc/Cx
if \\type=2 then ->26
newline; caption modified # weighted # hex# parameters # (a,c)
a=lambda/sqrt(3*Ax); c=lambda/(2*sqrt(Cx))
Sa=a*erax/2\\; Sc=c*ercx/2
print(a,1,8); print(Sa,1,8)
print(c,1,8); print(Sc,1,8)
->30
26: newline; caption modifed weighted # tetragonal # parameters # (a,c)
a=lambda/\\(2*sqrt(Ax)); c=lambda/(2*sqrt(Cx))
Sa=a*erax/2; Sc=c*ercx/2
print(a,1,8); print(Sa,1,8)
print(c,1,8); print(Sc,1,8)
->30

21: comment orthorhombic weighting by Lawn's method

cycle i=N-I+1,1,N
W(i)=w(i)*((h(i)^/a^)/((h(i)^/a^)+(k(i)^/b^)+(l(i)^/c\\^)))
repeat

LEAST SQUARES ANALYSIS(I,type,stage,h,k,l,U,R,W,f,A,B,C,D,era,erb,erc)

Ax=AA+A
erax=era/Ax

cycle i=N-I+1,1,N
W(i)=w(i)*((k(i)^/b^)/((h(i)^/a^)+(k(i)^/b^)+(l(i)^/c^)))
repeat
```

```
LEAST SQUARES ANALYSIS (I,type,stage,h,k,l,U,R,W,f,A,B,C,D,era,erb,erc\\)

Bx=BB+B
erbx=erb/Bx

cycle i=N-I+1,1,N
W(i)=w(i)*((l(i)"/c")/((h(i)"/a")+(k(i)"/b")+(l(i)"/c")))
repeat

LEAST SQUARES ANALYSIS(I,type,stage,h,k,l,U,R,W,f,A,B,C,D,era,erb,erc)

Cx=CC+C
ercx=erc/\\\\\\\Cx

newline; caption modifed weight\\ed & orthorhombic& parameters(a,b,c)
a=lambda/(2*sqrt(Ax)); b=lambda/(2\\\\\\*sqrt(Bx)); c=lambda/(2*sqrt(Cx))
Sa=a*erax/2; Sb=b*erbx/2; Sc=c*ercx/2
newline; print(a,1,8); print(Sa,1,8)
print(b,1,8); print(Sb,1,8)
print(c,1,8); print(Sc,1,8)

30: newline; newline;

caption extrapolation & graphs
->NN(type)
NN(0): captio\\n cubic
cycle i=N-I+1,1,N
aa=lambda*(sqrt(h(i)"+l(i)"+k(i)"))/(2*sin(ZH(i)))
newline
print(aa,1,5)
print(h(i),1,0)
print(k(i),1,0)
print(l(i),1,0)
dd=((cos(ZH(i)))"/sin(ZH(i)))+(cos(ZH(i)))"/ZH(i)
print(dd,1,5)
if U(i)<1 then caption rejected
repeat
```

```
->1
NN(1): caption hexagonal
cycle i=N-I+1,1,N
aa=(lambda/sin(ZH(i)))*sqrt(((h(i)^+k(i)^+h(i)*k(i))/3)+(l(i)*a)^/((2*c)^))
cc=(lambda/sin(ZH(i)))*sqrt((h(i)^+k(i)^+h(i)*k(i))*(c^/(3*a^))+l(i)^/4)
newline
print(aa,1,5)
print(cc,1,5)
print(h(i),1,0); print(k(i),1,0); print(l(i),1,0)

dd=((cos(ZH(i)))^/sin(ZH(i)))+(cos(ZH(i)))^/ZH(i)
print(dd,1,5)
if U(i)<1 then caption rejected
repeat
->1
NN(2): caption tetragonal
cycle i=N-I+1,1,N
aa=(lambda/sin(ZH(i)))*sqrt(((h(i)^\\+k(i)^)/4)+((l(i)*a\\/(2*c))^))
cc=(lambda/sin(ZH(i)))*sqrt(((h(i)^+k(i)^)*c^/(4*a^))+l(i)^/4)
\\newline
print(aa,1,5)
print(cc,1,5)
print(h(i),1,0); print(k(i),1,0); print(l(i),1,0)
dd=((cos(ZH(i)))^/sin(ZH(i)))+(cos(ZH(i)))^/ZH(i)
print(dd,1,5)
if U(i)<1 then caption rejected
repeat

->1
NN(3): newline; caption orthorhombic
cycle i=N-I+1,1,N
aa=(lambda/(2*sin(ZH(i))))*sqrt(h(i)^+(k(i)^*a^/b^) +(l(i)^*a^/c^))
bb=(lambda/(2*sin(ZH(i))))*sqrt((h(i)^*b^/a^)\\+k(i)^+(l(i)^*b^/c^))
cc=(lambda/(2*sin(ZH(i))))*sqrt((h(i)^*c^/a^)+(k(i)^*c^/b^)+l(i)^)
newline
print(aa,1,5)
print(bb,1,5)
print(cc,1,5)
print(h(i),1,0); print(k(i),1,0); print(l(i),1,0)
dd=((cos(ZH(i)))^/sin(ZH(i)))+(cos(ZH(i)))^/ZH(i)
print(dd,1,5)
if U(i)<1 then caption rejected
repeat
->1

2:stop
```

```
routine LEAST SQUARES ANALYSIS (integer I,type,stage, integerarrayname c
h,k,l,U, arrayname R,W,f, realname A,B,C,D,era,erb,erc)

array s(1:2,1:2), m(1:3,1:3), p(1:4,1:4), S(1:2), M(1:3), P(1:4), c
a(1\\:400), b(1:400), c(1:400)
real det1, z1, ER, z2, z3, z4, zz
integer i,t,COUNT,n
switch J(0:3), \\L(0:3)

ER=0.005
->L(type)

L(0): cycle i=1,1,2
cycle t=1,1,2
s(i,t)=0; S(i)=0
repeat
repeat

n=0
cycle i=N-I+1,1,N
if U(i)<1 then ->1
if W(i)<0.0000001 then ->1
n=n+1; a(i)=h(i)^+k(i)^+l(i)^
s(1,1)=s(1,1)+W(i)*a(i)^
s(1,2)=s(1,2)+W(i)*f(i)*a(i)
s(2,1)=s(1,2)
s(2,2)=s(2,2)+W(i)*f(i)^
S(1)=S(1)+a(i)*R(i)*W(i)
S(2)=S(2)+f(i)*R(i)*W(i)
1:repeat
z1=s(2,2)
eqn solve(s,S,det1)
A=S(1); B=S(1); C=S(1); D=S(2)
zz=0
cycle i=N-I+1,1,N
if U(i)<1 then ->13
if W(i)<0.0000001 then ->13
zz=zz+W(i)*(a(i)*A+f(i)*D-R(i))^
13:repeat
era=sqrt(z1*zz/((n-2)*det1))
erb=era; er\\c=era
->2
```

```
L(1):cyclei=N-I+1,1,N
a(i)=h(i)^2+k(i)^2+h(i)*k(i); b(i)=l(i)^2
repeat
->3

L(2):cyclei=N-I+1,1,N
a(i)=h(i)^2+k(i)^2; b(i)=l(i)^2
repeat

3:cyclei=1,1,3
cycle t=1,1,3
m(i,t)=0; M(i)=0
repeat
repeat
repeat
n=0
cycle i=N-I+1,1,N
if U(i)<1 then ->4
if W(i)<0.0000001 then ->4
n=n+1
m(1,1)=m(1,1)+W(i)*a(i)^2
m(1,2)=m(1,2)+W(i)*a(i)*b(i)
m(1,3)=m(1,3)+W(i)*a(i)*f(i)
m(2,1)=m(1,2)
m(2,2)=m(2,2)+W(i)*b(i)^2
m(2,3)=m(2,3)+W(i)*b(i)*f(i)
m(3,1)=m(1,3)
m(3,2)=m(2,3)
m(3,3)=m(3,3)+W(i)*f(i)^2
M(1)=M(1)+W(i)*R(i)*a(i)
M(2)=M(2)+W(i)*R(i)*b(i)
M(3)=M(3)+W(i)*R(i)*f(i)
4:repeat
s(1,1)=m(2,2); s(1,2)=m(2,3)
s(2,1)=m(3,2); s(2,2)=m(3,3)
z1=det(s)
s(1,1)=m(1,1); s(1,2)=m(1,3)
s(2,1)=m(3,1); s(2,2)=m(3,3)
z2=det(s)
eqn solve(m,M,det1)
A=M(1); B=A; C=M(2); D=M(3)
zz=0
```

```
cycle i=N-I+1,1,N
if U(i)<1 then ->14
if W(i)<0.0000001 then ->14
zz=zz+W(i)*(a(i)*A +b(i)*C+f(i)*D-R(i))^
14:repeat

era=sqrt(z1*zz/((n-3)*det1))
erb=era
erc=sqrt(z2*zz/((n-3)*det1))
->2

L(3):cycle i=N-I+1,1,N
a(i)=h(i)^; b(i)=k(i)^; c(i)=l(i)^
repeat
5:cyclei=1,1,4
cyclet=1,1,4
p(i,t)=0 ; P(i)=0
repeat
repeat
n=0

cycle i=N-I+1,1,N
if U(i)<1 then ->6
if W(i)<0.0000001 then ->6
n=n+1
p(1,1)=p(1,1)+W(i)*a(i)^
p(1,2)=p(1,2)+W(i)*a(i)*b(i)
p(1,3)=p(1,3)+W(i)*a(i)*c(i)
p(1,4)=p(1,4)+W(i)*a(i)*f(i)
p(2,1)=p(1,2)
p(2,2)=p(2,2)+W(i)*b(i)^
p(2,3)=p(2,3)+W(i)*b(i)*c(i)
p(2,4)=p(2,4)+W(i)*b(i)*f(i)
p(3,1)=p(1,3)
p(3,2)=p(2,3)
p(3,3)=p(3,3)+W(i)*c(i)^
p(3,4)=p(3,4)+W(i)*c(i)*f(i)
p(4,1)=p(1,4)
p(4,2)=p(2,4)
p(4,3)=p(3,4)
p(4,4)=p(4,4)+W(i)*f(i)^
P(1)=P(1)+R(i)*W(i)*a(i)
P(2)=P(2)+R(i)*W(i)*b(i)
P(3)=P(3)+R(i)*W(i)*c(i)
P(4)=P(4)+R(i)*W(i)*f(i)
6:repeat
```

```
m(1,1)=p(2,2); m(1,2)=p(2,3); m(1,3)=p(2,4)
m(2,1)=p(3,2); m(2,2)=p(3,3); m(2,3)=p(3,4)
m(3,1)=p(4,2); m(3,2)=p(4,3); m(3,3)=p(4,4)
z1=det(m)
m(1,1)=p(1,1); m(1,2)=p(3,1); m(1,3)=p(4,1)
m(2,1)=p(3,1); m(2,2)=p(3,3); m(2,3)=p(3,4)
m(3,1)=p(4,1); m(3,2)=p(4,3); m(3,3)=p(4,4)
z2=det(m)
m(1,1)=p(1,1); m(1,2)=p(2,1); m(1,3)=p(4,1)
m(2,1)=p(2,1); m(2,2)=p(2,2); m(2,3)=p(4,2)
m(3,1)=p(4,1); m(3,2)=p(4,2); m(3,3)=p(4,4)
z3=det(m)
eqn solve(p,P,det1)
A=P(1); B=P(2); C=P(3); D=P(4)

zz=0
cycle  i=N-I+1,1,N
if U(i)<1 then ->15
if W(i)<0.0000001 then ->15
zz=zz+W(i)*(a(i)*A+b(i)*B+c(i)*C+f(i)*D-R(i))^2
15:repeat

era=z1*zz/((n-4)*det1)
erb=z2*zz/((n-4)*det1)
erc=z3*zz/((n-4)*det1)
era=sqrt(era); erb=sqrt(erb); erc=sqrt(erc);
->2

2:comment error check
if stage>0 then ->7
8:if ER<0.000511 then ->9
ER=ER-0.0005
9:COUNT=0
cycle i=N-I+1,1,N
->J(type)
J(0): if U(i)<1 then ->10
if |A*a(i)+D*f(i)-R(i)|<ER then ->10
U(i)=0; newline; caption rejected
print(a(i),1,0); print(ER,1,5);  COUNT=COUNT+1
->10
J(1):->J(2)
J(2): if U(i)<1 then ->10
if |A*a(i)+C*b(i)+D*f(i)-R(i)|<ER then ->10
U(i)=0; newline; caption rejected
print(a(i),2,0); print(b(i),2,0); print(ER,1,5);  COUNT=COUNT+1
->10
```

```
J(3): if U(i)<1 then ->10
 if |A*a(i)+B*b(i)+C*c(i)+D*f(i)-R(i)|<ER then ->10
U(i)=0; newline; caption rejected
print(a(i),2,0); print(b(i),2,0); print(c(i),2,0)
print(ER,1,5); COUNT=COUNT+1
10:repeat

if COUNT>(n-4) then ->11
if 0.000511>ER then ->12
if COUNT<1 then ->8
if ER>0.000511 then ->L(type)
12: if COUNT>0 then ->L(type)
if COUNT=0 and limit<0 then ->7
if ind<0 and CYCLE=0 then ->7
if COUNT=0 and ER<0.0003 then ->7
if limit>0 then ER=0.00025
if ER<0.0003 then ->9
->7
11:newline; caption rejections not completed fault in data
print(A,1,8); print(B,1,8); print(C,1,8); print(D,1,8)
newline
A=0; B=0; C=0; D=0
7:return
end


routine index (realname A,B,C, arrayname Z,ZZ, integer n,type, c
integername N, integerarrayname h,k,l)

integer i,hh,kk,ll,K
array q(1:400)
real df, ang
switch L(0:3), M(0:3)

N=0
cycle i=1,1,n
cycle hh=0,1,8
cycle kk=0,1,8
cycle ll=0,1,8
q(i)=(sin(Z(i)))^2
->L(type)

L(0): df=|q(i)-A*(hh^2+kk^2+ll^2)|
->2
L(1): df=|q(i)-A*(hh^2+kk^2+hh*kk)-C*ll^2|
->2
L(2): df=|q(i)-A*(hh^2+kk^2)-C*ll^2|
->2
L(3): df=|q(i)-A*hh^2-B*kk^2-C*ll^2|
2:if df>0.002 then ->1
```

```
K=0
3:N=N+1
h(N)=hh; k(N)=kk; l(N)=ll; ZZ(N)=Z(i)
K=K+1
newline
print(h(N),1,0\\); print(k(N),1,0); print(l(N),1,0)
ang=ZZ(N)*180/π; print(ang,2,4); print(s(i),2,4)
print(df,1,5)

->M(type)
M(0): if hh=kk and K<2 then ->3
if hh=ll and K<2 then ->3
if kk=ll and K<2 then  ->3
if hh=kk and kk=ll and K<6 then ->3
->1
M(1): if hh=kk and K<2 then ->3
->1
M(2): if hh=kk and K<2 then->3
->1
M(3):->1
1:repeat
repeat
repeat
repeat

return
end

end of program
```

APPENDIX III

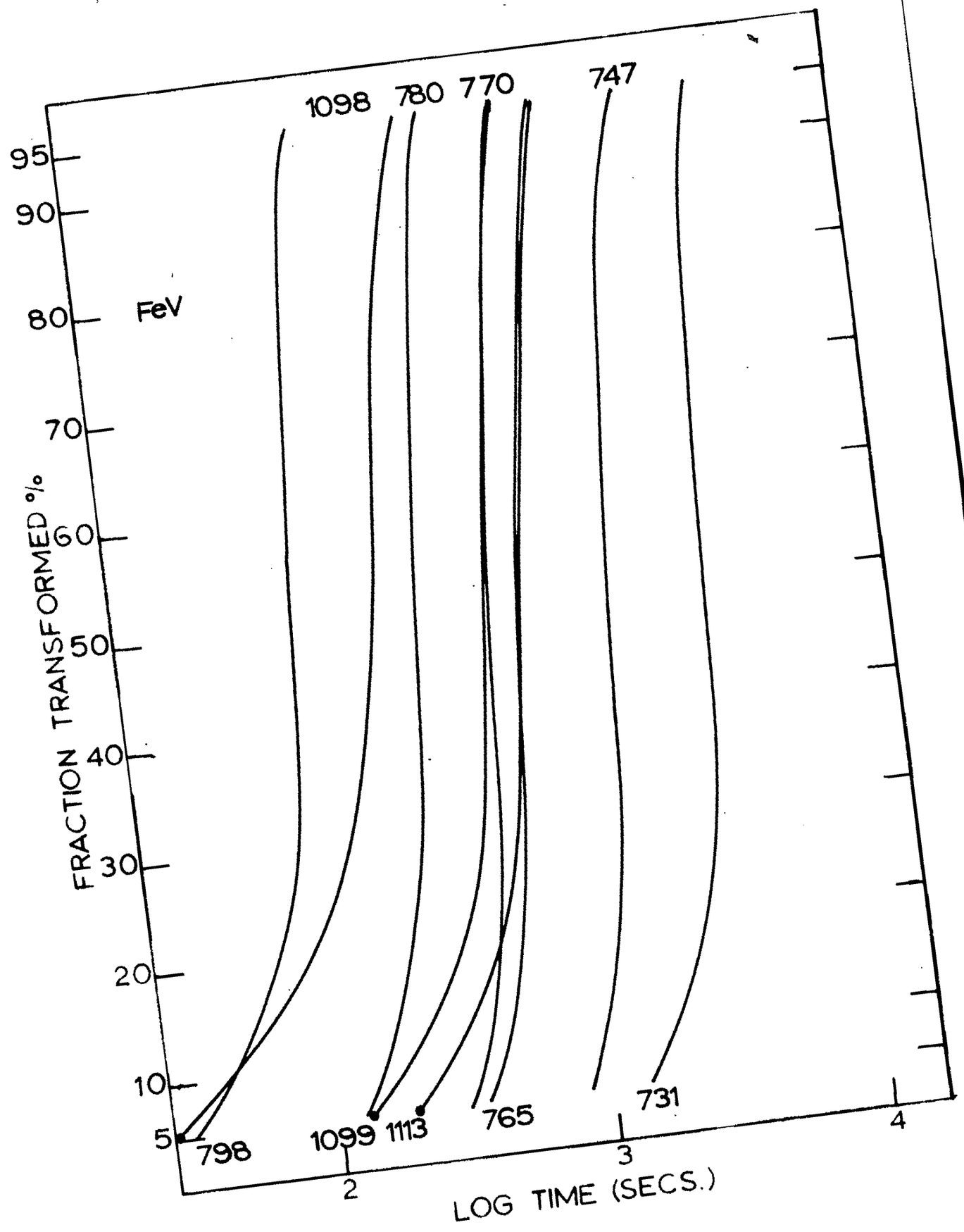
1098
780
770
747
95
90
80
FeV
70
60
50
40
30
20
10
5
FRACTION TRANSFORMED %
798
1099
1113
765
731
2
3
4
LOG TIME (SECS.)

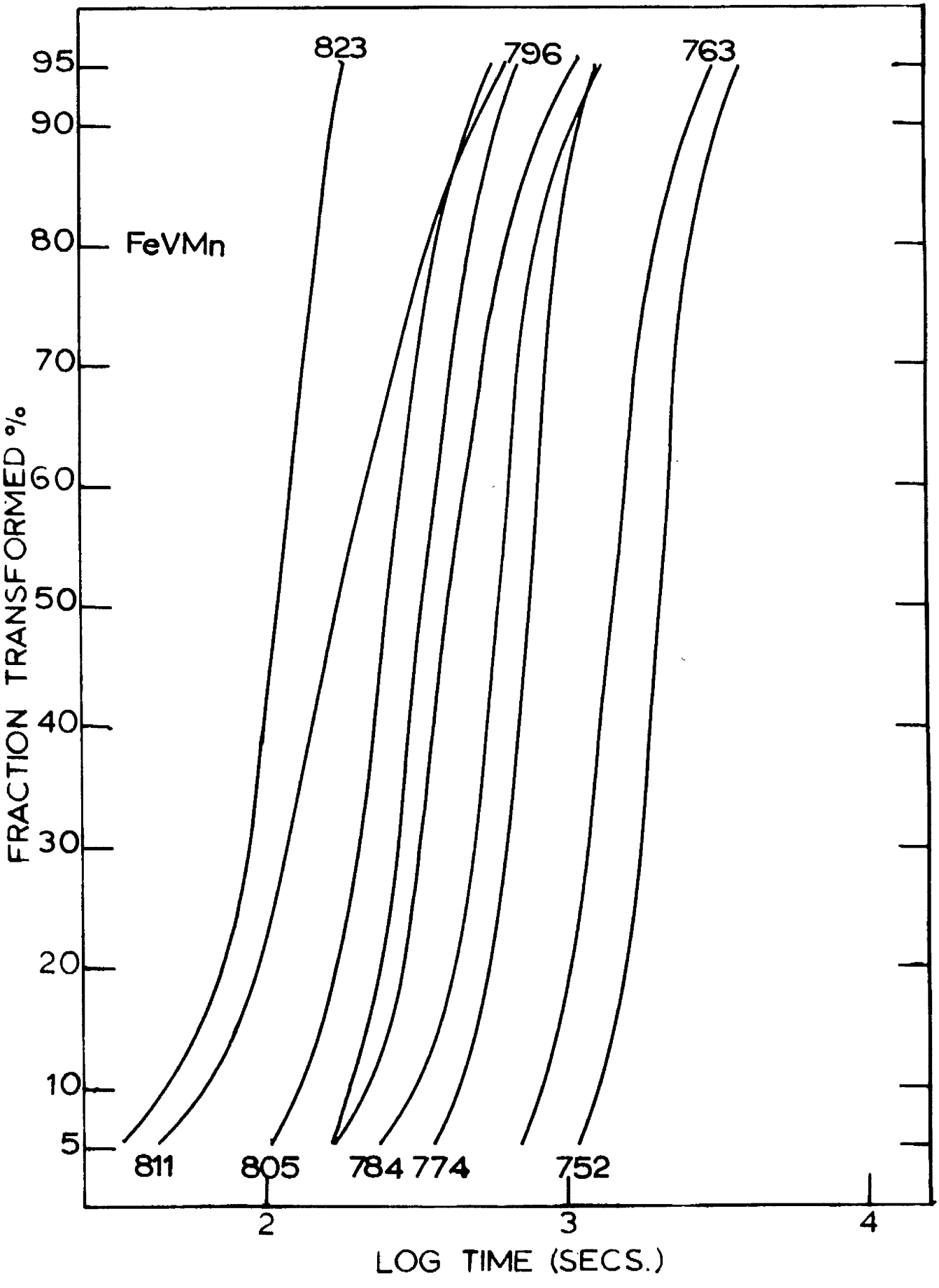
823
796
763
FeVMn
95
90
80
70
60
50
40
30
20
10
5
FRACTION TRANSFORMED %
811
805
784
774
752
2
3
4
LOG TIME (SECS.)

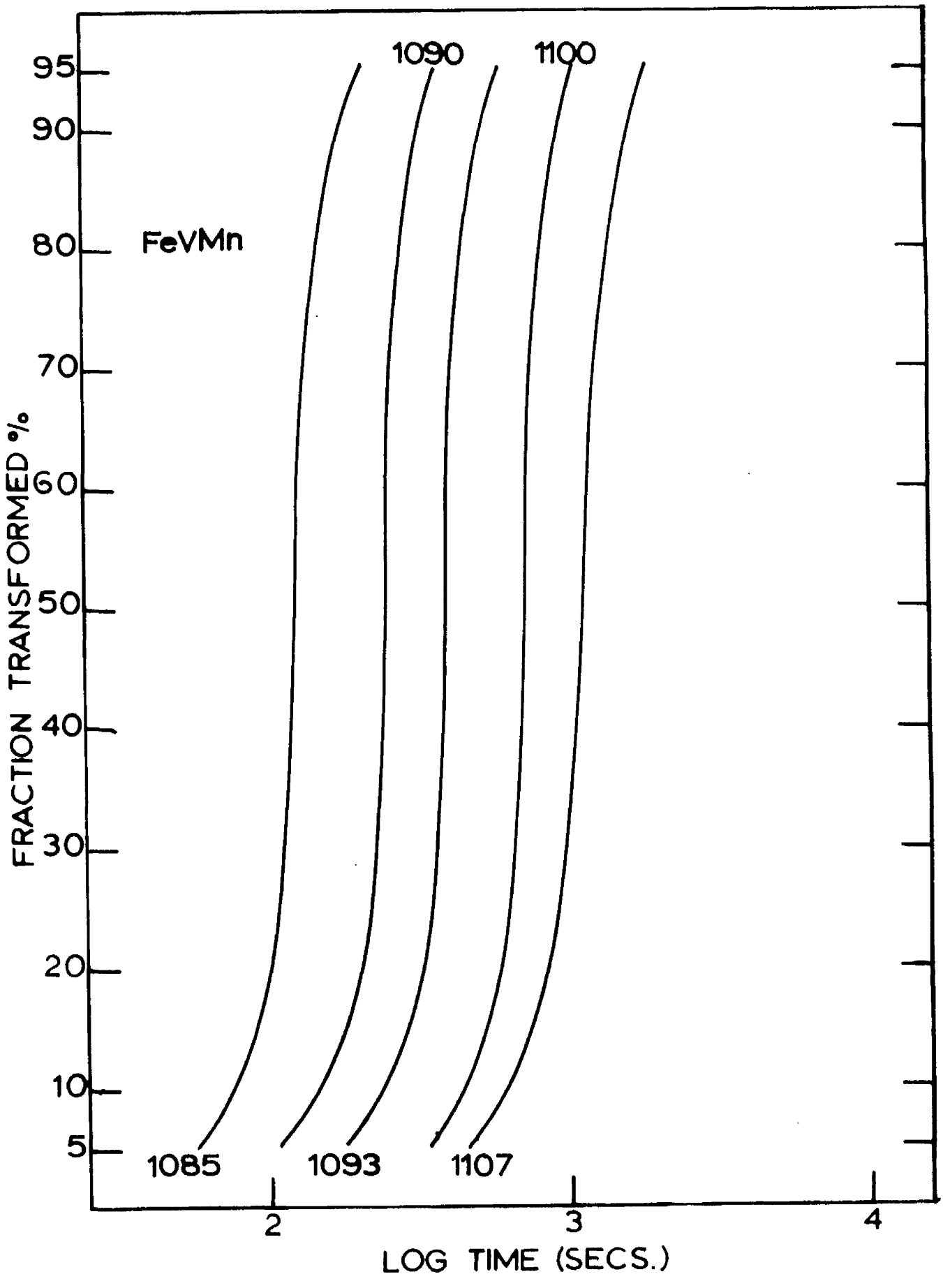
FeVMn
1090
1100
1085
1093
1107
95
90
80
70
60
50
40
30
20
10
5
FRACTION TRANSFORMED %
2
3
4
LOG TIME (SECS.)

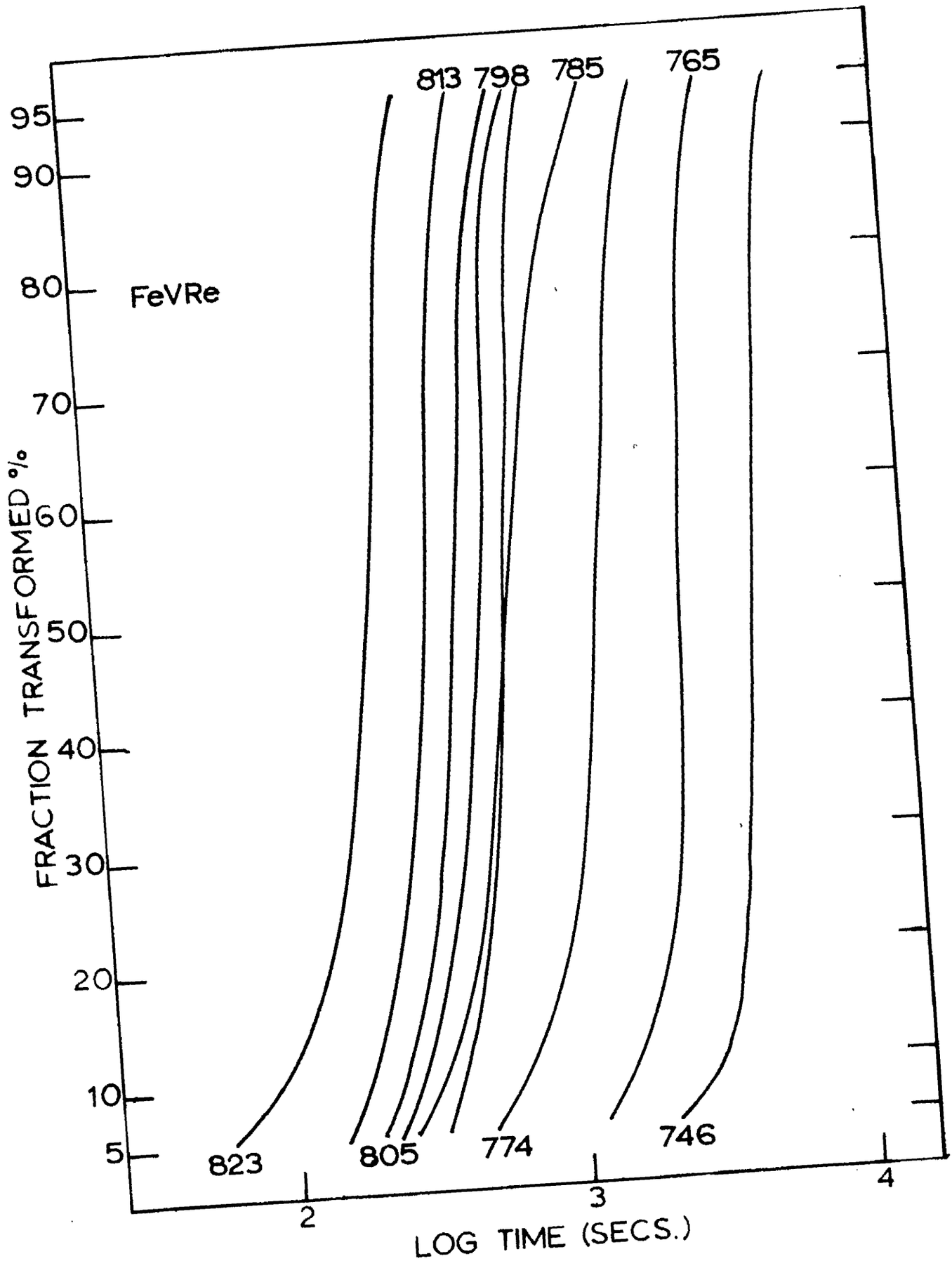
FeVRe
FRACTION TRANSFORMED %
95
90
80
70
60
50
40
30
20
10
5
813
798
785
765
823
805
774
746
2
3
4
LOG TIME (SECS.)

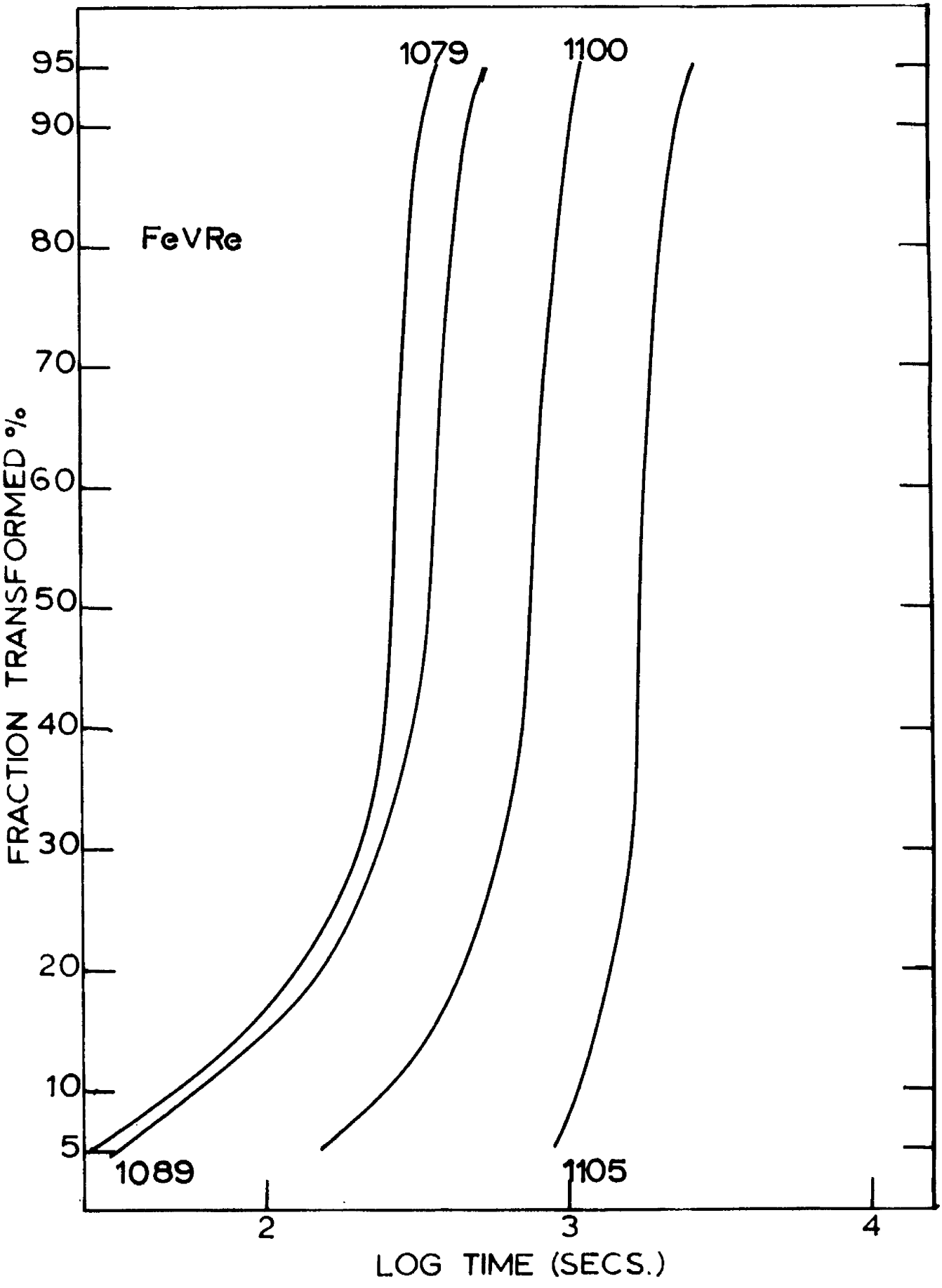
FeVRe
1079
1100
1089
1105
95
90
80
70
60
50
40
30
20
10
5
2
3
4
FRACTION TRANSFORMED %
LOG TIME (SECS.)

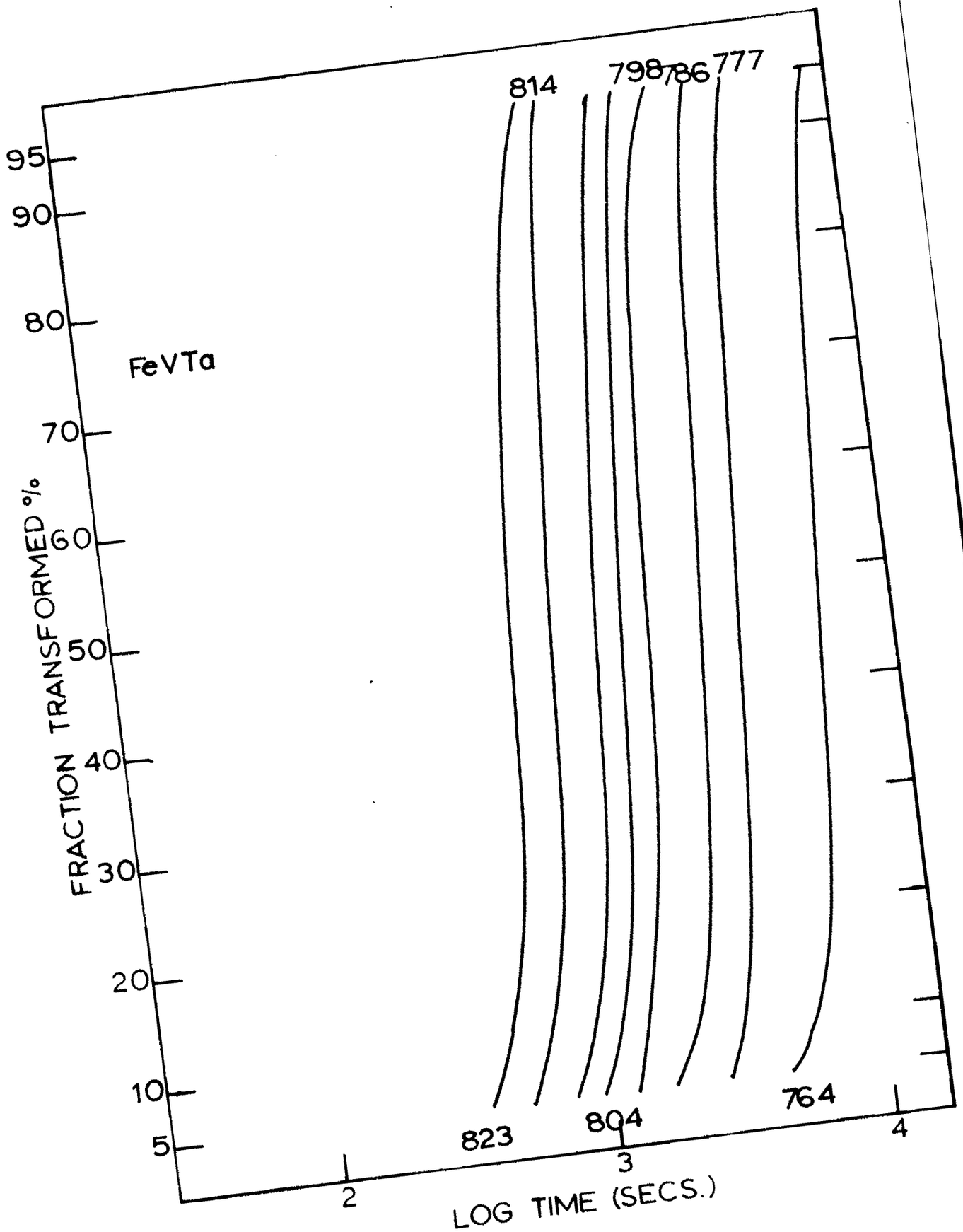
FeVTa
FRACTION TRANSFORMED %
95
90
80
70
60
50
40
30
20
10
5
814
798
786
777
764
823
804
2
3
4
LOG TIME (SECS.)

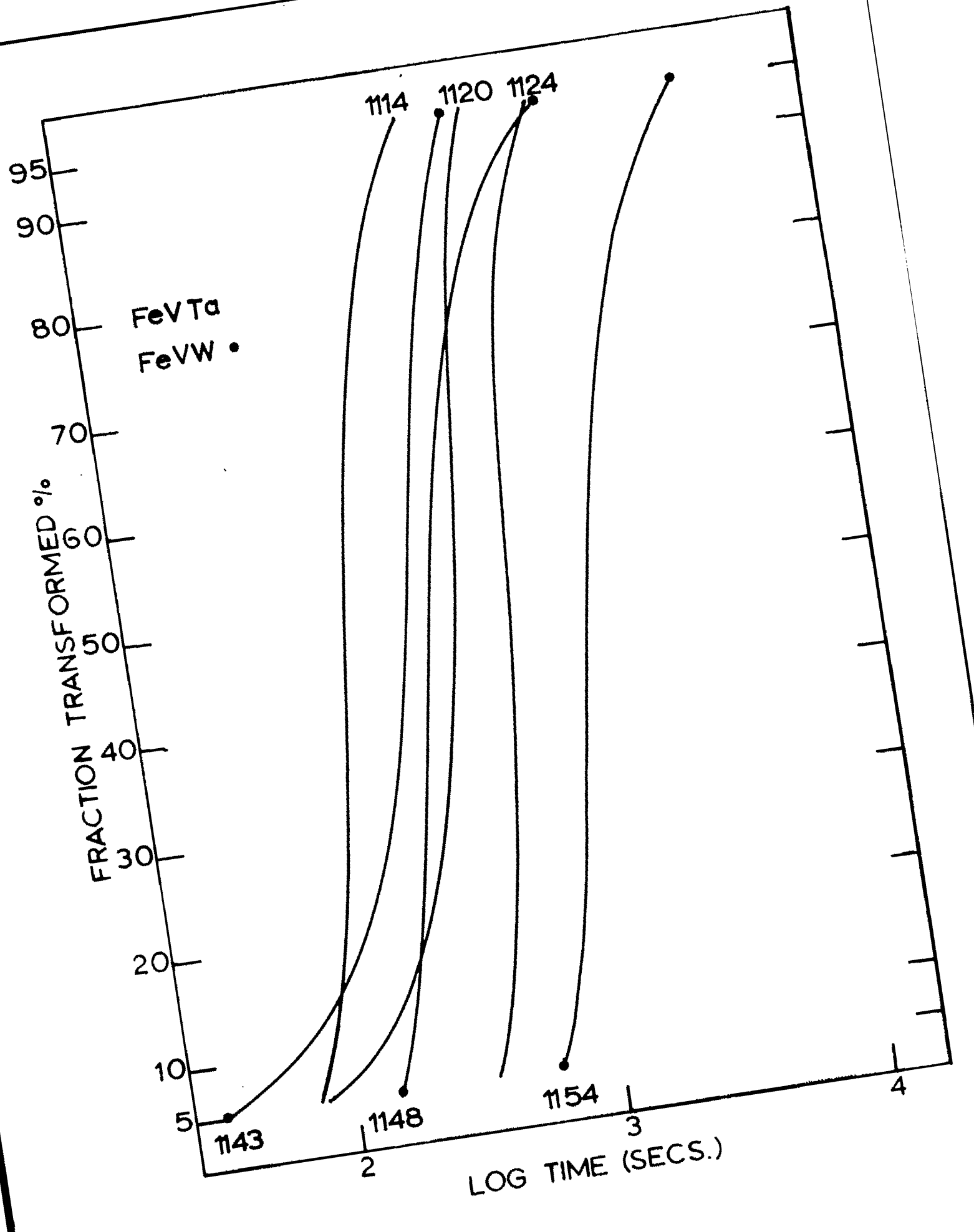
1114
1120
1124
95
90
80
70
60
50
40
30
20
10
5
FeVTa
FeVW •
FRACTION TRANSFORMED %
1143
1148
1154
2
3
4
LOG TIME (SECS.)

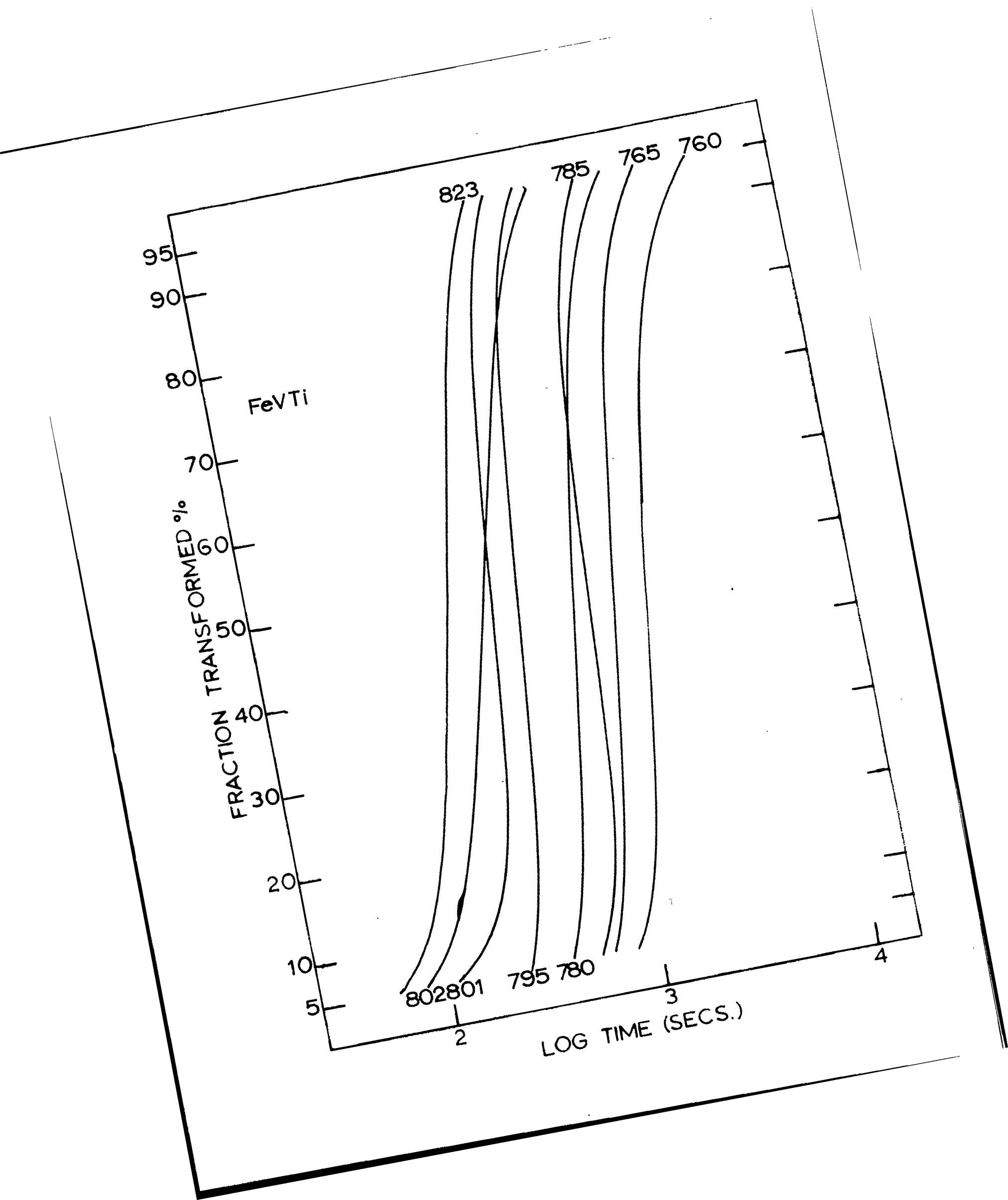
FeVTi
FRACTION TRANSFORMED %
95
90
80
70
60
50
40
30
20
10
5
2
3
4
LOG TIME (SECS.)
823
785
765
760
802
801
795
780

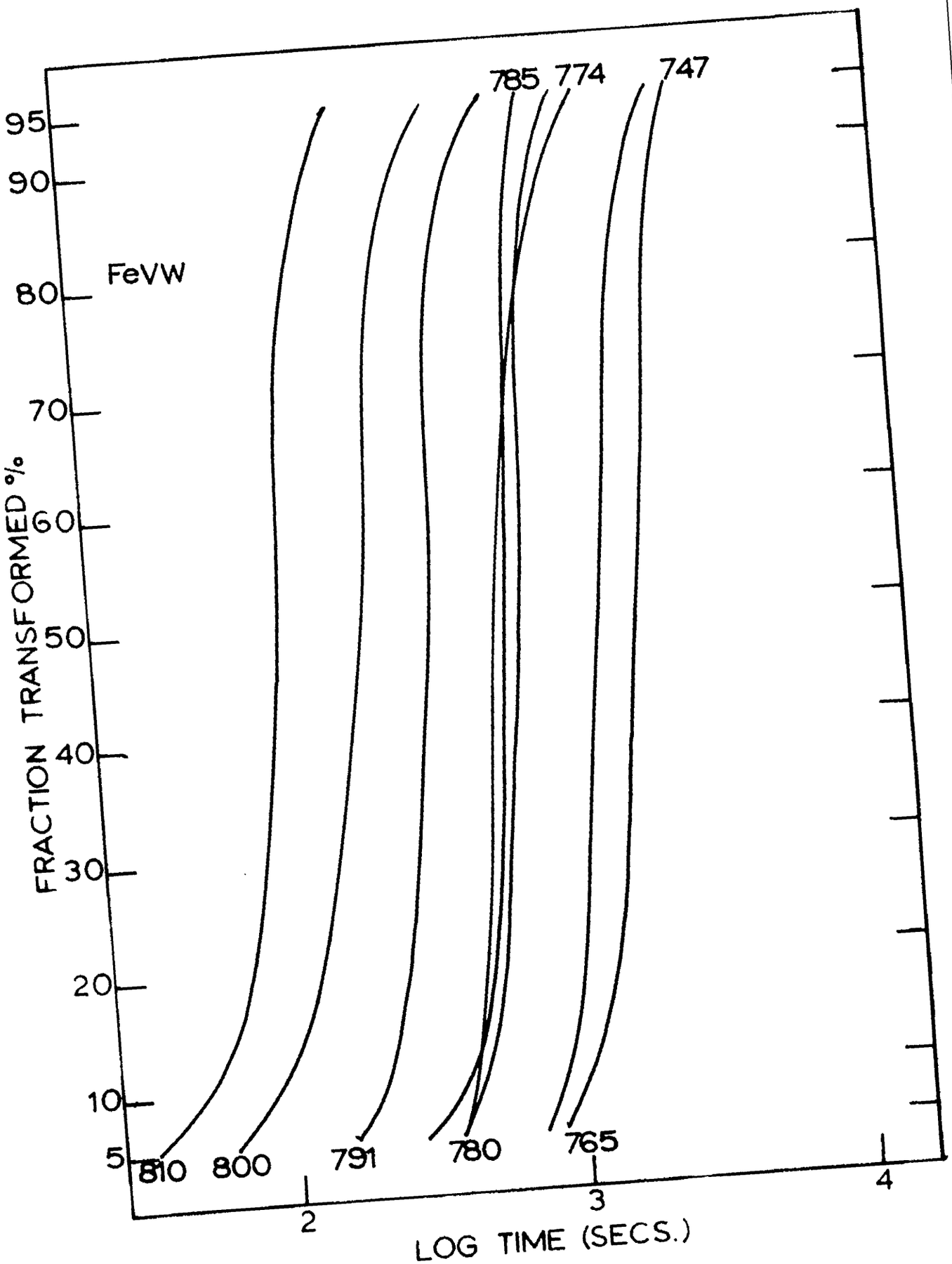
FeVW
FRACTION TRANSFORMED %
95
90
80
70
60
50
40
30
20
10
5
785
774
747
810
800
791
780
765
2
3
4
LOG TIME (SECS.)

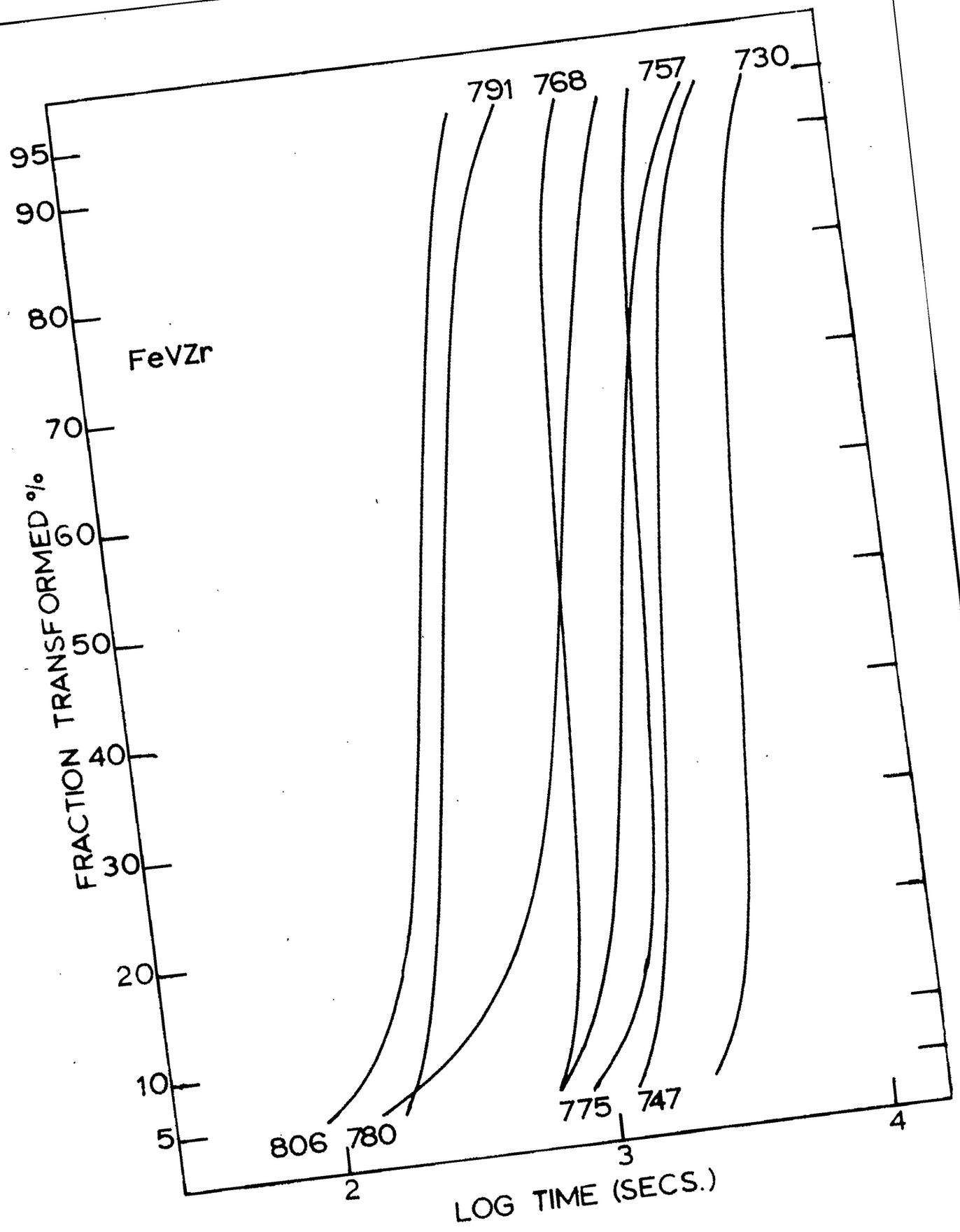
FeVZr
FRACTION TRANSFORMED %
95
90
80
70
60
50
40
30
20
10
5
791
768
757
730
806
780
775
747
2
3
4
LOG TIME (SECS.)

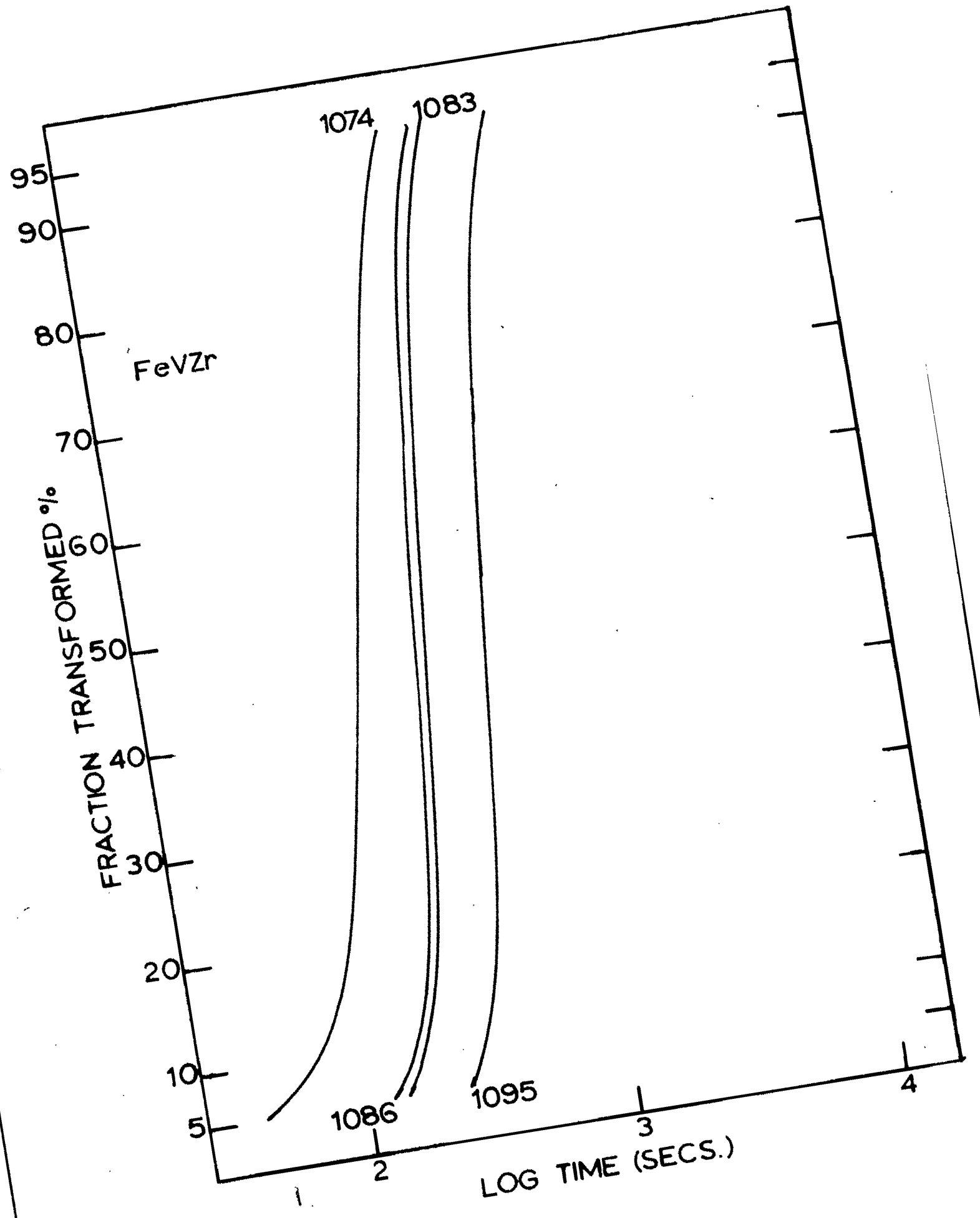
1074
1083
1086
1095
FeVZr
FRACTION TRANSFORMED %
95
90
80
70
60
50
40
30
20
10
5
1
2
3
4
LOG TIME (SECS.)